





INAUGURAL - DISSERTATION  
zur  
Erlangung der Doktorwürde  
der  
Naturwissenschaftlich-Mathematischen  
Gesamtfakultät  
der  
Ruprecht-Karls-Universität  
Heidelberg

vorgelegt von  
Dipl.-Phys. Erik Volk  
aus Frankenthal / Pfalz

Tag der mündlichen Prüfung: 10. Januar 2001



Messung des  $D^{*\pm}$ -Wirkungsquerschnittes  
im HERMES-Experiment

Gutachter: Dr. Antje Brüll  
Prof. Dr. Otto Nachtmann



Dissertation  
submitted to the  
Combined Faculties for the Natural Sciences and for Mathematics  
of the Rupertus Carola University of  
Heidelberg, Germany  
for the degree of  
Doctor of Natural Sciences

# **Measurement of the $D^{*\pm}$ Cross-section at HERMES**

presented by

Diplom-Physicist: Erik Volk

born in: Frankenthal / Pfalz , Germany

Heidelberg, 10. January 2001

Referees: Dr. Antje Brüll

Prof. Dr. Otto Nachtmann





## Messung des $D^{*\pm}$ -Wirkungsquerschnittes im HERMES-Experiment

Das Thema der vorliegenden Arbeit ist die Produktion von Charm-Quarks in der Elektron-Proton-Streuung. Der Nachweis erfolgt über die Identifikation von  $D^{*\pm}$ -Mesonen, die in der Fragmentation der primär erzeugten Charm-Quarks entstehen. Mittels der  $\Delta M$ -Methode werden die  $D^{*\pm}$ -Mesonen durch die Rekonstruktion der Zerfallskette  $D^{*+} \rightarrow D^0 \pi_s^+ \rightarrow (K^- \pi^+) \pi_s^+$  nachgewiesen.

Basierend auf den 1997 bei HERMES aufgezeichneten Daten wird der Wirkungsquerschnitt für die Elektroproduktion von  $D^{*\pm}$ -Mesonen bei stationärem Protonen-Target und einer Elektronen-Strahlenergie von 27.5 GeV extrahiert. Darauf aufbauend wird der Wirkungsquerschnitt für die Photoproduktion von Charm-Quarks bei einer Photonenergie von 15.5 GeV bestimmt. Der gemessene Wirkungsquerschnitt ist in guter Übereinstimmung mit dem einzigen anderen experimentellen Resultat bei vergleichbar niedrigen Photonenergien und in Einklang mit der Erwartung aus störungstheoretischen QCD-Rechnungen.

Mit Hilfe von zusätzlichen Daten, die in den Jahren 1998-2000 nach einem Ausbau des HERMES-Detektors aufgezeichnet wurden, erscheint es daher möglich, erstmalig die polarisierte Gluonverteilung aus der Charm-Produktion zu bestimmen.

## Measurement of the $D^{*\pm}$ Cross-section at HERMES

In this thesis, the production of charm quarks in lepton-nucleon scattering has been investigated. Open charm events are identified through the detection of  $D^{*\pm}$  mesons which are produced in the fragmentation of the charm quarks. The  $D^{*\pm}$  mesons are reconstructed in the decay chain  $D^{*+} \rightarrow D^0 \pi_s^+ \rightarrow (K^- \pi^+) \pi_s^+$  with the  $\Delta M$  method.

The total cross-section for the electroproduction of  $D^{*\pm}$  mesons on a proton target has been measured in a fixed target experiment with a lepton beam energy of 27.5 GeV. The analysis is based on data collected by HERMES in 1997. From this result, the open charm photoproduction cross section is determined for a photon energy of 15.5 GeV. The value for the cross section is found to be in good agreement with the only other experimental result at similarly low photon energies and does agree with the expectation of perturbative QCD.

With the upgrade of the HERMES detector and the large amount of additional data taken in 1998-2000, a first determination of the polarised gluon distribution from open charm production thus seems to be feasible.







# Contents

<b>1</b>	<b>Introduction</b>	<b>1</b>
<b>2</b>	<b>Deep-inelastic Lepton-Nucleon Scattering</b>	<b>3</b>
2.1	Inclusive Deep-inelastic Scattering . . . . .	5
2.1.1	Unpolarised Cross-section . . . . .	8
2.1.2	Polarised Cross-section and Asymmetries . . . . .	10
2.2	Quark Parton Model and Quantum Chromodynamics . . . . .	13
2.3	Semi-inclusive Deep-inelastic Scattering . . . . .	18
2.3.1	Fragmentation Functions . . . . .	18
2.3.2	Cross-sections and Asymmetries . . . . .	20
2.4	Nuclear Effects . . . . .	21
2.4.1	Nuclear Effects in Inclusive Structure Functions . . . . .	22
2.4.2	Hadronisation in a Nuclear Environment . . . . .	25
<b>3</b>	<b>Charm Production Near Threshold</b>	<b>29</b>
3.1	Production of Charm Quarks . . . . .	29
3.1.1	Photon-Gluon Fusion . . . . .	30
3.1.2	Additional Production Mechanisms . . . . .	32
3.1.3	Gluon Density . . . . .	34
3.2	Formation and Decay of Charmed Particles . . . . .	36
3.2.1	Monte Carlo Simulations . . . . .	39
<b>4</b>	<b>The HERMES Experiment</b>	<b>47</b>
4.1	The Polarised Electron Beam . . . . .	48
4.2	The HERMES Target Region . . . . .	50
4.3	The Spectrometer . . . . .	52
4.3.1	Tracking . . . . .	52
4.3.2	Particle Identification . . . . .	55
4.3.3	Luminosity . . . . .	58
4.3.4	Trigger . . . . .	60
4.3.5	Data Acquisition . . . . .	61
4.4	Software . . . . .	62

<b>5</b>	<b>Extraction of Cross-sections</b>	<b>65</b>
5.1	Detection Efficiencies . . . . .	66
5.1.1	Acceptance and Smearing . . . . .	66
5.1.2	Track Finding . . . . .	68
5.1.3	Trigger . . . . .	69
5.1.4	Data Acquisition System . . . . .	70
5.2	Time Integrated Luminosity . . . . .	71
5.3	Nuclear Cross-section Ratios . . . . .	72
5.4	Double Spin Asymmetries . . . . .	72
5.5	Data Selection . . . . .	73
<b>6</b>	<b>Quasi-real Photoproduction of <math>D^*</math> Mesons</b>	<b>77</b>
6.1	The Decays $D^{*\pm} \rightarrow (K^\mp \pi^\pm) \pi_s^\pm$ . . . . .	78
6.1.1	Monte Carlo Studies . . . . .	78
6.1.2	Event Selection . . . . .	80
6.1.3	Extracted Signals . . . . .	83
6.1.4	Background Subtraction . . . . .	84
6.2	Other Open Charm Channels . . . . .	88
6.3	Cross-section Determination . . . . .	93
6.3.1	Effective Luminosity . . . . .	93
6.3.2	Detection Efficiency Correction . . . . .	93
6.3.3	Isoscalar Targets . . . . .	95
6.3.4	$D^{*\pm}$ Cross-sections . . . . .	96
6.3.5	Open Charm Electroproduction Cross-section . . . . .	98
6.3.6	Open Charm Photoproduction Cross-section . . . . .	100
6.4	Monte Carlo Dependences . . . . .	102
6.5	Experimental Systematic Uncertainties . . . . .	103
<b>7</b>	<b>Summary</b>	<b>105</b>
<b>A</b>	<b>Definition of DIS kinematics</b>	<b>107</b>
<b>B</b>	<b>Charm Production: Model Dependences</b>	<b>109</b>
B.1	Production Probabilities of Primary Charmed Particles . . . . .	109
B.2	Energy Spectra . . . . .	113

---

<b>C Open Charm Cross-section: Model Dependences</b>	<b>119</b>
C.1 $D^{*\pm}$ Cross-sections . . . . .	119
<b>List of Figures</b>	<b>123</b>
<b>List of Tables</b>	<b>126</b>
<b>Bibliography</b>	<b>127</b>





# 1 Introduction

The goals of high energy physics are the exploration of the elementary constituents of matter and the derivation of the fundamental interactions between these constituents from as few and as simple first principles as possible. The present understanding of the structure of matter is represented by the Standard Model. It describes three of the four fundamental forces (electromagnetism, strong and weak interaction, gravitation) by formally very similar field theories: the electro-weak theory and Quantum Chromodynamics (QCD). The fundamental components of matter are elementary fermions (quarks and leptons) which interact through the exchange of gauge bosons (photons, gluons and the charged and neutral weak bosons). Even though the Standard Model is in very good agreement with all experimental results currently available, the description of compound objects such as the nucleon still lacks a derivation from first principles. To gain deeper insight, detailed investigations of the structure of the nucleons and related phenomena of the strong interaction can be used. One of the open questions there is how the spin of the nucleon is built up from its constituents. While the naive quark model successfully describes the magnetic moments of the nucleons, it fails in predicting the spin fraction carried by quarks. In 1987, the contribution from the quarks was measured to be consistent with zero, causing the so called “spin crisis”. Recent experiments found this value to be about 20%, still much less than the expectation from the relativistic quark model of about 60%.

Other sources of the nucleon spin are offered by various models of the nucleon structure: the spin alignment of sea and valence quarks may cancel in a complicated fashion, or the gluon intrinsic spin and/or parton orbital angular momenta may play important roles. As no rigorous conclusions may yet be calculated from QCD, experimental measurements of the nucleon spin structure are needed to distinguish amongst these interpretations.

First results on the spin contributions of quarks of different flavour have been obtained by SMC and HERMES. From semi-inclusive deep-inelastic scattering it was inferred that the contributions of the sea quarks to the nucleon spin is negligible. How to access the orbital angular momentum contribution is presently very much under discussion. Only recently a possible theoretical basis was developed through the description of exclusive processes such as deep-virtual Compton scattering in terms of off-forward parton distributions [Ji:97a, Ji:97b]. The explicit relation of this formalism to future measurements is only beginning to develop.

The contribution from gluon intrinsic spin can be derived from the scaling violations of the inclusive spin structure functions of the nucleon in deep-inelastic reactions. While this method has been successfully used to extract the unpolarised gluon distribution function, data with sufficiently high precision over a large range in momentum transfer are not yet available in the polarised case.

Consequently, the polarised gluon distribution is only poorly constrained, although there is some indication for the integral to be positive [BFR:96, E154:97, SMC:98].

A more direct access to the polarised gluon distribution is possible through the photon gluon fusion process. A first attempt for such a direct extraction has recently been performed at HERMES for the photoproduction of hadron pairs with large transverse momenta [HERMES:00a]. This result – also yielding a positive value for the gluon polarisation – however suffers from a rather large uncertainty related to the contributions of various background processes for the production of light quarks to the observed asymmetry. A much more reliable extraction can be achieved through the production of heavy quarks. Open charm production has already been successfully used in both the deep-inelastic and photoproduction regimes to derive the unpolarised gluon distribution [H1:99]. The remarkably good agreement also in comparison to the results obtained from the scaling violations of the inclusive structure functions can be understood as an important confirmation for the application of perturbative QCD and the universality of the gluon distribution in these processes. Several experimental proposals have recently been submitted to measure the polarised gluon distribution via the production of open charm [COMPASS:96, PHE:92, STAR:99].

In this thesis, the open charm photoproduction cross section is determined from the reconstruction of  $D^{*\pm}$  decays for a photon energy of 15.5 GeV. The analysis is based on data collected by HERMES in 1997. The value for the cross section is found to be in good agreement with the only other experimental result at similarly low photon energies and does agree with the expectation of perturbative QCD. With the upgrade of the HERMES detector and the large amount of additional data taken in 1998-2000, a first determination of the polarised gluon distribution from open charm production thus seems to be feasible.

## 2 Deep-inelastic Lepton-Nucleon Scattering

A scattering process is called *inelastic* if the number and/or types of the particles in the final state are different from those in the initial state. In contrast to an elastic process, inelastic scattering can be related to the breakup of at least one of the particles in the initial state and therefore be used to investigate the substructure of the participating probes. If the wavelength associated with the four-momentum exchanged in the interaction (the wavelength is inversely proportional to the absolute value of the four-momentum) is small compared to the dimensions of one of the initial particles the process is called *deep-inelastic*.

In lepton-nucleon scattering  $\ell + N \rightarrow \ell' + X$  a measurement is called *inclusive* if only the outgoing lepton  $\ell'$  is detected while in the *semi-inclusive* case also particles of the hadronic final state  $X$  are recorded in coincidence. If all particles in the final state and their kinematics are known the measurement is *exclusive*.

Inelastic lepton-nucleon scattering is mediated through the electroweak interaction. For centre of mass energies small compared to the high masses of the carriers of the weak force – the  $W^\pm$  and  $Z^0$  bosons – electromagnetic processes are however dominant. The lowest order electromagnetic contribution to deep-inelastic lepton-nucleon scattering – the one-photon exchange graph – is schematically depicted in Fig. 2.1. The importance of contributions from multi-photon exchange processes can be measured by comparing results from deep-inelastic scattering experiments utilising oppositely charged leptons. The interference between one- and two-photon exchange is sensitive to the charge of the lepton beam. Experimentally there is no evidence that the cross-section ratio  $\sigma(e^+)/\sigma(e^-)$  deviates from unity [LP:82].

Due to the particular circumstances at HERA and HERMES where longitudinally polarised electrons or positrons with an energy<sup>1</sup> of 27.5 GeV interact with a stationary target the follow-

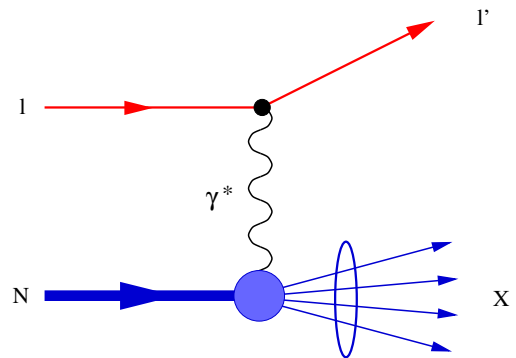


Figure 2.1: Schematic diagram of deep-inelastic lepton-nucleon scattering.

<sup>1</sup>Throughout this work the common convention  $\hbar = c = 1$  for the system of units will be used.

ing sections will focus on charged leptons and electromagnetic processes within the one-photon exchange approximation.

Before going into the details of the scattering process it is useful to define a set of Lorentz-invariant kinematical quantities. The four-momentum and spin four-vector of the lepton will be denoted with  $\mathbf{k}$  and  $\mathbf{s}$  respectively; analogously  $\mathbf{k}'$ ,  $\mathbf{s}'$  for the scattered lepton and  $\mathbf{P}$ ,  $\mathbf{S}$  for the target nucleon (see Fig. 2.2).

A frame of particular interest to the experimentalist is the laboratory frame. In a fixed target experiment as HERMES and when neglecting the thermal motion of the target atoms as well as the Fermi motion of the nucleons within the atoms, this frame coincides with the nucleon rest frame. This is a good approximation when the energies of incident and scattered leptons are large compared to the lepton mass.<sup>2</sup>

With these conventions and notations the centre of mass energy  $\sqrt{s}$  is given by

$$s \equiv (\mathbf{k} + \mathbf{P})^2. \quad (2.1)$$

A virtual photon is exchanged between lepton and target nucleon which carries the four-momentum

$$\mathbf{q} = \mathbf{k} - \mathbf{k}'. \quad (2.2)$$

The negative squared four-momentum transfer is then given by the expression

$$Q^2 \equiv -\mathbf{q}^2 = -(\mathbf{k} - \mathbf{k}')^2 > 0, \quad (2.3)$$

while with

$$\nu \equiv \frac{\mathbf{P} \cdot \mathbf{q}}{M} \stackrel{Lab}{=} E - E', \quad (2.4)$$

$$y \equiv \frac{\mathbf{P} \cdot \mathbf{q}}{\mathbf{P} \cdot \mathbf{k}} \stackrel{Lab}{=} \frac{\nu}{E} \quad (2.5)$$

the absolute and relative energy transfers of the lepton to the nucleon in the laboratory frame can be defined. They range between  $0 < \nu < E$  and  $0 < y < 1$  respectively.

The transferred momentum and energy are carried away by the hadronic final state which has a squared invariant mass of

$$W^2 \equiv (\mathbf{P} + \mathbf{q})^2 = M^2 + 2 M \nu - Q^2 \geq M^2 = \mathbf{P}^2. \quad (2.6)$$

With the definition of the dimensionless variable

$$x \equiv \frac{-\mathbf{q}^2}{2 \mathbf{P} \cdot \mathbf{q}} = \frac{Q^2}{2 M \nu} = \frac{Q^2}{Q^2 + W^2 - M^2} \quad (2.7)$$

a measure for the inelasticity of the process is obtained. Its physical range is given by  $0 < x \leq 1$  as can be seen by Eq. 2.6. The limit  $x = 1$  corresponds to case of elastic scattering, where  $W^2 = M^2$ .

The most important kinematical variables and their definitions are summarised in Tab. A.1.

---

<sup>2</sup>Please note that in many of the formulas which are only valid in the laboratory frame also the squared lepton mass is neglected.

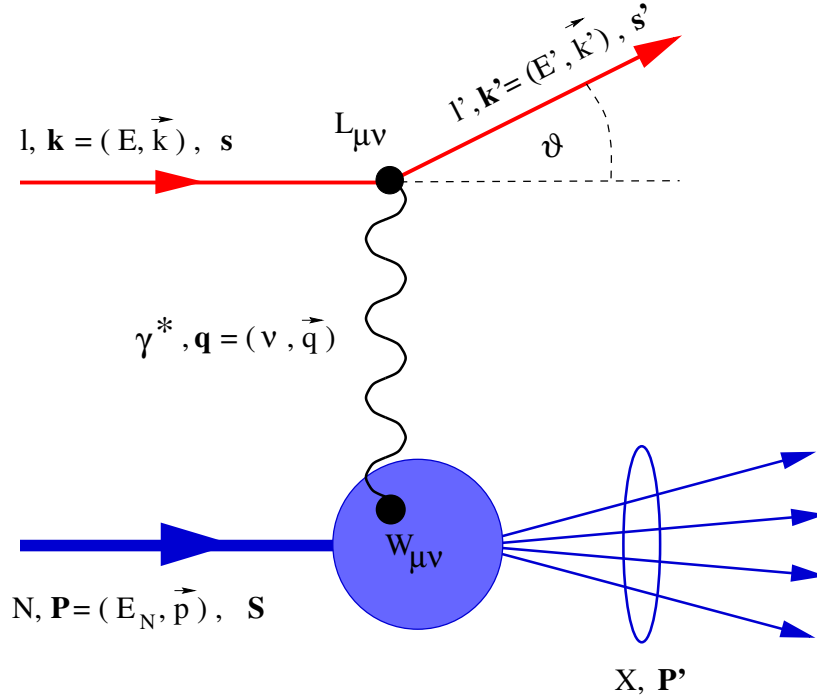


Figure 2.2: Schematic picture of deep-inelastic lepton-nucleon scattering in the one-photon exchange approximation.

## 2.1 Inclusive Deep-inelastic Scattering

In the one-photon exchange approximation the differential deep-inelastic cross-section for detecting the scattered lepton in the solid angle  $d\Omega$  and the energy range  $[E', E' + dE']$  can be written as (see [AEL:95, LP:82])

$$\frac{d\sigma}{d\Omega dE'}(\mathbf{k}, \mathbf{s}, \mathbf{P}, \mathbf{S}; \mathbf{k}', \mathbf{s}') = \frac{\alpha^2}{2MQ^4} \frac{E'}{E} L_{\mu\nu}(\mathbf{k}, \mathbf{s}; \mathbf{k}', \mathbf{s}') W^{\mu\nu}(\mathbf{q}; \mathbf{P}, \mathbf{S}), \quad (2.8)$$

where  $\alpha$  is the electromagnetic fine structure constant.

The leptonic tensor  $L_{\mu\nu}$  appearing in Eq. 2.8 is calculable in quantum electrodynamics (QED). Since the polarisation of the scattered lepton cannot be measured at HERMES, a summation over the states  $\mathbf{s}'$  will be performed. Then the leptonic tensor can be split into symmetric ( $S$ ) and antisymmetric ( $A$ ) parts under the exchange of  $\mu$  and  $\nu$

$$\begin{aligned} L_{\mu\nu}(\mathbf{k}, \mathbf{s}; \mathbf{k}') &\equiv \sum_{\mathbf{s}'} L_{\mu\nu}(\mathbf{k}, \mathbf{s}; \mathbf{k}', \mathbf{s}') \\ &= L_{\mu\nu}^{(S)}(\mathbf{k}; \mathbf{k}') + i L_{\mu\nu}^{(A)}(\mathbf{k}, \mathbf{s}; \mathbf{k}'). \end{aligned} \quad (2.9)$$

The symmetric part is spin-independent

$$L_{\mu\nu}^{(S)}(\mathbf{k}; \mathbf{k}') = 2 \left[ \mathbf{k}_\mu \mathbf{k}'_\nu + \mathbf{k}'_\mu \mathbf{k}_\nu - g_{\mu\nu} (\mathbf{k} \cdot \mathbf{k}' - m^2) \right], \quad (2.10)$$

and the spin information is contained in the antisymmetric part

$$L_{\mu\nu}^{(A)}(\mathbf{k}, \mathbf{s}; \mathbf{k}') = 2m \epsilon_{\mu\nu\alpha\beta} s^\alpha (\mathbf{k} - \mathbf{k}')^\beta. \quad (2.11)$$

Here  $m$  is the lepton mass,  $g_{\mu\nu}$  the metric tensor, and  $\epsilon_{\alpha\beta\gamma\delta}$  the totally antisymmetric Levi-Civita tensor with the convention  $\epsilon_{0123} = +1$ .

The hadronic tensor  $W_{\mu\nu}$  in Eq. 2.8 however cannot be derived from first principles. Using Lorentz covariance, parity and current conservation of the electromagnetic current as well as invariance under time reversal the hadronic tensor for a spin- $\frac{1}{2}$  target can also be split into a spin-independent symmetric and a spin-dependent antisymmetric part

$$W_{\mu\nu}(\mathbf{q}; \mathbf{P}, \mathbf{S}) = W_{\mu\nu}^{(S)}(\mathbf{q}; \mathbf{P}) + i W_{\mu\nu}^{(A)}(\mathbf{q}; \mathbf{P}, \mathbf{S}). \quad (2.12)$$

The ansatz

$$\begin{aligned} \frac{1}{2M} W_{\mu\nu}^{(S)}(\mathbf{q}; \mathbf{P}) &= \left( -g_{\mu\nu} + \frac{\mathbf{q}_\mu \mathbf{q}_\nu}{\mathbf{q}^2} \right) W_1(\mathbf{P} \cdot \mathbf{q}, \mathbf{q}^2) \\ &+ \left[ \left( \mathbf{P}_\mu - \frac{\mathbf{P} \cdot \mathbf{q}}{\mathbf{q}^2} \mathbf{q}_\mu \right) \left( \mathbf{P}_\nu - \frac{\mathbf{P} \cdot \mathbf{q}}{\mathbf{q}^2} \mathbf{q}_\nu \right) \right] \frac{W_2(\mathbf{P} \cdot \mathbf{q}, \mathbf{q}^2)}{M^2}, \end{aligned} \quad (2.13)$$

$$\begin{aligned} \frac{1}{2M} W_{\mu\nu}^{(A)}(\mathbf{q}; \mathbf{P}, \mathbf{S}) &= \epsilon_{\mu\nu\alpha\beta} \mathbf{q}^\alpha \left\{ M S^\beta G_1(\mathbf{P} \cdot \mathbf{q}, \mathbf{q}^2) \right. \\ &+ \left. [(\mathbf{P} \cdot \mathbf{q}) S^\beta - (\mathbf{S} \cdot \mathbf{q}) \mathbf{P}^\beta] \frac{G_2(\mathbf{P} \cdot \mathbf{q}, \mathbf{q}^2)}{M} \right\}, \end{aligned} \quad (2.14)$$

introduces four scalar functions  $W_1$ ,  $W_2$ ,  $G_1$ ,  $G_2$  to describe the inner structure of the target. These structure functions can only depend on the two independent scalar combinations of  $\mathbf{q}$  and  $\mathbf{P}$  which can be chosen to be  $\nu$  and  $Q^2$ .

Equivalently one can use the dimensionless structure functions

$$\begin{aligned} F_1(\nu, Q^2) &= M W_1(\nu, Q^2), & g_1(\nu, Q^2) &= M^2 \nu G_1(\nu, Q^2), \\ F_2(\nu, Q^2) &= \nu W_2(\nu, Q^2), & g_2(\nu, Q^2) &= M \nu^2 G_2(\nu, Q^2), \end{aligned} \quad (2.15)$$

which will have an intuitive interpretation in the quark parton model (QPM) (see Sec. 2.2).

In case of very high energies, when the weak interaction cannot be neglected, only Lorentz and  $CP$  invariance can be used to reduce the number of degrees of freedom in the hadronic tensor. The most general form for the hadronic tensor then includes eight scalar structure functions [AEL:95], three unpolarised ( $F_1$ ,  $F_2$ ,  $F_3$ ), and five polarised ones ( $g_1$ ,  $g_2$ ,  $g_3$ ,  $g_4$ ,  $g_5$ ).

A different approach to deep-inelastic scattering relates the hadronic tensor with the off-shell photo-absorption cross-section in forward scattering of polarised virtual photons off polarised nucleons using the optical theorem [LP:82, Hey:74]. There are four independent amplitudes involved, specified by the helicities of the virtual photon and the nucleon (all other amplitudes are related by parity and time-reversal invariance). Conventionally the four transitions are labeled by the total angular momentum  $J_z$  involved and a “L” or “T” to indicate a “longitudinal” ( $\lambda_\gamma = 0$ ) or “transverse” ( $\lambda_\gamma = +1$ ) photon.

Initial		Final		Label	
$\lambda_\gamma$	$\Lambda_N$	$\lambda'_\gamma$	$\Lambda'_N$	$J_z$	
1	$\frac{1}{2}$	1	$\frac{1}{2}$	$\frac{3}{2}$	T
1	$-\frac{1}{2}$	1	$-\frac{1}{2}$	$\frac{1}{2}$	T
0	$-\frac{1}{2}$	1	$\frac{1}{2}$	$\frac{1}{2}$	LT
0	$\frac{1}{2}$	0	$\frac{1}{2}$	$\frac{1}{2}$	L

Table 2.1: *Notation for transitions in forward virtual Compton amplitudes.*

Introducing

$$\gamma^2 \equiv \frac{Q^2}{\nu^2} = \frac{4M^2 x^2}{Q^2}, \quad (2.16)$$

the relations between the structure functions, the imaginary parts of the forward virtual Compton amplitudes  $A_{\lambda'\Lambda';\lambda\Lambda}$ , and the photo-absorption cross-sections are<sup>3</sup>

$$\begin{aligned} \sigma_{\frac{1}{2}}^T(\nu, Q^2) &\propto \text{Im } A_{1\frac{1}{2};1\frac{1}{2}} = \frac{1}{M} (F_1 + g_1 - \gamma^2 g_2), \\ \sigma_{\frac{3}{2}}^T(\nu, Q^2) &\propto \text{Im } A_{1-\frac{1}{2};1-\frac{1}{2}} = \frac{1}{M} (F_1 - g_1 + \gamma^2 g_2), \\ \sigma_{\frac{1}{2}}^L(\nu, Q^2) &\propto \text{Im } A_{0\frac{1}{2};0\frac{1}{2}} = \frac{1}{M} \left( \frac{1+\gamma^2}{2x} F_2 - F_1 \right), \\ \sigma_{\frac{1}{2}}^{LT}(\nu, Q^2) &\propto \text{Im } A_{0-\frac{1}{2};1\frac{1}{2}} = \frac{1}{M} \gamma (g_1 + g_2), \end{aligned} \quad (2.17)$$

where the same proportionality factor  $4\pi^2\alpha/K$  appears in all four equations, with  $K$  being the flux factor for virtual photons. In a possible convention introduced by Hand [Han:63] it evaluates to  $K = \nu - Q^2/2M$ . One then usually introduces asymmetry parameters for the virtual photon nucleon scattering according to

$$A_1(\nu, Q^2) \equiv \frac{\sigma_{\frac{1}{2}}^T - \sigma_{\frac{3}{2}}^T}{\sigma_{\frac{1}{2}}^T + \sigma_{\frac{3}{2}}^T} = \frac{1}{F_1} (g_1 - \gamma^2 g_2), \quad (2.18)$$

$$A_2(\nu, Q^2) \equiv \frac{\sigma_{\frac{1}{2}}^{LT}}{\frac{1}{2} (\sigma_{\frac{1}{2}}^T + \sigma_{\frac{3}{2}}^T)} = \frac{1}{F_1} \gamma (g_1 + g_2). \quad (2.19)$$

These asymmetries quantify the differences in the cross-sections involving a helicity change of the nucleon without ( $A_1$ ) and with ( $A_2$ ) a helicity change of the photon [Rob:90]. Using these expressions one can express the polarised structure functions in terms of the virtual photon asymmetries  $A_1$  and  $A_2$

$$g_1(\nu, Q^2) = \frac{F_1}{1 + \gamma^2} (A_1 - \gamma A_2), \quad (2.20)$$

$$g_2(\nu, Q^2) = \frac{F_1}{1 + \gamma^2} \left( -A_1 + \frac{1}{\gamma} A_2 \right). \quad (2.21)$$

<sup>3</sup>For sake of brevity and readability the obvious dependences on  $\nu$  and  $Q^2$  will be omitted for the rest of this section in the RHS of formulas.

Abbreviating additionally the longitudinal and transverse photo-absorption cross-sections with

$$\sigma_L(\nu, Q^2) \equiv \sigma_{\frac{1}{2}}^L, \quad (2.22)$$

$$\sigma_T(\nu, Q^2) \equiv \frac{1}{2} \left( \sigma_{\frac{1}{2}}^T + \sigma_{\frac{3}{2}}^T \right), \quad (2.23)$$

their ratio relates the unpolarised structure functions  $F_1$  and  $F_2$

$$R(\nu, Q^2) \equiv \frac{\sigma_L}{\sigma_T} = \left( 1 + \gamma^2 \right) \frac{F_2}{2x F_1} - 1. \quad (2.24)$$

It is found to be very small at large values of  $Q^2$  [Rit:83] while at HERMES with  $\langle Q^2 \rangle \approx 2.5 \text{ GeV}^2$  it ranges from  $R = 0.32 \dots 0.19$  for  $x = 0.02 \dots 0.7$  and was measured to be identical within errors for proton and neutron (see Fig. 2.3).

At large values of  $Q^2$  the relations between the polarised structure functions simplify significantly. Not only can be seen from Eq. 2.16 that  $\gamma^2$  gets very small but also it can be shown that

$$|A_2|^2 \leq R. \quad (2.25)$$

Therefore instead of Eqs. 2.18 and 2.20 often only the approximations

$$A_1 \approx \frac{g_1}{F_1}, \quad g_1 \approx A_1 \frac{F_2}{2x [1 + R]}, \quad (2.26)$$

are used.

### 2.1.1 Unpolarised Cross-section

The unpolarised inclusive cross-section of deep-inelastic scattering is obtained by averaging Eq. 2.8 over the spin states of the initial particles and summing over the spin states of the scattered lepton

$$\begin{aligned} \frac{d\sigma_{\text{unp}}}{d\Omega dE'}(\mathbf{k}, \mathbf{P}; \mathbf{k}') &= \frac{1}{4} \sum_{\mathbf{s}, \mathbf{S}, \mathbf{s}'} \frac{d\sigma}{d\Omega dE'}(\mathbf{k}, \mathbf{s}, \mathbf{P}, \mathbf{S}; \mathbf{k}', \mathbf{s}') \\ &= \frac{\alpha^2}{2MQ^4} \frac{E'}{E} L_{\mu\nu}^{(S)}(\mathbf{k}; \mathbf{k}') W^{\mu\nu(S)}(\mathbf{q}; \mathbf{P}). \end{aligned} \quad (2.27)$$

Using the explicit expressions 2.10 and 2.14 for the symmetric parts of the leptonic and hadronic tensors the dependence of the cross-section on the scattering angle  $\vartheta$  of the outgoing lepton can be derived

$$\frac{d\sigma_{\text{unp}}}{d\Omega dE'} = \frac{4\alpha^2 E'^2}{Q^4} \left[ \frac{2}{M} F_1(\nu, Q^2) \sin^2\left(\frac{\vartheta}{2}\right) + \frac{1}{\nu} F_2(\nu, Q^2) \cos^2\left(\frac{\vartheta}{2}\right) \right]. \quad (2.28)$$



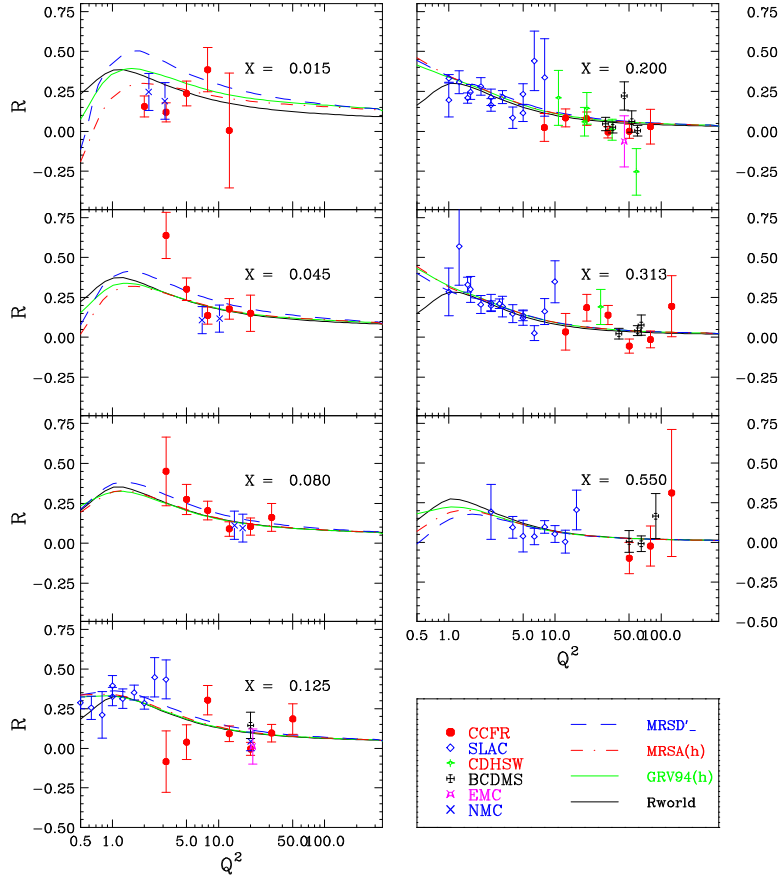


Figure 2.3: World data for the ratio of longitudinal and transverse photo-absorption cross-sections of free nucleons,  $R(x, Q^2) = \sigma_L/\sigma_T$ , taken from [CCFR:98].

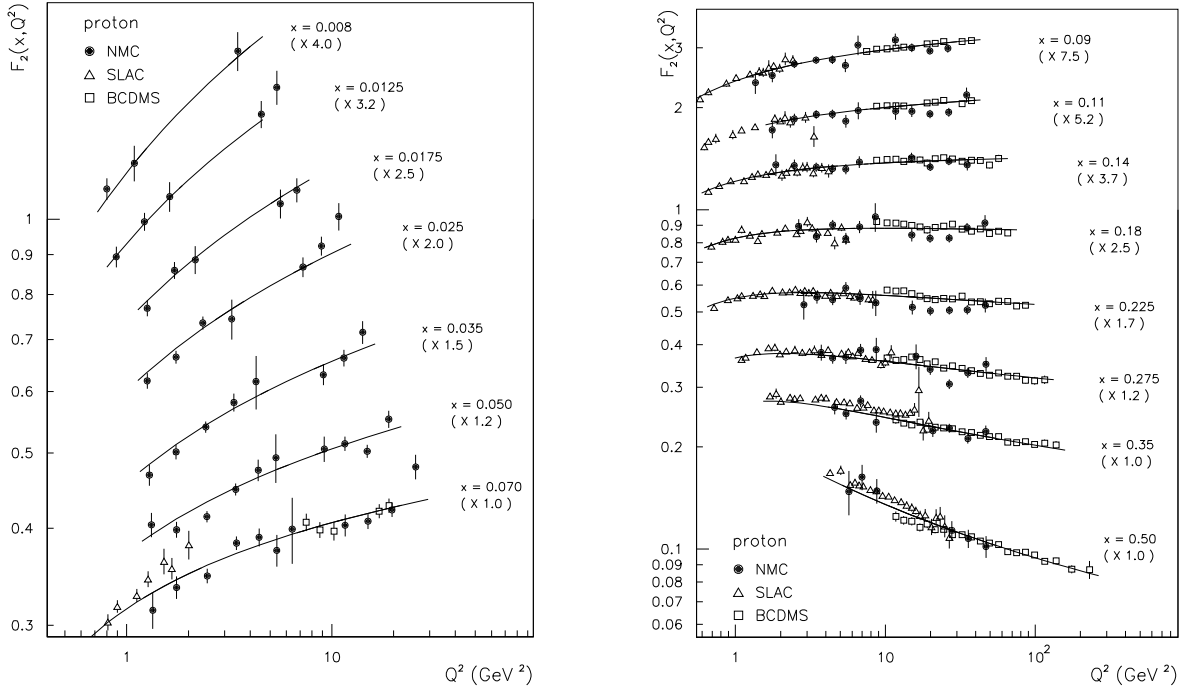


Figure 2.4: World data on the proton structure function  $F_2^p$  from fixed target experiments and the result of a QCD fit [NMC:97].

Integrating out the trivial dependence on the azimuthal angle, substituting  $F_1$  with  $R$ , and transforming the variables leads to

$$\frac{d\sigma_{\text{unp}}}{dx dQ^2} = \frac{4\pi\alpha^2}{xQ^4} \left[ 1 - y - \frac{Q^2}{4E^2} + \frac{y^2 + \frac{Q^2}{E^2}}{2(1 + R(x, Q^2))} \right] F_2(x, Q^2). \quad (2.29)$$

Precise measurements for the structure function  $F_2$  of proton and deuteron have been performed by a series of experiments covering a wide kinematic range of  $10^{-6} \leq x \leq 0.9$  and  $0.1 \text{ GeV}^2 \leq Q^2 \leq 5 \cdot 10^3 \text{ GeV}^2$ . The world data for  $F_2^p$  from fixed target experiments are shown in Fig. 2.4 while results from colliders can be found in [C<sup>+</sup>:98].

### 2.1.2 Polarised Cross-section and Asymmetries

To get access to the polarised structure functions of the nucleon one needs to single out the term containing the asymmetric parts of leptonic and hadronic tensor in the cross-section formula Eq. 2.8. This can be achieved by taking the difference of the cross-sections with opposite target spin orientations  $-\mathbf{S}$  and  $\mathbf{S}$

$$\sum_{s'} \left[ \frac{d\sigma}{d\Omega dE'}(\mathbf{k}, \mathbf{s}, \mathbf{P}, -\mathbf{S}; \mathbf{k}', s') - \frac{d\sigma}{d\Omega dE'}(\mathbf{k}, \mathbf{s}, \mathbf{P}, \mathbf{S}; \mathbf{k}', s') \right] = \frac{\alpha^2}{2MQ^4} \frac{E'}{E} L_{\mu\nu}^{(A)}(\mathbf{k}, \mathbf{s}; \mathbf{k}') W^{\mu\nu(A)}(\mathbf{q}; \mathbf{P}, \mathbf{S}). \quad (2.30)$$

Denoting the angle between  $\mathbf{k}$  and  $\mathbf{S}$  with  $\alpha$  and the angle between the scattering plane (defined by  $\mathbf{k}$  and  $\mathbf{k}'$ ) and the polarisation plane (defined by  $\mathbf{k}$  and  $\mathbf{S}$ ) with  $\phi$  this cross-section difference is for a longitudinally polarised lepton<sup>4</sup> given by the expression

$$\frac{d\sigma}{d\Omega dE'}(\alpha + \pi) - \frac{d\sigma}{d\Omega dE'}(\alpha) = \frac{4\alpha^2}{M\nu Q^2} \frac{E'}{E} \left[ (E \cos \alpha + E' \cos \vartheta) g_1 + \frac{2E E'}{\nu} (\cos \Theta - \cos \alpha) g_2 \right], \quad (2.31)$$

where  $\cos \Theta \equiv \sin \vartheta \sin \alpha \cos \phi + \cos \vartheta \cos \alpha$ . See also Fig. 2.5 for an illustration of the involved angles. Experimentally most interesting are the cases  $\alpha = 0$  and  $\alpha = \pi/2$  in the laboratory frame. In the first case the lepton and nucleon spins are aligned parallel ( $\Rightarrow$ ) or antiparallel ( $\Leftarrow$ ) and

$$\frac{d(\sigma^{\Rightarrow} - \sigma^{\Leftarrow})}{d\Omega dE'} = \frac{4\alpha^2}{M\nu Q^2} \frac{E'}{E} \left[ (E + E' \cos \vartheta) g_1 + \frac{Q^2}{\nu} g_2 \right], \quad (2.32)$$

---

<sup>4</sup>Transversely polarised leptons are impractical to deal with since in the cross-section differences a factor  $m/E$  appears which will make these differences vanishingly small in the high energy limit.

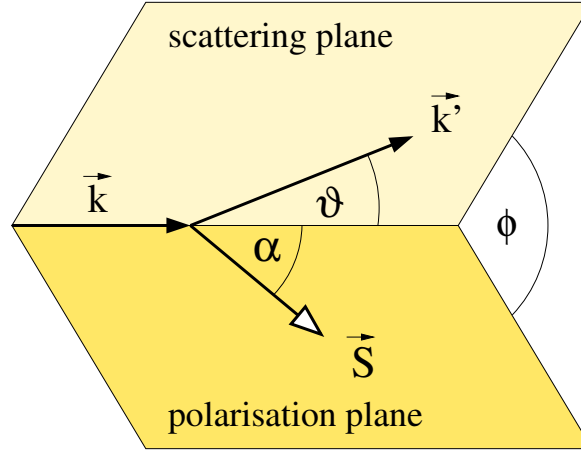


Figure 2.5: Definition of scattering angles in polarised DIS.

while in the second case the target spin is transversely oriented with respect to the lepton spin and

$$\frac{d(\sigma^{\rightarrow\downarrow} - \sigma^{\rightarrow\uparrow})}{d\Omega dE'} = \frac{4\alpha^2 E'}{M\nu Q^2 E} \left[ g_1 + \frac{2E}{\nu} g_2 \right]. \quad (2.33)$$

Measuring these two linear combinations of  $g_1$  and  $g_2$  would in principle allow to extract  $g_1$  and  $g_2$  individually. However, measuring cross-section differences precisely is experimentally very difficult. Instead the following asymmetries are usually measured

$$A_{\parallel} \equiv \frac{\sigma^{\rightarrow\leftarrow} - \sigma^{\rightarrow\rightarrow}}{\sigma^{\rightarrow\leftarrow} + \sigma^{\rightarrow\rightarrow}}, \quad A_{\perp} \equiv \frac{\sigma^{\rightarrow\downarrow} - \sigma^{\rightarrow\uparrow}}{\sigma^{\rightarrow\downarrow} + \sigma^{\rightarrow\uparrow}}. \quad (2.34)$$

These asymmetries are related to the virtual photo-absorption asymmetries  $A_1$ ,  $A_2$  (see Eqs. 2.18 and 2.19) through

$$A_{\parallel} = D(A_1 + \eta A_2), \quad A_{\perp} = D\left(\xi A_2 - \frac{\eta}{\xi} A_1\right). \quad (2.35)$$

Here the abbreviations

$$D \equiv \frac{1 - (1-y)\epsilon}{1 + \epsilon R}, \quad (2.36)$$

$$\epsilon = \frac{4(1-y) - \gamma^2 y^2}{4(1-y) + 2y^2 + \gamma^2 y^2}, \quad (2.37)$$

$$\xi \equiv \sqrt{\frac{2\epsilon}{1+\epsilon}}, \quad (2.38)$$

$$\eta \equiv \frac{Q^2 \gamma \epsilon}{xs[1 - (1-y)\epsilon]}, \quad (2.39)$$

were used.  $D$  can be interpreted as the depolarisation factor in the spin transfer from the initial lepton to the virtual photon and  $\epsilon$  replaces the ratio of probabilities for the emission of a

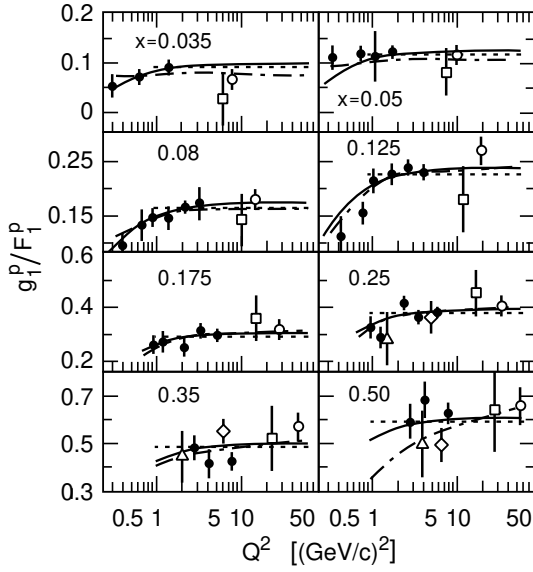
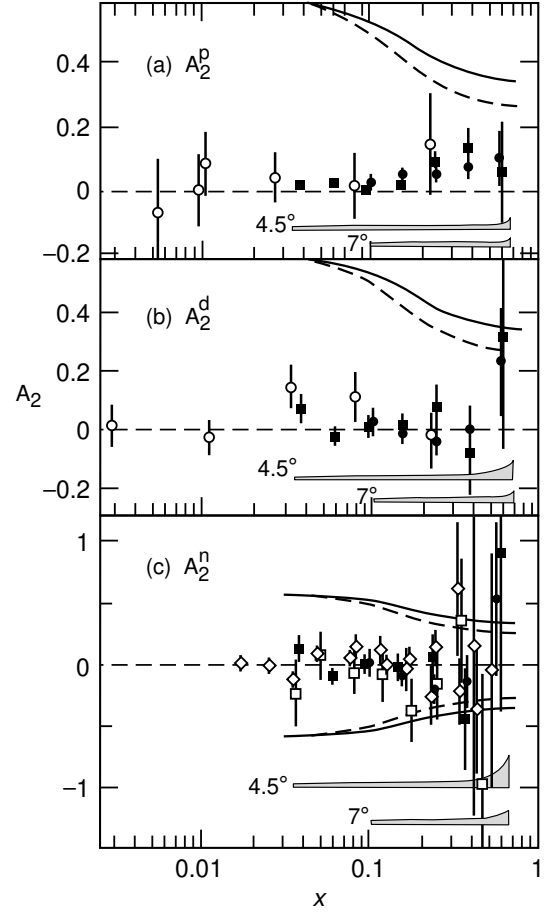


Figure 2.6: Results for the virtual photon asymmetries  $A_1$  and  $A_2$  from [E143:98].

Top: The virtual photon asymmetry  $A_1 \approx g_1/F_1$  for the proton as a function of  $Q^2$  in different bins of  $x$ . The lines represent various fits to the data.

Right:  $A_2$  for proton, deuteron, and neutron as a function of  $x$  together with the positivity limits.



longitudinally or transversely polarised photon.  $\xi$  and  $\eta$  just depend on kinematical variables. It turns out that  $\eta$  is small and similar to Sec. 2.1 the approximations

$$\frac{g_1}{F_1} \approx A_1 \approx \frac{A_{\parallel}}{D}, \quad g_1 \approx \frac{A_{\parallel}}{D} \frac{F_2}{2x[1+R]}, \quad (2.40)$$

can be made.

## 2.2 Quark Parton Model and Quantum Chromodynamics

Experiments already performed at the end of the sixties showed that the unpolarised structure functions  $F_1$  and  $F_2$  are to a large extent independent of  $Q^2$ . These first measurements were performed at  $x$  values of about 0.2 and at momentum transfers of few GeV [Pan:68, B<sup>+</sup>:69a, B<sup>+</sup>:69b, FK:72]. At the same time Bjorken [Bjo:69] predicted a scale invariance of the structure functions in the so called *Bjorken-limit*

$$F_{1,2}(\nu, Q^2) = F_{1,2}(x) + \mathcal{O}\left(\frac{1}{Q^2}\right) \quad \text{for } \nu, Q^2 \rightarrow \infty; x = \frac{Q^2}{2M\nu} \text{ fixed.} \quad (2.41)$$

$x$  is therefore often referred to as Bjorken- $x$  or  $x_{\text{Bj}}$ . The scaling behaviour in the – at that time experimentally accessible – energy range of few GeV<sup>2</sup> was nevertheless surprising.

These findings led to the development of the *parton model* [BP:69, Fey:72] which allows an intuitive interpretation of deep-inelastic scattering and its scale invariance. In the parton model the assumption is made that deep-inelastic lepton-nucleon scattering is an elastic scattering of the lepton off point-like components of the nucleon with spin  $\frac{1}{2}$  and charge  $e_f \neq 0$  – the *partons*. Since the measured structure functions are smooth functions of  $x$ , many partons have to be present. At large momentum and energy transfers  $Q^2, \nu$  (Bjorken-limit) and therefore small wavelengths  $\lambda \propto 1/Q$  for the exchanged virtual photon and short interaction times  $\tau \propto 1/\nu$ , an incoherent scattering off the individual partons takes place. To describe the kinematics of the scattering process a coordinate system is used in which the nucleon momentum is very large compared to parton masses and transverse momenta, the *Breit frame* (see Fig. 2.7). In this frame the scattering can be understood as the absorption of the virtual photon by one parton inside a bunch of parallel flying partons while all others remain unaffected [Fey:69, Nac:77]. The interacting parton has to carry a momentum fraction of the total nucleon momentum  $P$  which equals  $\xi = Q^2/2M\nu$ .

To derive the deep-inelastic structure functions  $F_1, F_2$  in the parton model one uses the resemblance between Eq. 2.28 and the cross-section for elastic lepton scattering off a point-like spin- $\frac{1}{2}$  object with mass  $m_f$  and charge  $e_f$  (*Rosenbluth formula*)

$$\frac{d\sigma_{\text{elas}}}{d\Omega dE'} = \frac{4\alpha^2 E'^2 e_f^2}{Q^4} \left[ \left( \frac{Q^2}{2m_f^2} \sin^2\left(\frac{\vartheta}{2}\right) + \cos^2\left(\frac{\vartheta}{2}\right) \right) \delta\left(\nu - \frac{Q^2}{2m_f}\right) \right] \quad (2.42)$$

to choose

$$\begin{aligned} F_1^{\text{el}} &= \frac{1}{2} e_f^2 \frac{MQ^2}{2m_f^2\nu} \delta\left(1 - \frac{Q^2}{2m_f\nu}\right) = \frac{1}{2} e_f^2 \frac{x}{\xi_f} \delta(\xi_f - x), \\ F_2^{\text{el}} &= e_f^2 \delta\left(1 - \frac{Q^2}{2m_f\nu}\right) = e_f^2 \xi_f \delta(\xi_f - x). \end{aligned} \quad (2.43)$$

with the definition  $\xi_f \equiv m_f/M$ . This mass fraction equals the momentum fraction of the parton (*Nachtmann variable*) in the Breit frame. Denoting furthermore the probabilities to find a parton of type  $f$  with momentum fraction  $\xi$  and spin parallel/antiparallel to the nucleon spin with  $q_f^{\uparrow\uparrow/\uparrow\downarrow}(\xi)$  (*parton density function*, PDF), abbreviating

$$q_f(x) \equiv q_f^{\uparrow\uparrow}(x) + q_f^{\uparrow\downarrow}(x) \quad , \quad \Delta q_f(x) \equiv q_f^{\uparrow\uparrow}(x) - q_f^{\uparrow\downarrow}(x), \quad (2.44)$$

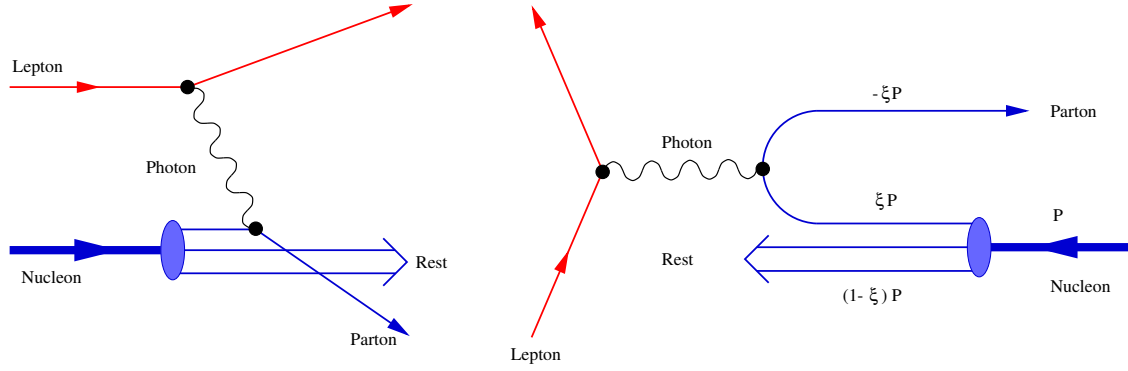


Figure 2.7: Deep-inelastic lepton-nucleon scattering in the parton model: general (left) and Breit frame (right).

and building the incoherent sum of elastic contributions

$$F_{1,2}(x) = \sum_f \int_0^1 d\xi q_f(\xi) F_{1,2}^{el}(\xi, x), \quad (2.45)$$

the unpolarised structure functions can be written as

$$F_1(x) = \frac{1}{2} \sum_f e_f^2 q_f(x) \quad , \quad F_2(x) = x \sum_f e_f^2 q_f(x). \quad (2.46)$$

Similarly the polarised structure functions can be derived as

$$g_1(x) = \frac{1}{2} \sum_f e_f^2 \Delta q_f(x) \quad , \quad g_2(x) = 0. \quad (2.47)$$

In the parton model therefore only one independent unpolarised structure function remains

$$F_2(x) = 2xF_1(x). \quad (2.48)$$

This relation is known as the *Callan-Gross relation* [CG:69]. Equivalently the ratio of longitudinal to transverse photo-absorption cross-sections in Eq. 2.24 is expected to vanish in the Bjorken-limit

$$R(x) = \frac{F_2(x) - 2xF_1(x)}{F_2(x)} = 0. \quad (2.49)$$

The fact that  $R$  is measured to be very small at large  $Q^2$  [Rit:83] is supporting the parton model picture and basically rules out the existence of additional charged partons which are no fermions. An analogous calculation for charged spin-0 particles shows that such partons would lead to  $R = \infty$ .

However if these charged fermionic partons would be the only constituents of the nucleon, the total nucleon momentum should be reproduced when integrating their momentum distribution

$$I = \int_0^1 \sum_f e_f^2 x q_f(x) dx = \int_0^1 F_2(x) dx. \quad (2.50)$$

Experimentally it was found that the charged partons only account for about half of the nucleon momentum [SSV:88]. Therefore more parton types must exist to carry the remaining momentum, however they may neither be fermions nor interact electromagnetically or weakly.

In the *Quark Parton Model* (QPM) which also includes the theory of strong interactions (*Quantum Chromodynamics*, QCD [Nac:86]) these additional partons are identified with the carriers of the strong force, the *gluons*, and the fermionic partons with the *quarks*. *Scaling violations* of the structure functions are expected due to the coupling of the quarks to the gluons while originally in the parton model the partons were assumed not to interact. Intuitively the scaling violations can be pictured in the following way.  $Q^2$  determines the wavelength of the virtual photon and therefore the spacial area which can be resolved. When going to values of  $Q^2 > Q_0^2$  one increases the resolution and what was taken as a parton at scale  $Q_0^2$  can now be surrounded by a cloud of other partons. Since these additional partons were radiated of the first parton they can only have smaller momentum fractions  $x$ . On the other hand the probability to find a parton with large  $x$  decreases with increasing  $Q^2$  since the momentum fraction can be shared amongst several partons. Later experiments with higher precision [NMC:97] confirmed that at small values of  $x$  the unpolarised structure functions are rising with  $Q^2$  while at larger values of  $x$  the opposite behaviour is observed (see also Fig. 2.4).

The basic processes of perturbative QCD are depicted in Fig. 2.8. Besides the emission and absorption of gluons by quarks similar to the coupling to photons in QED also three or four gluons can couple to each other. In a first order calculation the coupling strength is given by

$$\alpha_s(Q^2) = \frac{4\pi}{\left(11 - \frac{2}{3}n_f\right) \ln(Q^2/\Lambda^2)}, \quad (2.51)$$

where  $n_f$  denotes the number of active quark flavours and  $\Lambda$  the QCD scale parameter at which the perturbative approach breaks down. Usually  $\Lambda \approx 250$  MeV is taken. Defining furthermore

$$t \equiv \ln(Q^2/\Lambda^2), \quad (2.52)$$

$$\langle e^2 \rangle \equiv \frac{1}{n_f} \sum_f e_f^2, \quad (2.53)$$

$$[f \otimes h](x, t) \equiv \int_x^1 \frac{dy}{y} f\left(\frac{x}{y}, t\right) h(y, t), \quad (2.54)$$

and introducing the gluon density function  $g(x, t)$  as well as the singlet and non-singlet combinations of the quark and anti-quark densities

$$\Sigma(x, t) \equiv \sum_f q_f(x, t), \quad (2.55)$$

$$q^{NS}(x, t) \equiv \sum_f \left[ \frac{e_f^2}{\langle e^2 \rangle} - 1 \right] q_f(x, t), \quad (2.56)$$

the evolution of the parton densities as a function of  $Q^2$  is given by the Gribov–Lipatov–Altarelli–Parisi (GLAP) equations [GN:72a, GN:72b, AP:77]

$$\frac{d}{dt} q^{NS}(x, t) = \frac{\alpha_s(t)}{2\pi} [P_{qq}^{NS} \otimes q^{NS}](x, t), \quad (2.57)$$

$$\frac{d}{dt} \begin{bmatrix} \Sigma \\ g \end{bmatrix} (x, t) = \frac{\alpha_s(t)}{2\pi} \begin{bmatrix} P_{qq}^S & P_{qg} \\ 2n_f P_{gq} & P_{gg} \end{bmatrix} \otimes \begin{bmatrix} \Sigma \\ g \end{bmatrix} (x, t). \quad (2.58)$$

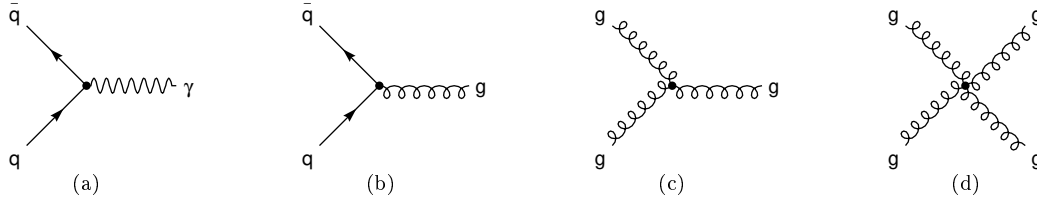


Figure 2.8: *Elementary processes of QED (a) and QCD (b – d): quark-antiquark annihilation to photon (a) and gluon (b), three (c) and four (d) gluon vertices.*

These equations allow the determination of the parton density functions at any  $Q^2$  once they are determined for a fixed value  $Q_0^2$ . The  $P_{ij}$  are the *splitting functions* for the unpolarised parton densities. The probability that a quark with momentum fraction  $x$  originates from a parent quark with momentum fraction  $y$  is given by  $\alpha_s(t)P_{qq}(x/y, t)$  while the probability that it is the result of a  $q\bar{q}$  pair production from a gluon with momentum fraction  $y$  is given by  $\alpha_s(t)P_{qg}(x/y, t)$ . Similar explanations hold for  $P_{gq}$  and  $P_{gg}$ . From these equations it can be seen that only the singlet combination  $\Sigma$  of the quarks couples to the gluon density  $g$  while the non-singlet part  $q^{NS}$  is decoupled from it. The evolution for polarised parton densities is simply given by replacing the unpolarised parton densities  $q_f$  and splitting functions  $P_{ij}$  with the polarised ones ( $\Delta q_f$  and  $\Delta P_{ij}$ ). However the evolution of the polarised parton densities is only formally equivalent to the unpolarised case since in general the polarised and unpolarised splitting functions differ.

The rather trivial expressions for the polarised and unpolarised structure functions Eqs. 2.46 and 2.47 in the parton model are in a perturbative QCD calculation given by [Alt:82]

$$F_1(x, t) = \frac{1}{2} \langle e^2 \rangle \left\{ c^{NS} \otimes q^{NS} + c^S \otimes \Sigma + 2n_f c^g \otimes g \right\} (x, t), \quad (2.59)$$

$$g_1(x, t) = \frac{1}{2} \langle e^2 \rangle \left\{ \Delta c^{NS} \otimes \Delta q^{NS} + \Delta c^S \otimes \Delta \Sigma + 2n_f \Delta c^g \otimes \Delta g \right\} (x, t), \quad (2.60)$$

where  $c^{S,NS,g}$  ( $\Delta c^{S,NS,g}$ ) denote the so-called unpolarised (polarised) flavour singlet ( $S$ ), non-singlet ( $NS$ ) and gluon ( $g$ ) coefficient functions. The coefficient and splitting functions are usually expanded in a power series of the coupling strength  $\alpha_s$  and the GLAP equations hold in each order of this expansion. In leading order  $\alpha_s^1$  (LO) the unpolarised and polarised singlet and non-singlet coefficient functions are given by  $\delta(1 - x/y)$  while the gluon coefficient function vanishes. In this order the structure functions are then again given by the simple expressions of Eqs. 2.46 and 2.47 with the parton model quark densities  $q_f(x)$  being replaced by  $Q^2$ -dependent densities  $q_f(x, t)$ . All coefficient and splitting functions have been computed to next-to-leading order (NLO) which allows a complete NLO QCD analysis of the scaling violations of  $F_1$  and  $g_1$ .

With this formalism precise measurements of the  $Q^2$  evolution of the structure functions allow in principle the determination of the individual parton density functions. As an example, the sensitivity of inclusive measurements to the unpolarised gluon density is illustrated in Fig. 2.9. The extracted gluon density is compared in Fig. 3.5 with another approach to access the gluon density function in the nucleon via heavy quark production and photon-gluon fusion, which is described in Sec. 3.1. However by comparing the available measurements for the unpolarised and



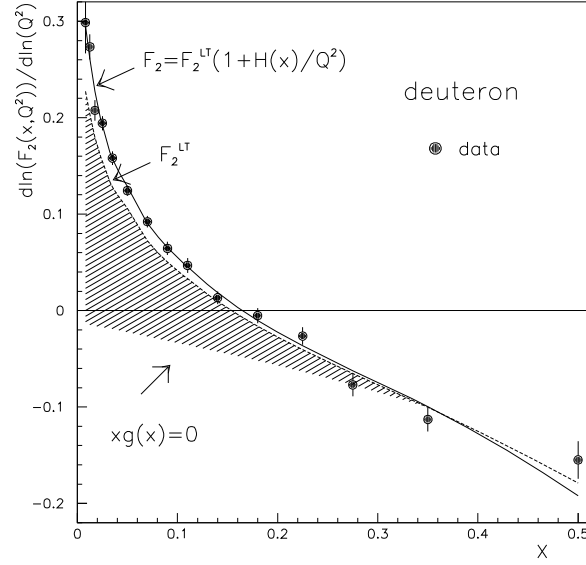


Figure 2.9: The logarithmic slope  $d \ln F_2 / d \ln Q^2$  of the deuteron structure function as measured by NMC and a comparison with the prediction from QCD in leading twist (dashed line,  $F_2^{LT}$ ) and with a phenomenological term for higher twist effects to fit the data (solid line) [NMC:93]. The contribution from gluons is represented by the shaded area and demonstrates the sensitivity of the scaling violations to the gluon distribution.

polarised structure functions (see Figs. 2.4 and 2.6), it becomes obvious that the polarised gluon density cannot be extracted the same way as long as the polarised inclusive data does not achieve higher precision over a large  $Q^2$  range. Also, with inclusive measurements of deep-inelastic lepton-nucleon scattering alone, the sensitivity to the anti-quark densities is poor.

Up to now masses and transverse momenta of the partons have been neglected as well as interactions of the struck parton with the target remnants. In a more detailed approach additional terms of  $\mathcal{O}\left(\frac{1}{Q^2}\right)$ ,  $\mathcal{O}\left(\frac{1}{Q^4}\right)$ , ... appear. To distinguish between these so-called *higher twist effects* and the dynamic QCD scaling violations, measurements have to cover a large  $Q^2$  range. The results at high values of  $Q^2$  are used to fit the QCD part. Deviations between this fit and the measurements at low values of  $Q^2$  are then attributed to the higher twist effects which can be phenomenologically parametrised as shown in Fig. 2.9. In contrast to higher order QCD corrections, higher twist effects introduce multi-particle correlations between the partons in the nucleon (see Fig. 2.10).

## 2.3 Semi-inclusive Deep-inelastic Scattering

In the previous sections only inclusive reactions have been considered where the kinematics of the scattered lepton is the only source of information. To ease the extraction of the individual quark distribution functions it would be favourable to know the flavour of the struck quark in the scattering process. However, due to the confinement property of QCD, this quark and the target remnant have to fragment into colour-neutral objects. The goal of semi-inclusive measurements is to gain access to the struck quark by looking at the process  $\ell + N \rightarrow \ell' + h + X$  (see also Fig. 2.11 for a schematic picture and Tab. A.1 for the definition of the most important kinematical variables of semi-inclusive scattering). In addition to the scattered lepton one or more particles from the hadronic final state have to be detected in coincidence. For the highest sensitivity to the structure information of the nucleon it is preferable to separate the *current fragments* which are produced in the fragmentation of the struck quark from those originating from the target remnant (*target fragments*). This separation can be experimentally attempted by selecting kinematical regimes for the hadronic final state in which an enhanced sensitivity to the current fragments is expected. Commonly selected are hadrons which are forward in the  $\gamma^*N$  centre of mass system ( $x_F > 0$ ), forward in the Breit frame, or fast in the laboratory system ( $z \geq z_0$  e.g.  $z_0 = 0.2$ ).

### 2.3.1 Fragmentation Functions

The fragmentation process is not calculable in perturbative QCD since it involves long distance processes with low  $Q^2$ . Instead it is parametrised by fragmentation functions  $D_f^h(x, Q^2; z)$  which denote the probability density that a hadron  $h$  with an energy fraction  $z$  of the energy of the virtual photon is produced when a quark of flavour  $f$  was struck in a scattering process described by  $x$  and  $Q^2$ . Due to momentum conservation the fragmentation functions are normalised such that

$$\sum_h \int_0^1 dz z D_f^h(x, Q^2; z) = 1. \quad (2.61)$$

In the QPM the scattering and fragmentation processes are independent (*factorisation*). This is a consequence of the assumption of quasi-free partons. If the fragmentation does not depend on the formation of the struck quark, the fragmentation function should even be independent of the underlying physics process creating the quark. Then the fragmentation functions should be identical in neutral and charged current scattering as well as in  $e^+e^-$  annihilation (*universality* of fragmentation functions). Factorisation is only justified if conservation laws like the conservation of the baryon number place no strong constraints on the formation of the hadronic final state. If enough energy is available to produce a high multiplicity in the final state (large values of  $W^2$ ) such constraints are usually negligible. In QCD the  $Q^2$  dependence of the fragmentation function  $D_f^h$  arises from gluon radiation off the final quark line similar to the scaling violations of the quark distribution functions  $q_f$  by gluon radiation off the initial quark line. Additionally, the exchange of gluons between the initial and final quark lines can break the factorisation assumption. However these effects are small in NLO QCD calculations.

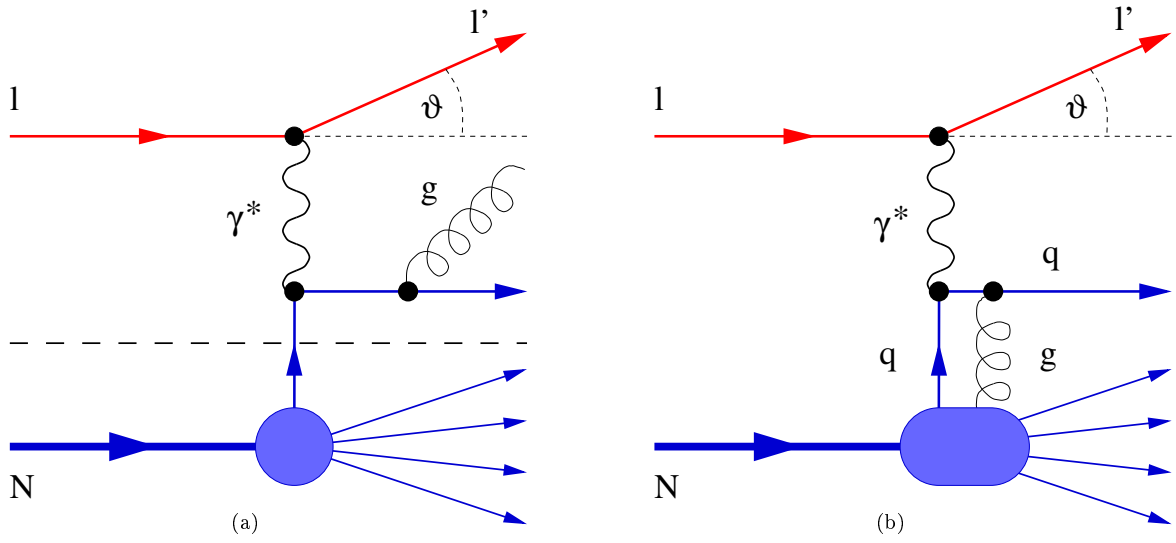


Figure 2.10: The QCD Compton process (QCDC) is schematically depicted in (a) as an example for higher order QCD corrections. No vertices appear below the dashed line with the spectator partons. In contrast to these corrections, higher twist effects introduce correlations between several partons of the nucleon (b).

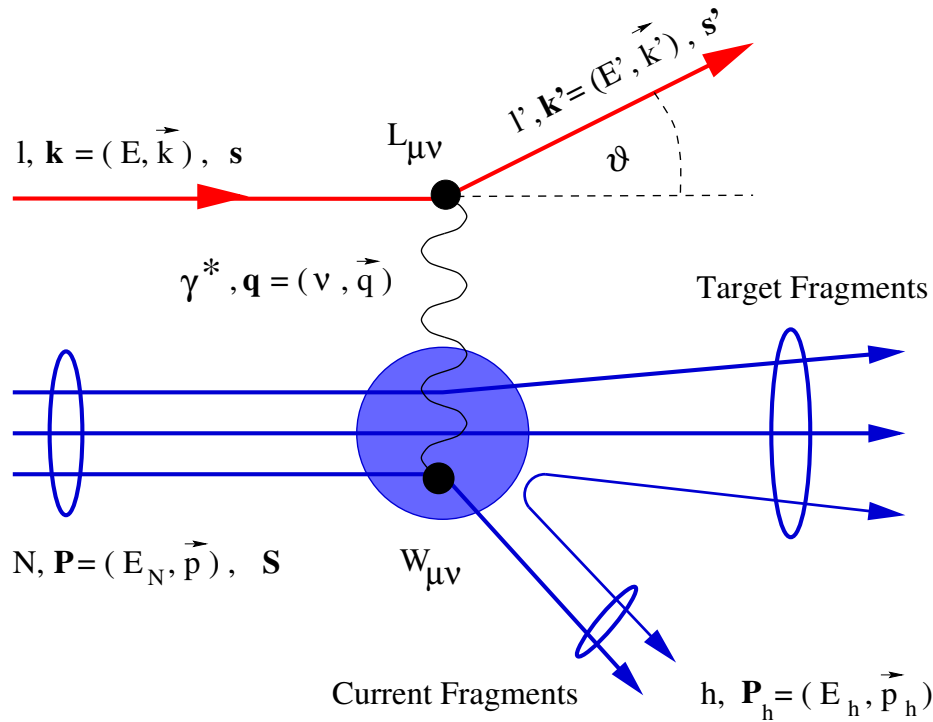


Figure 2.11: Schematic picture of semi-inclusive deep-inelastic lepton-nucleon scattering.

The fragmentation functions implicitly contain the probabilities to create quark-antiquark pairs from the vacuum. Because of the uncertainty principle these probabilities are inversely proportional to the squared quark masses. At HERMES energies, strange quarks are suppressed by about a factor 3-5 compared to up and down quarks while the creation of charmed and third generation quark pairs can be neglected in the fragmentation process.

Isospin and charge conjugation invariance are usually used to reduce the number of independent fragmentation functions. In the case of charged pions one can define

$$\begin{aligned} D^+ &\equiv D_u^{\pi^+} = D_{\bar{d}}^{\pi^+} = D_d^{\pi^-} = D_{\bar{u}}^{\pi^-}, \\ D^- &\equiv D_d^{\pi^+} = D_{\bar{u}}^{\pi^+} = D_u^{\pi^-} = D_{\bar{d}}^{\pi^-}. \end{aligned} \quad (2.62)$$

The so called favoured ( $D^+$ ) and unfavoured ( $D^-$ ) fragmentation functions have been measured in semi-inclusive DIS with pions in the forward region [EMC:89, Gei:98]. For additional assumptions on the fragmentation functions with respect to kaons and protons in deep-inelastic charged hadron production see e.g. [Kum:97].

Since it is not possible to calculate the fragmentation functions in perturbative QCD directly from first principles several phenomenological models have been developed to predict the fragmentation functions. The two most important models are the independent fragmentation model of Field and Feynman [FF:78] and the LUND string fragmentation model [AGIS:81, AGIS:83]. A detailed description of these models as implemented into the JETSET Monte Carlo generator is given in [Sjö:94] while the tuning to the HERMES data is described in [Gei:98, Tal:98].

### 2.3.2 Cross-sections and Asymmetries

After normalisation to the inclusive cross-section  $\sigma$  the unpolarised production of a hadron of type  $h$  in the final state can be expressed in LO QCD in terms of fragmentation functions and unpolarised quark distribution functions as

$$\frac{1}{\sigma} \frac{d\sigma^h}{dz}(x, Q^2; z) = \frac{\sum_f e_f^2 q_f(x, Q^2) D_f^h(x, Q^2; z)}{\sum_f e_f^2 q_f(x, Q^2)}. \quad (2.63)$$

Under the assumption that the fragmentation process does not depend on the relative orientation of quark and nucleon spin one can define semi-inclusive structure functions in complete analogy to the inclusive case as

$$F_2^h(x, Q^2; z) = 2x \frac{1}{2} \sum_f e_f^2 q_f(x, Q^2) D_f^h(x, Q^2; z), \quad (2.64)$$

$$g_1^h(x, Q^2; z) = \frac{1}{2} \sum_f e_f^2 \Delta q_f(x, Q^2) D_f^h(x, Q^2; z). \quad (2.65)$$

Continuing the analogy with the inclusive case and assuming  $A_2^h = 0$  the semi-inclusive spin asymmetry  $A_1^h$  can be written as

$$A_1^h(x, Q^2; z) = \frac{g_1^h(x, Q^2; z)}{F_1^h(x, Q^2; z)},$$

$$\begin{aligned}
&= \frac{\sum_f e_f^2 \Delta q_f(x, Q^2) D_f^h(x, Q^2; z)}{\sum_{f'} e_{f'}^2 q_{f'}(x, Q^2) D_{f'}^h(x, Q^2; z)}, \\
&= \frac{A_{||}^h(x, Q^2; z)}{D}.
\end{aligned} \tag{2.66}$$

For the extraction of the polarised quark densities it is useful to rewrite the formula for  $A_1^h$  slightly

$$\begin{aligned}
A_1^h(x, Q^2; z) &= \frac{\sum_f e_f^2 \Delta q_f(x, Q^2) D_f^h(x, Q^2; z)}{\sum_{f'} e_{f'}^2 q_{f'}(x, Q^2) D_{f'}^h(x, Q^2; z)}, \\
&= \sum_f \frac{e_f^2 q_f(x, Q^2) D_f^h(x, Q^2; z)}{\sum_{f'} e_{f'}^2 q_{f'}(x, Q^2) D_{f'}^h(x, Q^2; z)} \frac{\Delta q_f(x, Q^2)}{q_f(x, Q^2)}, \\
&\equiv \sum_f P_f^h(x, Q^2; z) \frac{\Delta q_f(x, Q^2)}{q_f(x, Q^2)}.
\end{aligned} \tag{2.67}$$

The newly introduced unpolarised quantity, the hadron purity  $P_f^h(x, Q^2; z)$ , gives the probability that a quark of flavour  $f$  was struck when observing a hadron  $h$  with the energy fraction  $z$  in the final state. The semi-inclusive spin asymmetry  $A_1^h$  is then given by summing the products of purities and quark polarisations, which are the ratios of the polarised and unpolarised quark density distributions, over all contributing quark flavours. By measuring the hadron asymmetries for different hadron types together with the inclusive asymmetry

$$A_1(x, Q^2) = \frac{\sum_f e_f^2 \Delta q_f(x, Q^2)}{\sum_{f'} e_{f'}^2 q_{f'}(x, Q^2)}, \tag{2.68}$$

the individual contributions from the quark polarisations can be disentangled. For more details about the purity method and the extraction of polarised quark distributions at HERMES see [Fun:98, Ruh:99, Tip:99].

## 2.4 Nuclear Effects

The energy scales of nuclear physics with binding energies of few MeV and average nucleon momenta due to Fermi motion of about 250 MeV are significantly lower than the typical momentum transfers of many GeV involved in deep-inelastic scattering. Therefore one could expect the cross-section for scattering off a nucleus in the deep-inelastic regime to be given by the sum of the cross-sections for scattering off its individual nucleons. To reveal deviations from this expectation caused by the nuclear environment, one can compare the cross-sections measured on bound nucleons and on deuterium. Because of its small binding energy, deuterium is chosen as the best approximation for a free, isoscalar nucleon. Since the structure functions  $F_2^p$  of the proton and  $F_2^n$  of the neutron are different due to the different quark contents of these particles, this comparison is only meaningful after a compensation for the isospin quantum numbers of the nucleus under study. The isoscalarity correction to equalise the proton and neutron numbers for

a nucleus with nucleon number  $A$  and atomic number  $Z$  (and therefore  $N = A - Z$  neutrons) can be accomplished with the substitution

$$\sigma^A \rightarrow \frac{\sigma^A - \frac{N-Z}{A}\sigma^n}{1 - \frac{N-Z}{A}}. \quad (2.69)$$

Here and throughout the rest of this section all cross-sections are normalised *per nucleon* and not per nucleus, that is to be divided by the number  $A$  of nucleons in the nucleus.  $F_2$  will also be referred to per nucleon. Furthermore, if not stated otherwise, all cross-section and structure function ratios presented will be corrected for non-isoscalarity.

### 2.4.1 Nuclear Effects in Inclusive Structure Functions

After a straight forward transformation of the formula for the unpolarised inclusive deep-inelastic cross-section Eq. 2.29, the dependence of the cross-section on the structure functions can be written as

$$d\sigma \propto F_2(x, Q^2) \frac{1 + \epsilon R(x, Q^2)}{1 + R(x, Q^2)}, \quad (2.70)$$

where the proportionality factor just depends on kinematical variables. As a reminder,  $R$  denotes the ratio of longitudinal to transverse photo absorption cross-sections while  $\epsilon$  is the ratio of probabilities for the emission of longitudinally or transversely polarised photons. These quantities were defined in Eqs. 2.24 and 2.37. The cross-section ratio then becomes

$$\frac{\sigma^A}{\sigma^D} = \frac{F_2^A}{F_2^D} \frac{1 + \epsilon R^A}{1 + R^A} \frac{1 + R^D}{1 + \epsilon R^D}. \quad (2.71)$$

As can be seen from this equation the cross-section ratio is identical to the ratio of the structure functions  $F_2^A$  and  $F_2^D$  if either  $\epsilon = 1$  or  $R^A = R^D$ .

In the QPM  $F_2$  is proportional to the momentum distribution of the quarks inside a free nucleon weighted by the square of their charges (Eq. 2.46). Since the momentum fraction  $x$  is extracted from the measured quantities under the assumption of a stationary nucleon, corrections were expected for  $F_2^A(x)$  because of Fermi motion of the nucleons inside the nucleus. At  $x \gtrsim 0.5$  this led to the prediction of a large increase of the structure function ratio (see e.g. [FS:81, SU:85]). Significant deviations from this predicted behaviour were surprisingly discovered in 1983 when the European Muon Collaboration (EMC) published first results for this ratio in the deep-inelastic scattering regime using iron [EMC:83c]. Since then many experiments have confirmed the observation of a nuclear dependence for several different target materials. As an example the results for  $^{40}\text{Ca}$  are shown in Fig. 2.12. Besides the additional finding of  $Q^2$  independent nuclear effects it nicely illustrates the general  $x$  dependence common to all nuclei. Several  $x$  regions with distinct behaviour can be identified:

- For  $x \lesssim 0.06$  a depletion of the ratio is observed (*shadowing*). This effect was known from experiments with  $Q^2 < 1 \text{ GeV}^2$  but expected to vanish with increasing  $Q^2$ . Instead it is found to be independent of  $Q^2$  and to increase with increasing nucleon number  $A$ .

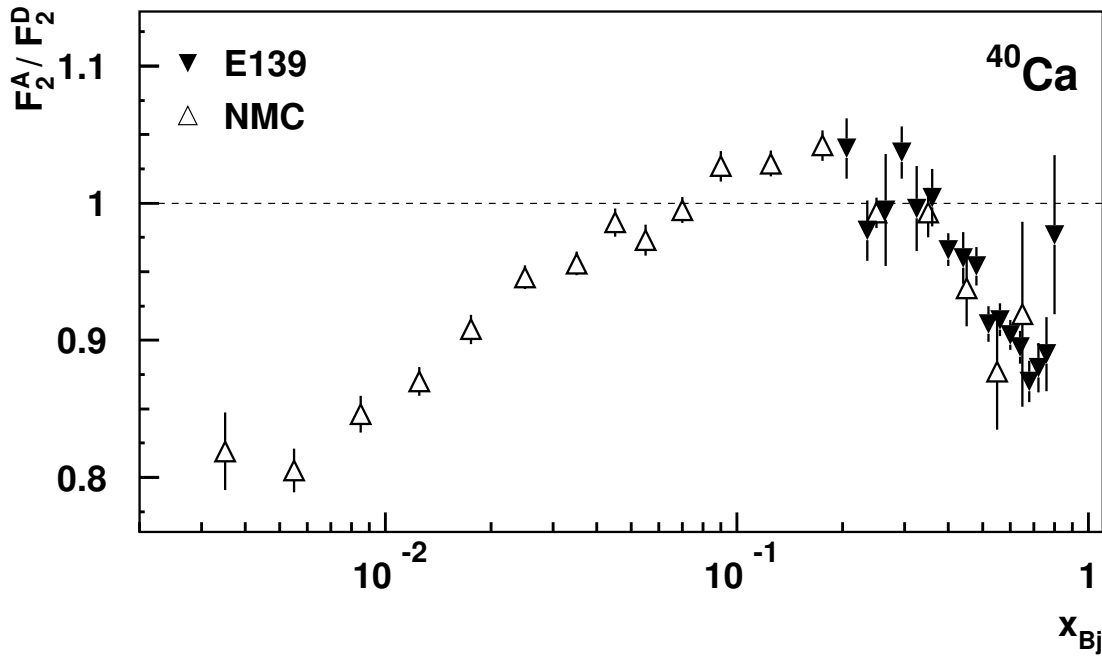


Figure 2.12: The  $x$ -dependence of the  $F_2$  structure function ratio for calcium and deuterium [E139:94, NMC:95].

The general behaviour is explained by two types of models. In *generalised vector meson dominance models* the virtual photon fluctuates to a superposition of vector mesons which interact hadronically with the nucleus. The mesons are mainly absorbed on the surface of the nucleus and the inner nucleons are “shadowed” by the surface ones.

In *partonic models* low momentum partons can spread over a large longitudinal distance due to the uncertainty principle. Partons from different nucleons may so overlap and fuse. Thus low  $x$  partons are reduced while those with higher  $x$  increase.

- For intermediate values of  $x$  ( $0.06 \lesssim x \lesssim 0.3$ ) the ratio is above unity and the nuclear structure function is larger than the one from a free nucleon (*anti-shadowing*). In partonic models this effect is a consequence of the low  $x$  behaviour and the approximate momentum balance between the low and intermediate  $x$  region is often used as an argument in favour of these models.
- For even larger values of  $x$  the ratio drops again below unity and reaches a minimum around  $x \approx 0.6$  (*EMC effect*).

In *binding models* the effect of the nuclear potential on the nucleons is described by a reduced effective nucleon mass leading to a shift to higher  $x$  values ( $x = Q^2 / (2M\nu)$ ). Other models require a change of the quark confinement size in nuclear matter to explain the EMC effect. Increasing confinement can be introduced through an increase of the nucleon size (*nucleon swelling*) or in the language of QCD through  $Q^2$  *rescaling*. Multi-quark *cluster models* on the other hand invoke deconfinement with the disappearance of the nucleon degrees of freedom in the nucleus.

- For  $x \gtrsim 0.8$  the ratio is again above unity, as expected due to Fermi motion.

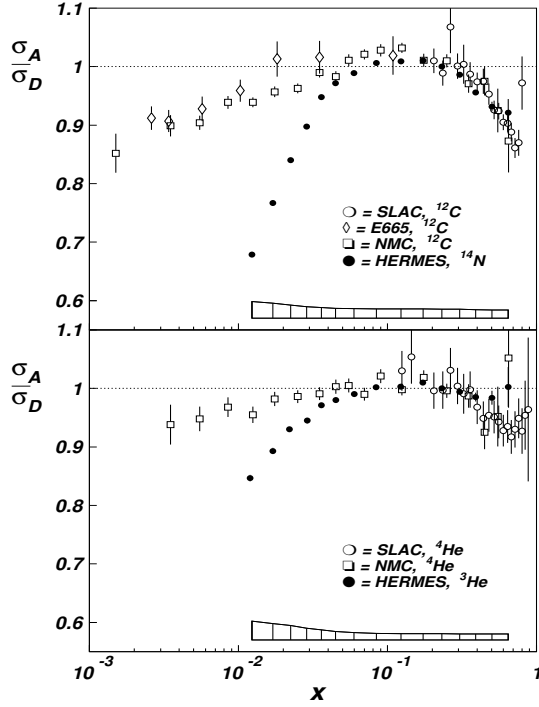


Figure 2.13: Ratios of cross-sections of inclusive deep-inelastic lepton scattering from nucleus  $A$  and  $D$  as a function of  $x$ .

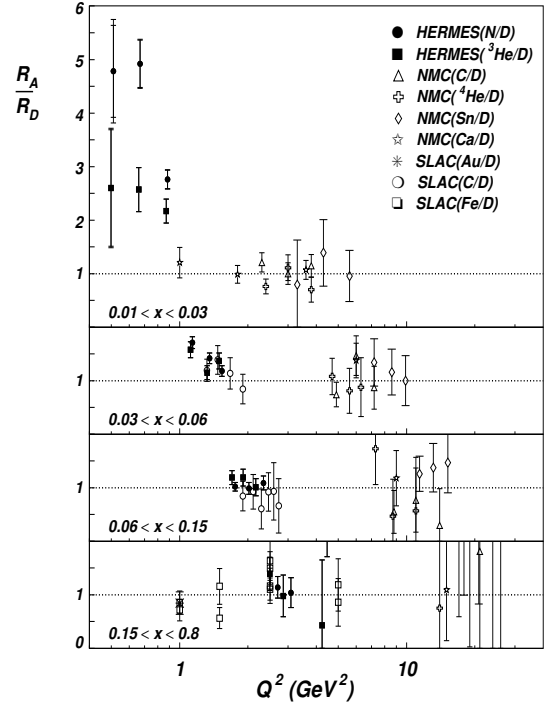


Figure 2.14: The ratio  $R^A/R^D$  for nucleus  $A$  and  $D$  as a function of  $Q^2$  for four different  $x$  bins.

Since  $F_2$  shows an  $A$ -dependence one has to ask whether  $R$  changes in a nuclear environment as well or whether the longitudinal and transverse photo absorption cross-sections show the same behaviour which then will cancel in  $R$ . As mentioned earlier in Sec. 2.1,  $R$  is steeply decreasing as a function of  $Q^2$  and identical within errors for proton and neutron. The world data for  $\Delta R = R^A - R^D$  do not reveal any significant  $A$ -dependence in the  $Q^2$ -region  $1 \text{ GeV}^2 < Q^2 < 20 \text{ GeV}^2$  either [E140:90, E140:94, E143:99, NMC:92, NMC:96]. For lower values of  $Q^2$  however ( $0.3 \text{ GeV}^2 < Q^2 < 1 \text{ GeV}^2$ ) cross-section ratios measured recently at HERMES in deep-inelastic lepton scattering (Fig. 2.13) show a large difference to results from the before mentioned experiments at higher values of  $Q^2$ . The  $\epsilon$ -dependence of this data has been used to extract values for the ratio  $R^A/R^D$  which are presented in Fig. 2.14. The above mentioned published data on  $\Delta R$  have been converted to  $R^A/R^D$  and added to this figure. A strong  $Q^2$  dependence is seen at low  $x$  and  $Q^2$  which represents the first observation of a nuclear effect in  $R$  [HERMES:00b, vH:00, Shi:00].

Several mechanism have been proposed which can lead to an enhancement of  $R^A$  over  $R^D$ . In leading twist an enhanced gluon distribution in a nuclear environment causes  $R^A > R^D$  [GP:96]; however the effect is expected to be small. Higher twist effects with an enhancement of the quark-gluon correlations in nuclei also increase  $R^A$  [EFP:82, BR:90] and are additionally supported by the steep  $Q^2$  dependence of the  $R^A/R^D$  data.



### 2.4.2 Hadronisation in a Nuclear Environment

Since already the inclusive cross-section is modified it seems likely that also new effects appear for the hadron production off a nucleus compared to the free nucleon case. To disentangle the effects on the formation of the final state from those depending on the virtual photon absorption described in the previous section, one usually studies the so called *attenuation ratio*

$$R_A^{att}(\nu, Q^2; z) \equiv \frac{\left(\frac{1}{\sigma} \frac{d\sigma^h}{d\nu dz}(\nu, Q^2; z)\right)_A}{\left(\frac{1}{\sigma} \frac{d\sigma^h}{d\nu dz}(\nu, Q^2; z)\right)_D}. \quad (2.72)$$

The ratios of semi-inclusive and inclusive cross-sections which appear in both the numerator and the denominator are given in LO QCD in Eq. 2.63. Recall that  $z$  denotes in the laboratory frame the fraction of the virtual photon energy carried by the hadron  $h$ . The attenuation ratio allows to experimentally study the quark propagation inside the nucleus. After the formation, hadrons will experience rescattering when travelling through the surrounding medium and hadron spectra will become softer than for the production off free nucleons.  $R_A^{att}$  will therefore be in general less than unity for high values of  $z$ . The later the formation of the hadron takes place after the initial hard  $\gamma^*$ -parton interaction, the shorter gets the average path length to traverse the nucleus. The rescattering probability decreases and the softening eventually vanishes. Simple phenomenological models to predict the hadron *formation time*  $\tau_f$  are either based on the hadron kinematics [Got:74]

$$\tau_f = \frac{E_h}{M_h} \tau_h = \frac{z \nu}{M_h} \tau_h, \quad (2.73)$$

or on the kinematics of the struck quark [BC:83]

$$\tau_f = \frac{E_q}{m_q} \tau_q = \frac{\nu}{m_q} \tau_q. \quad (2.74)$$

$\tau_h$  and  $\tau_q$  are free parameters of the models while  $M_h$  and  $m_q$  denote the hadron and quark masses. A refined approach includes the LUND string fragmentation model [BG:87] and is illustrated in Fig. 2.15. After the initial hard interaction a string builds up between the struck quark and the target fragment. The string will eventually break up and create new  $q\bar{q}$ -pairs from the vacuum. The *constituent time*  $\tau_c$  and the *formation time*  $\tau_f$  specify the time between the  $\gamma^*$ -parton interaction and the creation of the first and last constituent quark of a hadron respectively. Since the final hadron arises from the string between the two space points corresponding to  $\tau_c$  and  $\tau_f$  this string has to contain the energy of the hadron. The string energy is determined by the string constant  $\kappa$  and the stretching of the string, so the two time scales are related through

$$\tau_f - \tau_c = \frac{z \nu}{\kappa}. \quad (2.75)$$

In these models the attenuation ratio is related to the probability that neither the hadronic fluctuations, the hadron constituents nor the hadron itself interact with the nucleus. For  $\tau_c = 0$  the simpler models are recovered. Information on the involved time scales and cross-sections can be gained by comparison with experimental data.

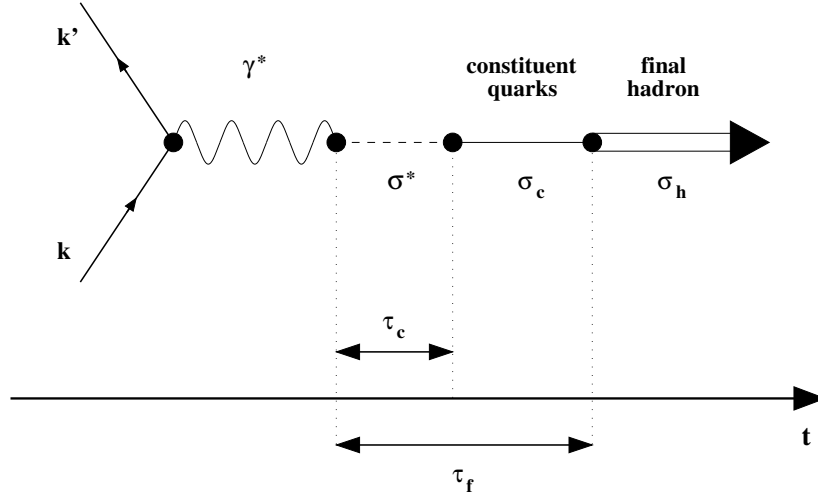


Figure 2.15: Illustration of different time scales and interaction cross-sections involved in the space-time structure of the hadronisation. The formation time  $\tau_f$  denotes the time between the initial hard  $\gamma^*$ -parton interaction and the formation of the hadron while the constituent time  $\tau_c$  gives the time scale for a hadronic fluctuation of the virtual photon before the first constituent of the final hadron is created.  $\sigma^*$  describes possible interactions before the constituent quarks exist,  $\sigma_c$  interactions of the constituent quarks and  $\sigma_h$  is assumed to be the meson-nucleon cross-section above resonances ( $\sigma_h \approx 20 - 25 \text{ mb}$ ).

A different approach to describe the production of leading hadrons is based on perturbative QCD [Kop:90, KNP:96]. The hadronisation of a highly virtual quark is therein assumed to take place through *gluon bremsstrahlung* and the deceleration of the quark is a result of the radiative energy loss. This energy loss is time and energy dependent and constrained by  $\nu(1-z)$  because of the additional assumption that the leading hadron consists of the leading quark which absorbed the virtual photon and an antiquark coming from the last emitted gluon. This constraint and the fact that a coloured object cannot travel over long distances through a nuclear medium leads to the prediction of a strong suppression in heavier nuclei for large values of  $z$ . The lower the energy  $\nu$  of the virtual photon the more this effect is enhanced and extends to lower values of  $z$ . As an example, Fig. 2.16 shows predictions of this model for the  $\nu$ ,  $z$ , and  $Q^2$  dependence of the nuclear suppression in copper. As seen from the  $\nu$  dependence of the attenuation ratio, nuclear effects in semi-inclusive deep-inelastic scattering can be best studied at energies of few GeV. Then the typical length scales corresponding to the involved time scales are comparable with nuclear dimensions. This makes HERMES a good facility to study these effects: the typical scales at HERMES range between 3 – 5 fm while they were much larger (10 – 50 fm) for previous experiments at CERN [EMC:91, NMC:91], and FERMILAB [E665:95].

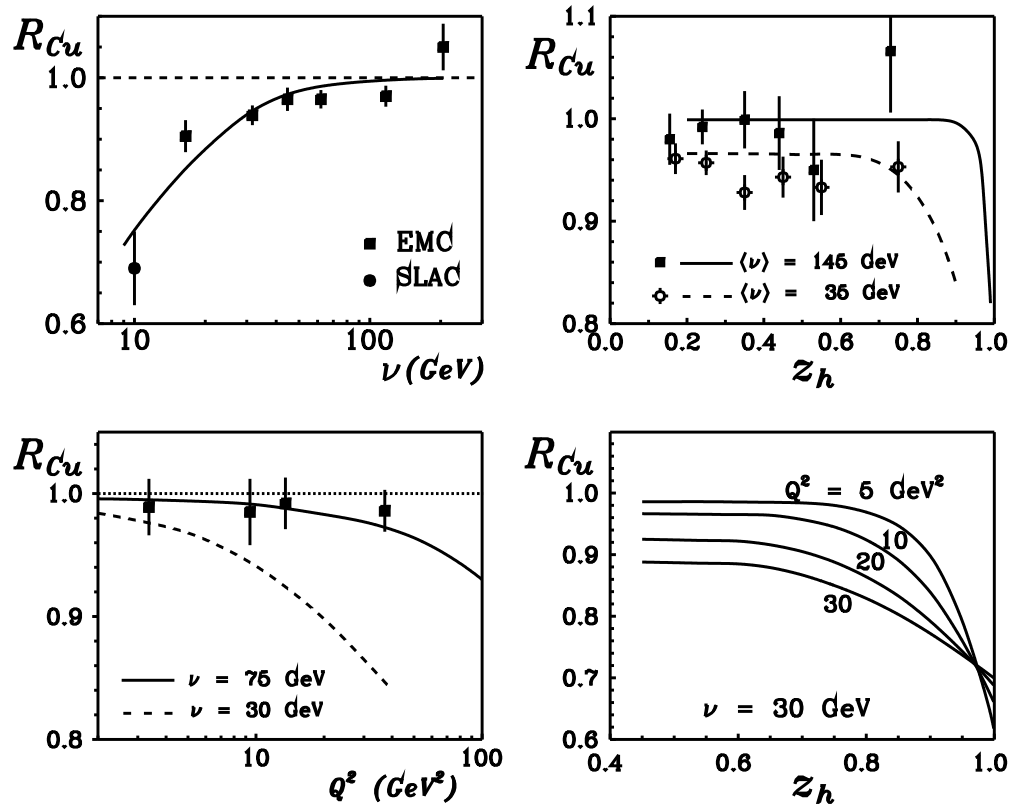


Figure 2.16: Nuclear suppression for copper in the gluon bremsstrahlung model. Predictions are shown for the  $\nu$  and  $z$  dependence in comparison with results obtained at SLAC and by EMC (upper row) as well as the  $Q^2$  and  $z$  dependence in the energy range of HERMES (lower row). For details see [KNP:96].



### 3 Charm Production Near Threshold

At the early 1960s, the four leptons of the first and second generation were discovered, while from the quarks only the up, down, and strange quarks were known. To complete the second generation and recover the missing symmetry between leptons and quarks, a fourth quark flavour was suggested [BG:64, GIM:70]. A new quantum number was introduced, the *charm*  $C$ , and the postulated quarks were supposed to have  $C = +1$ , charge  $q_c = +\frac{2}{3}e$  and mass  $m_c \approx 1-3$  GeV.

Experimental confirmation of the existence of charm quarks was achieved in 1974 when a  $c\bar{c}$  bound state was found at BNL [A<sup>+</sup>:74a] and SLAC [A<sup>+</sup>:74b]: the  $J/\Psi$  vector meson. Not much later charmed baryons ( $\Lambda_c$ ) were observed in bubble chamber experiments [C<sup>+</sup>:75b] and charmed mesons with  $C \neq 0$  were found. The lightest of these particles, which contain an up or down quark besides the heavy charm quark, are the pseudo scalar  $D$  mesons with spin  $J = 0$  ( $D^0$ ,  $D^\pm$ ) [G<sup>+</sup>:76, P<sup>+</sup>:76]. Soon afterwards also the vector mesons with spin  $J = 1$  ( $D^{*0}$ ,  $D^{*\pm}$ ) were discovered [G<sup>+</sup>:77, F<sup>+</sup>:77, N<sup>+</sup>:77]. These vector mesons decay through the strong force into the lighter scalar  $D$  mesons. Experimental evidence for meson states which contain a strange quark in addition to the charm quark ( $D_s^\pm$ ,  $D_s^{*\pm}$ ) was found in 1983 [C<sup>+</sup>:83].

#### 3.1 Production of Charm Quarks

Over the past 20 years, many experiments were performed to study the charm quarks. Depending on the type of the initial particles and the available energy, various processes can lead to the production of charm quarks. Our current understanding is dominated by experiments performed at  $e^+e^-$ -storage rings where a  $c\bar{c}$ -pair can be produced through the annihilation of the two leptons into a photon or a  $Z_0$ . In hadron-hadron scattering experiments, fusion or annihilation of two partons – quarks or gluons – can lead to the occurrence of charm quarks in the final state. In a similar way, in lepton-nucleon scattering charm quarks are predominately produced via the photon-gluon fusion process. In the following, this production mechanism will be discussed with a focus on the energy range of the HERMES experiment. With an energy of  $E_B = 27.5$  GeV for the electron beam at HERA, the centre of mass energy in the lepton-nucleon system is  $\sqrt{s} = \sqrt{m_e^2 + M^2 + 2ME_B} \approx 7.26$  GeV, relatively close to the charm production threshold of about 3 GeV. Near the threshold where charm production is experimentally poorly known up to

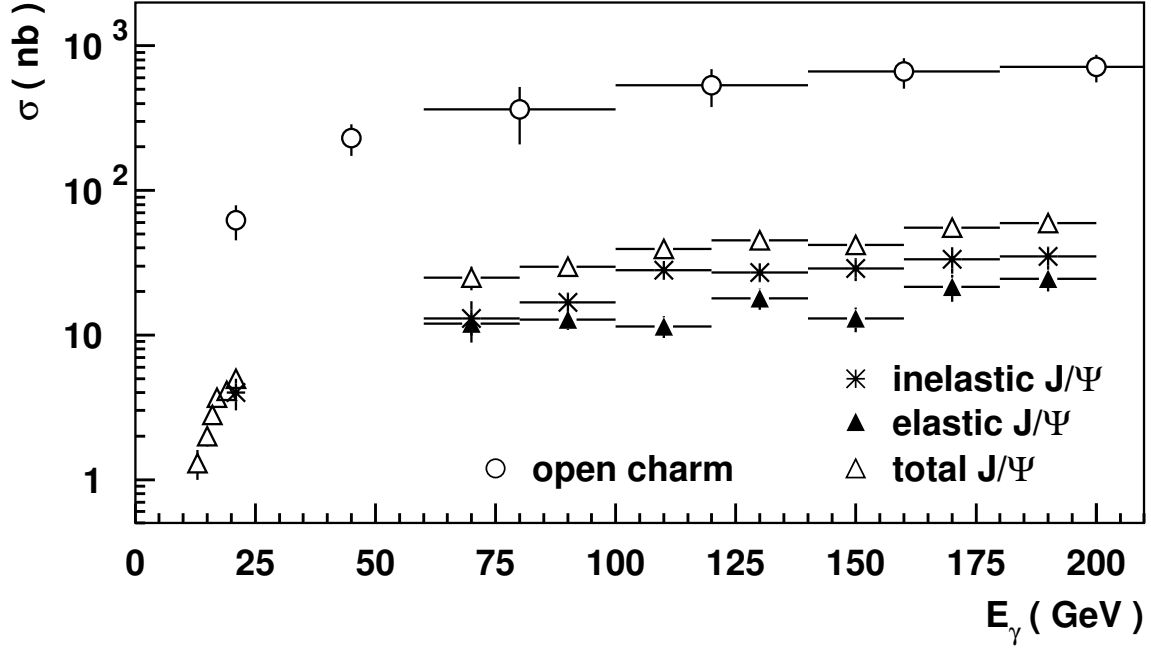


Figure 3.1: Cross-sections for the photoproduction of charm quark pairs as a function of the photon energy  $E_\gamma$  separately for particles with open and hidden charm. Shown are data from EMC [EMC:83a, EMC:83b], SLAC [ $A^+$ :86,  $C^+$ :75a], and PEC [ $A^+$ :87].

now, a strong increase in the cross-section can be observed (Fig. 3.1). In this kinematical regime, also theoretical predictions suffer from several difficulties such as the size of  $\alpha_s$  and the role of higher order corrections.

### 3.1.1 Photon-Gluon Fusion

As described in Sec. 2.2, lepton-nucleon scattering can be interpreted as the interaction of a boson ( $\gamma^*$ ,  $Z^0$ ,  $W^\pm$ ) radiated off the lepton with a parton of the nucleon. The relevant processes for the production of charm quarks are listed in Tab. 3.1. At moderate centre of mass energies, contributions from the  $Z^0$  and  $W^\pm$  bosons are negligible due to the high masses of these particles. Thus the only processes remaining are the direct scattering of the virtual photon off a quark or anti-quark in the nucleon and the *photon-gluon fusion* (PGF), where a gluon from the nucleon and the virtual photon merge under the production of a  $q\bar{q}$ -pair. A process can be attributed to the direct scattering if the participating charm quark was produced in a non-perturbative process. For charm quarks, this non-perturbative distribution has been measured to be very small and the photon-gluon fusion is the dominant process. Since the lepton-nucleon scattering cross-section is dominated by the exchange of virtual photons at low values for the four-momentum transfer  $Q^2$  (Eq. 2.29), it proceeds mainly through photoproduction with quasi-real photons ( $Q^2 \approx 0$ ). However, more reliable theoretical results can be obtained in the deep-inelastic regime with larger values of  $Q^2$ . In this case, the dependence of the data on the photon virtuality can be used as a further test of the perturbative QCD.

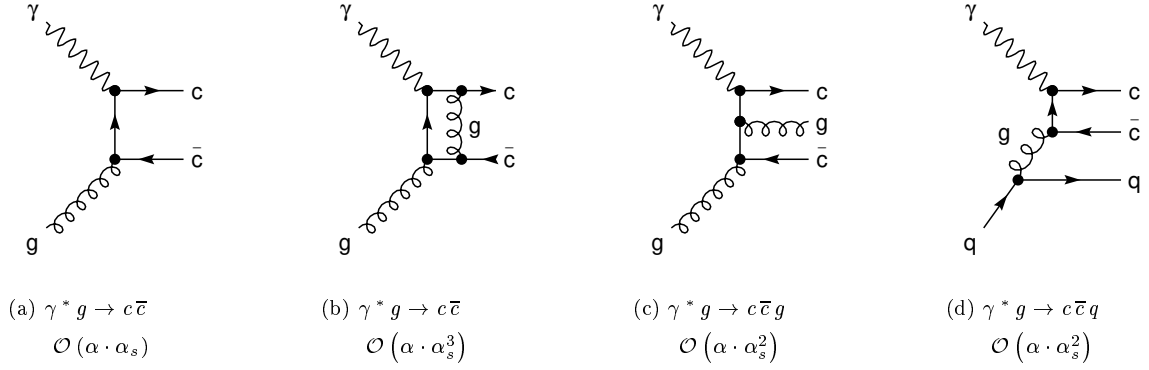


Figure 3.2: Feynman diagrams for the production of charm quarks through photon-gluon fusion including higher order corrections. The dominant correction term to the leading order process (a) is given by the gluon radiation process (c). An additional correction term of order  $\mathcal{O}(\alpha \cdot \alpha_s^2)$  occurs through the interference of the leading order process and the process (b), which form the same final state.

Complete calculations up to order  $\mathcal{O}(\alpha \cdot \alpha_s^2)$  are available for charm production in both the photoproduction [NDE:88, EN:89, FMNR:95, FNR:95] and the deep-inelastic scattering regime [HS:98]. Some of the graphs to be considered in higher order corrections are depicted in Fig. 3.2. In the case of photoproduction, the  $\mathcal{O}(\alpha \cdot \alpha_s^2)$  radiative corrections are about 60% of the LO cross-section and the NLO inclusive heavy quark distributions are found to be similar in shape to the LO distributions. The effect of the NLO corrections can therefore be described by an approximately constant  $K$ -factor [EN:89]. In contrast, the  $K$ -factor of DIS is strongly kinematics dependent.

The QCD predictions are however subject to rather large theoretical uncertainties. Especially at fixed target energies, the largest uncertainty is given by the dependence of the cross-section on the mass of the charm quark. Varying the charm quark mass between 1.2 GeV and 1.8 GeV changes the charm cross-section by more than a factor of 3 [EN:89]. Smaller dependences are observed for the uncertainties related to the renormalisation scale  $\mu$ , the QCD scale parameter  $\Lambda$  and the form of the gluon distribution. The uncertainty on the renormalisation scale  $\mu$  is illustrated in Fig. 3.3.

Neutral Current	Charged Current
$\gamma^*/Z_0 + c \rightarrow c$	$W^+ + q_{d,s} \rightarrow c$
$\gamma^*/Z_0 + \bar{c} \rightarrow \bar{c}$	$W^- + \bar{q}_{d,s} \rightarrow \bar{c}$
$\gamma^*/Z_0 + g \rightarrow c + \bar{c}$	$W^+ + g \rightarrow c + \bar{q}_{d,s}$
	$W^- + g \rightarrow \bar{c} + q_{d,s}$

Table 3.1: Charm production processes in lepton-nucleon scattering.

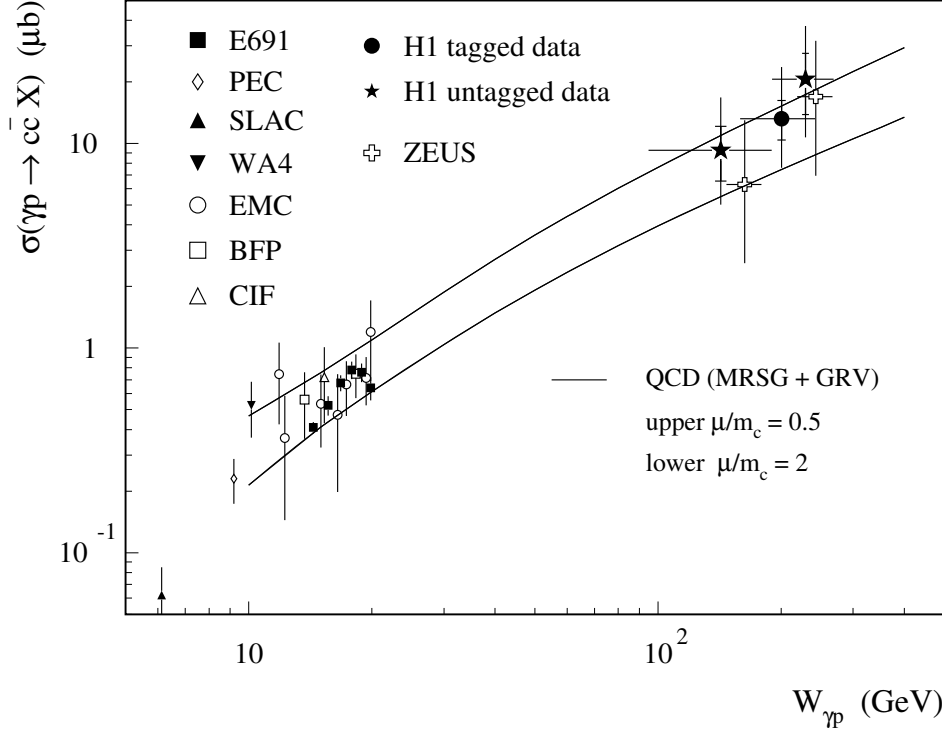


Figure 3.3: Total charm photoproduction cross-section as a function of the photon-nucleon centre of mass energy  $W_{\gamma p}$ . The solid lines represent the prediction of a NLO QCD calculation and delimit the range of values expected from varying the renormalisation scale within  $0.5 < \mu/m_c < 2$  [H1:96].

### 3.1.2 Additional Production Mechanisms

Several other processes besides the photon-gluon fusion exist in which charm quarks can be produced. However, as these mechanisms have a negligible contribution to the total cross-section near threshold, they will only be briefly mentioned here.

#### Non-perturbative (Intrinsic) Charm

Cross-section measurements for the hadro-production of charm performed in fixed target experiments at the end of the seventies could not be explained with leading order QCD calculations. A model introducing a non-perturbative  $c\bar{c}$ -content of the nucleon was suggested to explain the surplus in the measured cross-section for large values of  $x$  [BHPS:80, BPS:81]. In this model, the Fock representation of the proton wave function

$$|p\rangle = \alpha |uud\rangle + \beta |uudc\bar{c}\rangle + \dots$$

includes a small but non-zero probability  $\beta^2$  for an intrinsic charm quark pair. A value of  $\beta^2 = 1\%$  was chosen to explain the original data, also supported by theoretical estimates [HM:83, VBH:92]. In this model, the charm quark distribution as a function of  $x$  peaks around 0.25 and is the same



for quarks and anti-quarks. When additional data from H1 and ZEUS as well as NLO calculations became available, the measured cross-sections could be explained without intrinsic charm.

In an alternative to the intrinsic charm model described above, the charm sea is assumed to arise from quantum fluctuations of the nucleon to a virtual  $D^0 + \Lambda_c^+$  configuration [NNNT:96, MT:97, PNN<sup>+</sup>:98]. A natural prediction of this model is that the charm and anti-charm distributions are not symmetric. This meson cloud model for the long-range structure of the nucleon has been used extensively to describe various flavour symmetry breaking phenomena observed in deep-inelastic scattering and related experiments. It offers a natural explanation of the excess of the  $\bar{d}$ - over  $\bar{u}$ -distributions in the proton in terms of a pion cloud, which itself is a necessary ingredient of the nucleon by chiral symmetry. It also provides an intuitive framework to study the strangeness content of the nucleon, through the presence of the kaon cloud. Whether the same philosophy can be justified for a cloud of heavy charmed mesons and baryons around the nucleon is rather questionable given the large mass of the fluctuation.

### Resolved Processes

Besides the direct interaction with a parton of the nucleon, the photon can also interact as a particle with partonic sub-structure (resolved or hadronic component of the photon). Similar to the nucleon, the sub-structure of the photon can be described with structure functions. In LO QCD, charm quarks then can be produced via gluon-gluon fusion or quark-anti-quark annihilation of a parton inside the photon and a parton inside the nucleon:

$$\begin{aligned} g + g &\rightarrow c + \bar{c} \quad , \\ q + \bar{q} &\rightarrow c + \bar{c} \quad . \end{aligned}$$

These processes are – as the direct processes in LO – of order  $\mathcal{O}(\alpha \cdot \alpha_s)$ .

The contribution of the hadronic component of the photon to charm photoproduction is shown in Fig. 3.4, where NLO QCD predictions for the total charm photoproduction cross-section are given as a function of the photon-nucleon centre of mass energy [FMP<sup>+</sup>:97]. While at high energies the resolved processes become important and depend strongly on the chosen parametrisation for the photon structure functions, at lower energies such contributions can be neglected.

### Fragmentation

Because of their large mass, the creation of charm quarks in the fragmentation is highly suppressed [MN:92, Sey:94, Sey:95]. The average multiplicity per event for the creation of a  $c\bar{c}$ -pair by gluon splitting ( $g \rightarrow c\bar{c}$ ) was measured in  $e^+e^-$  collisions at LEP for hadronic  $Z^0$  decays to be roughly 2% [OPAL:95].

### Bottom Decays

As bottom quarks decay predominantly into charm quarks they are a potential source for charm production. The centre of mass energy at HERMES however is well below the threshold for the production of a  $b\bar{b}$ -pair where  $E_{th} = 2m_b \gtrsim 8 \text{ GeV}$ .

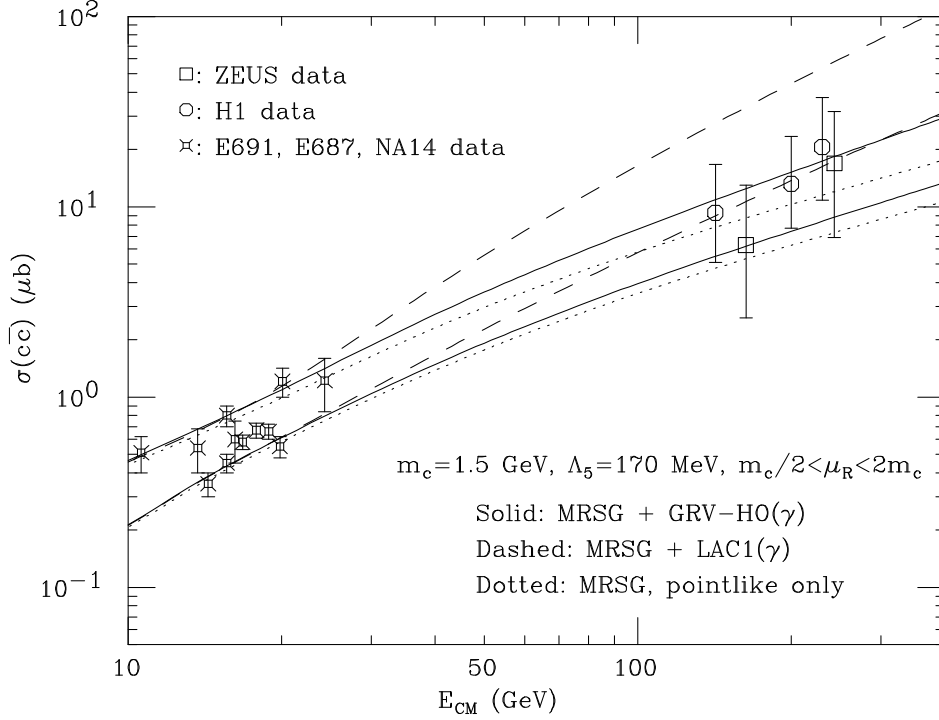


Figure 3.4: Total cross-section for the photoproduction of charm quark pairs as a function of the photon-nucleon centre of mass energy. Shown are NLO QCD predictions from [FMP<sup>+</sup>:97] for various structure function sets of nucleon and photon versus experimental results. Additionally, the theoretical uncertainty due to the choice of the renormalisation scale  $\mu_R$  is given by the band of predicted curves.

### 3.1.3 Gluon Density

Since photon-gluon fusion is the dominant process for charm production, the measurement of charmed particles in the final state can be used to get access to the gluon density functions of the nucleon.

For real photons, the unpolarised cross-section for the photoproduction of  $c\bar{c}$ -pairs can be factorised in a convolution of the gluon distribution function and the hard photon-gluon scattering sub-process

$$\sigma^{\gamma N \rightarrow c\bar{c}X}(\nu) = \int_{4m_c^2}^{2M\nu} d\hat{s} \hat{\sigma}^{\gamma g \rightarrow c\bar{c}}(\hat{s}) g(x_g, \hat{s}), \quad (3.1)$$

and analogously in the polarised case for the cross-section difference of anti-parallel and parallel photon and nucleon spin configurations

$$\Delta\sigma^{\gamma N \rightarrow c\bar{c}X}(\nu) = \int_{4m_c^2}^{2M\nu} d\hat{s} \Delta\hat{\sigma}^{\gamma g \rightarrow c\bar{c}}(\hat{s}) \Delta g(x_g, \hat{s}). \quad (3.2)$$

In these expressions denote  $\hat{s} = s(\gamma g)$  the square of the centre of mass energy of the photon-gluon system and  $x_g$  the fractional gluon momentum with respect to the nucleon momentum

$$x_g = \frac{s(\gamma g)}{s(\gamma N)} = \frac{\hat{s}}{2M\nu}. \quad (3.3)$$

The hard photon-gluon scattering sub-processes for the production of a  $c\bar{c}$ -pair can be expressed in LO QCD as

$$\hat{\sigma}^{\gamma g \rightarrow c\bar{c}}(\hat{s}) = e_c^2 \frac{2\pi\alpha\alpha_s(\hat{s})}{\hat{s}} \left[ -\beta(2 - \beta^2) + \frac{1}{2}(3 - \beta^4) \ln \frac{1+\beta}{1-\beta} \right], \quad (3.4)$$

$$\Delta\hat{\sigma}^{\gamma g \rightarrow c\bar{c}}(\hat{s}) = e_c^2 \frac{2\pi\alpha\alpha_s(\hat{s})}{\hat{s}} \left[ -3\beta + \ln \frac{1+\beta}{1-\beta} \right], \quad (3.5)$$

with  $\beta = \sqrt{1 - 4m_c^2/\hat{s}}$  being the centre of mass velocity of the charm quarks [Wat:82, GR:88].

In the case of lepton-nucleon scattering the incoming lepton beam is assumed to be equivalent to a broad-band beam of virtual photons, where the photon distribution in the electron is calculable in QED (Weizsäcker-Williams approach) [vW:34, Wil:34]. While real photons can only be transversely polarised, virtual photons may also have longitudinal polarisation and the double differential unpolarised cross-section for lepton-nucleon scattering can be expressed as the sum of the absorption cross-sections for transversely and longitudinally polarised virtual photons weighted with the corresponding fluxes  $\Gamma$  (see Sec. 2.1)

$$\frac{d\sigma^{\ell N}}{dQ^2 d\nu}(Q^2, \nu) = \Gamma_T(Q^2, \nu) \sigma_T^{\gamma^* N}(Q^2, \nu) + \Gamma_L(Q^2, \nu) \sigma_L^{\gamma^* N}(Q^2, \nu), \quad (3.6)$$

$$= \Gamma_T(Q^2, \nu) \left[ 1 + \epsilon R(Q^2, \nu) \right] \sigma_T^{\gamma^* N}(Q^2, \nu), \quad (3.7)$$

$$\equiv \Gamma(Q^2, \nu) \sigma_T^{\gamma^* N}(Q^2, \nu). \quad (3.8)$$

As a reminder,  $R = \sigma_L/\sigma_T$  is the ratio of the photo-absorption cross-sections and  $\epsilon = \Gamma_L/\Gamma_T$  the ratio of the virtual photon fluxes (see Eqs. 2.24 and 2.37). Comparison with the previous expression Eq. 2.29 for the differential cross-section allows the identification

$$\Gamma(Q^2, \nu) = \frac{\alpha}{\pi} \frac{\nu - \frac{Q^2}{2M}}{Q^2(\nu^2 + Q^2)} \left[ \left( 1 - \frac{\nu}{E} - \frac{Q^2}{4E^2} \right) (1 + R(Q^2, \nu)) + \frac{1}{2E^2} (\nu^2 + Q^2) \left( 1 - \frac{2m_\ell^2}{Q^2} \right) \right]. \quad (3.9)$$

In this formula terms proportional to  $m_\ell^2/Q^2$  – which were neglected in the deep-inelastic scattering case – have been kept as they can become important in the photoproduction limit ( $Q^2 \rightarrow 0$ ). The extrapolation to the cross-section for the photoproduction with real photons is possible by using a modified propagator term

$$\sigma_T^{\gamma^* N}(Q^2, \nu) = \left( 1 + \frac{Q^2}{M_0^2} \right)^{-2} \sigma^{\gamma N}(\nu), \quad (3.10)$$

where the mass scale  $M_0$  has to be adjusted to the process under investigation. For open charm production it has been extracted from a fit to experimental data to be in the range 3.4 GeV to 4.1 GeV for  $\nu$  values between 70 GeV and 200 GeV [EMC:83a].

This formalism has been used in NLO QCD to extract the unpolarised gluon density from the production of  $D^*$  mesons in deep-inelastic electro- and photoproduction [H1:99]. The very good

agreement in Fig. 3.5 is a nice verification of the theoretical understanding of this process in both kinematical regimes. The remarkably good agreement also in comparison to the results obtained from the  $Q^2$  evolution of the inclusive structure functions (Sec. 2.2) can be understood as an important confirmation for the application of perturbative QCD and the universality of the gluon distribution in these processes.

## 3.2 Formation and Decay of Charmed Particles

Up to now only the production of charm quarks has been considered. However, quarks are coloured objects and have to fragment into colour neutral objects due to the confinement property of QCD. After fragmentation, charmed particles can possess a non-zero charm quantum number (*open charm*) or contain the same number of  $c$ - and  $\bar{c}$ -quarks (*hidden charm*).

Even though the photon-gluon fusion model is applicable for both open and hidden charm production, the formation of the final state hadrons might be very different. The hidden charm production is commonly discussed in the framework of the *colour singlet model* (CSM) and the *colour octet model* (COM). There, the produced  $c$ - and  $\bar{c}$ -quarks are bound into a colour singlet object by the subsequent emission of one or more hard (CSM) or soft (COM) gluons. However, hidden charm production is not in the scope of this thesis. More about the colour singlet and octet models and their application to unpolarised and polarised hidden charm production at HERMES can be found in [Mei:00].

In lepton-nucleon scattering, the  $c\bar{c}$ -pair from the photon-gluon fusion process dominantly leads to charmed meson–anti-meson pairs or associated charmed baryon–anti-meson production. For open charm, the fragmentation is usually described in the standard schemes, but uses a harder fragmentation function to accommodate the higher mass of the charm quark. The fragmentation of a fast moving charm quark into a hadron  $H = (c\bar{q})$  and a light quark  $q$  can be described phenomenologically with the *Peterson fragmentation function* [PSSZ:83]

$$D_c^H(z) = \frac{N}{z [1 - 1/z - \epsilon_c / (1 - z)]^2}, \quad (3.11)$$

where  $z$  is the energy fraction of hadron  $H$  with respect to the charm quark and  $N$  is a normalisation such that  $\sum \int dz D_c^H(z) = 1$ . The free parameter  $\epsilon_c$  has to be extracted from fits to data. Typical values for  $\epsilon_c$  range from 0.025 to 0.075 for which the corresponding fragmentation functions are shown in Fig. 3.6. The smaller the value for this parameter, the harder the fragmentation process becomes.

Since the first discovery of the  $J/\Psi$  meson and the lightest charmed mesons, many more charmed particles have been found and their properties have been studied in detail. In the following only those charmed hadrons will be discussed which can be identified in a fixed target lepton-nucleon scattering experiment such as HERMES. This excludes the charmed baryons with the exception of the  $\Lambda_c$ . The quark contents and the masses for the – at HERMES – interesting charmed hadrons are listed in Tab. 3.2. The typical mass scales for charmed particles are around 2 GeV for open and 3 GeV for hidden charm.

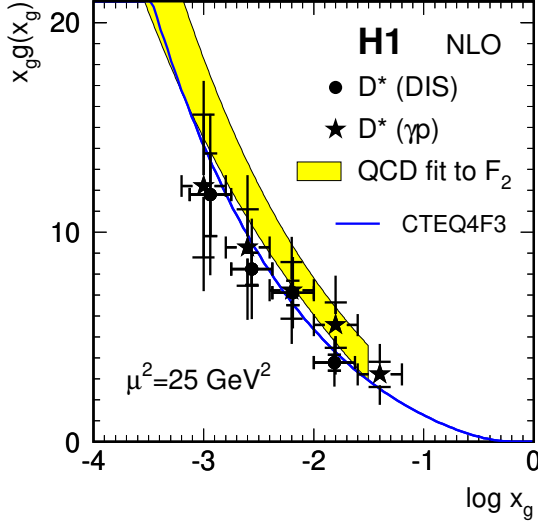


Figure 3.5: Gluon density in the proton extracted from charm electro- and photoproduction and comparison with indirect results from  $F_2$  scale breaking [H1:99].

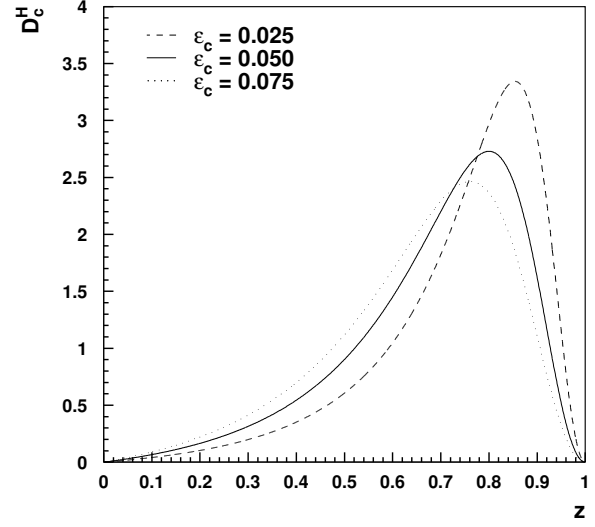


Figure 3.6: Peterson fragmentation function  $D_c^H(z)$  for different values of the phenomenological parameter  $\epsilon_c$ .

While the  $D^*$  vector mesons can decay strongly or electromagnetically into the pseudo-scalar  $D$  mesons (see also Tab. 3.3), the  $D$  mesons themselves are the lowest mass eigenstates for charm and can only decay weakly with typical lifetimes of  $\mathcal{O}$  (ps). In the weak interaction a  $c$ -quark can turn into a lighter  $s$ - or  $d$ -quark when radiating off a  $W^+$  boson. The large mass differences of the  $D$  mesons compared to mesons which contain only the light  $u$ ,  $d$ , and  $s$  quarks lead to many possible decay modes with rather small branching fractions and typically large multiplicities. A selection of interesting decay modes is listed in Tab. 3.4.

Particle	Quark Content	Mass (MeV)	Full Width (MeV)	Mean Lifetime (ps)
$D^{*0}, \bar{D}^{*0}$	$c\bar{u}, \bar{c}u$	$2006.7 \pm 0.5$	$< 2.1$	
$D^{*+}, D^{*-}$	$c\bar{d}, \bar{c}d$	$2010.0 \pm 0.5$	$< 0.131$	
$D_s^{*+}, D_s^{*-}$	$c\bar{s}, \bar{c}s$	$2112.4 \pm 0.7$	$< 0.19$	
$D^0, \bar{D}^0$	$c\bar{u}, \bar{c}u$	$1864.6 \pm 0.5$		$0.415 \pm 0.004$
$D^+, D^-$	$c\bar{d}, \bar{c}d$	$1869.3 \pm 0.5$		$1.057 \pm 0.015$
$D_s^+, D_s^-$	$c\bar{s}, \bar{c}s$	$1968.5 \pm 0.6$		$0.467 \pm 0.017$
$\eta_c$	$c\bar{c}$	$2979.8 \pm 2.1$	$13.2^{+3.8}_{-3.2}$	
$J/\Psi$	$c\bar{c}$	$3096.88 \pm 0.04$	$0.087 \pm 0.005$	
$\Lambda_c^+, \bar{\Lambda}_c^+$	$udc, \bar{u}\bar{d}\bar{c}$	$2284.9 \pm 0.6$		$0.206 \pm 0.012$

Table 3.2: Particle properties for a selected list of charmed particles [ $C^+$ :98].

$M(D^{*+}) - M(D^0) = 145.4 \text{ MeV}$	$m(\pi^\pm) = 139.57 \text{ MeV}$
$M(D^{*+}) - M(D^+) = 140.7 \text{ MeV}$	
$M(D^{*0}) - M(D^0) = 142.1 \text{ MeV}$	
$M(D^{*0}) - M(D^+) = 137.4 \text{ MeV}$	$m(\pi^0) = 134.95 \text{ MeV}$
$M(D^{*+}) - M(D^{*0}) = 3.3 \text{ MeV}$	
$M(D^+) - M(D^0) = 4.7 \text{ MeV}$	

Table 3.3: Mass differences between various combinations of  $D$  and  $D^*$  mesons. As a reference the masses of the lightest mesons  $\pi^\pm$  and  $\pi^0$  are additionally given [C<sup>+</sup>:98]. Only the first three combinations correspond to physically possible strong decays. The lower three combinations would involve changes in the charge but are below the  $\pi^\pm$  mass threshold.

Decay Channel	Branching Fraction (%)	Final State Particles
$D^0 \rightarrow K^- \pi^+$	$3.85 \pm 0.09$	2
$\rightarrow \bar{K}^0 \pi^0$	$2.12 \pm 0.21$	4
$\rightarrow \bar{K}^0 \pi^+ \pi^-$	$5.4 \pm 0.4$	4
$\rightarrow K^- \pi^+ \pi^0$	$13.9 \pm 0.9$	4
$\rightarrow K^- \pi^+ \pi^+ \pi^-$	$7.6 \pm 0.4$	4
$\rightarrow K^+ K^-$	$0.43 \pm 0.02$	2
$\rightarrow \pi^+ \pi^-$	$0.15 \pm 0.01$	2
$\rightarrow K^- \ell^+ \nu_\ell$	$3.50 \pm 0.17$	2
$D^+ \rightarrow \bar{K}^0 \pi^+$	$2.89 \pm 0.26$	3
$\rightarrow K^- \pi^+ \pi^+$	$9.0 \pm 0.6$	3
$\rightarrow \bar{K}^0 \pi^+ \pi^0$	$9.7 \pm 3.0$	5
$\rightarrow K^- \pi^+ \pi^+ \pi^0$	$6.4 \pm 1.1$	5
$\rightarrow \bar{K}^0 \pi^+ \pi^+ \pi^-$	$7.0 \pm 0.9$	5
$\rightarrow K^+ \bar{K}^0$	$0.74 \pm 0.10$	3
$\rightarrow K^+ K^- \pi^+$	$0.88 \pm 0.08$	3
$\rightarrow \pi^+ \pi^0$	$0.25 \pm 0.07$	3
$\rightarrow \pi^+ \pi^+ \pi^-$	$0.36 \pm 0.04$	3
$\rightarrow \bar{K}^0 \ell^+ \nu_\ell$	$6.8 \pm 0.8$	3
$D^{*0} \rightarrow D^0 \pi^0$	$61.9 \pm 2.9$	$\geq 4$
$\rightarrow D^0 \gamma$	$38.1 \pm 2.9$	$\geq 3$
$D^{*+} \rightarrow D^0 \pi^+$	$68.3 \pm 1.4$	$\geq 3$
$\rightarrow D^+ \pi^0$	$30.6 \pm 2.5$	$\geq 5$
$\rightarrow D^+ \gamma$	$1.1^{+2.1}_{-0.7}$	$\geq 4$

Table 3.4: Selected decay channels for the  $D$  and  $D^*$  mesons [C<sup>+</sup>:98]. The charged conjugate decays are also possible. The last column of the table gives the number of particles to be reconstructed. In this number, the decays  $\pi^0 \rightarrow \gamma\gamma$  and  $K^0, \bar{K}^0 \rightarrow K_S^0 \rightarrow \pi^+ \pi^-$  ( $K_L^0$  are not detectable with the HERMES spectrometer) are implicitly assumed, while for the semi-leptonic decays the neutrino is not counted.

### 3.2.1 Monte Carlo Simulations

All Monte Carlo studies for open charm production presented in the following are based on the *AROMA* event generator which simulates the production of heavy quark flavours in lepton-nucleon scattering through the boson-gluon fusion process [IRS:96]. Since the involved energies are moderate, electroweak processes are excluded in the simulations. For the hadronisation, *JETSET* is used which supports several fragmentation models [Sjö:94]. The most important ones are the independent fragmentation and the *LUND* string model. Fragmentation functions have to be used in both models to describe the momentum and energy sharing between a newly formed hadron and the remaining quark or diquark system. A large number of different fragmentation functions are available, since they cannot be derived from first principles.

For the light quarks the *LUND* symmetric fragmentation function has been chosen. Its default parameters in *JETSET* are adjusted to describe data at high energies where hard parton showers are important. At the much lower energies of *HERMES* the need for a softer fragmentation arises and a better description of the data can be obtained with retuned parameters. In the following the two parameter sets for the *LUND* symmetric fragmentation function will be denoted as the Default and the *HERMES* set respectively.

For the charm quarks, the default mass value of *JETSET* is chosen ( $m_c = 1.35 \text{ GeV}$ ) and two alternatives are studied for their fragmentation: a modification of the *LUND* symmetric fragmentation function according to the Bowler space-time picture of string evolution and the phenomenological Peterson fragmentation function introduced in the previous section which results in a harder fragmentation for the heavy quarks.

The independent fragmentation model does not a priori conserve energy, momentum or flavour and the handling of gluon fragmentation is not unique. Here, an algorithm has been chosen which obeys the conservation laws by compensating any imbalance according to the particle energies. Gluons are assumed to fragment like a light quark-anti-quark pair, sharing the gluon energy according to the Altarelli-Parisi splitting function.

If not explicitly stated otherwise, for all results presented in the following sections the *LUND* string model together with the Peterson fragmentation function using  $\epsilon_c = 0.050$  has been used. For further references to the fragmentation models and the tuning of the fragmentation parameters to the *HERMES* data, see also Sec. 2.3.1.

### Production Probabilities

For the most prominent particles, the production probabilities per open charm event in lepton-proton scattering are presented in Fig. 3.7 as a function of the lepton beam energy. In this figure also particles from possible subsequent decays of the primarily produced charmed baryons and mesons are included. The underlying mechanisms however can be better studied when looking at the primarily produced charmed particles only.

As can be seen in Fig. 3.8, large differences in the primary production probabilities for charmed particles and their anti-particles are predicted, both for the absolute values and the energy dependence. While for the anti-particles the probabilities change only slowly with the beam energy,

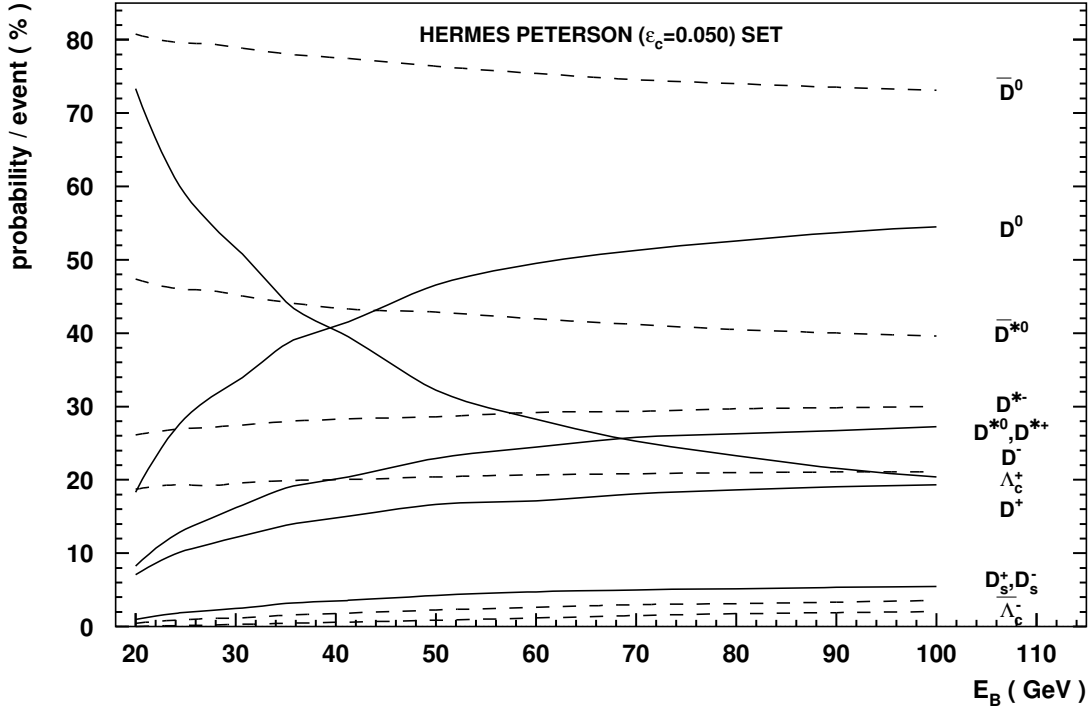


Figure 3.7: Charmed particle production probabilities per open charm event for photon gluon fusion in lepton proton scattering as a function of the lepton beam energy  $E_B$ . Shown are the results of Monte Carlo simulations based on the AROMA event generator for the Peterson fragmentation set with  $\epsilon_s = 0.050$  (see text). For a better visibility, the results for particles and anti-particles are plotted with solid and dashed lines respectively.

they are strongly energy dependent especially for the charmed baryons and  $D^{*+}$ ,  $D^{*0}$  mesons. Charmed baryons are primarily produced in about 60% of the open charm events at HERMES energies; anti-baryons almost never occur. At beam energies of 100 GeV this fraction decreases to about 25%, but still about a factor ten less anti-baryons than baryons are produced.

The suppression of anti-baryons can be explained through the conservation of the baryon number in the scattering process. The proton target has a positive baryon number, which – not only for charmed baryons – naturally leads to an excess of baryons over anti-baryons in the final state. For each anti-baryon an additional baryon is necessary to keep the balance. Sufficient energy has to be available in the final state to allow the production of the two rather massive particles. The increase in the production threshold from 2.3 GeV for  $\Lambda_c$ -production to 3.2 GeV for  $\bar{\Lambda}_c N$  reduces the available phase space and leads to the observed suppression of the charmed anti-baryons, especially at low energies.

The fact that a large fraction of events contains charmed baryons at all is a consequence of strong correlations between the  $c$ - and  $\bar{c}$ -quarks produced in the hard interaction and the remnants of the struck nucleon present in the LUND string model. The strength of the correlations decreases with increasing centre of mass energy, explaining the reduced baryon production probability at higher lepton beam energies. Another consequence are the asymmetries between the charmed mesons and anti-mesons which are largest at small energies. The  $c$ -quark can only form a meson with an



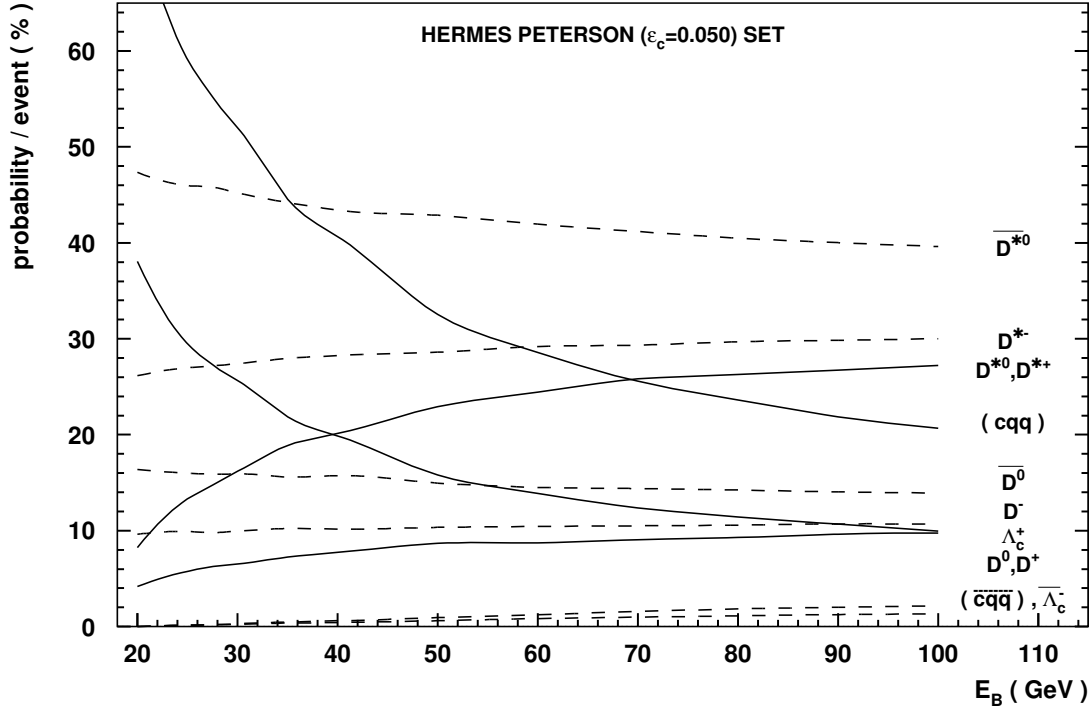


Figure 3.8: Production probabilities of primarily produced charmed particles per open charm event for photon gluon fusion in lepton-proton scattering as a function of the lepton beam energy  $E_B$ .

anti-quark from the nucleon sea or from a virtual  $q\bar{q}$ -pair produced in the fragmentation process. The  $\bar{c}$ -quark on the other hand has additional phase space through the valence quarks from the struck nucleon. This picture is furthermore supported by the asymmetry in the production rates for the  $D^{*-}$  and  $\bar{D}^{*0}$  mesons which both have the valence quark flavours of the proton as the light quark partner of the  $\bar{c}$ -quark. This asymmetry can be understood in terms of the excess of the  $u$ - over  $d$ -quark distributions in the proton with a dilution due to the symmetric production of these flavours in the fragmentation process. In the small  $x$ -region mainly probed in the charm production, this excess is smaller than the factor 2 for the integrated distributions. In this kinematical region the sea quark distributions are very similar, leading to basically identical production probabilities for the  $D^{*+}$  and  $D^{*0}$  mesons which do not contain a valence quark flavour of the proton.

In other models, such as longitudinal excitation, the production of charmed and anti-charmed hadrons is expected to be exactly symmetric. Experimentally however, large asymmetries in the production of charmed and anti-charmed hadrons have been observed [A<sup>+</sup>:86, A<sup>+</sup>:87, NA14/2:93].

Since the valence quarks can carry a large fraction of the nucleon momentum, differences are also expected for the energy spectra of the various charmed particle types. This will be studied in the next section.

## Energy Spectra

The following studies are for a lepton beam energy of  $E_B = 27.5$  GeV, matching the experimental conditions at HERMES.

As expected, the  $c$ - and  $\bar{c}$ -quarks produced in the photon-gluon fusion process have the same energy distributions (Fig. 3.9a). After the hadronisation however, significant differences are observable between the energy spectra for the primarily produced charmed hadrons and anti-hadrons (Fig. 3.9b). To understand these differences, it is best to distinguish the two dominantly occurring charmed final state types: charmed meson–anti-meson pairs and associated charmed baryon–anti-meson production. In the case of pair production, the  $c$ -quark energy is on average higher than the  $\bar{c}$ -quark energy (Fig. 3.9e). The opposite behaviour is observed for the associated baryon production where not only the mean of the distribution is shifted but also completely different shapes are obtained (Fig. 3.9c). As for the production probabilities, these energy spectra can be understood qualitatively by the difference between sea and valence quarks and the correlations with the target remnants. In this picture, the production of charmed baryons is favoured at low  $c$ -quark energies since the correlations with the target remnants are largest when both have similar velocities (Fig. 3.9c). As both diquarks from the target remnant and quarks from the fragmentation are typically low energetic, most of the binding energy necessary for the formation of charmed hadrons has to be provided by the  $c$ -quarks. This leads on average to lower energies after the hadronisation compared to the  $c$ -quark energies. For the  $\bar{c}$ -quarks on the other hand, the valence quarks represent additional phase space and their relatively high energy (compared to quarks from fragmentation) allows lower energetic  $\bar{c}$ -quarks to fragment into open charm anti-mesons (Fig. 3.9e).

However, the situation is more complex as indicated by the double-peak structure visible in the energy spectrum of the charmed mesons (Fig. 3.9f). Another classification of the final states is possible through the multiplicity of primarily produced hadrons containing the light  $u$ -,  $d$ -, and  $s$ -quarks only (“light hadrons”). In the string model, this number can be identified with the number of string breaks. When looking at the energy distributions as a function of the light hadron multiplicity (Fig. 3.10), the differences in the meson and anti-meson energies are mainly due to the – for meson–anti-meson pair production – lowest possible multiplicity of 1. Already at multiplicities of 2 for the light hadrons, the production is essentially symmetric for charmed mesons and anti-mesons. Also the differences between charmed baryons and anti-mesons get smaller the higher the multiplicity becomes. Since the average multiplicity increases with the centre of mass energy, more symmetric energy spectra independent of the charmed final state can be expected at higher lepton beam energies. On the other hand, the complex situation for the hadronisation at low energies makes the charm production near threshold a useful tool to learn more about the details of the fragmentation process. For completeness, it should be mentioned that for the associated charmed baryon production also multiplicity 0 is possible which is not shown in Fig. 3.10 since the energy distributions are very similar to those for multiplicity 1.

## Model Dependences

It has to be clearly stated that all the Monte Carlo simulations presented here are depending on the details of the fragmentation model used in the simulation. As an example, the dependence of the primary production probabilities on the parameters of the LUND symmetric fragmentation is

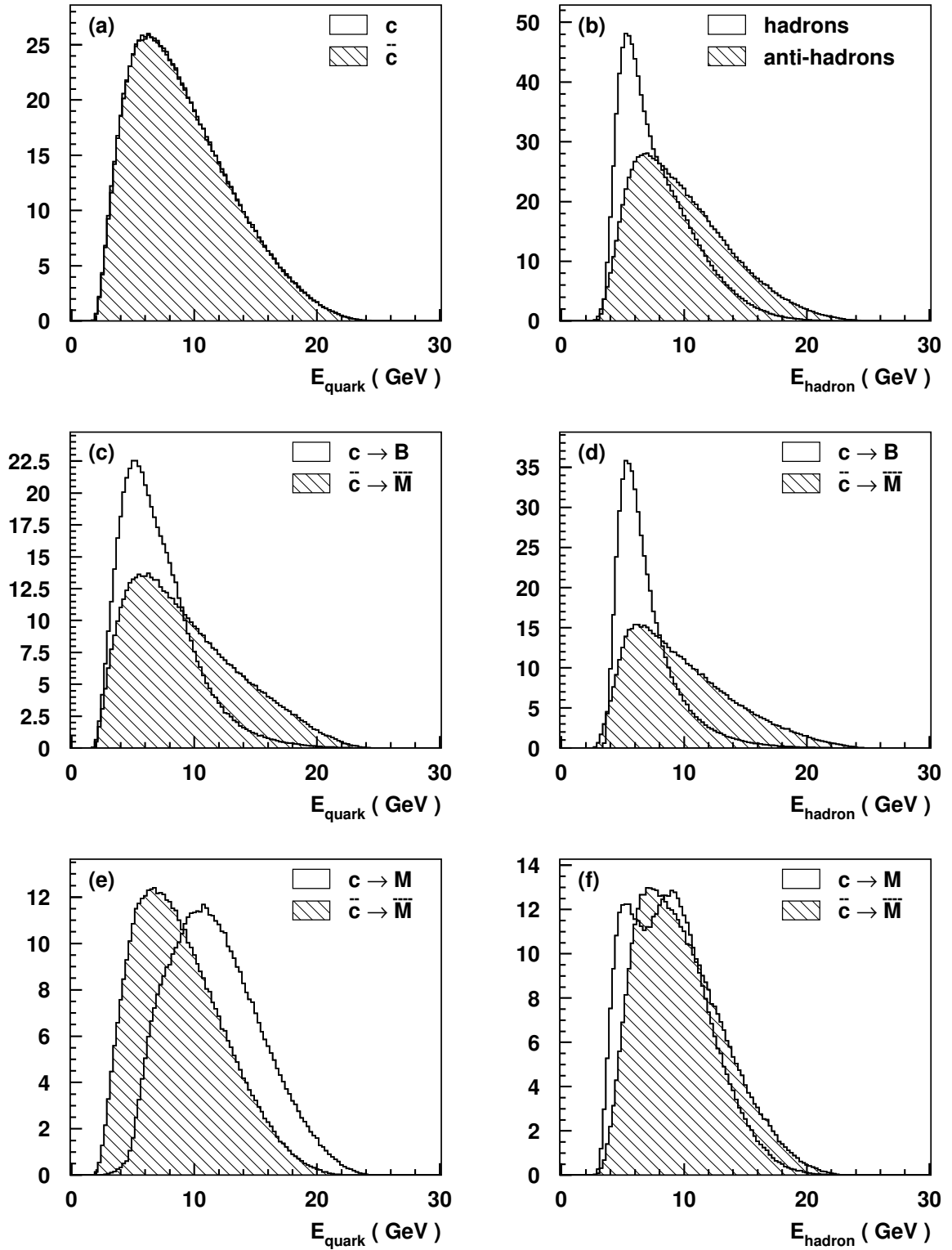


Figure 3.9: Comparison of the energy distributions for charmed particles and anti-particles on the quark and hadron level. The cases of associated baryon-anti-meson production (figures (c) and (d)) and meson-anti-meson pair production (figures (e) and (f)) are separately shown.

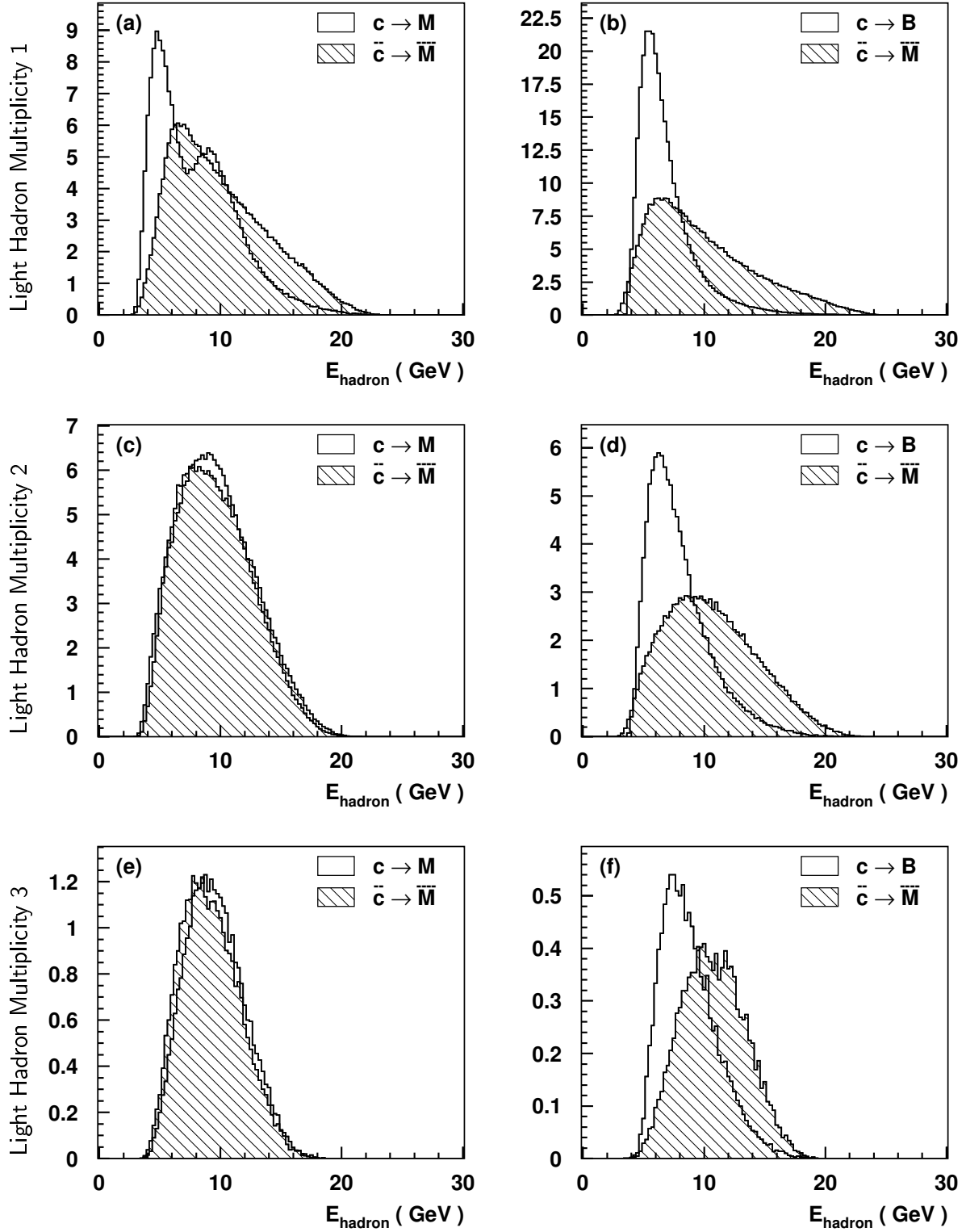


Figure 3.10: Comparison of the energy distributions for charmed hadrons and anti-hadrons depending on the multiplicity of primarily produced light hadrons in the final state. The cases of meson–anti-meson pair production (figures (a), (c) and (e)) and associated baryon–anti-meson production (figures (b), (d) and (f)) are separately shown.

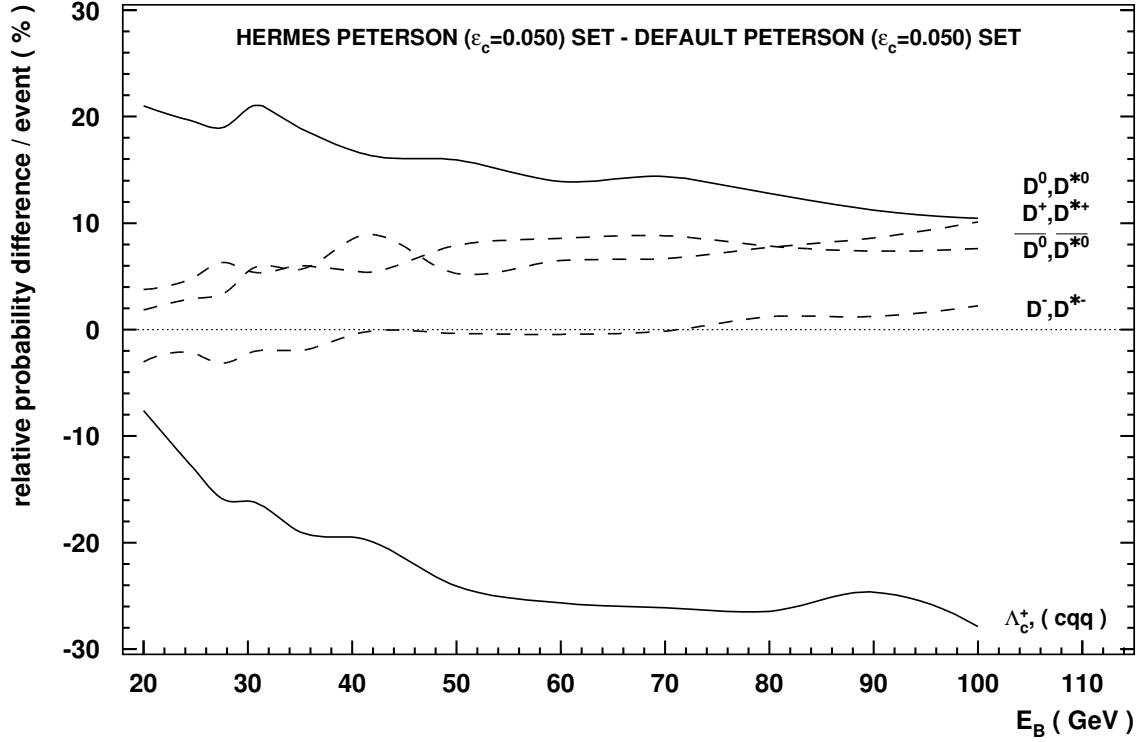


Figure 3.11: Differences in the production probabilities of primarily produced charmed particles per open charm event for various fragmentation models and functions. Shown are only the results for open charm mesons and baryons; anti-baryons have been neglected since due to the small absolute probabilities large relative deviations are possible.

shown in Fig. 3.11. Further examples for the dependences on the above discussed fragmentation models and fragmentation functions can be found in appendix B.1 (Figs. B.1 - B.3). Please note, that the sometimes oscillating behaviour of the differences in these figures is caused by the statistical precision of the Monte Carlo simulations. No large dependences of the production probabilities on the fragmentation models are visible for open charm mesons containing the  $\bar{c}$ -quark. All results agree to better than 10%. For the fragmentation of the  $c$ -quark however relative deviations up to 20% occur. The reason for these larger deviations are due to the uncertainties in the relative fragmentation into mesons or baryons. The largest deviations occur when comparing estimates obtained with the HERMES set to those from the Default set for the parameters of the LUND symmetric fragmentation function.

For the energy spectra, the mean and the width of the distributions for charmed hadrons and anti-hadrons are presented in Tab. 3.5 for the different fragmentation sets. These two parameters have been chosen even though they are not suited to uniquely characterise the partially complex shapes. The energy dependences on the fragmentation sets are as expected. The HERMES set realises a softer fragmentation compared to the Default set for the parameters of the LUND symmetric fragmentation function. Similarly for the dependence on the Peterson fragmentation parameter  $\epsilon_c$ . The smaller the value for  $\epsilon_c$ , the higher the average energy. This parameter also controls the shape of the charmed meson energy spectrum at a light hadron multiplicity of 1 (Fig. 3.10a). With a harder fragmentation function, the higher energetic peak in the distribution becomes more and more important.

Fragmentation Model	Fragmentation Function Set		Charmed Partner								
			Meson			Baryon			Meson or Baryon		
			$p$ (%)	$\langle E \rangle$ ( GeV)	$\sigma$ ( GeV)	$p$ (%)	$\langle E \rangle$ ( GeV)	$\sigma$ ( GeV)	$p$ (%)	$\langle E \rangle$ ( GeV)	$\sigma$ ( GeV)
LUND string	HERMES, Peterson $\epsilon_c = 0.025$	$(\bar{c}X)$	44.69	9.83	3.51	55.31	9.83	4.20	100.00	9.83	3.90
		$(cX)$	99.79	7.90	3.10	0.21	–	–	100.00	7.90	3.10
		all	144.47	8.50	3.36	55.53	9.83	4.19	200.00	8.87	3.66
LUND string	HERMES, Peterson $\epsilon_c = 0.050$	$(\bar{c}X)$	44.73	9.83	3.51	55.27	9.80	4.17	100.00	9.82	3.89
		$(cX)$	99.78	7.78	2.98	0.22	–	–	100.00	7.78	2.98
		all	144.51	8.42	3.29	55.49	9.80	4.17	200.00	8.80	3.61
LUND string	HERMES, Peterson $\epsilon_c = 0.075$	$(\bar{c}X)$	44.71	9.83	3.51	55.29	9.78	4.16	100.00	9.80	3.89
		$(cX)$	99.78	7.72	2.92	0.22	–	–	100.00	7.72	2.92
		all	144.48	8.37	3.26	55.52	9.77	4.16	200.00	8.76	3.59
LUND string	HERMES	$(\bar{c}X)$	44.68	9.81	3.50	55.32	9.70	4.13	100.00	9.75	3.87
		$(cX)$	99.77	7.42	2.69	0.23	–	–	100.00	7.43	2.69
		all	144.45	8.16	3.16	55.55	9.70	4.13	200.00	8.59	3.53
LUND string	Default, Peterson $\epsilon_c = 0.050$	$(\bar{c}X)$	37.41	9.33	3.44	62.59	9.23	3.96	100.00	9.27	3.77
		$(cX)$	99.57	8.27	3.19	0.43	–	–	100.00	8.28	3.19
		all	136.98	8.56	3.30	63.02	9.23	3.95	200.00	8.77	3.53
LUND string	Default	$(\bar{c}X)$	37.50	9.34	3.44	62.50	9.24	3.97	100.00	9.27	3.78
		$(cX)$	99.58	8.27	3.20	0.42	–	–	100.00	8.27	3.19
		all	137.08	8.56	3.30	62.92	9.23	3.96	200.00	8.77	3.54
Independent	HERMES	$(\bar{c}X)$	43.49	9.78	3.49	56.51	9.71	4.10	100.00	9.74	3.85
		$(cX)$	99.70	7.82	3.08	0.30	–	–	100.00	7.82	3.08
		all	143.19	8.42	3.34	56.81	9.70	4.09	200.00	8.78	3.61
Independent	Default	$(\bar{c}X)$	36.22	9.28	3.41	63.78	9.15	3.90	100.00	9.20	3.73
		$(cX)$	99.46	8.35	3.31	0.54	–	–	100.00	8.35	3.31
		all	135.68	8.60	3.36	64.32	9.15	3.89	200.00	8.77	3.55

Table 3.5: Fragmentation model dependences in the production of charmed hadrons. Listed are the production probabilities  $p$  and the mean  $\langle E \rangle$  and variance  $\sigma^2$  of the energy spectra.

## 4 The HERMES Experiment

The HERMES detector is located in the east section of the HERA electron-proton collider facility at DESY in Hamburg, Germany. The experiment was proposed in 1990 [HERMES:90] and approved in 1993 after a significant electron polarisation could be demonstrated. The installation was carried out in the 94/95 HERA winter shutdown and data taking started in spring 1995. While the HERA electron beam can be polarised, the current machine configuration does not allow a polarisation of the proton beam. As the primary goals of the HERMES experiment – the measurement of the double spin asymmetries in inclusive and semi-inclusive deep-inelastic scattering – require both leptons and nucleons to be polarised, HERMES operates in a fixed target mode and only the 27.5 GeV polarised electron beam gets utilised, while the unpolarised 820 GeV proton beam passes through the apparatus without interaction. Polarised nucleons are provided by a polarised internal gas target in a windowless storage cell. Figure 4.1 shows the electron storage ring of HERA with the experiments (HERMES, H1, ZEUS, HERA-B) in the four straight sections. H1 and ZEUS operate in colliding mode to study unpolarised deep-inelastic scattering at high energies with a centre of mass energy of  $\sqrt{s} = 300$  GeV in a kinematical region that is not accessible for fixed target experiments. HERA-B only uses particles in the halo of the proton beam which are scattered off target wires at high luminosities to study CP-violation in B-meson systems.

At HERA, electrons or positrons can be stored in the lepton ring. During 1995, 1996, and 1997, HERA operated with positrons; in 1998 improvements of the vacuum system allowed the usage of electrons. As the electro-weak processes under study at H1 and ZEUS are sensitive to the sign of the lepton charge, the lepton charge was again changed several times since then. At HERMES, where the weak processes are negligible due to the lower centre of mass energy, most of the physics program is insensitive to the lepton charge. An exception is the process of deeply virtual Compton scattering, where a lepton charge asymmetry is expected. Additionally, the data with the different lepton charge might be used for systematic studies.

As the data analysed in this work predominantly originate from the 1997 data taking period of HERMES, in the following sections special emphasis will be given to the experimental setup during that year.

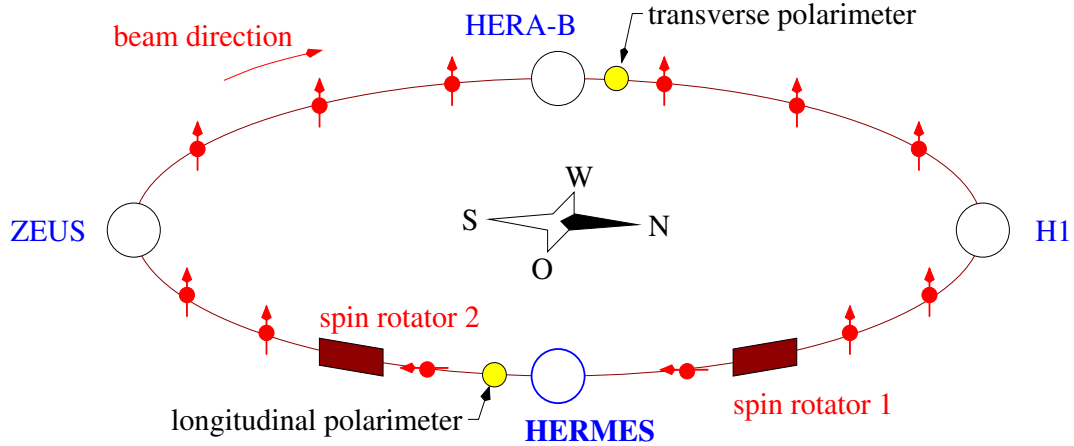


Figure 4.1: The electron storage ring of HERA at DESY. While a transverse polarisation is inherent for the storage ring, longitudinal polarisation at HERMES is achieved by two spin rotators in front of and after the interaction point. The spin of the electrons is symbolised by the small arrows. The transverse and longitudinal polarisations are measured by independent polarimeters.

## 4.1 The Polarised Electron Beam

In a storage ring an electron beam builds up a transverse polarisation as a consequence of a small asymmetric spin flip amplitude in the synchrotron radiation (Sokolov-Ternov effect) [ST:64]. The maximum polarisation is reached asymptotically. At the 27.5 GeV lepton energy of HERA, the build-up time is approximately 40 minutes and the asymptotic value is about 90%. Due to depolarisation effects, typical maximum polarisations of 60% are reached. To achieve the longitudinal polarisation necessary for the polarised physics program of HERMES, spin rotators are installed in front and behind the detector (see also Fig. 4.1). The longitudinal polarisation can be routinely reversed to reduce systematic effects while a *flat machine* (only transverse polarisation) is used for systematic studies and polarisation optimisation. The beam polarisation is measured by two Compton polarimeters scattering circularly polarised laser light off the beam. The *transverse polarimeter* utilises the fact that the Compton cross-section on transversely polarised leptons shows a spin-dependent azimuthal distribution. The centre of gravity of backscattered photons is measured in a position sensitive calorimeter and a top-bottom asymmetry of the position distribution can be used to derive the beam polarisation [Due:95, Oel:95]. The laser intensity is chosen such that on average only 0.01 photons backscatter per electron bunch (single-photon method). Since 1997 the *longitudinal polarimeter* measures the longitudinal polarisation of the beam near the HERMES interaction point. As measurement principle it uses the spin-dependent angular distribution of the Compton cross-section on longitudinally polarised leptons which translates into a spin-dependent energy spectrum. By using laser pulses of high intensity several thousand photons are backscattered per bunch and with their energy-weighted spin asymmetry the beam polarisation can be measured separately for each individual bunch [Bec:00].



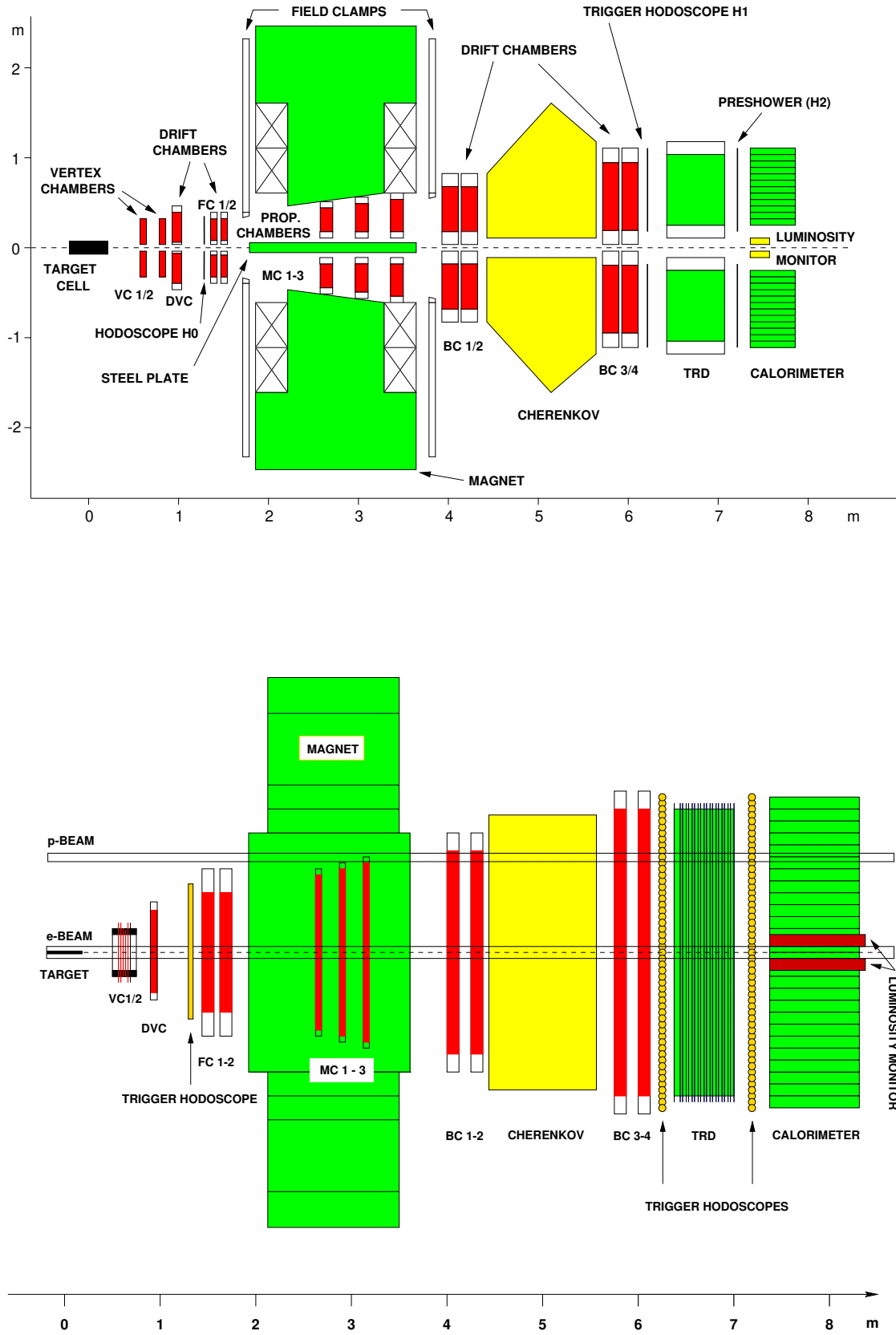


Figure 4.2: Schematic side and top view of the HERMES spectrometer.

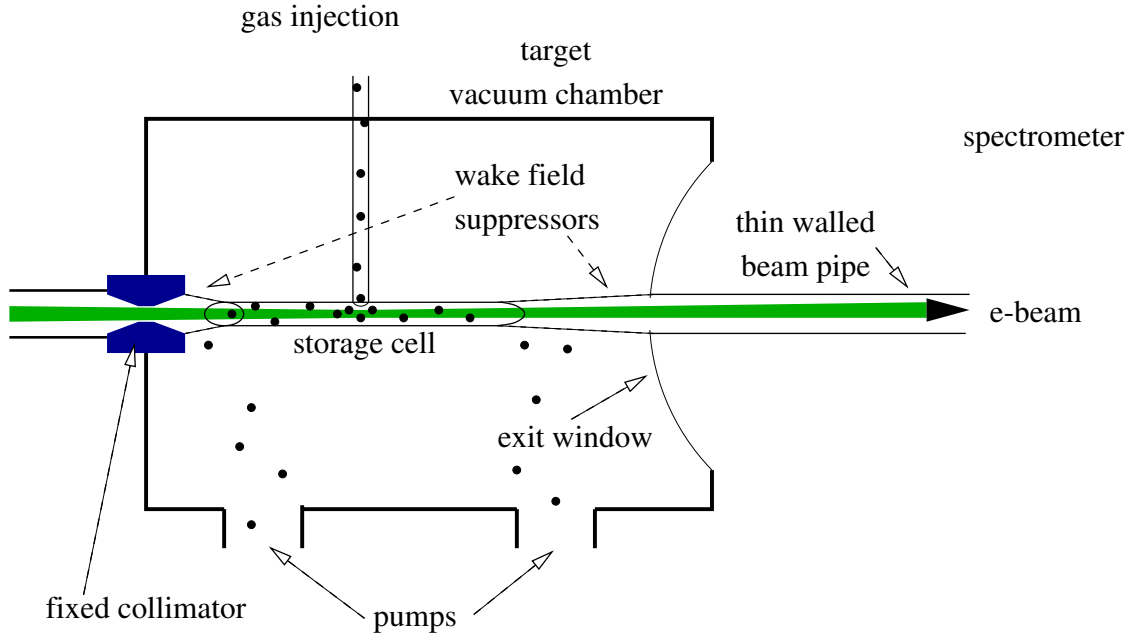


Figure 4.3: *Schematic diagram of the HERMES target region. An internal storage cell is used to increase the target density by about two orders of magnitude compared to a free atomic beam.*

## 4.2 The HERMES Target Region

Traditionally fixed target experiments use external beams and solid or liquid targets, where high target densities can be achieved. However, such targets are usually built of mixed materials and the presence of heavier nuclei makes it necessary to apply nuclear corrections. Moreover, in polarised experiments additionally only a small fraction of the atoms in the target are polarisable, introducing a low dilution factor. Furthermore massive cell windows might be necessary, which in addition to the high target density cause multiple scattering and energy loss for particles originating from the scattering process.

At HERMES the technique of an internal gas target inside a storage ring is used instead. A thin-walled cryogenically cooled storage cell is placed inside a vacuum chamber (see Fig. 4.3). The cell consists of an open-ended elliptical tube and is constructed from ultra-pure aluminium with a uniform wall thickness of  $75\,\mu\text{m}$ . Feed and sampling tubes intersect in the centre of the cell. A system of movable and fixed collimators is used to protect the cell and the spectrometer from synchrotron light and particle showers produced in the electron ring upstream of the target region. To maintain the ultra-high vacuum within the accelerator beam line the leaking gas atoms are pumped at both ends of the storage cell. The target cell geometry and the cooling increase the target density by about two orders of magnitude compared to a free atomic jet target.

To realise polarised proton, deuterium, and  $^3\text{He}$  targets two different setups exist. In 1995 an infrared laser was used to polarise  $^3\text{He}$  atoms by meta-stability exchange optical pumping in a glass cell. Details can be found in [dS<sup>+</sup>:98]. In 1996 and 1997 an atomic beam source (ABS) of

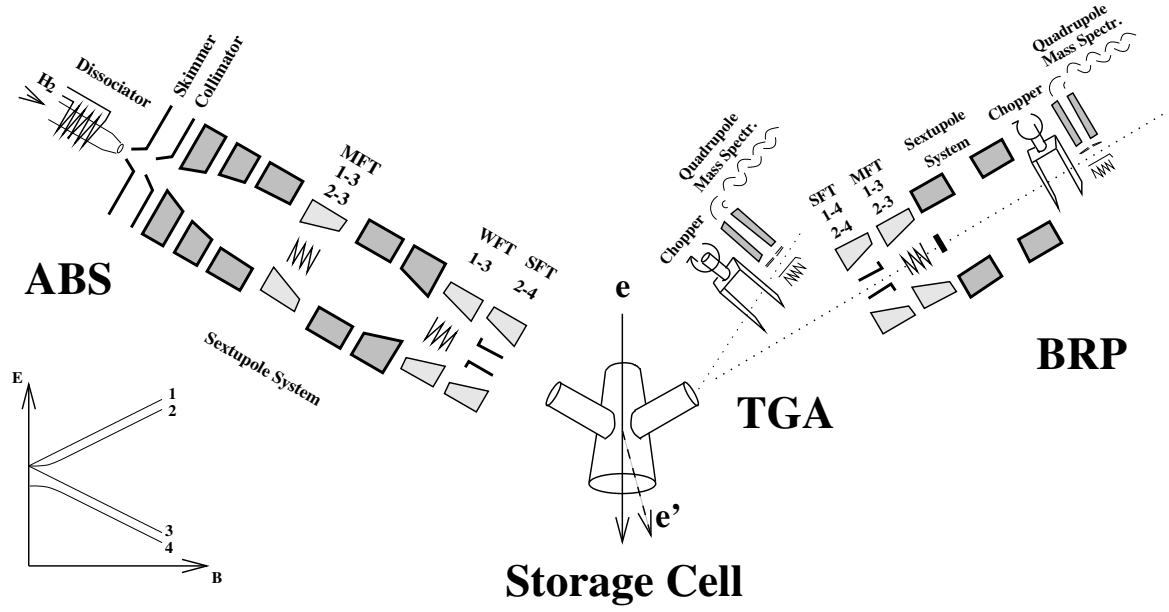


Figure 4.4: Schematic diagram of the polarised hydrogen target used in 1996 and 1997. An atomic beam source (ABS) injects nuclearly polarised hydrogen atoms into the storage cell. The composition of the gas from atomic and molecular hydrogen as well as possible contaminations from heavier nuclei are determined with a target gas analyser (TGA). A Breit-Rabi polarimeter (BRP) measures the nuclear polarisation of the hydrogen atoms.

polarised hydrogen was employed (see Fig. 4.4). The ABS is based on the Stern-Gerlach separation of electron spin in an inhomogeneous magnetic field. Molecular hydrogen is dissociated by radio frequency discharge into hydrogen atoms and an unpolarised beam is formed by a cooled nozzle and skimmers. The atomic beam leaving the dissociator is directed into an inhomogeneous magnetic field generated by a sequence of sextupole magnets. Atoms with electron spin along the local magnetic field direction are focused while other states are defocused and subsequently pumped. The selected atomic beam consists of two hyperfine states with opposite nuclear spin direction. Using high frequency transitions the population of one of the hyperfine states can be exchanged by a state with opposite nuclear spin direction to form an atomic beam consisting of two hyperfine states with parallel nuclear spin. Since 1998 the ABS provides polarised deuterium.

The polarisation of the hydrogen atoms inside the target cell is measured by a Breit-Rabi polarimeter (BRP). A small fraction of the target gas is extracted from the storage cell into the BRP to measure the relative populations of the hyperfine states and thus the nuclear polarisation of the sample. In order to suppress the recombination of hydrogen atoms, the cell is coated by Dri-film and a layer of ice [Bra:95, Kol:98b]. The cell is operated at a temperature of about 100 K. The target proton polarisation  $p_T$  inside the cell is calculated from the polarisation  $p_{BRP}$  of the hydrogen atoms analysed in the BRP and the atomic fraction measured in the target gas analyser (TGA) according to

$$p_T = \alpha_0 [c_\alpha \alpha_R + (1 - c_\alpha \alpha_R) \beta] c_P p_{BRP}, \quad (4.1)$$

where  $1 - \alpha_0 = 0.01 \pm 0.01$  is the fraction of protons entering the cell in molecules and  $1 - c_\alpha \alpha_R$  the fraction of atoms that recombined in molecules.  $c_\alpha$  and  $c_P$  are corrections

for sampling efficiencies of TGA and BRP, respectively. The value of  $c_{\alpha}\alpha_R$  was  $0.93 \pm 0.04$  in 1997. The quantity  $\beta$  is defined as the ratio of the polarisation of protons in molecules from recombination to the polarisation of protons in atoms. A  $\beta$ -measurement on deuterium using a different cell geometry and magnetic field was carried out at NIKHEF and a value of  $\beta = 0.8 \pm 0.3$  was reported [vdB<sup>+</sup>:97]. From measurements at HERMES,  $\beta$  at present is constrained to  $0.2 \leq \beta \leq 1.0$ . During data taking the nuclear polarisation direction has been reversed every 45 seconds while technically spin flip times below one second are feasible. The average proton polarisation was 88% in 1997 with a fractional systematic error of 4.5%.

An unpolarised gas feed system is able to deliver various gas types over a wide density range. In general the unpolarised target density is only limited by its impact on the beam lifetime. Unpolarised data taking at HERMES has been performed with densities of  $10^{15} - 10^{17}$  nucleons/cm<sup>2</sup>.

## 4.3 The Spectrometer

The HERMES spectrometer is a conventional forward angle spectrometer common to fixed target experiments. Because of the special environment at HERA with the two storage rings the detector is designed in two identical halves above and below the beam plane (see Fig. 4.2). The beams are protected against the magnetic field of the spectrometer magnet by a pair of iron plates (*septum plate*) which limits the vertical scattering angle acceptance. The layout of the spectrometer can be divided in three parts, the front and back regions separated by the main spectrometer magnet. In the front region only tracking detectors are installed to obtain a good tracking and vertex resolution. The only exception is an additional trigger hodoscope which was added in 1996 to reduce background events due to particle showers initiated by the proton beam which enter the detector from the back. In the back region detectors for tracking, particle identification, and triggering are employed. The origin of the HERMES coordinate system coincides with the centre of the target. The positive  $z$ -axis is oriented along the electron beam axis while the positive  $x$ -axis points to the centre of the electron ring. For a right-handed coordinate system it follows that the positive  $y$ -axis has to point vertically upwards. A detailed description of the HERMES spectrometer is given in [HERMES:93, HERMES:98].

### 4.3.1 Tracking

The tracking system consists of micro-strip gas chambers (referred to as vertex chambers, VC) and drift chambers upstream of the magnet (drift vertex chambers, DVC, and front chambers, FC), three proportional chambers in the magnetic field (magnet chambers, MC), and two sets of drift chambers downstream of the magnet (back chambers, BC). The tracking detectors are constructed from planes that measure the position of a charged track along a coordinate perpendicular to the wire respectively strip orientation and the beam direction. The horizontal coordinate  $x$  is measured by planes with a vertical orientation while the  $u$  and  $v$  coordinates are

CHAMBER	Vertex		Drift vertex	Front		Magnet			Back	
Detector name	VC1	VC2	DVC	FC1	FC2	MC1	MC2	MC3	BC1/2	BC3/4
mm from target	731	965	1100	1530	1650	2725	3047	3369	4055	5800
Active area										
Horizontal (mm)	323	393	474	660	660	996	1210	1424	1880	2890
Vertical (mm)	137	137	290	180	180	263	306	347	520	710
Cell design	Micro-strip gas		Horizontal drift	Horizontal drift		MWPC			Horizontal drift	
Cell width (mm)	0.193		6	7		2			15	
A-C plane gap (mm)	3		3	4		4			8	
Anode (A) material	200 $\mu$ m glass(Al)		W(Au)	W(Au)		W(Au)			W(Au)	
Anode wire diameter	7 $\mu$ m		30 $\mu$ m	20 $\mu$ m		25 $\mu$ m			25 $\mu$ m	
Potential wire mat'l	Al strip		Be-Cu(Au)	Al(Au)					Be-Cu(Au)	
Potential wire dia.	85 $\mu$ m		50 $\mu$ m	50 $\mu$ m					127 $\mu$ m	
Cathode (C) material	Al on glass		Al on Mylar	Al on Mylar		Be-Cu wires			C on Kapton	
Cathode thickness	200 $\mu$ m		34 $\mu$ m	6.4 $\mu$ m		90 $\mu$ m @ 0.5 mm pitch			25.4 $\mu$ m	
Gas composition:	DME/Ne		Ar/CO <sub>2</sub> /CF <sub>4</sub>	Ar/CO <sub>2</sub> /CF <sub>4</sub>		Ar/CO <sub>2</sub> /CF <sub>4</sub>			Ar/CO <sub>2</sub> /CF <sub>4</sub>	
(%)	50/50		90/5/5	90/5/5		65/30/5			90/5/5	
U,V stereo angle	$\pm 5^\circ$ , $-90^\circ$		$\pm 30^\circ$	$\pm 30^\circ$		$\pm 30^\circ$			$\pm 30^\circ$	
Resolution/plane ( $\sigma$ )	65 $\mu$ m		220 $\mu$ m	225 $\mu$ m		700 $\mu$ m			275 $\mu$ m	
Wires in X plane	1674	2046	80	96	96	496	608	720	128	192
Wires in U,V plane	2170	2170	96	96	96	512	608	720	128	192
Module configuration	VUX XVV		XX'UU'VV'	UU'XX'VV'		UXV			UU'XX'VV'	
Rad. length/module	0.8%		0.25%	0.075%		0.29%			0.26%	
Number of modules (upper or lower)	1	1	1	1	1	1	1	1	2	2
Channels/module	6014	6386	544	576	576	1520	1824	2160	768	1152
Total channels	24800		1088	2304		11 008			7680	

Table 4.1: *Properties of the HERMES tracking chambers.*

given by planes which are tilted by  $\pm 30^\circ$  to the vertical. In Tab. 4.1 the properties of the tracking detectors are summarised. The magnetic field of the main spectrometer magnet provides an integrated field strength of 1.3 Tm for the momentum reconstruction.

The HERMES reconstruction program (HRC) [Wan:96] uses a tree-search algorithm for the track finding and a look-up table for the momentum determination of the tracks. Both techniques allow a very fast event reconstruction with small intrinsic resolutions. (The contribution of HRC to the precision of the track momentum determination is better than  $\Delta p/p = 0.5\%$ .) The track parameters are determined separately in the forward and backward part of the spectrometer, which are separated by the magnet. In each part, which contains 24 active planes, the track projections (*treelines*) on the three coordinates  $u$ ,  $v$ ,  $x$  of the tracking devices are determined by an iterative pattern recognition algorithm. The hit pattern in the detector planes are compared to a pattern data base and combinations, which cannot originate from a straight track, are rejected. The resolution of the hit pattern is doubled in each iteration step and eleven iterations are used for the track finding. The treelines of the  $u$ ,  $v$ ,  $x$  coordinates are then combined to spatial *partial tracks* before and after the magnet. Matching forward and backward partial tracks have then to be assigned through the magnetic field, forming *full tracks*. This matching can be done by a position comparison in the centre of the magnet or with the help of the proportional chambers inside the magnet by applying a Kalman filter. Additionally, the magnet chambers give access to tracks with low momenta which experience large deflections in the magnetic field and do not reach sufficient tracking planes in the backward region (*short tracks*).

HRC is able to operate with any combination of tracking devices in the front region as not all of them were available from the beginning of the data taking in 1995. In the original design only the VC and FC detectors were foreseen for the front region and their use in the tracking constitutes the standard reconstruction method (*STD*). The VC however suffered from difficulties in the

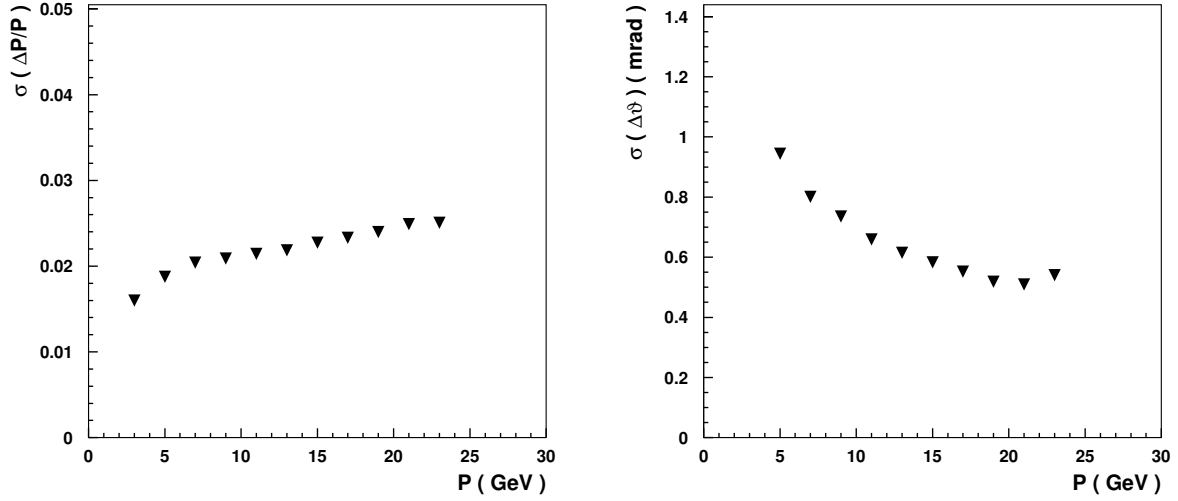


Figure 4.5: *Momentum and scattering angle resolutions in the HERMES spectrometer for the force-bridge method (NOVC), deduced from Monte Carlo studies.*

production of APC readout chips, the performance of the substitute prototype chips resulted in low plane efficiencies (60 – 90%) and many “hot” channels. They were therefore not included in the reconstruction. Instead it was decided to install additional tracking detectors for the front region, the DVC, which became available only in 1997. To nevertheless ensure a reliable and accurate tracking in the front region despite the long lever arm and rather large resolution of the FC, an alternative track reconstruction method was developed. The matching of forward and backward partial tracks is again based on the track positions in the centre of the magnet, but with larger tolerances than in the STD method because of the worse resolution. Then the match point as defined by the backward partial track is used to refine the front partial track by pivoting it about a conserved space point in the centre of the front drift chambers. Thus, the forward partial track is forced to agree at the magnet midpoint with the presumably higher-quality information from the backward partial track. This *force-bridging method* is referred to as the *NOVC* method as it is only utilising the FC and BC detectors, and was also used successfully for the 1995/96 physics analysis, with approximately a factor of two loss of resolution in kinematic quantities relative to what could be expected if the VC were fully operational. For consistency reasons, the NOVC method was also used in the reconstruction of the unpolarised data from 1997 to allow the combination with data sets from the previous years. In case the DVC detectors are included in the tracking, the name of the corresponding reconstruction method will be modified accordingly (“STD+DVC” or “NOVC+DVC”).

The momentum and scattering angle resolutions for the force-bridging method are shown in Fig. 4.5. The results are deduced from Monte Carlo studies using a detailed description of the detector geometry based on GEANT [B<sup>+</sup>:93]. The momentum resolution  $\Delta p/p$  for the scattered lepton is in the range of 1 – 3%, depending on the kinematics. A large part of this smearing is caused by multiple scattering in the detector material a particle has to traverse. The amount of material inside the acceptance is illustrated in Fig. 4.6. On the left hand side the integrated radiation length for a particle originating from the centre of the target and passing under a vertical angle of  $\theta_y = 50$  mrad through the centre of the detector ( $\theta_x = 0$  mrad) is given as a function

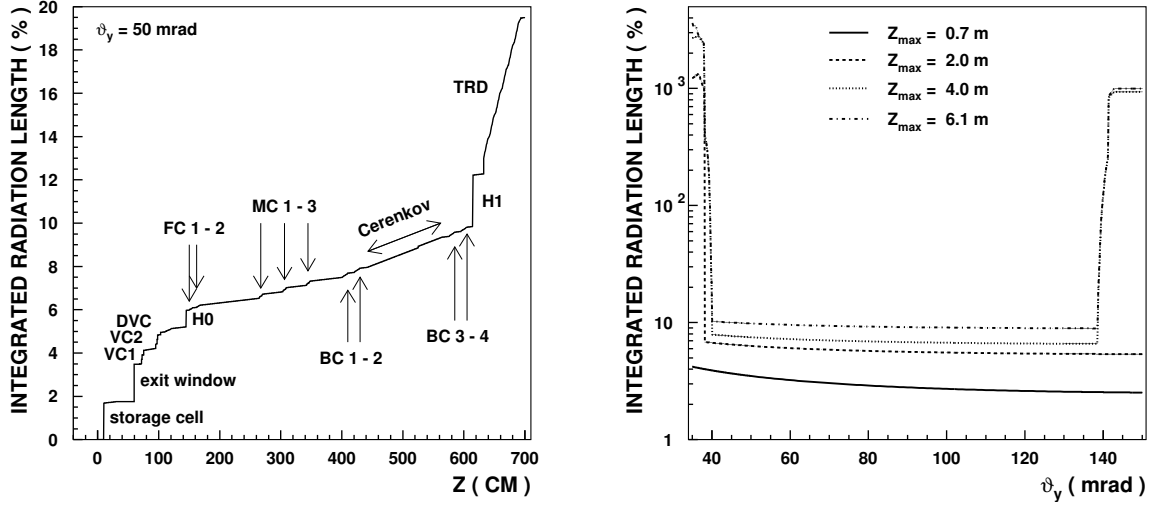


Figure 4.6: *Integrated radiation length of the HERMES spectrometer as the result of a detailed simulation of the detector geometry based on GEANT [B<sup>+</sup>:93]. See text for a description of the plots.*

of the position along the beam axis. The integrated radiation length is everywhere well below 10% of a radiation length. The vertical angular acceptance in the centre of the spectrometer can be seen on the right hand side where the integrated radiation lengths at the  $z$ -positions before the first and after the last tracking detector in the front ( $z = 0.7$  m, 2.0 m) and back part ( $z = 4.0$  m, 6.1 m) of the spectrometer are shown as a function of the vertical scattering angle. The angular acceptance is determined by the frames of the proportional chambers inside the magnet gap. For a particle originating from the centre of the target, scattering angles projected on the vertical and horizontal axes of  $40 \text{ mrad} \leq |\theta_y| \leq 140 \text{ mrad}$  and  $|\theta_x| \leq 170 \text{ mrad}$  respectively are accepted, giving access to a scattering angle in the range of  $40 \text{ mrad} \leq \theta \leq 220 \text{ mrad}$ .

### 4.3.2 Particle Identification

#### Electron Hadron Separation

In order to keep the electron identification efficiency above 95% and the contamination of hadrons in the electron sample below 1% over the entire kinematic range, a hadron rejection factor of better than  $10^4$  is necessary since the rate of low momentum hadrons from photo-production is much higher than the rate of DIS electrons with the same momentum. This goal was achieved by the combination of four different types of particle identification (PID) detectors: a lead-glass calorimeter, two plastic scintillator hodoscopes, one of which is preceded by two radiation lengths of lead and which acts as a preshower detector, a transition radiation detector, and a threshold Čerenkov detector. The specifications of these detectors and further details can be found in [HERMES:98]; the detector responses to hadrons and electrons from these devices are presented in Fig. 4.7 exemplary for the 1997 data.

Rather than imposing hard cuts on the individual detector signals, the responses are converted into *conditional probabilities*  $\mathcal{L}_D^i$  which give the probability that a given signal is recorded by detector D when a particle of type  $i$  passes the detector. These conditional probabilities are derived by comparing the detector response functions for leptons and hadrons generated either from test beam data, from clean particle samples obtained from restrictive cuts on the other PID detectors, or from Monte Carlo simulations. The individual conditional probabilities for each available PID detector are combined to overall conditional probabilities

$$\mathcal{L}^i \equiv \prod_D \mathcal{L}_D^i, \quad (4.2)$$

which are related to the probabilities  $P^i$  that a track originated from a particle of type  $i$  through the incident particle fluxes  $\phi^i$

$$P^i = \frac{\phi^i \mathcal{L}^i}{\sum_j \phi^j \mathcal{L}^j}. \quad (4.3)$$

For the separation of leptons from hadrons the quantity  $PID$  is introduced as the logarithm of the ratio of conditional probabilities that the particle is a lepton  $l$  or a hadron  $h$

$$PID \equiv \log_{10} \frac{\mathcal{L}^l}{\mathcal{L}^h}. \quad (4.4)$$

This quantity is related to the true probabilities  $P^l$  and  $P^h$  by

$$PID = \log_{10} \frac{P^l}{P^h} + \log_{10} \frac{\phi^h}{\phi^l}. \quad (4.5)$$

As the TRD detector consists of six modules, the responses from these individual modules are combined into the logarithmic likelihood  $PID_{\text{TRD}}$  [Men:98]

$$PID_{\text{TRD}} \equiv \log_{10} \frac{\mathcal{L}_{\text{TRD}}^l}{\mathcal{L}_{\text{TRD}}^h} \equiv \log_{10} \frac{\prod_{m=1}^6 \mathcal{L}_{\text{TRD},m}^l}{\prod_{m=1}^6 \mathcal{L}_{\text{TRD},m}^h}, \quad (4.6)$$

while the responses of calorimeter, threshold Čerenkov detector, and preshower counter are combined into the logarithmic likelihood  $PID_3$  [Kai:97]

$$PID_3 \equiv \log_{10} \frac{\mathcal{L}_{\text{CAL}}^l \cdot \mathcal{L}_{\text{CER}}^l \cdot \mathcal{L}_{\text{PRE}}^l}{\mathcal{L}_{\text{CAL}}^h \cdot \mathcal{L}_{\text{CER}}^h \cdot \mathcal{L}_{\text{PRE}}^h}. \quad (4.7)$$

These two quantities are then usually joined into

$$PID \equiv \log_{10} \frac{\mathcal{L}_{\text{CAL}}^l \cdot \mathcal{L}_{\text{CER}}^l \cdot \mathcal{L}_{\text{PRE}}^l \cdot \mathcal{L}_{\text{TRD}}^l}{\mathcal{L}_{\text{CAL}}^h \cdot \mathcal{L}_{\text{CER}}^h \cdot \mathcal{L}_{\text{PRE}}^h \cdot \mathcal{L}_{\text{TRD}}^h} = PID_3 + PID_{\text{TRD}}. \quad (4.8)$$

Distributions for these quantities from the 1997 data are shown in Fig. 4.8.



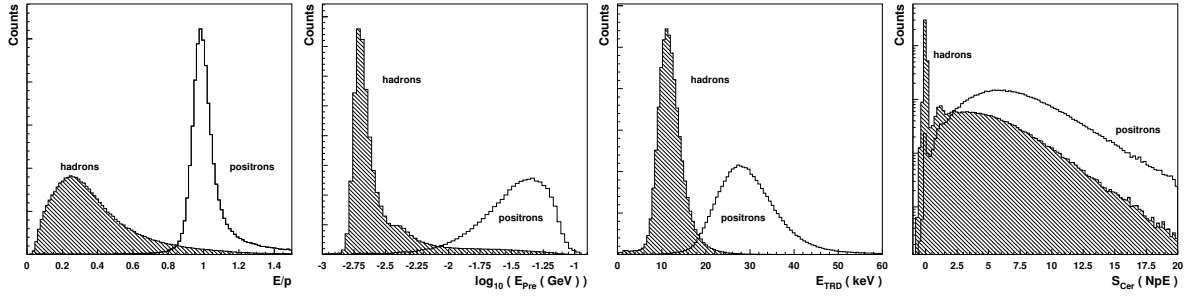


Figure 4.7: Responses of the particle identification detectors to semi-inclusive events with a positron and at least one hadron for 1997 data: ratio of calorimeter energy and momentum, preshower signal, truncated mean value for the transition radiation detector, number of photoelectrons detected by the threshold Čerenkov counter (from left to right). The counts on the y-axes are in arbitrary units for all plots.

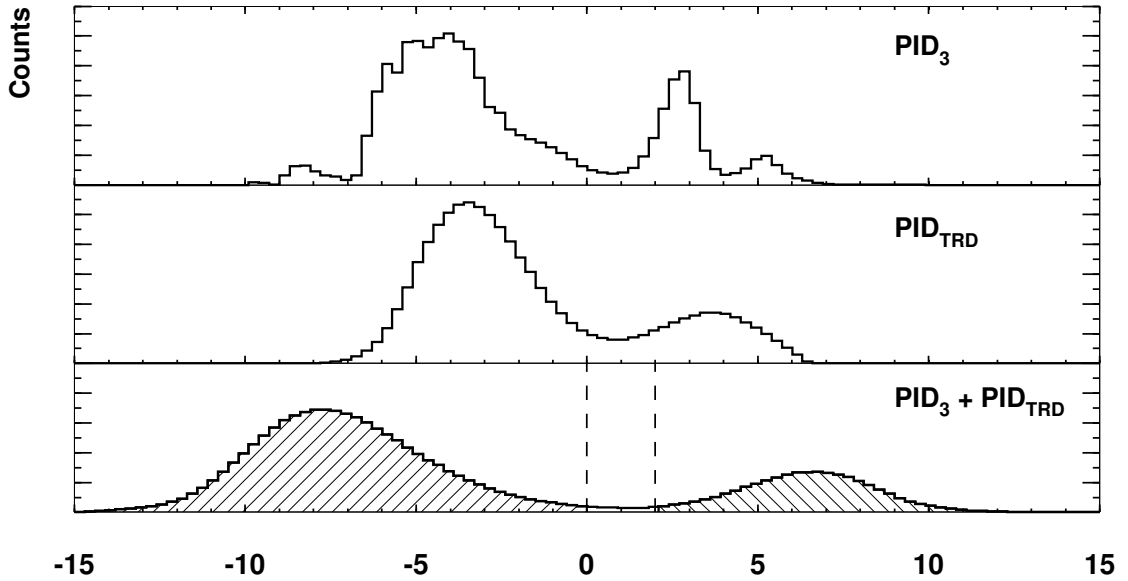


Figure 4.8: PID parameters for all particle tracks from 1997 data:  $PID_3$  from the combined responses of calorimeter, threshold Čerenkov detector, and preshower;  $PID_{TRD}$  from the responses of the individual TRD modules, and the sum of the two parameters. The dashed lines in the bottom plot indicate possible cuts to separate hadrons ( $PID_3 + PID_{TRD} < 0$ ) from leptons ( $PID_3 + PID_{TRD} > 2$ ). The counts on the y-axis are in arbitrary units.

### Pion Kaon Separation

The weight of the threshold Čerenkov detector in the likelihood analysis for the lepton-hadron separation is rather small. The main function of this detector is to distinguish pions from other hadrons. An adjustable gas mixture at atmospheric pressure of nitrogen and perfluorobutane,  $C_4F_{10}$ , is used as radiator. During the first year of operation, the radiator was pure nitrogen, while in 1996 and 1997 a mixture of 70% nitrogen and 30% perfluorobutane was used, for which the Čerenkov momentum thresholds for pions, kaons, and protons are 3.8, 13.6 and 25.8 GeV, respectively. For the determination of the pion identification efficiency, a clean sample of pions could be obtained through the decay of diffractively produced  $\rho^0$  into two pions:  $\rho^0 \rightarrow \pi^+\pi^-$ . Since no sufficient statistics for a reliable extraction can be obtained in this channel at HERMES, the pion identification efficiency is instead parametrised in terms of the average number  $N_0$  of photoelectrons observed for a particle with  $\beta \approx 1$  and the pion momentum threshold

$$\epsilon = 1 - e^{-N_0 \left(1 - \frac{\gamma_t^2}{\gamma^2}\right)}, \quad (4.9)$$

with  $\gamma = (1 - \beta^2)^{-\frac{1}{2}}$  and  $\beta = p/E$ .  $N_0$  and the momentum threshold can be determined using high statistics electron and hadron samples, respectively. The thus obtained pion identification efficiency as a function of the pion momentum averaged for the 1997 data taking period is plotted in Fig. 4.9 [dSHJ<sup>+</sup>:00]. The pion identification efficiency is for momenta of 4.5 GeV around 80% and increases asymptotically to unity. For momenta larger than 7.5 GeV efficiencies above 99% are achieved.

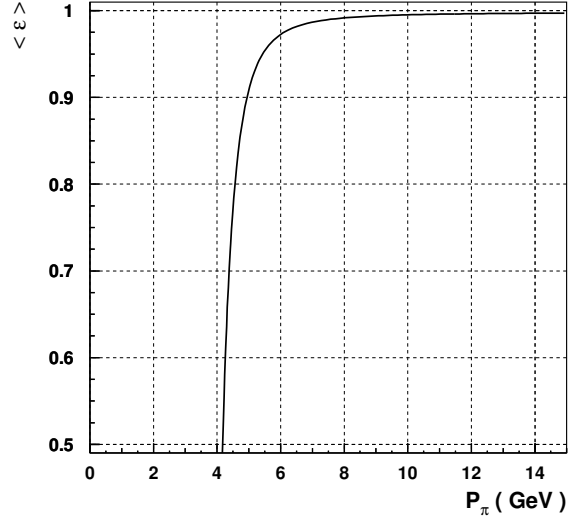


Figure 4.9: *Pion identification efficiency as a function of the pion momentum. Shown is the average efficiency for the 1997 data set.*

### 4.3.3 Luminosity

For a fixed target experiment the luminosity  $\mathcal{L}$  can be defined as the product of the flux  $\phi_B$  of beam particles and the number  $N_T$  of target particles within the beam cross-section

$$\mathcal{L} \equiv \phi_B N_T. \quad (4.10)$$

It is therefore possible to deduce the luminosity from the beam current  $I_B$  and the target density  $n_T$  only ( $\mathcal{L} \propto I_B n_T$ ). However, these quantities are difficult to measure to the required precision. To achieve a better accuracy, the luminosity measurement is based on the elastic

scattering of beam electrons from target gas electrons  $e^-e^- \rightarrow e^-e^-$  (Moller scattering). In case of a positron beam, Bhabha scattering ( $e^+e^- \rightarrow e^+e^-$ ) and the annihilation into photon pairs ( $e^+e^- \rightarrow \gamma\gamma$ ) are used. The cross-sections are known precisely from QED, including radiative corrections. The scattered particles are detected in coincidence by two calorimeter modules mounted 7.2 m downstream the interaction region to the left and right side of the beam pipe [Ben:98a]. Due to the high radiation background in the region very near to the beam, each calorimeter module consists of 12 NaBi(WO<sub>4</sub>)<sub>2</sub> crystals, which have a very high radiation hardness. The coincidence rate  $R_L$  is about 130 Hz for a beam current of 20 mA and an areal target density of  $10^{15}$  nucleons/cm<sup>2</sup>. This allows to measure the luminosity with a statistical uncertainty of about 1% within 100 s. From the coincidence rate the luminosity can be determined using the relation

$$\mathcal{L} = \frac{\dot{N}}{\sigma} = \frac{R_L}{\int_{\Delta\Omega} d\Omega \epsilon(\Omega) \frac{d\sigma_{\text{Bhabha}}}{d\Omega}} \equiv R_L C_{\text{Lumi}} . \quad (4.11)$$

The loss of part of the count rate due to the finite size of the luminosity monitor is reflected by restricting the integral over the Bhabha cross-section to the angular acceptance  $\Delta\Omega$  of the detector. Furthermore, a correction for the detection efficiency  $\epsilon(\Omega)$  is applied. The normalisation constant  $C_{\text{Lumi}}$  was determined with the help of a Monte Carlo simulation to be [Ben:98b]

$$C_{\text{Lumi}} = 0.448 \mu\text{b}^{-1} . \quad (4.12)$$

Because of the strong dependence of the Bhabha cross-section on the scattering angle, the acceptance represents the dominant contribution to the systematic error of 6.4% for the determination of an absolute luminosity [Ben:98a]. For many measurements such as cross-section ratios and asymmetries only relative luminosities are needed. In this case the acceptance of the luminosity monitor becomes irrelevant and the systematic uncertainty decreases below 1.5%. However, an additional complication occurs for the polarised measurements due to the spin dependence of the Bhabha cross-section. Even though the polarised target is operated in a mode to deliver only nuclear polarisation and no polarisation for the shell electrons, small inefficiencies in the high frequency transitions for the hyperfine states as well as a transfer of the nuclear spin to the electron shell in atomic spin exchange collisions lead to a remaining electron polarisation of 1 – 2% in the target cell [Wei:98]. To avoid a bias in the luminosity measurement due to the Bhabha asymmetry, it has therefore been decided to fit the luminosity over time intervals much longer than the typical spin-flip time of the target. As the luminosity is proportional to the beam current and the target density (Eq. 4.10) and the target density is normally kept constant during polarised data taking, the time dependence of the luminosity should therefore be given by the time dependence of the beam current, which follows an exponential function

$$\mathcal{L}(t) = \exp\left(-\frac{1}{\tau} (t - t_0) + \beta\right) . \quad (4.13)$$

The lifetime  $\tau$  of the beam was here assumed to be constant. Besides for the highest beam currents, where additional interactions of beam particles within one bunch occur, this assumption is justified. Typically a fit extends over a whole fill, which in average lasts several hours. Only in case of instabilities in the beam current because of partial beam losses or in the target density, a fill is split into up to three separate fit intervals. A typical example for a fit can be seen in Fig. 4.10.

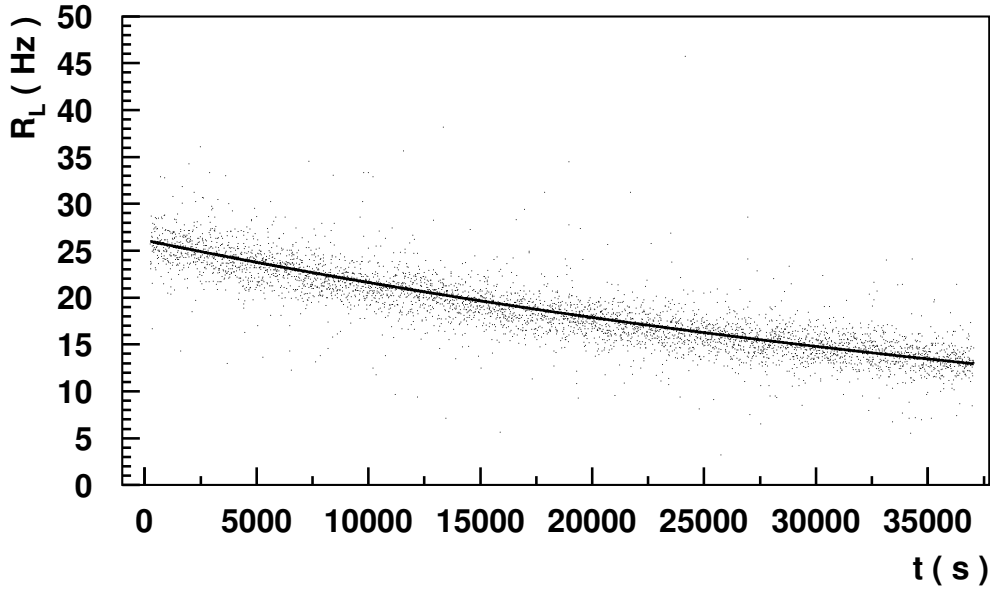


Figure 4.10: The Bhabha coincidence rate  $R_L$  as measured by the luminosity monitor for a typical fill during polarised data taking in 1997. The statistically varying single measurements have been fitted by an exponential function. The start of the data taking in the fill has been taken as the origin on the time axis for this figure.

As cross-sections for heavier nuclei are commonly quoted per nucleon, it is best to adopt this convention also for the luminosity. Then a correction factor  $f_A$ , given by the ratio of nucleons to shell electrons in the nuclei, has to be applied for each target gas type A

$$f_A \equiv \begin{cases} 1.0 & : \text{ } ^1\text{H}, \\ 1.5 & : \text{ } ^3\text{He}, \\ 2.0 & : \text{ } ^2\text{D}, ^{14}\text{N}. \end{cases} \quad (4.14)$$

#### 4.3.4 Trigger

The function of the trigger system is to distinguish interesting events from background events and to initiate the digitisation and readout of the detector signals. The HERMES trigger hierarchy is potentially capable of four levels, for which the technical prerequisites are available. Up to now, however, only the first-level trigger was implemented. This first-level trigger decision is made within about 400 ns of the event using prompt signals of the scintillator hodoscopes, the calorimeter, and a few wire chambers. The main physics triggers correspond to deep-inelastic scattering and photo-production processes (where no lepton is detected). All physics triggers are required to be in coincidence with the accelerator bunch crossing signal (HERA clock). In addition to the physics ones, triggers for detector monitoring and calibration are available.

The DIS trigger selects events containing an electron or positron by requiring hits in the scintillator hodoscopes, H0, H1, and H2 (see Fig. 4.2) together with sufficient energy deposited in a cluster in the calorimeter. During unpolarised running the calorimeter threshold was set to 3.5 GeV while for polarised running it was lowered to 1.4 GeV to increase the accessible  $y$ -range and improve the acceptance for semi-inclusive particles.

The photo-production trigger detects hadrons that are typically produced at low  $Q^2$  and decay to two or more charged particles. The trigger requires at least one charged track in both the upper and lower detector halves, as identified by the three hodoscopes and the first backward drift chamber (BC1).

### 4.3.5 Data Acquisition

The HERMES data acquisition system (DAQ) is divided in two spatially separated parts. The front-end electronics is located in a trailer close to the experiment. It is connected to the online workstation cluster via two SCSI interfaces realised as a fibre optical link. The backbone of the front-end is based on Fastbus technology with CERN Host Interfaces (CHI) as masters which are equipped with DSP-based Struck Fastbus Readout Engines (FRE) to improve their performance. The drift chamber signals are read out by LeCroy Time to Digital Converters (TDC), while the vertex and magnet chambers use APC and PCOS4 based readout systems, respectively, without timing or analog information. Each photomultiplier tube as well as TRD channel is fed to TDCs and ADCs (Analog to Digital Converter). The collected event information is processed by the FREs and can be compressed by almost a factor of two before an event is built and sent to the distributing online workstation (Alpha 5/266) located in the counting room. During data taking the incoming events are written as EPIO files (Experimental Physics Input Output Package [M<sup>+</sup>:93]), to a 56 GB disk array hosted by further workstations linked via FDDI. Between two HERA fillings the raw data files are then transferred via a FDDI connection to a taping robot located in the computing centre at the DESY main site. Additionally the data is locally written to tape for backup purposes. The maximal DAQ throughput is 5.0 MB/s corresponding to an event rate of 500 Hz. Despite these high rates the deadtime during standard data taking is typically well below 10%.

To ease data storage and processing, the data taking is split into the recording of individual *runs* corresponding to a fixed amount of data. Usually, runs span about 10 minutes during polarised data taking, while for unpolarised running they are typically shorter because of the higher achievable target densities and the correspondingly higher trigger rates. In a run, the readout of the complete spectrometer for the accepted triggers (*events*) gets stored together with additional information for the synchronisation with the external slow control data. This synchronisation usually happens with a precision of one second, while a much faster synchronisation is possible with *scaler events* in the order of 10  $\mu$ s. Scalers are internal counters of the DAQ system, which store the numbers of generated and accepted triggers. They are read out every ten seconds, defining a *burst*.

## 4.4 Software

The software used at HERMES can be generally grouped in two parts. While the *online system* is used to run the experiment and record the raw data, the *offline software* processes this data and transforms it into a form more suitable for physics analyses. The latter uses a very modular and data-structure driven layout. The following list gives a short (and incomplete) overview of the main software packages in use at HERMES. The interplay of some of these packages can be seen in Fig. 4.11, where an overview over the data production scheme is shown.

ADAMO (“ALEPH Data Model”):

is the central database used at HERMES. Through highly organised data structure and description based on the entity-relationship model [Pro:94] it allows safe and portable data handling. The logical structure of the data is stored and passed along with the data. Various formats are supported for data storage (generic ADAMO file, GAF).

DAD (“Distributed ADAMO Database”):

This client-server extension to ADAMO was developed at HERMES to allow central maintenance and distribution of the data by implementing efficient interprocess communication mechanism in ADAMO format [WAD<sup>+</sup>:95]. DAD allows efficient storage of the data through on-the-fly (de)compression.

PINK (“PINK is not KUIP”):

is an interface to the Tcl/Tk package [Ous:94] which is useful for the rapid implementation of utility programs for data checking and analysis [ADF<sup>+</sup>:95]. It also allows the easy creation of Graphical User Interfaces (GUI) for the visualisation of the data.

HDC (“HERMES Decoder”):

converts the raw data from EPIO format into information in ADAMO format suitable for the further processing in the reconstruction phase. It makes use of various time-dependent mapping, geometry, and calibration data which is provided by central DAD production servers.

HRC (“HERMES Reconstruction”):

uses a tree-search algorithm for the track finding and a look-up table for the momentum determination of the tracks [Wan:96]. Both techniques allow a very fast event reconstruction with small intrinsic resolutions.

GMC (“Generator Monte Carlo”):

is a modular frame to provide final states from various external Monte Carlo generators in a common format suitable to be processed by the HERMES analysis chain. It furthermore allows a standardised and easy control over all parameters of the generators [DGMV:97].

HMC (“HERMES Monte Carlo”):

tracks the final states generated by GMC through a detailed model of the HERMES detector geometry based on GEANT [B<sup>+</sup>:93]. Calibration data and detailed models allow a realistic simulation and digitisation of the detector responses similar to the output of

HDC [DGMV:97]. This allows to process both real and Monte Carlo data with HRC without the need to distinguish between the input type of the data.

HANNA:

is an event-driven analysis frame which is able to synchronise slow control data with the event stream [Fun:98].

ACE (“Alignment, Calibration and Efficiency”):

calculates calibration and efficiency data for the tracking detectors [Kol:98a].

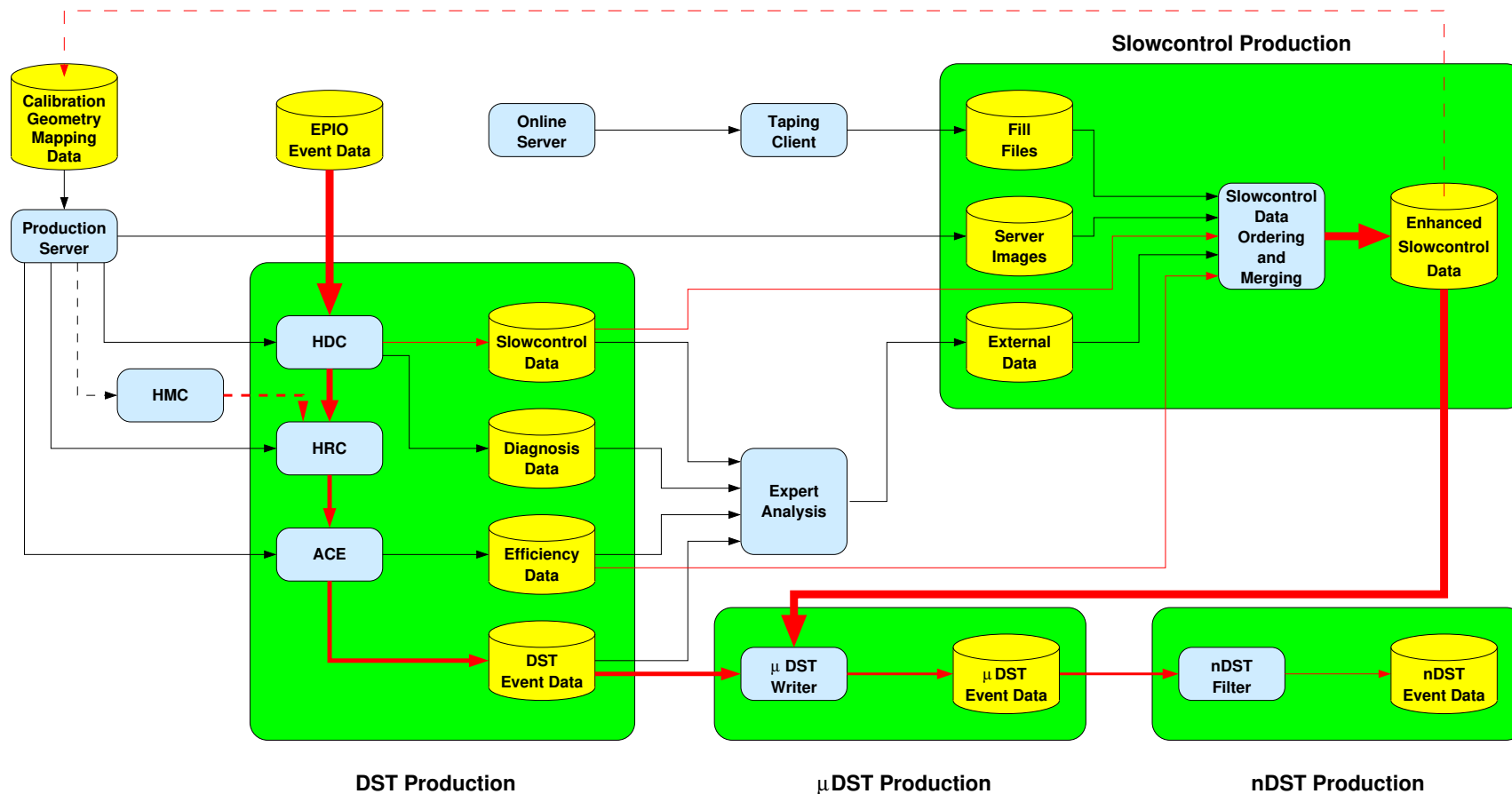


Figure 4.11: Offline data production scheme. The cylinders represent data files stored on disk and/or tape, small boxes data processing programs. A hierarchical grouping into the phases of data summary tape (DST), slow control,  $\mu$ DST, and nDST production are indicated by the bigger boxes (after [Fun:98]). An iterative procedure can be applied to improve the calibration data. Physics analyses are usually performed on the  $\mu$ DST event data files. Additional improvements concerning data size and processing time can be obtained by pre-filtering the data on global event topologies (nDST). The identical software chain is used to process Monte Carlo data which allows to test the production software and analysis programs.



## 5 Extraction of Cross-sections

To measure the cross-section associated with a certain process, one usually exploits the proportionality between the cross-section  $\sigma$  and the count rate  $\dot{N}$

$$\frac{d\dot{N}}{d\mathbf{p}}(t; \mathbf{p}) = \mathcal{L}(t) \frac{d\sigma}{d\mathbf{p}}(\mathbf{p}), \quad (5.1)$$

where the proportionality is given by the luminosity  $\mathcal{L}(t)$ . Here,  $t$  denotes the time and  $\mathbf{p}$  any set of kinematical variables. The luminosity has been assumed to be independent of the kinematical variables  $\mathbf{p}$  which is the case for HERMES.

For a real experiment however, detector effects complicate the situation. As will be explained in more detail in the following sections, acceptance and detection efficiency effects have to be taken into account. Denoting the correction functions with  $\mathcal{A}$  and  $\mathcal{E}$  respectively, which can depend on both  $t$  and  $\mathbf{p}$ , Eq. 5.1 becomes

$$\frac{d\dot{N}}{d\mathbf{p}}(t; \mathbf{p}) = \mathcal{A}(t; \mathbf{p}) \mathcal{E}(t; \mathbf{p}) \mathcal{L}(t) \frac{d\sigma}{d\mathbf{p}}(\mathbf{p}). \quad (5.2)$$

The time dependent parts of the correction factors are often combined with the luminosity into the so called *effective luminosity*

$$\mathcal{L}_{\text{eff}}(t) = \mathcal{A}'(t) \mathcal{E}'(t) \mathcal{L}(t). \quad (5.3)$$

After integrating over the time dependence, the cross-section is given by the expression

$$\frac{d\sigma}{d\mathbf{p}}(\mathbf{p}) = \frac{1}{\mathcal{A}(\mathbf{p}) \mathcal{E}(\mathbf{p})} \frac{\int dt \frac{d\dot{N}}{d\mathbf{p}}(t; \mathbf{p})}{\int dt \mathcal{L}_{\text{eff}}(t)} \equiv \frac{1}{\mathcal{A}(\mathbf{p}) \mathcal{E}(\mathbf{p}) L_{\text{eff}}} \frac{dN}{d\mathbf{p}}(\mathbf{p}). \quad (5.4)$$

The time integrals have to be evaluated separately for the effective luminosity and the count rate. Otherwise, especially in the case of low count rates, statistical fluctuations would be unnecessarily enhanced and at times of zero count rate all corrections be neglected.

The primary tasks of the cross-section measurement therefore are the determination of the occurrences  $N$  of the process under investigation and of the time integrated effective luminosity  $L_{\text{eff}}$  within the same time period. In a second step the influence of the detector acceptance has to be taken into account.

## 5.1 Detection Efficiencies

Many requirements have to be considered in the design of a spectrometer for a high energy physics experiment. The physical requirements are adjusted to the main physics measurements which are in the case of HERMES double spin asymmetries in inclusive and semi-inclusive deep-inelastic scattering. Additional constraints due to the laboratory environment as well as cost and time reasons typically result in a limited spectrometer acceptance and not all of the physically occurring events can be detected with the spectrometer. Several effects can contribute to these detection inefficiencies and the losses have to be corrected for in a cross-section measurement. The separation between the various effects is however not unique.

### 5.1.1 Acceptance and Smearing

The HERMES spectrometer has a limited acceptance because of the special environment at HERA (see also Sec. 4.3). Particles can completely miss the active aperture of the tracking and particle identification detectors (most noticeably for scattering angles below 40 mrad) or be bend outside the aperture by the main spectrometer magnet due to too low momenta (important for momenta below 2 GeV). The acceptance function  $\mathcal{A}$  denotes the probability that an event with given kinematics is detectable with an – besides the acceptance – ideal detector. The acceptance function is best parametrised as a function of the momentum vectors of the particles to be detected

$$\mathcal{A} = \mathcal{A}(\{|\vec{p}_i|, \vartheta_i, \varphi_i\}), \quad (5.5)$$

but can be specified for any suitable set of kinematical variables. Because of the complexity of the problem, the acceptance function is usually determined with the help of Monte Carlo simulations. The momentum and angular distributions of the produced particles depend on the underlying physics process and their correct simulation would require the knowledge of the cross-section to be measured. Fortunately, an exact simulation of these distributions is not necessary to quantify the acceptance function as long as the full physically possible phase space is covered by the simulation.

While traversing the various detectors and magnetic fields of the spectrometer, the particles produced in the scattering process can undergo secondary interactions. Examples are multiple scattering, external bremsstrahlung, various other energy loss mechanisms, and decays. These additional interactions can either stop a particle or change its momentum vector. The kinematic variables calculated from a reconstructed track then differ from the true kinematics of the associated particle at the time of its production. Also the reconstruction algorithm, resolutions and misalignments of the tracking chambers can cause such smearing and have been investigated in detail in [Wan:96]. However, only the true kinematics give access to the cross-section, which should be measured. The impact on differential cross-sections is obvious, but also total cross-sections can be affected. For example, the invariant mass of a decaying particle can in general not be correctly reconstructed when the momenta of the decay products are wrongly measured. A similar effect occurs, when particles are misidentified. Contaminations lead to wrong assumptions

about the properties of the particle such as for instance the mass or the production process. All derived kinematical quantities which are based on these assumptions are then wrongly calculated.

To derive the true kinematical distributions from the measured ones (*unfolding procedure*), the kinematical plane can be segmented into bins. One correction possibility is then to multiply the measured distributions with the ratio of generated and reconstructed distributions from a Monte Carlo simulation

$$C_{\text{Smeas}}^{\text{MC}} = \left( \frac{N_{\text{Gen}}}{M_{\text{Rec}}} \right)^{\text{MC}}, \quad (5.6)$$

what represents generalised efficiencies. However, this bin-to-bin correction cannot take into account large migrations of events from one bin to the others and neglects the unavoidable correlations between adjacent bins. It is only a valid approximation if the amount of migration between bins is negligible and if the standard deviation of the resolution is smaller than the bin size.

In a more sophisticated approach, a migration matrix  $\mathcal{M}_{ij}$  is introduced, which gives the probability that an event which was measured in bin  $i$  actually belongs to bin  $j$ . The measured distribution  $M_i$  and the true one  $N_j$  are then connected by the relation

$$M_i = \sum_j \mathcal{M}_{ij} N_j. \quad (5.7)$$

The binning should be chosen such that the resulting migration matrix is nearly diagonal, which is a sign of minimal smearing effects. The migration matrix can be derived from Monte Carlo simulations and then be inverted for the unfolding. However, inversion problems can occur for singular matrices or the inverse matrix may even not exist. In case it exists, statistical fluctuations in the measured distributions could be strongly enhanced when multiplied with the inverse migration matrix. Also, in contrast to the case of the acceptance function, a precise knowledge of the involved cross-sections is necessary to accurately derive the migration matrix.

To achieve a better accuracy, instead of the matrix inversion, the unfolding procedure can be implemented using an iterative algorithm based on Bayes' theorem described in [d'A:95a, d'A:95b], where the generated distributions are adjusted according to a comparison of the measured and reconstructed simulated distributions. Usually, the effects of the acceptance and cuts on the kinematical variables are also included in the determination of the migration matrix. This matrix is then referred to as the detector response function as it describes how the true distributions get distorted by the influence of the spectrometer.

The Monte Carlo simulations used for the determination of the detector response function require a detailed description of all detector effects. Such simulations, which involve the tracking of particles through the spectrometer, are very time consuming. To achieve enough statistical precision, time dependent effects usually cannot be included in the simulations and have to be corrected for separately. Relevant time dependent effects for the studies described in this section are the contribution of the tracking detector efficiencies to the reconstruction efficiency and the trigger efficiencies.

### 5.1.2 Track Finding

The combined effect of the tracking detector efficiencies and the requirements of the reconstruction program HRC on the number of hits per track is contained in the *permuted plane efficiencies* (PPE). To avoid potential biases in the determination of the efficiency of a single tracking chamber plane  $i$ , track samples are selected which could have been reconstructed even without the presence of the plane under investigation. The efficiency  $\epsilon_i$  for this plane is then calculated as

$$\epsilon_i = \frac{\# \text{ tracks with hit in plane } i}{\# \text{ tracks selected for plane } i} \equiv \frac{N_{\text{success}}^i}{N_{\text{entries}}^i}. \quad (5.8)$$

Two possible strategies can be followed to decide whether a hit in plane  $i$  is present or not [Kol:98a]. For the *software efficiency*, hits are only accepted within the same road width around the track impact point on the plane as used by HRC for the track finding. The *hardware efficiency* on the other hand samples a wider region around the impact point. For the wire chambers, a hit at either the closest or second closest wire is accepted, corresponding to a road width of a full drift cell size. The software efficiencies therefore include inefficiencies caused by resolutions and/or misalignments of the tracking detectors as well as multiple scattering. As these effects are stable over time and included in the detector response function introduced in the previous section, in the following the hardware efficiencies are used.

To quantify the impact of the hardware efficiencies  $\{\epsilon_i\}_{i=1,\dots,N}$  of each individual tracking plane  $i$  on the track finding, one has to form all possible hit patterns. In a hit pattern, each plane  $i$  contributes either a factor  $\epsilon_i$  or a factor  $(1 - \epsilon_i)$ , depending on whether a hit is assigned to the plane or whether the plane is assumed to be inefficient. A summation over all those hit patterns, which fulfil the requirements imposed by HRC on the number and combinations of hits for the formation of treelines and partial tracks then finally yields the permuted plane efficiencies for the forward and backward partial tracks.

The efficiency for a full track is determined as the product of the efficiencies for the two partial tracks. This neglects the effect of the bridging, which is assumed to be independent of the plane efficiencies. Monte Carlo studies have shown that for the NOVC reconstruction method the extracted hardware efficiencies reproduce the true plane efficiencies and that a correction for the inclusive deep-inelastic scattering cross-section based on the hardware efficiencies and neglecting the bridging efficiency corrects the reconstruction losses due to the plane efficiencies to better than 0.5%, even down to permuted plane efficiencies of 70% [Vol:97].

For the NOVC reconstruction method, the dependence of the permuted plane efficiencies  $\epsilon_{\text{PPE}}$  on the plane efficiencies can be seen in Fig. 5.1 under the assumption of a common efficiency  $\langle\epsilon\rangle$  for all tracking planes. The lower redundancy in the front region (12 tracking planes compared to 24 in the back) causes a strong dependence, while the back region is insensitive to plane efficiencies down to almost 90%.

The distributions of the permuted plane efficiencies for full tracks in the unpolarised data set of 1997, which utilises the NOVC reconstruction method, can be seen in Fig. 5.2. A clear dependence on the particle type is observed. The average efficiency for hadrons is around 96.5% while the one for electrons is very close to unity.

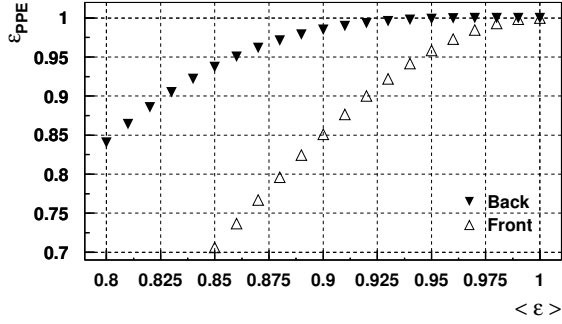


Figure 5.1: *Permutated plane efficiencies  $\epsilon_{\text{PPE}}$  for forward and backward partial tracks reconstructed with the NOVC method under the assumption of a common efficiency  $\langle \epsilon \rangle$  for all tracking planes.*

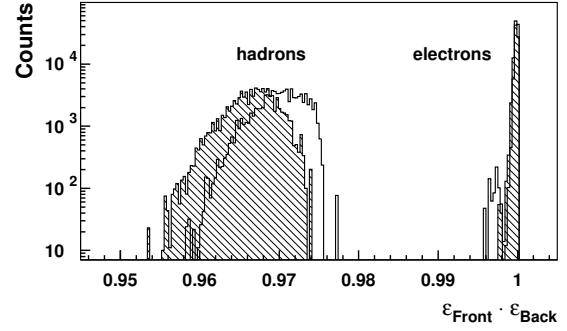


Figure 5.2: *Permutated plane efficiencies of full tracks for electrons and hadrons. Shown are the distributions for the 1997 unpolarised data set after data quality cuts in top (hatched) and bottom detectors (open).*

### 5.1.3 Trigger

The function of the trigger is to filter out potentially interesting events from the huge amount of interactions occurring during data taking. Even though only highly efficient detectors such as hodoscopes are typically used to build a trigger decision, a remaining inefficiency cannot be excluded. Also, since the performance of the data acquisition system depends strongly on the trigger rates (see next paragraph), not all generated readout requests for triggers firing at high rates can be sent to the DAQ system. In case of such *pre-scaling*, only every N-th trigger is processed, leading to an additional inefficiency.

To determine the efficiency of a trigger, the efficiencies of all components contributing to this trigger have to be calculated. For this purpose sub-triggers are recorded, where exactly one of the components in the trigger is missing. For instance, as described in Sec. 4.3.4, the DIS trigger selects events containing a positron or electron by requiring hits in the scintillator hodoscopes H0, H1, and H2, as well as a cluster in the calorimeter

$$T(\text{DIS}) = T(\text{H0} \cdot \text{H1} \cdot \text{H2} \cdot \text{Ca}) . \quad (5.9)$$

The efficiency of the hodoscope H0 can be calculated from the sample  $T(\text{H1} \cdot \text{H2} \cdot \text{Ca})$  of events containing a positron, where the sub-trigger not including H0 fired, and the sub-sample of these events where also the DIS trigger fired

$$\epsilon(\text{H0}) = \frac{T(\text{H1} \cdot \text{H2} \cdot \text{Ca}) \cap T(\text{DIS})}{T(\text{H1} \cdot \text{H2} \cdot \text{Ca})} . \quad (5.10)$$

Analogously, the efficiencies for H1, H2, and the calorimeter can be computed. The efficiency of the DIS trigger is then given by the expression

$$\epsilon_{\text{DIS}} = \epsilon(\text{H0}) \epsilon(\text{H1}) \epsilon(\text{H2}) \epsilon(\text{Ca}) . \quad (5.11)$$

Details about the determination of the trigger efficiencies for both the DIS and the photoproduction trigger can be found in [Mei:00]. The efficiency of the DIS trigger as a function of the

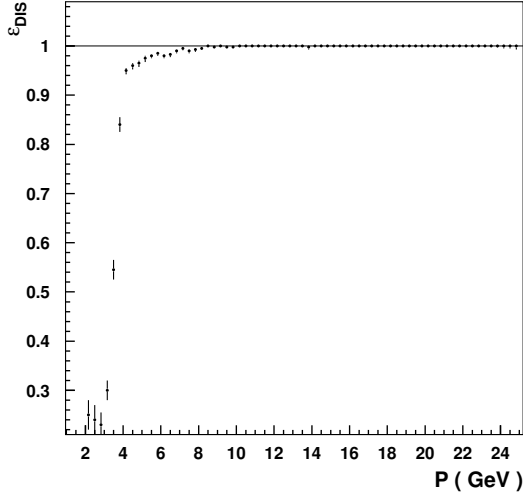


Figure 5.3: *DIS trigger efficiency as a function of the positron momentum for the unpolarised data sample from 1997 with a calorimeter threshold of 3.5 GeV. The turn on at the threshold is clearly visible.*

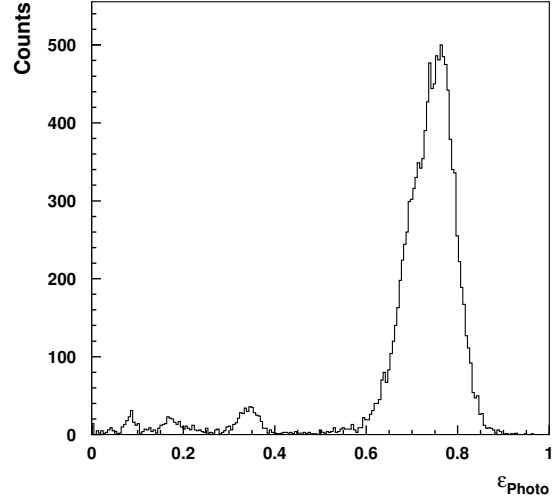


Figure 5.4: *Photoproduction trigger efficiency on a run-by-run basis for the unpolarised data sample from 1997. Runs with an efficiency below 50% originate from periods where this trigger was pre-scaled.*

positron momentum can be seen in Fig. 5.3 for the unpolarised data sample from 1997 with a calorimeter threshold of 3.5 GeV. For the photoproduction trigger, the efficiency is determined on a run-by-run level and is shown in Fig. 5.4 for the same data set. Runs with an efficiency below 50% originate from periods where this trigger was pre-scaled.

#### 5.1.4 Data Acquisition System

The DAQ system needs a certain time to read out the spectrometer and process the event information. While it is busy, the DAQ system blocks newly generated trigger requests and the associated events are lost. The time to process one event is independent of the trigger rate. The higher the trigger rate, however, the more triggers are generated within the event processing time and the percentage of events, which can be accepted, decreases above a certain threshold linearly. The ratio of the numbers for accepted and generated triggers of a certain type  $j$  determines the dead time fraction  $\delta_j$  for this trigger

$$\delta_j = 1 - \frac{T_{\text{acc}}^j}{T_{\text{gen}}^j}. \quad (5.12)$$

In principle, a distinction of trigger types should not be necessary in case all triggers are generated randomly in time, but the pre-scaling of triggers might introduce interference effects. The effect of the pre-scaling is not included in the dead time fraction as only the generated triggers after the pre-scaling are recorded in  $T_{\text{gen}}^j$ .

After an event was generated by the event builder of the DAQ system, it is processed in several stages. In case of problems during the intermediate stages, events can get lost. As an example,

one of the steps is to transmit the event data from the front-end electronics located in a trailer close to the experiment to an online workstation cluster (see also Sec. 4.3.5). For performance reasons, the generated events are buffered and only blocks of events are transmitted. In case of transmission errors, the corrupted blocks have to be refused. Even though such problems occur rarely, they can effect a non-negligible fraction of events within a single run due to the buffering. These losses are determining the so called artificial dead time fraction

$$\delta_{\text{DAQ}} = 1 - \frac{N_{\text{acc}}}{N_{\text{gen}}} . \quad (5.13)$$

Both dead time fractions are available for each burst. As the lost events are not available during the analysis, a correction has to be applied on the burst-level for the efficiency of the DAQ system

$$\epsilon_{\text{DAQ}}^j = (1 - \delta_j) (1 - \delta_{\text{DAQ}}) . \quad (5.14)$$

For the 1997 data taking, the values for the dead time fraction typically do not exceed 10% even at the highest throughput rates of the DAQ system of 500 Hz. The artificial dead time fraction introduces a negligible correction during normal operation, but is suited to detect periods with problems in the data recording.

## 5.2 Time Integrated Luminosity

As described in Sec. 4.3.3, the HERMES luminosity monitor measures the coincidence rate  $R_L$  of lepton pairs from Bhabha- or Moller-scattering off the shell electrons in the target atoms. The luminosity  $\mathcal{L}$  is given by the expression

$$\mathcal{L}(t) = f_A C_{\text{Lumi}} R_L(t) , \quad (5.15)$$

where  $f_A$  is a target dependent correction factor to get the luminosity per nucleon and  $C_{\text{Lumi}}$  is a normalisation constant taking into account the Bhabha cross-section and detector effects. Since the coincidence rate  $R_L$  is measured for each burst, the time integrated effective luminosity  $L_{\text{eff}}$  per nucleon can be evaluated by a summation over all accepted bursts, weighted with the burst length  $\Delta_{\text{Burst}}$  and the combined efficiency correction factor  $\mathcal{E}'(t)$

$$\begin{aligned} L_{\text{eff}} &\equiv \int dt \mathcal{E}'(t) \mathcal{L}(t) \\ &= \sum_{i \in \{\text{Bursts}\}} \Delta_{\text{Burst}}(t_i) \mathcal{E}'(t_i) f_A C_{\text{Lumi}} R_L(t_i) \\ &\equiv \sum_{i \in \{\text{Bursts}\}} L_{\text{eff}}(t_i) . \end{aligned} \quad (5.16)$$

### 5.3 Nuclear Cross-section Ratios

The extraction of nuclear cross-section ratios is – in general – experimentally an easier task than the measurement of an absolute cross-section. Many of the detector effects and systematic uncertainties cancel or are at least suppressed since only the differences between corrections for the different target types have to be considered. As an example, the systematic uncertainty associated with the measurement of absolute luminosities at HERMES is 6.4%, while relative luminosities can be determined to better than 1.5% [Ben:98a]. Time dependent effects become irrelevant if the time scale for the variations is large compared to the time inbetween exchanges of the target gas (typically about 2 hours) and if about the same statistics is collected for every target within each measurement cycle.

### 5.4 Double Spin Asymmetries

The measurement of double spin asymmetries in deep-inelastic scattering is effectively again the measurement of a cross-section ratio. The experimental asymmetry  $A_{\parallel} \equiv \frac{\sigma_{\rightarrow\rightarrow} - \sigma_{\rightarrow\leftarrow}}{\sigma_{\rightarrow\rightarrow} + \sigma_{\rightarrow\leftarrow}}$  for deep-inelastic scattering of longitudinally polarised lepton off polarised nucleons was introduced in Eq. 2.34, where  $\sigma_{\rightarrow\rightarrow}$  and  $\sigma_{\rightarrow\leftarrow}$  denote the polarised cross-sections for parallel ( $\rightarrow$ ) and antiparallel ( $\leftarrow$ ) orientation of lepton and nucleon spins. Exploiting furthermore the relation to the unpolarised cross-section  $\sigma_0 = \frac{1}{2} (\sigma_{\rightarrow\rightarrow} + \sigma_{\rightarrow\leftarrow})$ , one can rewrite the polarised cross-sections as

$$\sigma_{\rightarrow\leftarrow} = \sigma_0 \left[ 1 - A_{\parallel} \right]. \quad (5.17)$$

Combining these expressions with Eqs. 5.2 and 5.16, one obtains for the number of expected scattering events within one burst

$$n(t) = \mathcal{A}(t) \mathcal{E}(t) L_{\text{eff}}(t) \sigma_0 \left[ 1 \mp p_B(t) p_T(t) A_{\parallel} \right]. \quad (5.18)$$

The possible dependence on kinematical variables has been skipped for simplicity. In addition, a correction for depolarising effects for both the leptons and the nucleons has been introduced through the time-dependent beam and target polarisation values  $p_B$  and  $p_T$ .

Excluding time periods with problems in the operation of the spectrometer, the detector acceptance and the detection efficiencies show no spin dependence in the investigated data samples. Variations in time of the detector efficiencies occur only on time scales much longer than the very short spin-flip times below 45 s between the polarisation states of the target nucleons. Only the efficiency of the data acquisition system  $\epsilon_{\text{DAQ}}$  will be kept in the effective luminosity.  $\mathcal{A}$  and  $\mathcal{E}$  can therefore be treated as time and spin independent and cancel in the final formula for the asymmetry.



Abbreviating the sums over all accepted bursts in the parallel spin state by defining

$$N^{\vec{\Rightarrow}} \equiv \sum_{i \in \{\vec{\Rightarrow}\}} n_i, \quad (5.19)$$

$$L^{\vec{\Rightarrow}} \equiv \sum_{i \in \{\vec{\Rightarrow}\}} L_i^{\text{eff}}, \quad (5.20)$$

$$P^{\vec{\Rightarrow}} \equiv \sum_{i \in \{\vec{\Rightarrow}\}} (L_{\text{eff}} p_{\text{B}} p_{\text{T}})_i, \quad (5.21)$$

and analogously  $N^{\vec{\Leftarrow}}, L^{\vec{\Leftarrow}}, P^{\vec{\Leftarrow}}$  in the anti-parallel spin state, one can easily derive the following formula for the cross-section asymmetry

$$A_{\parallel} = \frac{N^{\vec{\Leftarrow}} L^{\vec{\Rightarrow}} - N^{\vec{\Rightarrow}} L^{\vec{\Leftarrow}}}{N^{\vec{\Leftarrow}} P^{\vec{\Rightarrow}} + N^{\vec{\Rightarrow}} P^{\vec{\Leftarrow}}}. \quad (5.22)$$

The statistical error  $\delta A_{\parallel}$  on the measured asymmetry  $A_{\parallel}$  is calculated from the statistical uncertainty of the count rate which follows a Poisson distribution. For sufficiently large numbers of scattering events  $\delta N = \sqrt{N}$  and

$$\delta A_{\parallel} = \sqrt{\left(\frac{\partial A_{\parallel}}{\partial N^{\vec{\Rightarrow}}} \delta N^{\vec{\Rightarrow}}\right)^2 + \left(\frac{\partial A_{\parallel}}{\partial N^{\vec{\Leftarrow}}} \delta N^{\vec{\Leftarrow}}\right)^2}, \quad (5.23)$$

$$= \frac{L^{\vec{\Leftarrow}} P^{\vec{\Rightarrow}} + L^{\vec{\Rightarrow}} P^{\vec{\Leftarrow}}}{(N^{\vec{\Leftarrow}} P^{\vec{\Rightarrow}} + N^{\vec{\Rightarrow}} P^{\vec{\Leftarrow}})^2} \sqrt{(N^{\vec{\Rightarrow}})^2 N^{\vec{\Leftarrow}} + (N^{\vec{\Leftarrow}})^2 N^{\vec{\Rightarrow}}}. \quad (5.24)$$

## 5.5 Data Selection

The HERMES experiment contains many complex subsystems. To allow a bias-free usage of the recorded data in an analysis, the reliability and stability of each individual component of the spectrometer relevant for an analysis has to be guaranteed. For this purpose each component is permanently monitored during the data taking. Normally, variations in the detector behaviour take place on much longer timescales than the recording of individual events which is in the order of few  $\mu\text{s}$ . The data from the monitoring tasks is therefore usually referred to as *slow control data*. In case of problems or instabilities, events collected during the affected time periods have to be excluded from the analysis. Various quality parameters for the detection of these problematic time periods have been defined offline from consistency checks. To be independent of statistical fluctuations in the determination of these parameters, different time intervals have to be studied, depending on the detector under investigation.

Since not always all subsystems of the spectrometer are used in each individual analysis, the data quality criteria have to be chosen according to the requirements of the extraction formalism in use. However, these criteria should not be correlated to the physical process under study. A summary of the data quality selection criteria for the 1997 data set is given in Tab. 5.1.

## General

The first stage of the data selection uses the logbook information recorded manually during the data taking. Time periods with systematic studies for detector components, inoperable detectors or problems related to the accelerator operation are excluded from the analysis.

Several additional sources of data quality information are available for the later stages. During the data production the partially redundant information can be used for additional consistency checks. Whenever these consistency checks are ambiguous or indicate possibly unreliable detector performance, the associated data is not used in the analysis.

Most of the data quality checks are performed independently for the upper and lower half of the HERMES spectrometer. Even though not absolutely necessary it is required that always both spectrometer halves are passing all selection criteria.

In the following only selection criteria based on physical reasons are described for the various sub-systems. Besides, the requirement of reliable measurements for the detector components is a prerequisite.

## Trigger

For the quasi-real photoproduction analysis only events where the photoproduction trigger fired where accepted. Additionally, runs with an trigger efficiency below 50% were excluded.

## Data acquisition

The first burst of every recorded run is excluded since at the beginning of a run initialisation processes do affect the performance of the detectors and the time synchronisation. The burst length is constrained to  $0 \leq \Delta_{\text{Burst}} \leq 11$  s. To keep the size of the corrections within reasonable limits, the deadtime correction factors are limited to  $0.6 \leq \epsilon_{\text{DAQ}} \leq 1$ .

## Luminosity

The range of the luminosity is constrained to ensure sufficient statistics in each run and to exclude unphysical measurements. For the polarised data the time development of the luminosity has been fitted additionally to an exponential behaviour to avoid problems due to the Bhabha asymmetry and decrease the statistical error in the measurements. The fitted coincidence rate  $\mathcal{L}$  of the luminosity monitor is required to be in the range  $5 \text{ Hz} \leq \mathcal{L} \leq 60 \text{ Hz}$ .

For the unpolarised data the target density was not kept constant but rather optimised with respect to beam lifetime considerations. A fit is therefore not possible and the raw coincidence rate is required to be in the range  $7.5 \text{ Hz} \leq \mathcal{L} \leq 1250 \text{ Hz}$ . For few runs with very high densities the upper limit is increased to 1750 Hz.

The gain of the calorimeter of the luminosity monitor was continuously monitored with a laser gain-monitoring system and the measured coincidence rates accordingly corrected. Times with potential problems in the gains were not used in the analysis.

### Target performance

From the unpolarised data only those runs are selected where the target gas type is uniquely identifiable and shows no contamination.

For the polarised data, time periods in which the target spin direction was changing are excluded from the analysis. A lower limit is set for the absolute value of the measured target polarisation  $p_T$  to avoid data with too low weight in the analysis ( $0.7 \leq |p_T|$ ). Also the allowed range for the molecular fractions  $\alpha_0$  and  $\alpha_R$  is constrained to ensure an almost pure atomic hydrogen target ( $0.97 \leq \alpha_0 \leq 1$  and  $0.7 \leq \alpha_R \leq 1.3$ ).

No requirements are directly placed on the target density; instead cuts are applied on the luminosity measurements.

### Beam current and polarimetry performance

A minimal beam current is required to ensure sufficient statistics in each run ( $5 \text{ mA} \leq I_B \leq 50 \text{ mA}$ ).

For the polarised analysis the time development of the beam polarisation  $p_B$  was smoothed to be less sensitive to statistical fluctuations in the measurements. A minimum polarised value is required as in the case of the target polarisation to remove data with low weights ( $0.3 \leq |p_B| \leq 0.8$ ).

### Tracking

If the charged particle flux hitting the tracking detectors gets too large (for example due to spikes in the background), the current drawn by the detectors can exceed a certain limit. To avoid possible damage of the devices, the high voltage supply gets shortly interrupted. Such *trips* were monitored by the slow control tasks for the high voltage system and the corresponding data are excluded from the analysis. Because of this trip detection it is sufficient to compute the permuted plane efficiencies only for a full run. This significantly decreases the statistical error in their determination. The range for the permuted plane efficiencies is limited to  $0.95 \leq \epsilon_{\text{PPE}} \leq 1$  for the unpolarised data and to  $0.90 \leq \epsilon_{\text{PPE}} \leq 1$  for the polarised data.

### Particle identification

The performance of the PID detectors is most important for the electron-hadron separation. The hadron identification is less sensitive since in the analysis presented here only decaying particles are investigated, where the additional identification through the invariant mass is possible. However, to avoid systematic uncertainties due to varying background conditions and contaminations and the problems with their correction, efficiency cuts are imposed on the transition radiation and the Čerenkov detectors. This ensures a typical electron identification efficiency of above 95% while keeping the hadron contamination below 1%.

The PID detectors are also included in the trip detection system and the gains of the preshower and main calorimeter are continuously monitored with the laser gain-monitoring system.

Criterion	Unpolarised Data	Polarised Data
Logbook	OK	
$\mu$ DST production	OK	
Reconstruction method	NOVC	
Target Gas	$H_2, D_2, N_2$	$\vec{H}$
Target Data Quality		OK
HV Trips	Excluded	
GMS Lumi/H2	OK	
GMS Calorimeter	OK	
TRD	OK	
Čerenkov	OK	
First Burst	Reject	
Burst Length	$0\text{ s} \leq \Delta_{\text{Burst}} \leq 11\text{ s}$	
Beam Current	$5\text{ mA} < I_B < 50\text{ mA}$	
Luminosity Trigger Rate	$7.5\text{ Hz} \leq \mathcal{L} \leq 1250\text{ Hz}$	$5\text{ Hz} \leq \mathcal{L}_{fit} \leq 60\text{ Hz}$
DAQ Efficiency	$0.6 \leq \epsilon_{DAQ} \leq 1$	
Trigger Efficiency	$0.5 \leq \epsilon_{Photo} \leq 1.$	
Tracking Efficiency	$0.95 \leq \epsilon_{Front} \cdot \epsilon_{Back} \leq 1.$	$0.90 \leq \epsilon_{Front} \cdot \epsilon_{Back} \leq 1.$
Beam Polarisation		$30\% \leq  p_B  \leq 80\%$
Target Polarisation		$70\% \leq  p_T $
Atomic Fraction		$0.97\% \leq \alpha_0 \leq 1.$
Degree of Dissociation		$0.7\% \leq \alpha_R \leq 1.3$

Table 5.1: Summary of the data quality criteria for the 1997 data set.

## 6 Quasi-real Photoproduction of $D^*$ Mesons

Reconstruction of open charm events at HERMES is a non-trivial task since the charm production near threshold is almost negligible compared to the quasi-real photoproduction cross-section for light quarks. Even though combinatorial background typically decreases rapidly for increasing invariant masses, the invariant mass spectra in the region of the  $D$  meson masses are still dominated by combinatorial background. Particles in background events at high invariant masses can be correlated or uncorrelated. Correlated particles originate from decaying particles with lower masses where at least one of the decay products is misidentified as a heavier particle. The wrongly assigned particle mass shifts the computed invariant mass to higher values. Uncorrelated particles can be directly produced in the fragmentation process or result from independent decays. While in the decays of lighter particles and in the fragmentation process predominantly pions are produced, in most of the decay modes of charmed particles the charm quark decays weakly into a strange quark leading to one or more kaons in the final state. A significant reduction of the combinatorial background can therefore be achieved with an identification of kaons.

The low centre of mass energy at HERMES – which implies low momenta for the decay products – together with the forward spectrometer of HERMES and its limited acceptance cause the fraction of reconstructable open charm events to be very small. As a rule of thumb, the fraction of reconstructable events decreases due to the acceptance and detector effects by about one order of magnitude for every additional particle requested in the final state. Also, the background situation gets typically worse the more particles are requested in the final state. Thus only decay modes with low multiplicities are promising candidates for the open charm search. Unfortunately, the  $D$  mesons have many possible decay modes with rather small branching fractions and large multiplicities [C<sup>+</sup>:98]. This is caused by the large mass differences between the  $D$  mesons and mesons which only contain the light  $u$ ,  $d$ , and  $s$  quarks.

Even though more particles are involved in the final state than for the direct search of the  $D$  mesons, many other advantages are associated with the decay chain  $D^* \rightarrow D\pi$ . The difference between the  $D^*$  and the  $D$  masses is just above the  $\pi$  mass to allow this strong decay (see also Tab. 3.3). The energy

$$Q = M(D^*) - \sum_i M_i \quad (6.1)$$

available in the decay is very small and the momentum of the  $\pi$  is at the very lower edge of the phase space. Since the combinatorial background is spread more evenly over the phase space, a rather strong background suppression can be achieved. Second, the difference between the  $D^*$

and  $D$  masses can be measured experimentally with a much higher accuracy than the masses themselves as most experimental uncertainties cancel. Finally, due to the intermediate  $D$  meson state, the additional kinematical requirement of the  $D$  mass can be used to furthermore reduce the background. In principle, also the separation between the production and decay vertex of the  $D$  meson could be used to improve the background situation. Since the lifetimes related to the weak decays are of order 1 ps (corresponding to decay lengths of order 100  $\mu\text{m}$ ), the secondary decay vertices are however not resolvable with the HERMES spectrometer.

Following the arguments given above, the most promising candidates for the open charm search are the decay

$$D^{*+} \rightarrow D^0 \pi_s^+ \rightarrow (K^- \pi^+) \pi_s^+$$

and its charge-conjugate channel

$$D^{*-} \rightarrow \bar{D}^0 \pi_s^- \rightarrow (K^+ \pi^-) \pi_s^-.$$

To be able to distinguish the two pions in the final state, the subindex  $s$  has been added to the pion from the  $D^*$  decay. This convention has been chosen as – due to the limited phase space for its momentum – this pion is in general much slower than the pion from the  $D^0$  decay. In the following the two above mentioned decay channels will be abbreviated through the shorter notation  $D^{*\pm} \rightarrow (K^\mp \pi^\pm) \pi_s^\pm$ .

## 6.1 The Decays $D^{*\pm} \rightarrow (K^\mp \pi^\pm) \pi_s^\pm$

Since it is necessary to use kinematical information in the reconstruction of these decays to achieve a sufficient background suppression, the expected behaviour of the  $D^{*\pm}$  mesons and their decay products was studied with the help of Monte Carlo simulations. As mentioned earlier, the Monte Carlo studies presented in this section are based on the AROMA event generator which simulates the production of heavy quark flavours in lepton-nucleon scattering through the boson-gluon fusion process [IRS:96]. The hadronisation was performed within the LUND string model as implemented in JETSET. For the light quarks, the LUND symmetric fragmentation function for the light quarks with parameters tuned to the HERMES data was used. To accomplish a harder fragmentation for the heavy charm quarks, the Peterson fragmentation function with  $\epsilon_c = 0.050$  was chosen for this quark flavour. The generated events were tracked with HMC through a detailed model of the HERMES spectrometer in its 1997 setup and then reconstructed with HRC using the NOVC reconstruction method.

### 6.1.1 Monte Carlo Studies

#### Kinematic distributions

The energies of the  $D^*$  and  $D^0$  mesons in the decays  $D^{*\pm} \rightarrow (K^\mp \pi^\pm) \pi_s^\pm$  are strongly correlated. The  $D^0$  always carries between 90 and 95% of the  $D^*$  energy due to the small

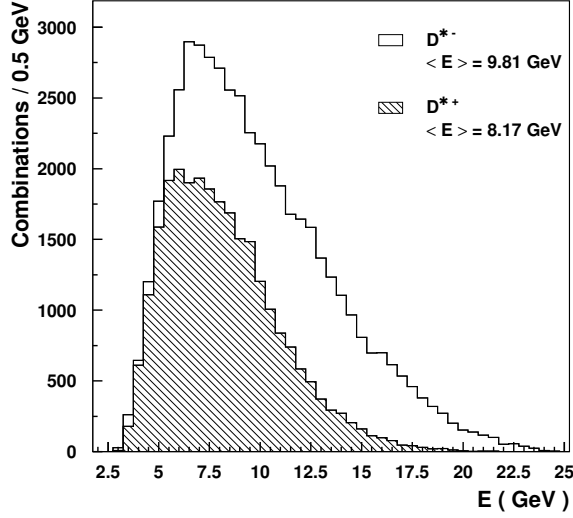


Figure 6.1: *Generated energy distributions for the  $D^{*+}$  and  $D^{*-}$  mesons in the decays  $D^{*\pm} \rightarrow (K^\mp \pi^\pm) \pi_s^\pm$ .*

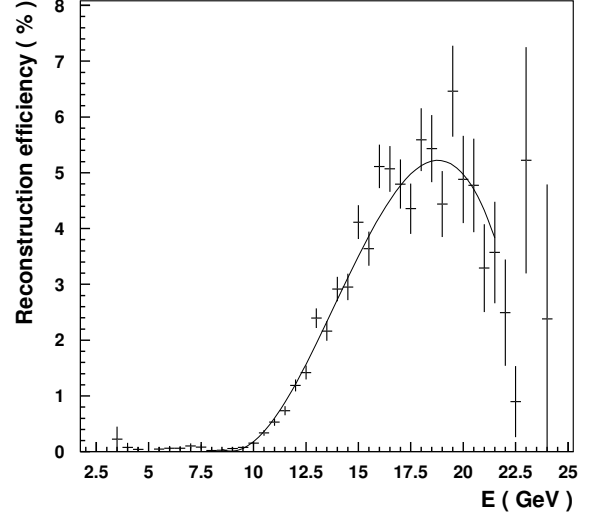


Figure 6.2: *Reconstruction efficiency as a function of the  $D^*$  energy in the decays  $D^{*\pm} \rightarrow (K^\mp \pi^\pm) \pi_s^\pm$ .*

mass difference between the two particles. The opening angle in the laboratory frame is generally below  $1^\circ$  and both particles reflect the direction of the primarily created charm quark. Due to these correlations it is sufficient to study the energy distributions of the  $D^{*\pm}$  mesons which are shown in Fig. 6.1. As already discussed in Sec. 3.2.1, significant differences are visible between the energy spectra of the  $D^{*+}$  and  $D^{*-}$  mesons. However, within errors the reconstruction efficiency for a given  $D^*$  energy is the same for both particles. This reconstruction efficiency reveals a strong energy dependence (Fig. 6.2) and effectively only decays with a  $D^*$  energy larger than approximately 8 GeV can be reconstructed. Besides the reconstruction efficiency which includes the acceptance of the spectrometer and the effects of the track reconstruction also the event selection criteria contribute to the total detection efficiency. The detection efficiency and its correction in the cross-section determination will therefore be revisited in more detail after the event selection cuts have been discussed.

For the reconstructable decays, the reconstructed momentum distributions of the decay products are shown in Fig. 6.3. A large fraction of the kaons and pions from the  $D^0$  decay have momenta in the range 4.5 – 13.5 GeV where the Čerenkov detector can efficiently identify pions. The momenta of the slow pions  $\pi_s$  from the  $D^*$  decay do not exceed 2.5 GeV. It is worth mentioning that this is not an effect of the acceptance of the HERMES spectrometer, but rather again the consequence of the

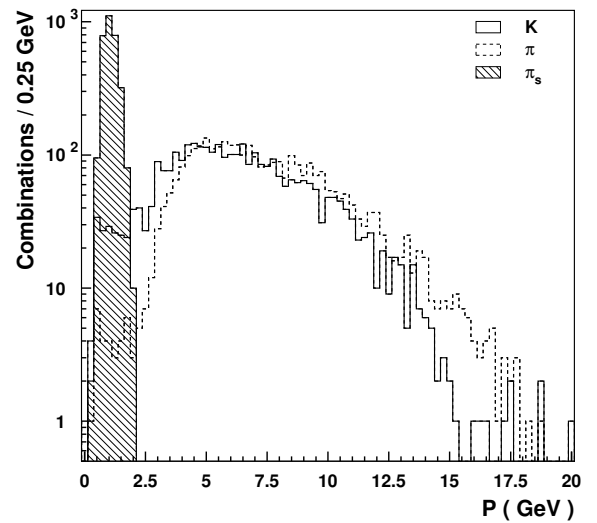


Figure 6.3: *Reconstructed momentum distributions for the decay products in the decays  $D^{*\pm} \rightarrow (K^\mp \pi^\pm) \pi_s^\pm$ .*

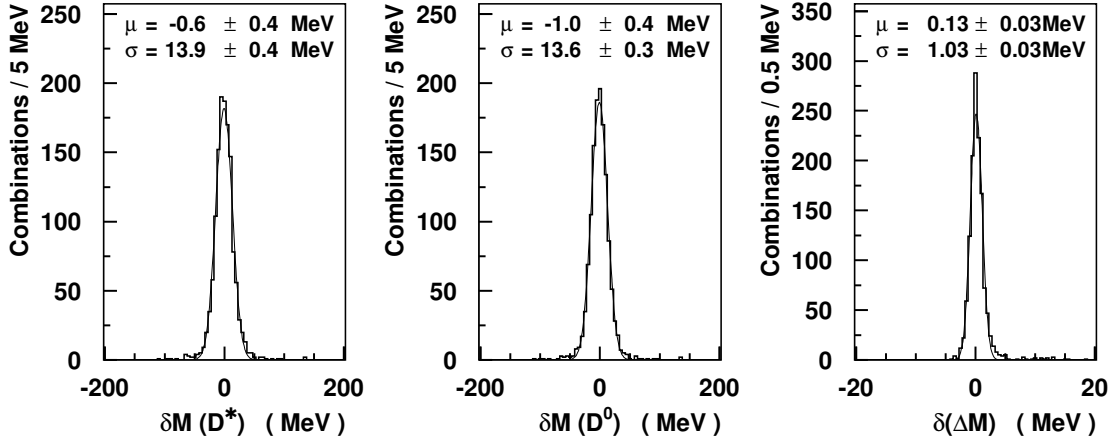


Figure 6.4: Resolutions for the  $D^*$  mass (left),  $D^0$  mass (middle) and the mass difference  $\Delta M = M(D^{*\pm}) - M(D^0)$  in the decays  $D^{*\pm} \rightarrow (K^\mp \pi^\pm) \pi_s^\pm$ .

small mass difference between the  $D^*$  and  $D^0$  mesons. A large fraction of the  $\pi_s$  has even such small momenta that the particles cannot pass through the HERMES magnet. Due to the large deflections in the magnetic field these particles get bend out of the acceptance of the tracking and particle identification detectors in the backward region of the spectrometer. However, a momentum determination down to 0.3 GeV for part of these particles is possible with the help of the tracking chambers installed inside the magnet. This track type, the so called short tracks, contributes about 45% to the sample of reconstructable  $D^{*-}$  decays. For the  $D^{*+}$  – which have a lower average energy – this fraction is with about 55% even higher. Since all particle identification detectors of HERMES are located in the backward part of the spectrometer, no particle identification can be performed for this track type. The contamination from other particles than pions in this kinematical regime however is expected to be less than 10%.

### Mass resolutions

The expected resolutions for the reconstructed masses of the  $D^*$  and  $D^0$  mesons as well as the mass difference  $\Delta M = M(D^{*\pm}) - M(D^0)$  are presented in Fig. 6.4. Shown are the deviations of the reconstructed values from the true masses together with Gaussian fits to the distributions. For both the  $D^*$  and  $D^0$  mesons the resolution is around 14 MeV, but a much better resolution of about 1 MeV is obtained for the mass difference. No systematic shifts are expected for the reconstructed masses. Also, no significant differences in the mass resolutions are seen between  $D^{*+}$  and  $D^{*-}$ .

### 6.1.2 Event Selection

The event selection criteria used in the analysis of the decays  $D^{*\pm} \rightarrow (K^\mp \pi^\pm) \pi_s^\pm$  will be described in the following. Here, those cuts are motivated which have not been discussed in the preceding sections. The exact cut values can be found in Tab. 6.1.



Criterion		Quantity	Range	Unit
Acceptance		$ \vartheta_x $	$[0, 180]$	mrاد
		$ \vartheta_y $	$[40, 140]$	mrاد
$K$ candidate:	track type charge PID momentum Čerenkov signal	$PID_3 + PID_{\text{TRD}}$ $p(K)$ $Cer(K)$	full $-1$ ( $+1$ ) $\leq 0$ $[4.5, 13.5]$ $\leq 0.35$	track  GeV NPE
$\pi$ candidate:	track type charge PID momentum Čerenkov signal	$PID_3 + PID_{\text{TRD}}$ $p(\pi)$ $Cer(\pi)$	full $+1$ ( $-1$ ) $\leq 0$ $[4.5, 13.5]$ $\geq 0.6$	track  GeV NPE
$\pi_s$ candidate:	track type charge PID (full tracks only)	$PID_3 + PID_{\text{TRD}}$	full or short $+1$ ( $-1$ ) $\leq 0$	track
$(K\pi)$ system:	$(K\pi)$ invariant mass			
	signal	$ M_{(K\pi)} - M_{D^0} $	$\leq 2$	$\sigma_M^{D^0}$
	sideband	$ M_{(K\pi)} - M_{D^0} $	$[4., 8.]$	$\sigma_M^{D^0}$
	vertex	$ z_{VTX} $ $t_{VTX}$	$\leq 25$ $\leq 0.75$	cm cm
$(K\pi\pi_s)$ system:	vertex	$ z_{VTX} $ $t_{VTX}$	$\leq 25$ $\leq 0.75$	cm cm
Signal:	mass difference	$ M_{(K\pi\pi_s)} - M_{(K\pi)} - (M_{D^{*\pm}} - M_{D^0}) $	$\leq 2$	$\sigma_{\Delta M}$

Table 6.1: Event selection criteria used in the analysis of  $D^{*\pm} \rightarrow (K^\mp \pi^\pm) \pi_s^\pm$  decays. All cuts are identical for  $D^{*+}$  and  $D^{*-}$ , only the charges of the particle candidates are different. The listed charges are for the  $D^{*+}$  decays with the opposite charges for the  $D^{*-}$  in brackets.

## Acceptance Cuts

A reliable usage of the tracking and particle identification detectors is only possible inside the sensitive area of these devices. A sufficient distance from the edges of the detectors has to be ensured to avoid losses in the detection and identification efficiencies and to guarantee an homogeneous distribution of these quantities over the used area. For this purpose, cuts on the horizontal and vertical projections of the scattering angle are imposed for all reconstructed tracks by requiring  $|\vartheta_x| \leq 180$  mrad and  $40 \text{ mrad} \leq |\vartheta_y| \leq 140$  mrad. The projections of the scattering angle  $\vartheta$  are given by the expressions  $\vartheta_x = \text{atan}(p_x/p_z)$  and  $\vartheta_y = \text{atan}(p_y/p_z)$  respectively,

where  $p_x$ ,  $p_y$  and  $p_z$  denote the horizontal, vertical, and longitudinal components of the particle momentum.

## Particle Identification

All reconstructed tracks have to be identified as hadrons to be accepted as candidates for the particles in the final state. This is accomplished by requiring  $PID = PID_3 + PID_{TRD} \leq 0$  for the PID parameter which was introduced in Sec. 4.3.2. An exception is made for the short tracks which are always considered to be a candidate for the slow pion. As mentioned before, no particle identification is available for those tracks but Monte Carlo studies show that about 90% of these tracks are indeed pions.

To achieve a sufficient background suppression pions have to be excluded from the kaon candidate sample. For this purpose, the Čerenkov detector information has been used. For the 1997 setup the Čerenkov momentum thresholds for pions and kaons are approximately 3.8 GeV and 13.6 GeV respectively. The pion identification efficiency for momenta of 4.5 GeV is around 80% and increases asymptotically to unity. For momenta larger than 7.5 GeV efficiencies above 99% are achieved [dSHJ<sup>+</sup>:00]. By limiting the momentum of the kaon candidates to the range of 4.5 – 13.5 GeV and requiring that the number of photo-electrons (NPE) is below 0.35, pions can therefore be excluded to a large extent. However, at momenta below 6 GeV the large pion flux and the inefficiency of the Čerenkov detector cause a significant pion contamination in the kaon sample. Additionally, a real kaon identification is not possible this way since also protons fulfil the requirements.

Another reduction of the background is possible by also limiting the momenta for the pion candidates to the range 4.5 – 13.5 GeV. Requiring a Čerenkov signal above 0.6 NPE thus results in a clean pion sample. Since most of the processes contributing to the background do not contain two high energetic particles, the requirement of a positive pion signal together with the less clean kaon “identification” suppresses background events very effectively.

## Decay Vertices

The  $D^*$  decay vertex is approximated by the point of closest approach between all tracks in the final state and analogously for the  $D^0$  using the kaon and pion candidates only. As mentioned before, at HERMES the production and decay vertices for charm events can not be separated. However, constraints on the decay vertices can ensure that the scattering process occurred inside the target. Only when excluding the possible scattering of the target cell walls and the collimating system in front of the target, the measured luminosities are meaningful. To match the size of the target cell and the expected vertex resolutions, the longitudinal and transverse vertex positions were constrained to  $|z_{VTX}| \leq 25$  cm and  $t_{VTX} = \sqrt{x_{VTX}^2 + y_{VTX}^2} \leq 0.75$  cm.

## Kinematic Cuts

Besides the limitations for the momenta of the kaon and pion candidates discussed above for the particle identification, cuts are applied on the reconstructed invariant masses of the  $(K\pi)$  and

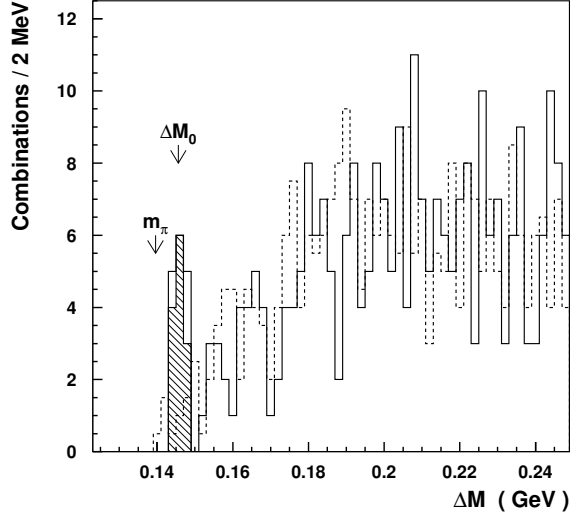


Figure 6.5: Mass difference spectra for the  $D^{*\pm}$  decay candidates (solid line) and a background sample obtained with the sideband method (dashed line).

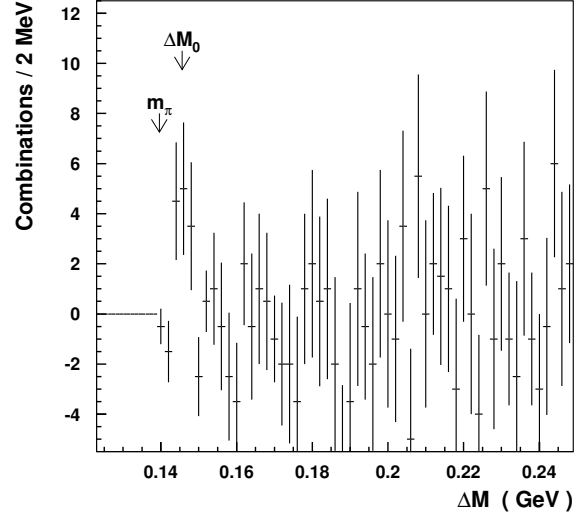


Figure 6.6: Background subtracted mass difference spectrum for the  $D^{*\pm}$  decay candidates. A clean signal can be observed near the expected mass difference.

$(K\pi\pi_s)$  systems, where the invariant mass of a system is defined as the absolute value of the sum of the four-momentum vectors over all particles contained in the system. All cut values are chosen as multiples of the expected resolutions which are taken according to Fig. 6.4 as

$$\sigma_M^{D^{*\pm}} = \sigma_M^{D^0} = 14.0 \text{ MeV}, \quad (6.2)$$

$$\sigma_{\Delta M} = 1.1 \text{ MeV}. \quad (6.3)$$

### 6.1.3 Extracted Signals

To use the entire data set for the extraction of a possible signal, in a first step no data quality cuts have been applied and all available data from 1997 reconstructed with the NOVC method are analysed. For the cross-section determination however, only data which passed the data quality criteria are used. Since an improvement in the resolution of more than one order of magnitude is expected for the resolution in the invariant mass difference  $\Delta M \equiv M_{(K\pi\pi_s)} - M_{(K\pi)}$  compared to the invariant mass of the  $(K\pi\pi_s)$  system, all results will be presented as a function of  $\Delta M$ .

The spectrum of the mass difference for both the  $D^{*+}$  and  $D^{*-}$  candidates together are shown in Fig. 6.5. A clean signal can be observed near the expected mass difference  $\Delta M_0 \equiv M_{D^{*\pm}} - M_{D^0} = 145.4 \text{ MeV}$ . The region  $\Delta M_0 \pm 2\sigma_{\Delta M}$  is highlighted through the shaded area and a background estimate obtained from the sidebands of the  $(K\pi)$  mass spectrum is overlaid (dashed histogram). When subtracting the estimated background, the distribution above the signal region scatters reasonably well around zero (Fig. 6.6). However, – when fitting the distribution with

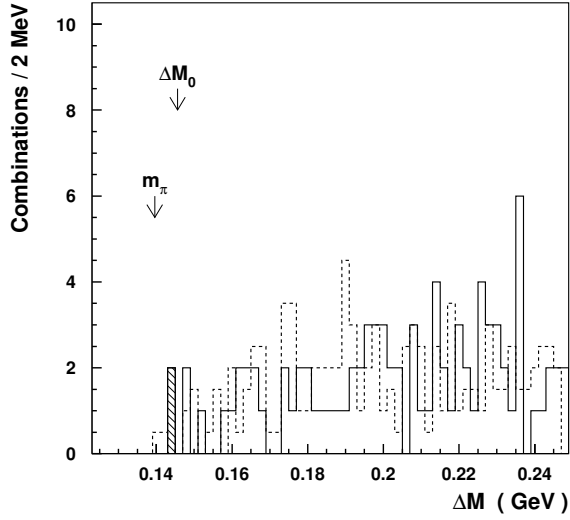


Figure 6.7: Mass difference spectra for the  $D^{*+}$  decay candidates (solid line) and a background sample obtained with the sideband method (dashed line).

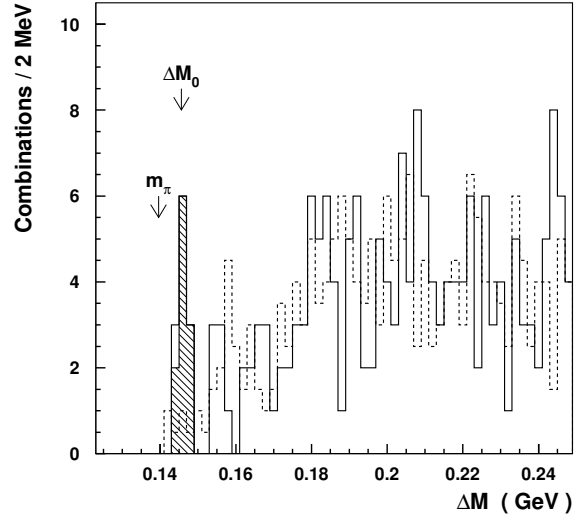


Figure 6.8: Mass difference spectra for the  $D^{*-}$  decay candidates (solid line) and a background sample obtained with the sideband method (dashed line).

a Gaussian for the signal and a constant for the background – there is some indication of an overestimate of the background contribution. A total number of 11  $D^{*\pm}$  candidates is suggested by this first extraction.

Since Monte Carlo studies suggest different yields for  $D^{*+}$  and  $D^{*-}$  mesons, the separate signals are shown in Figs. 6.7 and 6.8. While a clear signal is seen in the  $D^{*-}$  sample, no statistically significant signal is visible in the  $D^{*+} \rightarrow K^+\pi^-\pi_s^-$  decay channel.

### 6.1.4 Background Subtraction

To extract the production cross-section sections for the  $D^{*\pm}$  mesons, the background underneath the observed signal has to be estimated. Because of the required high invariant masses and the tight cuts on the  $D^0$  mass no other background sources than the combinatorial one is expected. Several different schemes are possible to determine the combinatorial background.

In the first approach, the invariant mass of the  $(K\pi)$  sub-system is constrained to a region sufficiently off the  $D^0$  mass to not contain any combinations from true  $D^0$  decays. To nevertheless reproduce the kinematics of the background in the signal region, this mass window, the *sideband*, should not be too far off. To improve the statistical accuracy, twice the signal width has been chosen with the region  $4\sigma_M^{D^0} \leq |M_{(K\pi)} - M_{D^0}| \leq 8\sigma_M^{D^0}$ .

Another way to determine the background is to fit the mass distribution with separate functional forms for signal and background. The integral over the background function can then be used as a measure for the background. Since the mass difference for the  $D^{*\pm}$  decays is close to the edge of the phase space, it is very difficult to find an appropriate functional form to describe the

background which can be fitted reliably. It is therefore preferable to constrain the mass difference  $\Delta M$  to the signal region and look instead at the invariant mass of the  $D^0$  candidates where a much smoother behaviour of the background can be expected. The same event selection criteria as before are applied, only the  $D^0$  mass cut gets replaced by the requirement  $|\Delta M - \Delta M_0| \leq 2\sigma_{\Delta M}$ . In the resulting distribution the background can be fitted with a straight line or an exponential function. For the signal function a Gaussian has been chosen. Due to the limited statistics the mean and width of the Gaussian were fixed to the expected values from the Monte Carlo studies. While the normalisation for the Gaussian changes dramatically, no significant change in the number of background events is observed when releasing one or both constraints.

In principle, a third background model may be obtained by considering the wrong charge sign combinations  $K^+\pi^-\pi_s^+$ ,  $K^-\pi^+\pi_s^-$ ,  $K^+\pi^+\pi_s^-$  or  $K^-\pi^-\pi_s^+$ , which all cannot stem from a physical  $D^{*\pm}$  decay. For a reliable background description however it would be required that the particle fluxes for positively and negatively charged particles are the same. Since this is not the case at HERMES, this method will not be used.

The number of candidates before and after the background subtraction using different models are summarised in Tab. 6.2. Very similar results have been obtained in a completely independent analysis [Bro:98]. Due to the low statistics in the  $D^{*+}$  channel the background in the combined  $D^{*\pm}$  decays has been determined instead. The background for the  $D^{*+}$  sample can then be approximated by the difference of the estimates for the  $D^{*\pm}$  and  $D^{*-}$  background. In this table also the signals obtained when changing the cuts on the  $D^0$  mass and the mass difference independently from two to three  $\sigma$  are given. All background subtraction schemes agree very nicely and also the variations of the mass cuts show no inconsistencies. It however has to be noted that due to the low statistics no smooth behaviour for the various cuts can be expected since one candidate more or less unavoidably implies large relative changes.

The number of candidates which are remaining after all data quality criteria have been applied are summarised in Tab. 6.3 separately for the different targets used during data taking and in Tab. 6.4 for the combined data set.

$ \Delta M - \Delta M_0  \leq 2 \sigma_{\Delta M}$					
Channel	$ M_{(K\pi)} - M_{D^0} $	no background correction	sideband method	polynomial fit	exponential fit
$D^{*\pm}$	$\leq 2 \sigma_M^{D^0}$	13.0	11.0	10.7	10.7
	$\leq 3 \sigma_M^{D^0}$	15.0	12.0	11.5	11.6
$D^{*-}$	$\leq 2 \sigma_M^{D^0}$	11.0	9.5	9.4	9.3
	$\leq 3 \sigma_M^{D^0}$	13.0	10.8	10.5	10.5
$ \Delta M - \Delta M_0  \leq 3 \sigma_{\Delta M}$					
Channel	$ M_{(K\pi)} - M_{D^0} $	no background correction	sideband method	polynomial fit	exponential fit
$D^{*\pm}$	$\leq 2 \sigma_M^{D^0}$	16.0	12.5	11.9	12.1
	$\leq 3 \sigma_M^{D^0}$	18.0	12.8	11.9	12.1
$D^{*-}$	$\leq 2 \sigma_M^{D^0}$	12.0	10.0	9.2	9.2
	$\leq 3 \sigma_M^{D^0}$	14.0	11.0	9.8	9.8

Table 6.2: Signals for the  $D^{*\pm}$  and  $D^{*-}$  decays before and after the background subtraction with the various methods described in the text. No data quality cuts have been applied. Please note that the  $D^{*\pm}$  and  $D^{*-}$  samples are not statistically independent.

Channel	$ \Delta M - \Delta M_0 $	$ M_{(K\pi)} - M_{D^0} $	$^1\vec{H}$	$^1H$	$^2D$	$^{14}N$	all targets
$D^{*-}$	$\leq 2 \sigma_{\Delta M}$	$\leq 2 \sigma_M^{D^0}$	2	1	1	2	6
		$\leq 3 \sigma_M^{D^0}$	3	1	1	2	7
	$\leq 3 \sigma_{\Delta M}$	$\leq 2 \sigma_M^{D^0}$	2	2	1	2	7
		$\leq 3 \sigma_M^{D^0}$	3	2	1	2	8
$D^{*+}$	$\leq 2 \sigma_{\Delta M}$	$\leq 2 \sigma_M^{D^0}$	1	0	1	0	2
		$\leq 3 \sigma_M^{D^0}$	1	0	1	0	2
	$\leq 3 \sigma_{\Delta M}$	$\leq 2 \sigma_M^{D^0}$	1	2	1	0	4
		$\leq 3 \sigma_M^{D^0}$	1	2	1	0	4

Table 6.3: Signals for the  $D^{*+}$  and  $D^{*-}$  decays without background subtraction for the individual target types where  $^1\vec{H}$  denotes polarised hydrogen. All data quality cuts have been applied. In the polarised data sample, all 3  $D^{*-}$  candidates are in the parallel spin state while the  $D^{*+}$  candidate is in the anti-parallel state.

	$ \Delta M - \Delta M_0 $	$ M_{(K\pi)} - M_{D^0} $	NB	BS	BP	BE	Average	Confidence Intervals		
								68.27% C.L.	90% C.L.	95% C.L.
$D^{*\pm}$	$\leq 2 \sigma_{\Delta M}$	$\leq 2 \sigma_M^{D^0}$	8	7.5	6.6	6.9	7.0	4.30 - 10.32	2.96 - 12.99	2.33 - 14.29
		$\leq 3 \sigma_M^{D^0}$	9	8.2	6.9	7.4	7.5	4.83 - 11.29	2.91 - 13.80	2.91 - 15.27
	$\leq 3 \sigma_{\Delta M}$	$\leq 2 \sigma_M^{D^0}$	11	10.0	8.6	8.9	9.2	5.81 - 12.82	3.91 - 15.81	3.30 - 17.29
		$\leq 3 \sigma_M^{D^0}$	12	10.5	8.4	8.8	9.4	6.33 - 13.79	4.51 - 16.50	3.85 - 17.84
$D^{*-}$	$\leq 2 \sigma_{\Delta M}$	$\leq 2 \sigma_M^{D^0}$	6	6.0	5.3	5.3	5.5	3.32 - 8.78	1.90 - 10.97	1.90 - 12.25
		$\leq 3 \sigma_M^{D^0}$	7	7.0	5.9	6.0	6.3	3.75 - 9.80	3.06 - 12.02	2.27 - 13.31
	$\leq 3 \sigma_{\Delta M}$	$\leq 2 \sigma_M^{D^0}$	7	6.5	5.4	5.4	5.8	3.25 - 9.30	2.56 - 11.53	1.97 - 12.81
		$\leq 3 \sigma_M^{D^0}$	8	7.2	5.6	5.6	6.3	3.80 - 9.82	2.51 - 12.49	2.33 - 14.29
$D^{*+}$	$\leq 2 \sigma_{\Delta M}$	$\leq 2 \sigma_M^{D^0}$	2	1.5	1.3	1.6	1.5	0.44 - 3.75	0.03 - 5.41	0.00 - 6.22
		$\leq 3 \sigma_M^{D^0}$	2	1.2	1.0	1.4	1.2	0.14 - 3.23	0.00 - 4.91	0.00 - 5.72
	$\leq 3 \sigma_{\Delta M}$	$\leq 2 \sigma_M^{D^0}$	4	3.5	3.2	3.5	3.4	1.84 - 6.28	1.17 - 8.10	0.87 - 9.26
		$\leq 3 \sigma_M^{D^0}$	4	3.3	2.8	3.2	3.1	1.34 - 5.78	0.74 - 7.60	0.37 - 8.76

Table 6.4: Signals for the  $D^{*\pm}$  decays before and after background subtraction after all data quality cuts have been applied. Here NB denotes the observed signals without background correction and BS, BP, BE the background subtracted signals according to the estimates from the sideband method, polynomial and exponential fits, respectively. Please note that the background estimates for the  $D^{*+}$  have been obtained as the difference between the estimates for the  $D^{*\pm}$  and  $D^{*-}$  samples. The final numbers for the signals have been obtained as the average of the estimates from the different background models. In the last three columns the confidence intervals for the Poisson signal mean for the most commonly used confidence levels (C.L.) are given. The numbers are taken from [FC:98] for a Poisson process with background where the mean of the background distribution has been approximated with the average background value.

## 6.2 Other Open Charm Channels

Even though the extracted  $D^{*\pm}$  signal is very clean, a confirmation of the obtained results by another open charm signal would be very valuable. As already discussed in the introduction to this chapter on page 77, the invariant mass spectra in the region of the  $D$  meson masses are still dominated by combinatorial background since the charm production near threshold is almost negligible compared to the quasi-real photoproduction cross-section for light quarks. Additional constraints have to be found to achieve a sufficient background suppression. One possible source for such constraints could be resonant decays of the  $D$  mesons, such as  $D^+ \rightarrow \bar{K}^{*0} \pi^+ \rightarrow (K^- \pi^+) \pi^+$  for example. Several resonant decay modes have been investigated for both the  $D^+$  and  $D^0$  mesons. For none of them a positive signal could be extracted either because the geometrical acceptance of the HERMES spectrometer is too small for such decays or no sufficient background suppression could be achieved. The best prospects are found for the decays of  $D^*$  mesons, for which some more decay modes will be discussed in the following. If not explicitly stated otherwise, for the rest of this section the mentioning of a certain decay mode always represents the sum of the specified decay mode and its charge conjugate channel.

### $D^{*0} \rightarrow D^0 \pi^0$

Following the arguments given before, all the advantages in the decay  $D^{*+} \rightarrow (K^- \pi^+) \pi_s^+$  should also be present in the equivalent decay for the  $D^{*0}$  mesons

$$D^{*0} \rightarrow D^0 \pi_s^0 \rightarrow (K^- \pi^+) \pi_s^0.$$

As shown in Sec. 3.2.1 and App. B, the production probabilities are expected to be the same for  $D^{*0}$  and  $D^{*+}$  mesons, but about a factor 1.6 higher for  $\bar{D}^{*0}$  mesons compared to  $D^{*-}$  mesons. The expected increase in the reconstructable signal however is partially compensated by the predicted lower average energy carried by the neutral  $D^*$  mesons.

Monte Carlo studies have been performed to estimate the number of reconstructable  $D^{*0}$  decays in the same data set analysed in the extraction of the  $D^{*\pm}$  signal. Since similar kinematics are expected for the  $D^0$  mesons in both decays, the  $D^0$  candidates are selected in analogy to the  $D^{*\pm}$  analysis according to Tab. 6.1. In the following, only  $D^{*0}$  decays will be considered where the  $D^0$  meson is reconstructable with the HERMES spectrometer.

In comparison to the  $D^{*\pm}$  decays, a complication arises through the decay of the low energetic pion  $\pi_s^0$ . It almost instantaneously decays with a branching fraction of over 98% into two photons. Due to the mass proportion of the heavy charmed  $D^{*0}$  meson and the light pion, the  $\pi_s^0$  energy is limited to below 2.5 GeV. Since this already rather low energy has to be shared between the two photons in the  $\pi^0$  decay, two typically very low energetic photons are occurring for which the acceptance of the HERMES spectrometer is a severe constraint. This is illustrated in Fig. 6.9, where the true energy spectra for the neutral pions and photons in the  $D^{*0}$  decays are shown before and after taking the geometrical acceptance into account.

Based on these energy spectra, the expected number of reconstructable  $D^{*0}$  decays can be computed. To be independent of the a priori unknown charm cross-section, this number has been normalised to the number of reconstructed  $D^{*+} \rightarrow (K^- \pi^+) \pi_s^+$  decays in the same



data set. The thus obtained normalised yield of reconstructable  $D^{*0}$  decays is shown in Fig. 6.10 as a function of the minimal photon energy  $E_\gamma$  requested for each photon from the  $\pi^0$  decay. At most about a factor 2 more  $D^{*0}$  than  $D^{*\pm}$  decays are expected when accepting all photon energies.

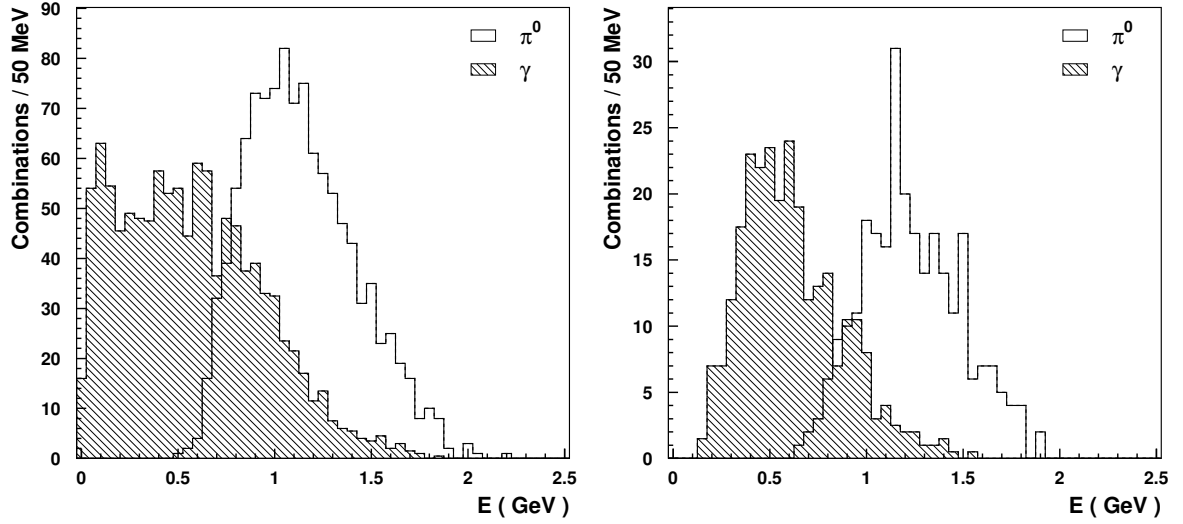


Figure 6.9: Energy spectra for neutral pions and photons from the decays  $D^{*0} \rightarrow D^0 \pi_s^0 \rightarrow (K^- \pi^+) (\gamma \gamma)$  when the  $D^0$  is reconstructable with the HERMES spectrometer. Shown are the distributions before (left) and after (right) taking into account the geometrical acceptance of the calorimeter for the photons from the  $\pi^0$  decay.

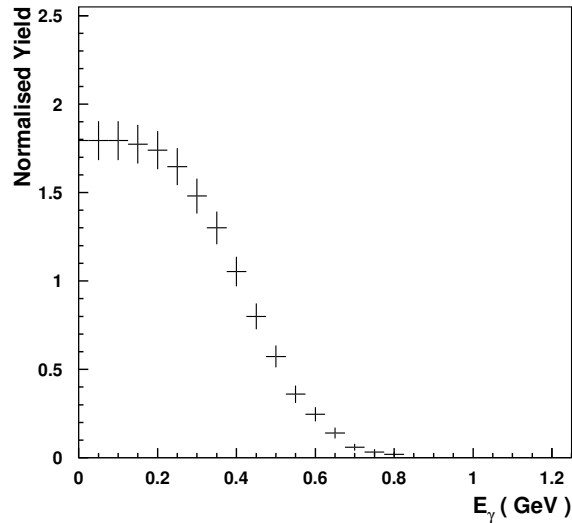


Figure 6.10: Yield of reconstructable  $D^{*0}$  decays normalised to the number of reconstructable  $D^{*\pm}$  decays as a function of the minimal photon energy requested for each photon from the  $\pi^0$  decay.

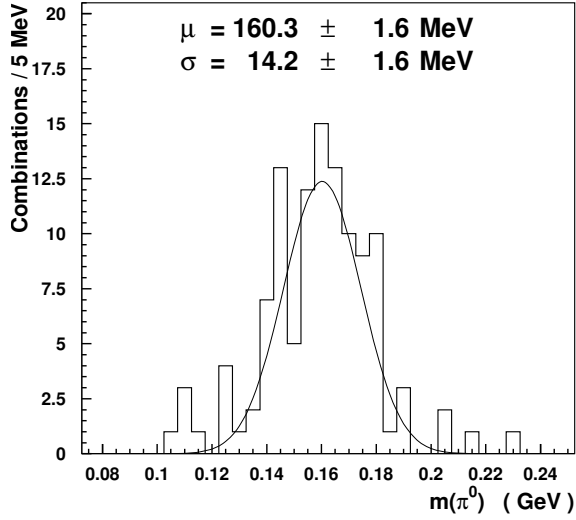


Figure 6.11: *Monte Carlo prediction for the reconstructed  $\pi^0$  mass spectrum in the decays of  $D^{*0}$  mesons.*

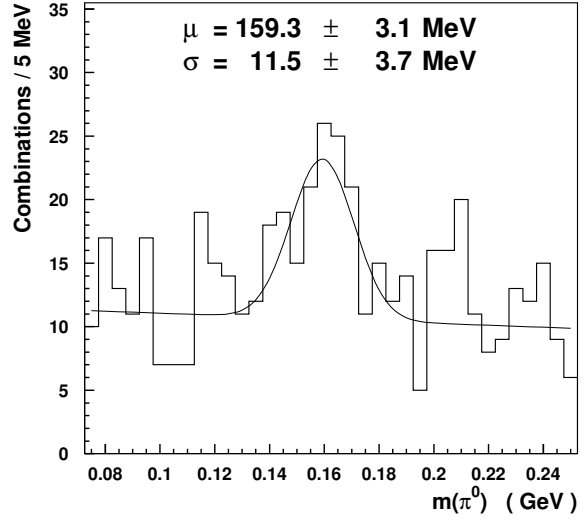


Figure 6.12: *Reconstructed mass spectrum for the  $\pi^0$  candidates in the decays of  $D^{*0}$  mesons.*

Up to now, the estimates have been based on the true energy spectra for the photons from the  $\pi^0$  decays. Low energetic photons however suffer from large (relative) energy losses in the detectors they have to penetrate before reaching the electromagnetic calorimeter and no good energy resolution can therefore be expected for these particles. While the energy loss in the various detectors is believed to be reliably implemented in the Monte Carlo, also a realistic description of the calorimeter response for low energetic photons is a pre-requisite to study their energy resolution. For performance reasons however, the modelling of the calorimeter response is only optimised for particle energies above few GeV matching the main purpose of the HERMES calorimeter, namely the triggering and particle identification at higher energies. The Monte Carlo predictions for low energetic photons have therefore to be handled with some caution.

The predicted mass resolution for the  $\pi^0$  is presented in Fig. 6.11. The reconstructed invariant mass of the two photons is shifted by about 25 MeV compared to the  $\pi^0$  mass. A similar effect is also observed in the experimental data for the reconstructed invariant mass of the  $\pi^0$  candidates (Fig. 6.12), giving some confidence in the Monte Carlo simulations. However, more detailed studies are necessary to understand this behaviour.

The inaccuracies in the  $\pi^0$  mass determination are directly propagated into the difference of the invariant masses of the  $D^{*0}$  and  $D^0$  candidates where a resolution of 10 – 20 MeV is expected. This is in clear contrast to the case of the  $D^{*\pm}$  decays, where a resolution of 1.1 MeV is achieved in the mass difference. This worse resolution significantly deteriorates the background situation since the reconstructable  $D^{*0}$  decays are spread over a larger phase space.

In addition to these complications, the HERMES calorimeter does not allow to separate photons with energies below 500 MeV from electronic noise. Moreover, to save disk space, the compressed  $\mu$ DSTs impose an even more restrictive cut of 800 MeV.

Motivated by these results, the following event selection criteria are applied in the extraction of

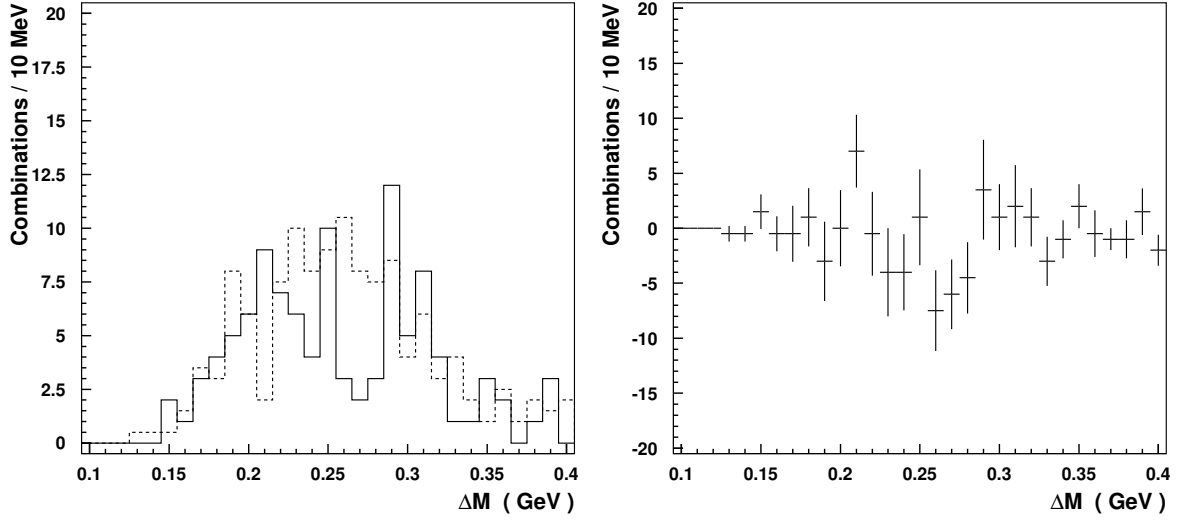


Figure 6.13: On the left hand side, the mass difference spectra for the  $D^{*0}$  decay candidates (solid line) and a background sample obtained with the sideband method (dashed line) are shown for the full 1997 data set. On the right hand side, the background subtracted distribution is presented.

the  $D^{*0}$  decays in addition to the already mentioned requirements for the  $D^0$  candidates

$$0.07 \text{ GeV} \leq m_{\pi^0} \leq 0.25 \text{ GeV} ,$$

$$E_\gamma \geq 0.8 \text{ GeV} , \quad E_{\pi^0} \leq 2.5 \text{ GeV} .$$

From the full 1997 data set, the spectra for the mass difference  $\Delta M \equiv M_{D^{*0}} - M_{D^0}$  presented in Fig. 6.13 have been extracted. No signal is observed in the expected mass window below 0.2 GeV, in agreement with the Monte Carlo expectations for the required high energies of the two photons.

### $D^{*0} \rightarrow D^0 \gamma$

Another possibility for the reconstruction of  $D^{*0}$  decays is the decay mode  $D^{*0} \rightarrow D^0 \gamma$ . Even though the branching fraction is about a factor 2 lower than in the  $D^{*0} \rightarrow D^0 \pi^0$  channel, the geometrical acceptance of the HERMES spectrometer is in favour of this decay mode as only one photon has to be detected. Additionally, this photon possesses on average a higher energy than the photons from the  $\pi^0$  decay and the problems discussed in the previous section are thus less severe.

However, this decay mode suffers from another severe disadvantage. In the case of the  $D^{*+} \rightarrow D^0 \pi^+$  and  $D^{*0} \rightarrow D^0 \pi^0$  decays, the available phase space for the pions is extremely limited since the difference between the  $D^*$  and  $D$  masses is just above the pion mass. A substantial background suppression is therefore possible, as this constraint is not present for the combinatorial background. Unfortunately, this phase space limitation is also not present for the  $D^{*0} \rightarrow D^0 \gamma$  decays and its absence does not allow to separate a possible signal for these decays from the

background. Additionally, the number of photons with these relatively low energies is very high thus resulting in enormous background.

### Other $D^0$ decay modes

Given the observed statistics in the 1997 data set for the decay chain  $D^{*+} \rightarrow D^0 \pi_s^+ \rightarrow (K^- \pi^+) \pi_s^+$  and the for HERMES typical rule of thumb that the fraction of reconstructable events decreases due to the acceptance by about one order of magnitude for every additional particle in the final state, it becomes obvious that no reconstructable signal can be expected for  $D^0$  decay modes with more than two decay products. A possible alternative with only two charged decay products is the decay  $D^0 \rightarrow K^+ K^-$ . In this decay channel, the perspectives for the background situation are excellent since a good pion suppression in the kaon candidate samples is possible at HERMES. Unfortunately, the branching fraction is about one order of magnitude smaller compared to the decay  $D^0 \rightarrow K^- \pi^+$  and again no reconstructable signal can be expected for the 1997 data set.

Since open charm decays are characterised by many possible decay modes with rather small branching fractions and typically large multiplicities, the number of reconstructable events can be significantly enhanced when not all of the decay products of the  $D^0$  mesons have to be reconstructed. Since the mass difference  $\Delta M \equiv M_{D^{*+}} - M_{D^0}$  in the decay  $D^{*+} \rightarrow D^0 \pi_s^+$  is mainly determined by the kinematics of the slow pion, the incomplete reconstruction of the  $D^0$  decay does not seriously affect the potential of the background suppression through the mass difference. It can even be shown that the difference of the squared invariant masses  $\Delta M^2 \equiv M_{D^{*+}}^2 - M_{D^0}^2$  cannot get larger for incompletely reconstructed  $D^0$  decays compared to fully reconstructed decays.

However, for the incomplete decays no strong constraint can be placed on the invariant mass of the  $D^0$  candidates. Due to the missing particles, the reconstructed invariant mass is shifted to lower values and the expected gain in the number of reconstructable  $D^*$  decays is vanishingly small compared to the increase in combinatorial background. Further background suppression could be achieved for example through the separation of the  $D^{*+}$  and  $D^0$  decay vertices which is unfortunately not possible with the HERMES tracking system. The incomplete decays therefore cannot be used for the extraction of open charm signals at HERMES unless an extremely accurate model for the description of the combinatorial background would be available.

## 6.3 Cross-section Determination

The general formalism used to extract the production cross-section for the  $D^{*\pm}$  mesons has been described in detail in Sec. 5. There the fundamental formula Eq. 5.4 was introduced

$$\frac{d\sigma}{d\mathbf{p}}(\mathbf{p}) = \frac{1}{\mathcal{A}(\mathbf{p}) \mathcal{E}(\mathbf{p}) L_{\text{eff}}} \frac{dN}{d\mathbf{p}}(\mathbf{p}). \quad (6.4)$$

In this formula  $\mathbf{p}$  denotes any set of kinematical variables,  $L_{\text{eff}}$  the effective luminosity including all time dependent corrections and  $\mathcal{A}$ ,  $\mathcal{E}$  are correction functions for the time-independent acceptance and detection efficiencies.

### 6.3.1 Effective Luminosity

In the determination of the integrated effective luminosity (Eq. 5.16), the time dependences in the efficiencies of the data acquisition system, the trigger and the track finding have been included into the efficiency correction factor  $\mathcal{E}'(t)$ . While the first two quantities are common to all photoproduction analyses, the track finding efficiency has to be determined from the special requirements of the investigated decay channels. Since three charged tracks are requested in the reconstruction of  $D^{*\pm}$  mesons, the track finding efficiency is computed as the product of the single track efficiencies

$$\epsilon_{\text{PPE}} = \sum_i w_i \epsilon_i^K \epsilon_i^\pi \epsilon_i^{\pi_s}, \quad (6.5)$$

neglecting any correlations in the track finding for high multiplicities. The summation in Eq. 6.5 hereby takes into account that different efficiencies are possible for the independent upper and lower detector halves and that the pion  $\pi_s$  from the  $D^*$  decay can be either a short or a full track. However, negligible differences in the correction factors have been found when taking into account the fluxes predicted by the Monte Carlo.

The time integrated luminosities for each individual target type are listed in Tab. 6.5 after all data quality cuts have been applied. The first row shows the measured values for the entire data set, the second one the measured luminosity for those data where the photoproduction trigger was not pre-scaled. Especially for the unpolarised hydrogen and deuterium data this corresponds to only about 50% of the full data set. The last row finally shows the effective luminosity. The additional loss of about 35% (compared to the second row) is mainly due to the inefficiency of the photoproduction trigger (around 80%) and the track finding efficiency.

### 6.3.2 Detection Efficiency Correction

Many different effects contribute to the total detection efficiency for a certain decay channel. While most of the detector effects have already been corrected for in the definition of the effective luminosity (contribution of the tracking detector efficiencies on the track finding and the

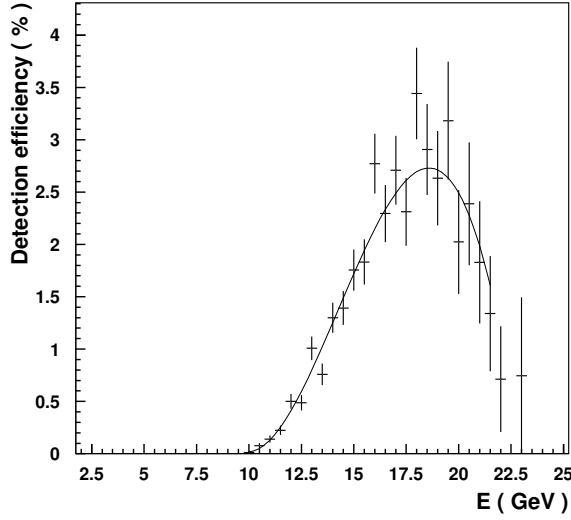


Figure 6.14: *Differential detection efficiency in the decays  $D^{*\pm} \rightarrow (K^\mp \pi^\pm) \pi_s^\pm$  after all event selection criteria have been applied.*

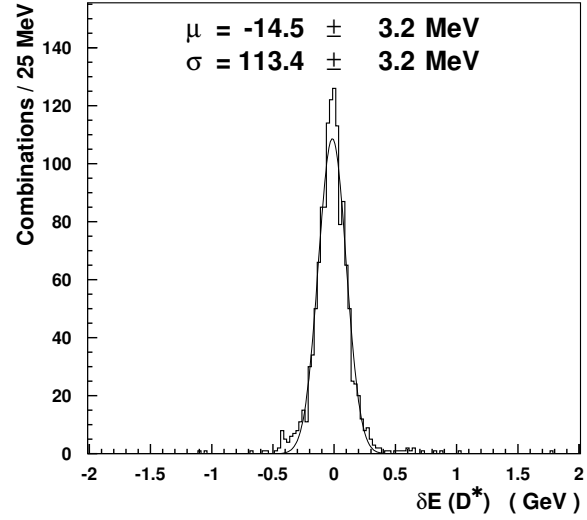


Figure 6.15: *Energy resolution for the  $D^{*\pm}$  mesons in the decays  $D^{*\pm} \rightarrow (K^\mp \pi^\pm) \pi_s^\pm$ .*

efficiencies of the data acquisition and trigger systems), several other contributions can not be determined from the data but have to be estimated with the help of Monte Carlo studies. The most important ones are the geometrical acceptance of the HERMES spectrometer, the influence of the detector materials on the track parameters, and the event selection criteria.

The differential detection efficiency as a function of the  $D^{*\pm}$  energy is shown once more in Fig. 6.14 after all event selection criteria have been applied (see Tab. 6.1). The event selection criteria increase the minimal energy for the  $D^{*\pm}$  mesons seen in the HERMES spectrometer to about 10 GeV (see also Fig. 6.2). The strong energy dependency suggests to accomplish the efficiency correction in two steps. First, the experimentally accessible energy range should be corrected for with the differential reconstruction efficiencies using the unfolding procedure described in Sec. 5.1. In a second step, the thus obtained cross-section which is corrected for all effects of the HERMES detector, has to be extrapolated into the energy range not accessible with the HERMES spectrometer. It should be noted that this extrapolation might strongly depend on

	photoproduction trigger included?	$^1\vec{H}$	$^1H$	$^2D$	$^{14}N$	all targets
$L_{\text{tot}}$	no	38.17	28.39	50.86	46.55	163.97
	yes	37.56	18.91	18.86	39.16	114.50
$L_{\text{eff}}$	yes	25.28	11.66	11.74	24.64	73.31

Table 6.5: *Uncorrected and effective time integrated luminosities in  $\text{pb}^{-1}$  split into the different target types where  $^1\vec{H}$  denotes polarised hydrogen. All data quality cuts have been included revealing the big impact of the pre-scaling on the unpolarised hydrogen and deuterium samples.*

the model used in the Monte Carlo simulation of the process. In contrary, for the first step the knowledge of the exact energy distribution is not a necessary pre-requisite to the Monte Carlo simulations. In principle, the obtained unfolded results could even be used to distinguish between different production mechanisms and thus minimise the systematic uncertainties associated with the simulations. However, the low statistics in the observed signals for the investigated decay channels does not allow to measure any energy dependence in the production of  $D^{*\pm}$  mesons. The unfolding therefore can only be performed after integrating out the energy dependence, where the true differential cross-section as a function of the energy has to be approximated by the model used in the Monte Carlo simulation. Since the expected migration is small due to the rather good energy resolution for the  $D^{*\pm}$  mesons (Fig. 6.15), the bin-to-bin correction with generalised Monte Carlo efficiencies as described in Sec. 5.1.1 will be used for the unfolding. The correction factor is then given through the integrated efficiency

$$\langle \epsilon \rangle(E_{min}) \equiv \frac{\int_{E_{min}}^{E_B} dE \epsilon(E) \frac{d\sigma^{MC}}{dE}(E)}{\int_{E_{min}}^{E_B} dE \frac{d\sigma^{MC}}{dE}(E)} = \frac{\int_{E_{min}}^{E_B} dE \frac{dM_{Rec}^{MC}}{dE}(E)}{\int_{E_{min}}^{E_B} dE \frac{dN_{Gen}^{MC}}{dE}(E)}. \quad (6.6)$$

For the unfolding inside the experimentally accessible energy range, the lower integration limit  $E_{min} = 10$  GeV was chosen; for  $E_{min} = 0$  GeV also the extrapolation to the full phase space is included. The corresponding correction factors will be denoted in the following as  $\langle \epsilon \rangle_{exp}$  and  $\langle \epsilon \rangle_{tot}$  respectively. Please note that in the determination of both these quantities only differential but no absolute cross-section estimates from the Monte Carlo are necessary.

The values for the integrated efficiencies obtained by this method are listed in Tab. 6.6 for various intermediate steps in the analysis. The main contribution to the detection inefficiency is due to the spectrometer acceptance. For the reconstructable decays, the momentum requirements to match the threshold of the Čerenkov detector for an efficient background suppression remove another 50% of the candidates. In total, about 40% of the reconstructable  $D^{*\pm}$  decays are passing all the event selection criteria. It is worth repeating once more that rather different detection efficiencies are expected for the  $D^{*+}$  and  $D^{*-}$  mesons. For the  $D^{*-}$  meson, the efficiency is found to be higher than the  $D^{*+}$  efficiency by about a factor 1.5 before and 1.8 after the extrapolation to the full energy range, being solely the consequence of the on average larger energy carried by this particle compared to the  $D^{*+}$  meson (see Fig. 6.1 and Sec. 3.2.1).

### 6.3.3 Isoscalar Targets

Up to now, only proton targets have been considered in the Monte Carlo simulations as this is the only target type AROMA can handle. In the experimental data, however, also deuterium and nitrogen targets are used and it is necessary to determine the detection efficiencies for the  $D^{*\pm}$  production off these targets as well. Under the assumptions of isospin invariance and identical gluon distributions in proton and neutron, the production cross-sections off a neutron are given by the proton cross-sections for the isospin partners of the  $D^{*\pm}$  mesons. Under an isospin

transformation (exchange of  $u$ - and  $d$ -quarks) the  $D^{*+}$  ( $D^{*-}$ ) is converted into a  $D^{*0}$  ( $\bar{D}^{*0}$ ) and the following relations can be obtained for the neutron cross-sections

$$\sigma^n(D^{*+}) = \sigma^p(D^{*0}), \quad \sigma^n(D^{*-}) = \sigma^p(\bar{D}^{*0}). \quad (6.7)$$

Since the decay properties of the  $D^{*\pm}$  mesons are independent of the production mechanism and the target type, the differential detection efficiencies as a function of the energy are the same for proton and neutron targets. The integrated detection efficiencies for the  $D^{*\pm}$  production on a neutron target can therefore be computed according to Eq. 6.6 using the (universal) differential efficiencies and the predicted differential cross-sections for the  $D^{*0}$  mesons. As can be seen from the last column in Tab. 6.7, no significant differences exist between the integrated detection efficiencies for proton and neutron targets. This implies that the differences between the  $u$ - and  $d$ - respectively  $\bar{u}$ - and  $\bar{d}$ -quark distributions have a negligible impact on the energy distribution of the produced charmed mesons. In the following, the average of the proton and neutron results will therefore be used as the final values for the integrated detection efficiencies.

### 6.3.4 $D^{*\pm}$ Cross-sections

Since the statistics is too small to determine the cross-sections for each target type independently, all target types will be combined. To nevertheless allow a physical interpretation, a correction has to be applied to convert the measured cross-section to an electroproduction cross-section for a pure proton or deuterium target. When neglecting nuclear effects, the cross-sections for deuterium and nitrogen are the same as both are isoscalar targets. Using the indices  $p$  for the proton and  $d$  for the isoscalar targets, the measured cross-section  $\sigma^{\text{mix}}$  can be written as

$$N^{\text{mix}} = N^p + N^d \quad \Rightarrow \quad \sigma^{\text{mix}} = \frac{L_{\text{eff}}^p \sigma^p + L_{\text{eff}}^d \sigma^d}{L_{\text{eff}}^p + L_{\text{eff}}^d}. \quad (6.8)$$

With the relation  $\sigma^d = \frac{1}{2}(\sigma^p + \sigma^n)$  and the definitions

$$\xi \equiv \frac{\sigma^n}{\sigma^p}, \quad (6.9)$$

$$R_{\text{eff}}^L \equiv \frac{L_{\text{eff}}^d}{L_{\text{eff}}^p}, \quad (6.10)$$

one obtains for the production cross-section on a proton target

$$\sigma^p = \sigma^{\text{mix}} \left[ 1 + \frac{1}{2} \frac{R_{\text{eff}}^L}{R_{\text{eff}}^L + 1} (\xi - 1) \right]^{-1} \equiv \sigma^{\text{mix}} C^p, \quad (6.11)$$

and similarly for the production cross-section on an isoscalar target

$$\sigma^d = \sigma^{\text{mix}} \left[ 1 + \frac{1}{R_{\text{eff}}^L + 1} \left( 1 - 2 \frac{\xi}{\xi + 1} \right) \right]^{-1} \equiv \sigma^{\text{mix}} C^d. \quad (6.12)$$



Cuts	$D^{*+}$	$D^{*-}$
Acceptance and Reconstruction	$1.6456 \pm 0.0355 \%$	$2.2568 \pm 0.0463 \%$
Particle Identification	$0.8552 \pm 0.0249 \%$	$1.2563 \pm 0.0347 \%$
Vertex Cut	$0.8251 \pm 0.0245 \%$	$1.2111 \pm 0.0341 \%$
$ M_{(K\pi)} - M_{D^0}  \leq 2 \sigma_M^{D^0}$	$0.7673 \pm 0.0236 \%$	$1.1211 \pm 0.0327 \%$
$ \Delta M - \Delta M_0  \leq 2 \sigma_{\Delta M}$	$0.7034 \pm 0.0226 \%$	$1.0306 \pm 0.0314 \%$
$\langle \epsilon \rangle_{exp}$	$0.7034 \pm 0.0226 \%$	$1.0306 \pm 0.0314 \%$
$\langle \epsilon \rangle_{tot}$	$0.2492 \pm 0.0210 \%$	$0.4398 \pm 0.0303 \%$

Table 6.6: Integrated efficiencies for the detection of  $D^{*\pm}$  decays at various intermediate steps of the analysis. Incremental values are given. The largest inefficiency is due to the acceptance of the spectrometer. For the particle identification mainly the momentum requirements contribute. The quoted errors are due to the limited statistics in the Monte Carlo simulations.

	$ \Delta M - \Delta M_0 $	$ M_{(K\pi)} - M_{D^0} $	$(\langle \epsilon^p \rangle + \langle \epsilon^n \rangle) / 2$	$\langle \epsilon^p \rangle - \langle \epsilon^n \rangle$
$D^{*\pm}$	$\leq 2 \sigma_{\Delta M}$	$\leq 2 \sigma_M^{D^0}$	$0.3826 \pm 0.0278 \%$	-0.0121%
		$\leq 3 \sigma_M^{D^0}$	$0.4019 \pm 0.0285 \%$	-0.0127%
	$\leq 3 \sigma_{\Delta M}$	$\leq 2 \sigma_M^{D^0}$	$0.3994 \pm 0.0284 \%$	-0.0127%
		$\leq 3 \sigma_M^{D^0}$	$0.4197 \pm 0.0291 \%$	-0.0134%
$D^{*-}$	$\leq 2 \sigma_{\Delta M}$	$\leq 2 \sigma_M^{D^0}$	$0.4398 \pm 0.0303 \%$	0.0076%
		$\leq 3 \sigma_M^{D^0}$	$0.4622 \pm 0.0311 \%$	0.0081%
	$\leq 3 \sigma_{\Delta M}$	$\leq 2 \sigma_M^{D^0}$	$0.4593 \pm 0.0310 \%$	0.0080%
		$\leq 3 \sigma_M^{D^0}$	$0.4830 \pm 0.0318 \%$	0.0084%
$D^{*+}$	$\leq 2 \sigma_{\Delta M}$	$\leq 2 \sigma_M^{D^0}$	$0.2492 \pm 0.0210 \%$	0.0085%
		$\leq 3 \sigma_M^{D^0}$	$0.2611 \pm 0.0215 \%$	0.0089%
	$\leq 3 \sigma_{\Delta M}$	$\leq 2 \sigma_M^{D^0}$	$0.2598 \pm 0.0214 \%$	0.0089%
		$\leq 3 \sigma_M^{D^0}$	$0.2720 \pm 0.0219 \%$	0.0092%

Table 6.7: Integrated efficiencies  $\langle \epsilon \rangle_{tot}$  for the detection of  $D^{*\pm}$  decays for the different mass and mass difference cuts used in the analysis. The quoted errors are due to the limited statistics in the Monte Carlo simulations.

The quantity  $\xi$  is estimated for the  $D^{*\pm}$  mesons with the help of the Monte Carlo to be

$$\begin{aligned}\xi_{D^{*\pm}} &= 1.4342, \\ \xi_{D^{*-}} &= 1.6666, \\ \xi_{D^{*+}} &= 1.0074.\end{aligned}\tag{6.13}$$

Now all necessary ingredients are at hand to calculate the  $D^{*\pm}$  electroproduction cross-sections. After integrating out the dependences on the kinematical variables in Eq. 6.4, the following final expression is obtained

$$\sigma_{D^{*\pm}}^{p,d} = \frac{C_{D^{*\pm}}^{p,d} N_{D^{*\pm}}}{L_{\text{eff}} \langle \epsilon \rangle_{\text{tot}}^{D^{*\pm}} \text{BR}(D^{*+} \rightarrow D^0 \pi^+) \text{BR}(D^0 \rightarrow K^- \pi^+)}.\tag{6.14}$$

Here,  $N_{D^{*\pm}}$  is the number of measured  $D^{*\pm}$  events,  $L_{\text{eff}}$  the time integrated effective luminosity and  $\langle \epsilon_{D^{*\pm}} \rangle$  the integrated detection efficiency which are given in Tabs. 6.4, 6.5 and 6.7 respectively.  $\text{BR}(D^{*+} \rightarrow D^0 \pi^+) = (68.3 \pm 1.4)\%$  and  $\text{BR}(D^0 \rightarrow K^- \pi^+) = (3.85 \pm 0.09)\%$  are the known branching ratios for the  $D^{*+} \rightarrow D^0 \pi^+$  and  $D^0 \rightarrow K^- \pi^+$  decays [C<sup>+</sup>:98].

The electroproduction cross-sections of  $D^{*\pm}$  mesons measured on a mixture of proton and isoscalar targets are summarised in Tab. 6.8. Consistent results are obtained for the various mass and mass difference cut combinations in the cases of the  $D^{*-}$  mesons and the combined  $D^{*\pm}$  signal. For the  $D^{*+}$  mesons, a large spread occurs in the measured cross-sections but is found to be consistent within the statistical errors. Therefore, the averaged cross-sections have been used to derive the cross-sections for the electroproduction of  $D^{*\pm}$  mesons on proton and isoscalar targets which are presented in Tab. 6.9. It should be emphasised here that the  $D^{*\pm}$  cross-section has been determined using separate correction factors for the combined signal and that it is thus not the same as the sum of the two individual  $D^{*+}$  and  $D^{*-}$  cross-sections.

### 6.3.5 Open Charm Electroproduction Cross-section

From the extracted  $D^{*\pm}$  cross-sections one can easily derive the total open charm production cross-section in electron-proton scattering

$$\sigma^{ep \rightarrow c\bar{c}X} = \left\{ \begin{array}{l} \frac{\sigma_{D^{*+}}^p}{\text{BR}(p; c \rightarrow D^{*+})}, \\ \frac{\sigma_{D^{*-}}^p}{\text{BR}(p; \bar{c} \rightarrow D^{*-})}, \\ \frac{\sigma_{D^{*\pm}}^p}{\text{BR}(p; c \rightarrow D^{*+}) + \text{BR}(p; \bar{c} \rightarrow D^{*-})}. \end{array} \right.\tag{6.15}$$

$\text{BR}(p; c \rightarrow D^{*+})$  and  $\text{BR}(p; \bar{c} \rightarrow D^{*-})$  denote the  $D^{*+}$  and  $D^{*-}$  production probabilities per open charm event discussed before (see Sec. 3.2.1 and Tabs. B.2 and B.3). These quantities depend on the nuclear environment in which the  $c\bar{c}$ -pair is produced (reflected by the index  $p$ )

	$ \Delta M - \Delta M_0 $	$ M_{(K\pi)} - M_{D^0} $	$\sigma^{\text{mix}}$ (pb)	$\Delta\sigma_{\text{stat}}$ (pb)	$\Delta\sigma_{\text{stat}}^{\text{MC}}$ (pb)
$D^{*\pm}$	$\leq 2\sigma_{\Delta M}$	$\leq 2\sigma_M^{D^0}$	949.1	$+450.2$ $-366.1$	$\pm 69.0$
		$\leq 3\sigma_M^{D^0}$	968.1	$+489.2$ $-344.6$	$\pm 68.7$
	$\leq 3\sigma_{\Delta M}$	$\leq 2\sigma_M^{D^0}$	1195.0	$+470.2$ $-440.3$	$\pm 85.0$
		$\leq 3\sigma_M^{D^0}$	1161.9	$+542.6$ $-379.5$	$\pm 80.6$
$D^{*-}$	$\leq 2\sigma_{\Delta M}$	$\leq 2\sigma_M^{D^0}$	648.8	$+386.9$ $-257.1$	$\pm 44.7$
		$\leq 3\sigma_M^{D^0}$	707.1	$+392.8$ $-286.2$	$\pm 47.6$
	$\leq 3\sigma_{\Delta M}$	$\leq 2\sigma_M^{D^0}$	655.1	$+395.3$ $-288.0$	$\pm 44.2$
		$\leq 3\sigma_M^{D^0}$	676.7	$+378.1$ $-268.5$	$\pm 44.5$
$D^{*+}$	$\leq 2\sigma_{\Delta M}$	$\leq 2\sigma_M^{D^0}$	312.3	$+468.4$ $-220.7$	$\pm 26.3$
		$\leq 3\sigma_M^{D^0}$	238.4	$+403.3$ $-210.6$	$\pm 19.6$
	$\leq 3\sigma_{\Delta M}$	$\leq 2\sigma_M^{D^0}$	678.9	$+575.1$ $-311.5$	$\pm 55.9$
		$\leq 3\sigma_M^{D^0}$	591.2	$+511.1$ $-335.7$	$\pm 47.6$

Table 6.8: Extracted cross-sections for the electroproduction of  $D^{*\pm}$  mesons on the experimentally used target mixture. Listed are the values obtained for the different mass and mass difference cuts. The quoted statistical errors give the confidence intervals for a confidence level of 68.27%.

	Target Mixture			Proton			Isoscalar Target		
	$\sigma^{\text{mix}}$ (pb)	$\Delta\sigma_{\text{stat}}$ (pb)	$\Delta\sigma_{\text{stat}}^{\text{MC}}$ (pb)	$\sigma^p$ (pb)	$\Delta\sigma_{\text{stat}}$ (pb)	$\Delta\sigma_{\text{stat}}^{\text{MC}}$ (pb)	$\sigma^d$ (pb)	$\Delta\sigma_{\text{stat}}$ (pb)	$\Delta\sigma_{\text{stat}}^{\text{MC}}$ (pb)
$D^{*\pm}$	1068.5	$+488.0$ $-382.6$	$\pm 75.8$	964.6	$+440.6$ $-345.4$	$\pm 68.4$	1174.0	$+536.2$ $-420.4$	$\pm 83.3$
$D^{*-}$	671.9	$+388.3$ $-275.0$	$\pm 45.3$	576.6	$+333.2$ $-236.0$	$\pm 38.8$	768.7	$+444.2$ $-314.6$	$\pm 51.8$
$D^{*+}$	455.2	$+489.5$ $-269.6$	$\pm 37.4$	454.4	$+488.6$ $-269.1$	$\pm 37.3$	456.1	$+490.4$ $-270.1$	$\pm 37.4$

Table 6.9: Averaged cross-sections for the electroproduction of  $D^{*\pm}$  mesons on the experimentally used target mixture and the thereof derived cross-sections for scattering off protons and isoscalar targets. The quoted statistical errors give the confidence intervals for a confidence level of 68.27%.

	Proton			Isoscalar Target		
	$\sigma^{ep}$ (pb)	$\Delta\sigma_{stat}$ (pb)	$\Delta\sigma_{stat}^{MC}$ (pb)	$\sigma^{ed}$ (pb)	$\Delta\sigma_{stat}$ (pb)	$\Delta\sigma_{stat}^{MC}$ (pb)
$D^{*\pm}$	2285.5	$^{+1044.0}_{-818.4}$	$\pm 162.2$	2285.5	$^{+1043.9}_{-818.4}$	$\pm 162.5$
$D^{*-}$	2110.2	$^{+1219.4}_{-863.7}$	$\pm 142.1$	2110.0	$^{+1219.3}_{-863.5}$	$\pm 142.3$
$D^{*+}$	3053.6	$^{+3283.5}_{-1808.4}$	$\pm 250.8$	3053.8	$^{+3283.4}_{-1808.4}$	$\pm 250.7$

Table 6.10: Total cross-section  $\sigma^{ep \rightarrow c\bar{c}X}$  for the electroproduction of open charm. The quoted statistical errors give the confidence intervals for a confidence level of 68.27%. The results for the isoscalar target are only presented to show the internal consistency of the extracted results.

and the centre of mass energy available in the scattering process. For HERMES energies, they are determined with the help of the Monte Carlo to

$$\begin{aligned} \text{BR}(p; c \rightarrow D^{*+}) &= 14.88\% , & \text{BR}(n; c \rightarrow D^{*+}) &= 14.99\% , \\ \text{BR}(p; \bar{c} \rightarrow D^{*-}) &= 27.32\% , & \text{BR}(n; \bar{c} \rightarrow D^{*-}) &= 45.54\% . \end{aligned} \quad (6.16)$$

The thus obtained total cross-section  $\sigma^{ep \rightarrow c\bar{c}X}$  for the production of open charm in electron-proton scattering at HERMES with a centre of mass energy of 7.26 GeV is shown in Tab. 6.10.

### 6.3.6 Open Charm Photoproduction Cross-section

While other leptonproduction measurements are available only for much higher beam energies [EMC:83a], in the same kinematical regime experiments utilising real photon beams have been performed (see Fig. 3.1). Before a direct comparison with these results is possible, the measured total electroproduction cross-section has to be converted into a photoproduction cross-section using the formalism described at the end of Sec. 3.1.1. Combining Eqs. 3.8 - 3.10, the relation between the two cross-sections is given by

$$\frac{d\sigma^{ep}}{dQ^2 d\nu}(Q^2, \nu) = \Gamma(Q^2, \nu) \left(1 + \frac{Q^2}{M_0^2}\right)^{-2} \sigma^{\gamma p}(\nu), \quad (6.17)$$

$$\equiv \tilde{\Gamma}(Q^2, \nu) \sigma^{\gamma p}(\nu), \quad (6.18)$$

where the modified propagator term from the extrapolation of the virtual photon cross-section  $\sigma_T^{\gamma^*p}(Q^2, \nu)$  to the photoproduction cross-section  $\sigma^{\gamma p}(\nu)$  has been combined with the virtual photon flux  $\Gamma(Q^2, \nu)$  for brevity. As a reminder,  $Q^2$  is the negative square of the four-momentum carried by the virtual photon in the scattering process while  $\nu$  gives in the laboratory frame the energy of the virtual photon (see also Tab. A.1 for the definitions of the kinematical variables).

At HERMES, only the total electroproduction cross-section is accessible experimentally. Thus Eq. 6.18 has to be integrated over  $Q^2$  and  $\nu$

$$\sigma^{ep} = \int d\nu \int dQ^2 \tilde{\Gamma}(Q^2, \nu) \sigma^{\gamma p}(\nu). \quad (6.19)$$

As the exact energy dependence of the photoproduction cross-section  $\sigma^{\gamma p}(\nu)$  is not known near threshold, this relation has been expanded through the introduction of an arbitrary energy scale  $\nu_0$

$$\sigma^{ep} = \Phi \sigma^{\gamma p}(\nu_0) + \int d\nu \int dQ^2 \tilde{\Gamma}(Q^2, \nu) [\sigma^{\gamma p}(\nu) - \sigma^{\gamma p}(\nu_0)], \quad (6.20)$$

where additionally the abbreviation  $\Phi = \int d\nu \int dQ^2 \tilde{\Gamma}(Q^2, \nu)$  for the integrated flux has been used. When choosing the energy scale  $\nu_0$  such that the last term in Eq. 6.20 vanishes, a simple relation is obtained between the photoproduction and electroproduction cross-sections

$$\sigma^{\gamma p}(\nu_0) = \frac{\sigma^{ep}}{\Phi}. \quad (6.21)$$

Under the assumption of a linear energy dependence for  $\sigma^{\gamma p}(\nu)$  near threshold,  $\nu_0$  is given by the flux weighted average energy

$$\nu_0^{lin} = \langle \nu \rangle = \frac{1}{\Phi} \int d\nu \int dQ^2 \tilde{\Gamma}(Q^2, \nu) \nu. \quad (6.22)$$

The integration limits, which have been suppressed in all previous expressions for brevity, have to be determined for the special case of the open charm production before the integrated flux  $\Phi$  and the flux weighted average energy  $\langle \nu \rangle$  can be evaluated numerically. While the maximal possible energy transfer is determined by the beam energy ( $\nu_{max} = E - m_e$ ), the lower limit on the energy transfer is given by the constraint that the four-momentum transfer in the scattering process has to be large enough to allow the creation of a final state containing charmed hadrons. Since for lepton-proton scattering the charmed final state with the lowest invariant mass is given by  $\Lambda_c + \overline{D}^0$ ,  $\nu_{min}$  evaluates to

$$W^2 \geq (M_{\Lambda_c} + M_{\overline{D}^0})^2 \Rightarrow \nu_{min} = \frac{(M_{\Lambda_c} + M_{\overline{D}^0})^2 - M_p^2}{2M_p}. \quad (6.23)$$

The same constraint can be used to determine the upper limit for the  $Q^2$  integration at a fixed value of  $\nu$

$$Q_{max}^2 = 2M_p (\nu - \nu_{min}). \quad (6.24)$$

The kinematical lower limit  $Q_{min}^2$  can be derived from the definitions of  $Q^2 = -(\mathbf{k} - \mathbf{k}')^2$  and the relative energy transfer in the laboratory frame  $y \stackrel{Lab}{=} \nu/E$

$$Q_{min}^2 = -2m_e^2 + 2E^2(1 - y - \beta\beta_y), \quad (6.25)$$

where  $\beta = \sqrt{1 - \frac{m_e^2}{E^2}}$  and  $\beta_y = \sqrt{(1 - y)^2 - \frac{m_e^2}{E^2}}$ .

Evaluating the integrals for the integrated flux  $\Phi$  and the flux weighted average energy  $\langle \nu \rangle$  numerically, one obtains the results

$$\Phi = 0.0260 \pm 0.0013, \quad (6.26)$$

$$\langle \nu \rangle = 15.5 \pm 1.0 \text{ GeV}. \quad (6.27)$$

While the quoted error for  $\Phi$  is due to the uncertainties related to the longitudinal component of the photon flux and the mass scale  $M_0$ , the error on  $\langle\nu\rangle$  is given by a crude estimate of any non-linearities in the energy dependence of the photoproduction cross-section near threshold.

Together with the electroproduction cross-section from the  $D^{*\pm}$  channel (Tab. 6.10), one obtains for the total open charm photoproduction cross-section  $\sigma^{\gamma p \rightarrow c\bar{c}X}$

$$\sigma^{\gamma p \rightarrow c\bar{c}X} = \left( 87.9^{+40.2}_{-31.5 \text{ stat}} \pm 6.2_{\text{stat/MC}} \right) \text{ nb},$$

where the quoted statistical errors give the confidence intervals for a confidence level of 68.27%.

## 6.4 Monte Carlo Dependences

The Monte Carlo simulations are an important tool in the extraction of the cross-sections presented in the previous sections. It is therefore inevitable to quantify how much the obtained results depend on the assumptions made in the simulations. While the detector effects of the HERMES spectrometer and their implementation in the Monte Carlo are understood to better than 5%, not much is known about the details of the fragmentation process for the production of charm quarks near threshold. As was shown in Sec. 3.2.1, both the production probabilities and the energy spectra of the charmed mesons depend on the Monte Carlo fragmentation model. Since the determination of the correction functions relies on a more or less exact description of these quantities, the impact of the fragmentation model on the  $D^{*\pm}$  cross-section analysis will be discussed in the following.

The differential detection efficiencies  $\epsilon(E)$  as a function of the charmed meson energy are independent of the fragmentation model since they only describe the acceptance and detector effects of the HERMES spectrometer. The determination of the integrated efficiencies  $\langle\epsilon\rangle$  introduced in Eq. 6.6 however requires an exact description of the energy dependence of the  $D^{*\pm}$  production cross-sections. Despite this requirement, all investigated fragmentation sets result into similar integrated efficiencies for the production on proton and neutron targets. However, the extrapolation from the experimentally accessible energies above 10 GeV to the full range introduces a rather large correction (Tab. 6.6). Thus it is worth to study the impact of the fragmentation model separately for the two energy ranges. The cross-sections for both energy ranges and the different fragmentation sets are shown in the appendix in Tab. C.1. For the  $D^{*-}$  mesons, almost no dependence on the fragmentation function for the charm quarks is observed. Nevertheless, differences of up to 10% in the experimentally accessible and 20% in the full energy range occur when changing the parameter set used for the LUND symmetric fragmentation function for the light quarks. Larger dependences are also seen for the  $D^{*+}$  mesons. Especially when using the LUND symmetric fragmentation function with the HERMES parameter set for all quark flavours, significantly different cross-sections are extracted. This rather soft fragmentation however is not believed to give a realistic description since the need for a harder fragmentation of the charm quarks is experimentally well established. This model will therefore not be considered in the following. It is worth mentioning that the fragmentation dependences for the  $D^{*+}$  and  $D^{*-}$  meson cross-sections have partially opposite behaviour, resulting in smaller dependences of 5% in the measured and 10% in the full energy range for the combined  $D^{*\pm}$  cross-section.

For the open charm cross-section as extracted from both the  $D^{*\pm}$  and  $D^{*-}$  signals (Tab. C.2), dependences of up to 20% are found, again mainly due to the fragmentation uncertainties of the light quarks. The dependence on the description of the heavy quark fragmentation is less than 5%. The corrections for the experimentally accessible  $D^*$  energies above 10 GeV and the extrapolation to the full energy range contribute about equally to this systematic uncertainty.

## 6.5 Experimental Systematic Uncertainties

Besides the already discussed dependence of the extracted cross-sections on the Monte Carlo simulations, also the experimentally measured quantities used in cross-section determination are subject to systematic uncertainties. The only relevant contributions are those associated with the determination of the effective luminosity and the impact of the event selection criteria on the reconstructed signal. For the measurement of the absolute luminosity, the systematic uncertainty has been determined to 6.4% (Sec. 4.3.3, [Ben:98a]). A uncertainty of 3% has been attributed to both the determination of the trigger efficiencies [Mei:00] and the determination of the track finding efficiencies.

The possibilities to evaluate the uncertainty of the cross-section measurement due to the event selection criteria with systematic studies are limited. Because of the small statistics in the signals which are integer numbers, no smooth behaviour can be expected when varying the event selection criteria. All cut values have been chosen independently from the analysed data itself but rather been motivated by Monte Carlo simulations and studies of inclusive track samples. The spectra for all quantities which are used in the event selection have been investigated and it has been ensured that the distributions show no conspicuous behaviour. Most of the cuts can be varied over a rather large range without changing the extracted signals at all and some of them are even redundant. As an example, the reconstructed vertices for the  $D^*$  and  $D^0$  candidates are strongly correlated and it is in principle sufficient to ensure that the  $D^*$  vertex is located in the target cell. For the background estimates, the application of the cuts and their variations do cause differences which are however completely negligible compared to the statistical errors of the signals.

Besides the variation of the cuts, several further studies were performed from which only two will be mentioned here. The Monte Carlo simulations predicted a small shift in the expectation value for the reconstructed mass difference compared to the true value. The extracted cross-sections are insensitive to the application of this shift.

In order to increase the statistics, it has also been tried to release the momentum requirements on the kaon and pion candidates. The minimal momentum accepted was lowered to 2 GeV for one or both particles. The Monte Carlo simulations predict an increase in the signal of about 40% for each particle. Before the background subtraction, gains in the signals of this order are observed. However, a comparable increase also occurs in the background estimates resulting in gains of only  $\approx 10\%$ . The results are more consistent with a constant signal than the Monte Carlo expectation but due to the low statistics there is no indication of an inconsistency.

A total systematic uncertainty of 9% is obtained when adding all contributions quadratically. In this number, the contribution of a possibly imperfect detector descriptions in the Monte Carlo has been included but not the dependency on the fragmentation model.



## 7 Summary

The total cross-section  $\sigma^{ep \rightarrow D^{*-} X}$  for the electroproduction of  $D^{*-}$  mesons on a proton target and the sum of the total cross-sections for  $D^{*+}$  and  $D^{*-}$  mesons have been measured in a fixed target experiment with a lepton beam energy of 27.5 GeV to be

$$\begin{aligned}\sigma^{ep \rightarrow D^{*-} X} &= \left(0.58^{+0.34}_{-0.24} \text{ stat} \pm 0.05_{\text{syst/exp}} \pm 0.12_{\text{syst/frag}}\right) \text{ nb} , \\ \sigma^{ep \rightarrow D^{*\pm} X} &= \left(0.96^{+0.45}_{-0.35} \text{ stat} \pm 0.09_{\text{syst/exp}} \pm 0.10_{\text{syst/frag}}\right) \text{ nb} .\end{aligned}\quad (7.1)$$

From the  $D^{*\pm}$  measurement, the open charm electroproduction cross-section has been determined to

$$\sigma^{ep \rightarrow c\bar{c} X} = \left(2.29^{+1.06}_{-0.83} \text{ stat} \pm 0.21_{\text{syst/exp}} \pm 0.46_{\text{syst/frag}}\right) \text{ nb} .$$

These results represent the first measurements for open charm in leptonproduction near the charm threshold. While other leptonproduction measurements are available for much higher beam energies [EMC:83a], in the same kinematical regime only experiments utilising real photon beams have been performed. To allow a comparison with these measurements, the electroproduction cross-section has been converted into a total open charm photoproduction cross-section for a photon energy of  $E_\gamma = (15.5 \pm 1.0) \text{ GeV}$

$$\sigma^{\gamma p \rightarrow c\bar{c} X} = \left(87.9^{+40.7}_{-32.1} \text{ stat} \pm 9.2_{\text{syst/exp}} \pm 17.6_{\text{syst/frag}}\right) \text{ nb} .$$

As the detection efficiency and the acceptance of the HERMES spectrometer does depend on the charm quark mass assumed in the simulation, the cross section has been reevaluated for a charm quark mass of 1.5 GeV (as assumed in the analysis of the earlier experiments). This resulted into an about 10% small cross-section compared to the value given above which was determined under the assumption of a charm quark mass of 1.35 GeV. The corrected cross-section

$$\sigma^{\gamma p \rightarrow c\bar{c} X} = \left(79.9^{+37.0}_{-29.2} \text{ stat} \pm 8.4_{\text{syst/exp}} \pm 16.0_{\text{syst/frag}}\right) \text{ nb}$$

is shown in Fig. 7.1 in comparison to other open and hidden charm photoproduction cross section measurements. Good agreement with the previous experiment from SLAC at  $E_\gamma = 20 \text{ GeV}$  ([A<sup>+</sup>:86]) is observed. The dashed curve in Fig. 7.1 shows the LO charm photoproduction cross section as given by the AROMA Monte Carlo generator. The upper solid curve is the same prediction multiplied by a  $K$ -factor of 2.3 obtained from a fit to the high energy data. The fact that this curve describes all the data very well seems to indicate that higher order corrections in

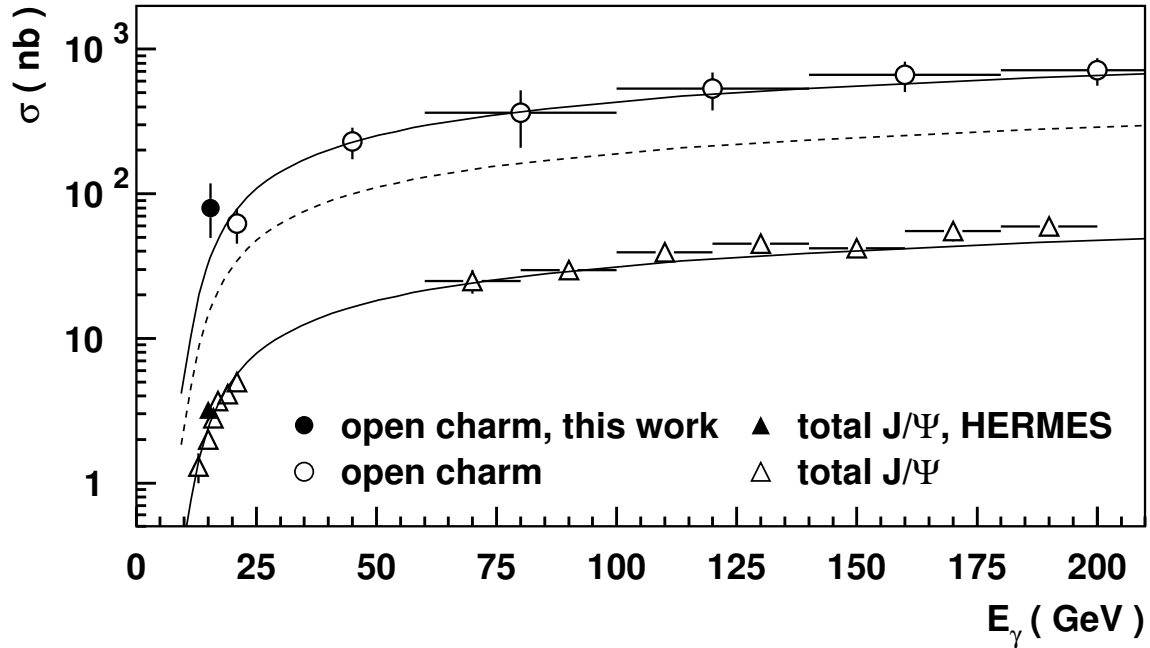


Figure 7.1: Cross-sections for the photoproduction of charm quark pairs as a function of the photon energy  $E_\gamma$  separately for particles with open and hidden charm. Shown are data from EMC [EMC:83a, EMC:83b], SLAC [ $A^+$ :86,  $C^+$ :75a], PEC [ $A^+$ :87], HERMES [Mei:00], and this work with statistical and systematical errors added in quadrature. The dashed curve is a LO prediction from AROMA for the open charm photoproduction cross-section using a charm quark mass of  $m_c = 1.5$  GeV. The upper solid line shows the same prediction multiplied by a fudge factor of 2.3 obtained in a fit to all open charm data but the one of this analysis. Similarly, the lower solid line is a result of a fit to all  $J/\Psi$  data, yielding a fudge factor of 0.165.

the photoproduction of open charm are rather independent of the photon energy. It furthermore indicates that the mass of the charm quark is not too different from 1.5 GeV. Finally, Fig. 7.1 also shows that the ratio of hidden to open charm photoproduction does not significantly depend on the photon energy.

While the present analysis is mainly limited by the small statistics in the investigated  $D^{*\pm}$  decay channels, an increase in statistics by a factor 3 can be expected from the very successful data taking of HERMES in the years 1998-2000. Additionally, for these new data, new kinematical regimes for the  $D^{*\pm}$  mesons can be exploited; in 1998 the threshold Čerenkov detector has been replaced by a Ring Imaging Čerenkov detector (RICH), which allows the identification of pions, kaons and protons over almost the entire kinematical range of the experiment. With these improvements it should be possible to get access to the  $D^{*\pm}$  energy distributions and gain additional information about the complex fragmentation process of charmed quarks near the charm production threshold. An indication for the differences in the production of charmed meson-anti-meson pairs and the associated charmed baryon-anti-meson production has already been observed through the rather different numbers of reconstructed  $D^{*+}$  and  $D^{*-}$  decays.

## Appendix A

### Definition of DIS kinematics

Basic Observables		
Variable	Description	
$\mathbf{k} = \begin{pmatrix} E \\ \vec{k} \end{pmatrix}$	Beam energy $E$ and momentum of incident lepton $\vec{k}$	
$\mathbf{k}' = \begin{pmatrix} E' \\ \vec{k}' \end{pmatrix}$	Energy $E'$ and momentum $\vec{k}'$ of scattered lepton	
$\mathbf{P} \stackrel{Lab}{=} \begin{pmatrix} M \\ \vec{0} \end{pmatrix}$	Nucleon mass $M$	
$\mathbf{P}_h = \begin{pmatrix} E_h \\ \vec{p}_h \end{pmatrix}$	Energy $E_h$ and momentum $\vec{p}_h$ of semi-inclusive hadron	

Derived Quantities		
Variable	Definition	Description
$\theta$	$\angle(\vec{k}', \vec{k})$	Scattering angle of lepton
$\mathbf{q}$	$\mathbf{k} - \mathbf{k}'$	Four-momentum of virtual photon
$Q^2$	$-\mathbf{q}^2 \stackrel{Lab}{=} 4EE' \sin^2(\theta/2)$	Negative square of four-momentum transfer
$s$	$(\mathbf{k} + \mathbf{P})^2 \stackrel{Lab}{=} M^2 + 2EM$	Squared centre of mass energy
$\nu$	$(\mathbf{P} \cdot \mathbf{q}) / M \stackrel{Lab}{=} E - E'$	Absolute energy transfer in the laboratory frame
$x$	$-\mathbf{q}^2 / (2 \mathbf{P} \cdot \mathbf{q}) = Q^2 / (2 M \nu)$	Bjorken's scaling variable
$y$	$\mathbf{P} \cdot \mathbf{q} / \mathbf{P} \cdot \mathbf{k} \stackrel{Lab}{=} \nu / E$	Relative energy transfer in the laboratory frame
$W^2$	$(\mathbf{P} + \mathbf{q})^2 = M^2 + 2 M \nu - Q^2$	Squared invariant mass of hadronic final state
$z$	$\mathbf{P} \cdot \mathbf{P}_h / \mathbf{P} \cdot \mathbf{q} \stackrel{Lab}{=} E_h / \nu$	Fractional energy of hadron in the laboratory frame
$\vec{p}_{  }$ $\vec{p}_T$	$(\vec{p}_h \cdot \hat{n}_q) \hat{n}_q$ $\vec{p}_h - \vec{p}_{  }$	Parallel and transverse momentum of hadron wrt. $\mathbf{q}$ in $\gamma N$ rest frame
$x_F$	$2\sqrt{\vec{p}_{  } \cdot \vec{p}_{  }} W^2 / (W^2 - \mathbf{p}_h \cdot \mathbf{p}_h)$	Feynman's scaling variable

Table A.1: Definition of kinematical variables in deep-inelastic scattering. Formulas only valid in the laboratory frame also neglect the squared lepton mass  $m^2$ .

## Appendix B

### Charm Production: Model Dependences

#### B.1 Production Probabilities of Primary Charmed Particles

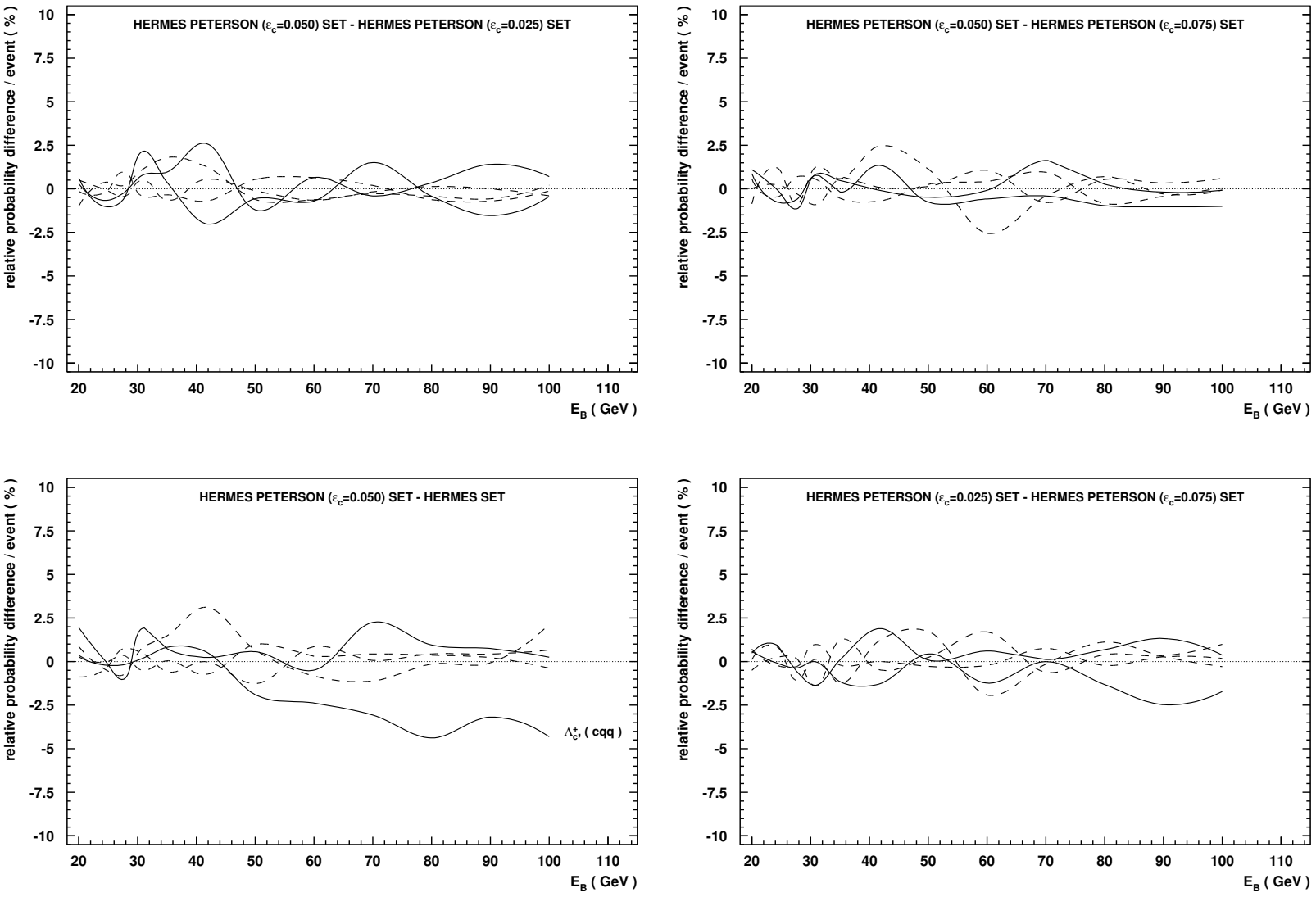


Figure B.1: Differences in the production probabilities of primarily produced charmed particles per open charm event for various fragmentation models and functions. Shown are only the results for open charm mesons and baryons; anti-baryons have been neglected since due to the small absolute probabilities large relative deviations are possible.

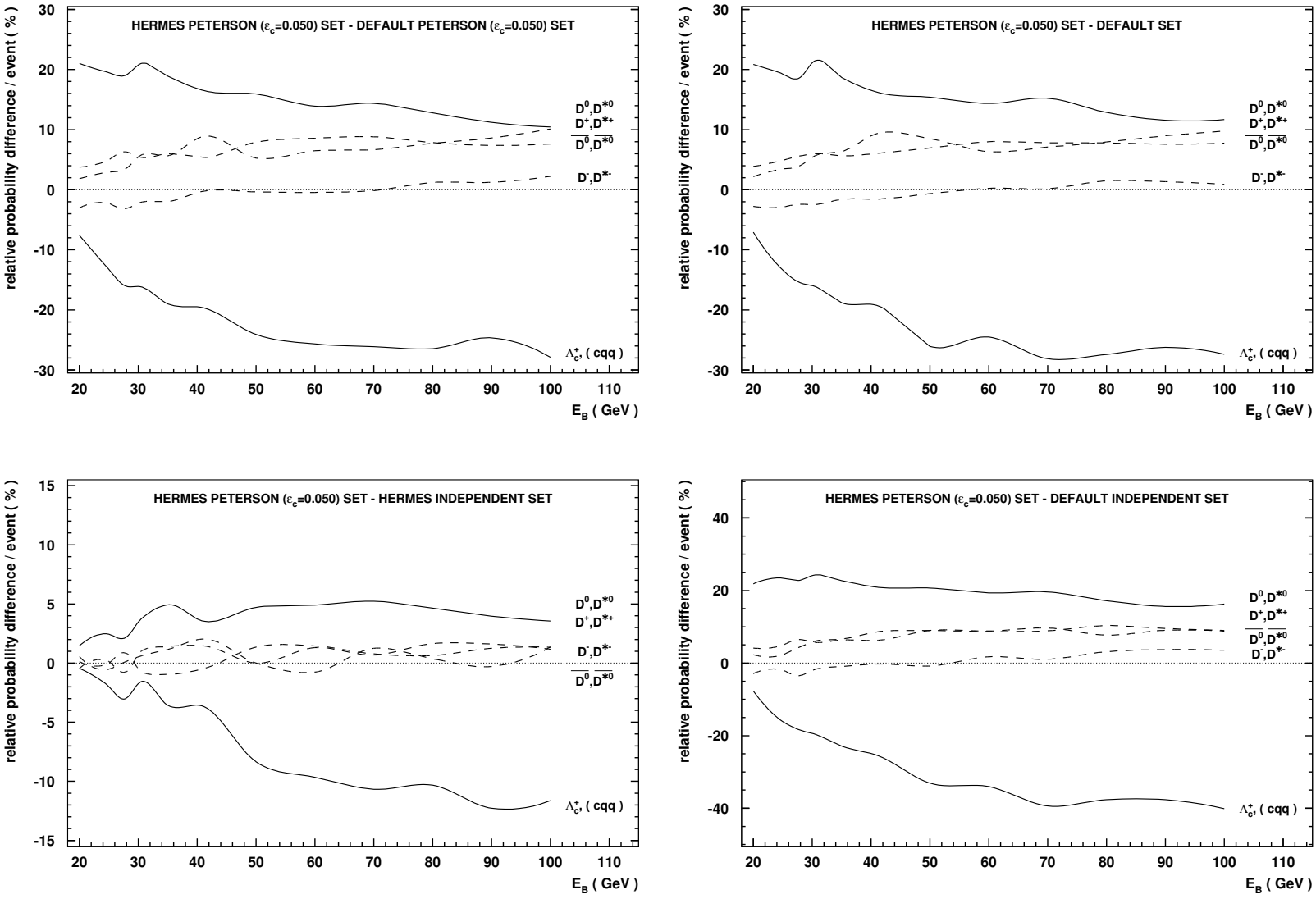


Figure B.2: Differences in the production probabilities of primarily produced charmed particles per open charm event for various fragmentation models and functions (cnt'd).

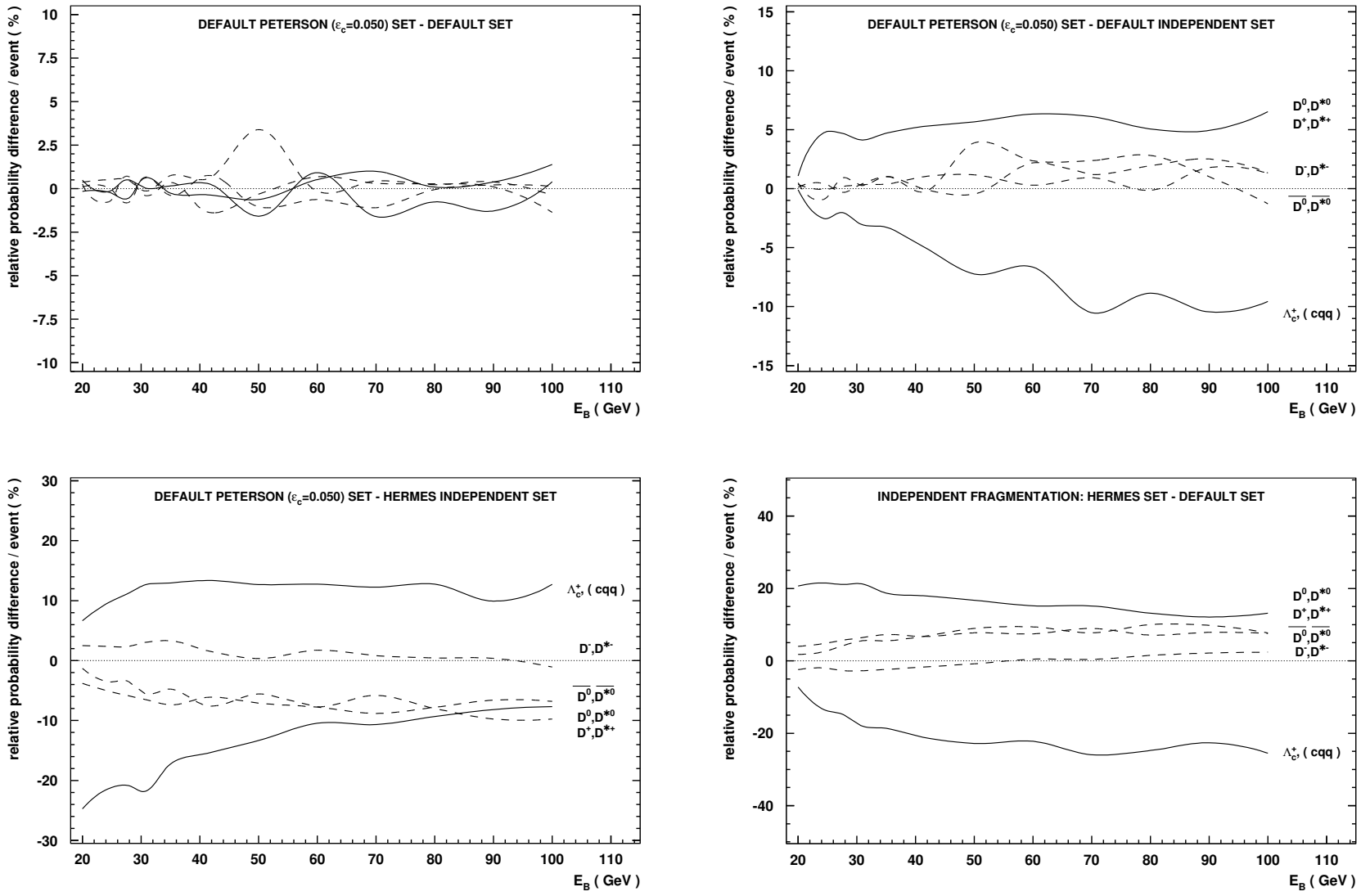


Figure B.3: Differences in the production probabilities of primarily produced charmed particles per open charm event for various fragmentation models and functions (cnt'd).



## B.2 Energy Spectra

Fragmentation Model	Fragmentation Function Set		Charmed Partner								
			Meson			Baryon			Meson or Baryon		
			$p$ (%)	$\langle E \rangle$ ( GeV)	$\sigma$ ( GeV)	$p$ (%)	$\langle E \rangle$ ( GeV)	$\sigma$ ( GeV)	$p$ (%)	$\langle E \rangle$ ( GeV)	$\sigma$ ( GeV)
LUND string	HERMES, Peterson $\epsilon_c = 0.025$	$(\bar{c}X)$	44.69	9.83	3.51	55.31	9.83	4.20	100.00	9.83	3.90
		$(cX)$	99.79	7.90	3.10	0.21	–	–	100.00	7.90	3.10
		all	144.47	8.50	3.36	55.53	9.83	4.19	200.00	8.87	3.66
LUND string	HERMES, Peterson $\epsilon_c = 0.050$	$(\bar{c}X)$	44.73	9.83	3.51	55.27	9.80	4.17	100.00	9.82	3.89
		$(cX)$	99.78	7.78	2.98	0.22	–	–	100.00	7.78	2.98
		all	144.51	8.42	3.29	55.49	9.80	4.17	200.00	8.80	3.61
LUND string	HERMES, Peterson $\epsilon_c = 0.075$	$(\bar{c}X)$	44.71	9.83	3.51	55.29	9.78	4.16	100.00	9.80	3.89
		$(cX)$	99.78	7.72	2.92	0.22	–	–	100.00	7.72	2.92
		all	144.48	8.37	3.26	55.52	9.77	4.16	200.00	8.76	3.59
LUND string	HERMES	$(\bar{c}X)$	44.68	9.81	3.50	55.32	9.70	4.13	100.00	9.75	3.87
		$(cX)$	99.77	7.42	2.69	0.23	–	–	100.00	7.43	2.69
		all	144.45	8.16	3.16	55.55	9.70	4.13	200.00	8.59	3.53
LUND string	Default, Peterson $\epsilon_c = 0.050$	$(\bar{c}X)$	37.41	9.33	3.44	62.59	9.23	3.96	100.00	9.27	3.77
		$(cX)$	99.57	8.27	3.19	0.43	–	–	100.00	8.28	3.19
		all	136.98	8.56	3.30	63.02	9.23	3.95	200.00	8.77	3.53
LUND string	Default	$(\bar{c}X)$	37.50	9.34	3.44	62.50	9.24	3.97	100.00	9.27	3.78
		$(cX)$	99.58	8.27	3.20	0.42	–	–	100.00	8.27	3.19
		all	137.08	8.56	3.30	62.92	9.23	3.96	200.00	8.77	3.54
Independent	HERMES	$(\bar{c}X)$	43.49	9.78	3.49	56.51	9.71	4.10	100.00	9.74	3.85
		$(cX)$	99.70	7.82	3.08	0.30	–	–	100.00	7.82	3.08
		all	143.19	8.42	3.34	56.81	9.70	4.09	200.00	8.78	3.61
Independent	Default	$(\bar{c}X)$	36.22	9.28	3.41	63.78	9.15	3.90	100.00	9.20	3.73
		$(cX)$	99.46	8.35	3.31	0.54	–	–	100.00	8.35	3.31
		all	135.68	8.60	3.36	64.32	9.15	3.89	200.00	8.77	3.55

Table B.1: Fragmentation model dependences in the production of charmed hadrons. Listed are the production probabilities  $p$  and the mean  $\langle E \rangle$  and variance  $\sigma^2$  of the energy spectra.

			Charmed Partner								
			Meson			Baryon			Meson or Baryon		
Fragmentation Model	Fragmentation Function Set		$p$ (%)	$\langle E \rangle$ ( GeV)	$\sigma$ ( GeV)	$p$ (%)	$\langle E \rangle$ ( GeV)	$\sigma$ ( GeV)	$p$ (%)	$\langle E \rangle$ ( GeV)	$\sigma$ ( GeV)
LUND string	HERMES, Peterson $\epsilon_c = 0.025$	$D^{*-}$	10.32	9.87	3.31	16.97	9.99	4.13	27.29	9.94	3.84
		$D^{*+}$	14.84	9.33	3.35	0.01	–	–	14.85	9.33	3.35
		$D^{*\pm}$	25.15	9.55	3.35	16.98	9.99	4.13	42.13	9.73	3.69
LUND string	HERMES, Peterson $\epsilon_c = 0.050$	$D^{*-}$	10.38	9.87	3.31	16.95	9.96	4.11	27.32	9.92	3.83
		$D^{*+}$	14.87	9.03	3.19	0.01	–	–	14.88	9.03	3.19
		$D^{*\pm}$	25.25	9.38	3.27	16.96	9.96	4.11	42.20	9.61	3.64
LUND string	HERMES, Peterson $\epsilon_c = 0.075$	$D^{*-}$	10.36	9.86	3.32	16.98	9.92	4.09	27.34	9.90	3.82
		$D^{*+}$	14.82	8.87	3.10	0.01	–	–	14.83	8.87	3.10
		$D^{*\pm}$	25.17	9.28	3.23	16.99	9.92	4.09	42.17	9.54	3.61
LUND string	HERMES	$D^{*-}$	10.34	9.84	3.30	16.91	9.83	4.07	27.25	9.84	3.79
		$D^{*+}$	14.86	8.20	2.80	0.01	–	–	14.87	8.20	2.80
		$D^{*\pm}$	25.19	8.87	3.12	16.92	9.83	4.07	42.11	9.26	3.56
LUND string	Default, Peterson $\epsilon_c = 0.050$	$D^{*-}$	8.85	9.43	3.26	19.09	9.38	3.91	27.94	9.39	3.71
		$D^{*+}$	11.84	9.31	3.31	0.01	–	–	11.85	9.31	3.31
		$D^{*\pm}$	20.68	9.36	3.29	19.10	9.38	3.91	39.79	9.37	3.60
LUND string	Default	$D^{*-}$	8.89	9.45	3.27	19.08	9.37	3.91	27.96	9.40	3.72
		$D^{*+}$	11.82	9.30	3.30	0.01	–	–	11.83	9.30	3.30
		$D^{*\pm}$	20.71	9.37	3.29	19.09	9.37	3.91	39.80	9.37	3.60
Independent	HERMES	$D^{*-}$	9.99	9.78	3.28	17.24	9.85	4.04	27.23	9.83	3.78
		$D^{*+}$	14.31	9.06	3.37	0.02	–	–	14.34	9.06	3.37
		$D^{*\pm}$	24.30	9.36	3.35	17.27	9.85	4.04	41.57	9.56	3.66
Independent	Default	$D^{*-}$	8.52	9.37	3.21	19.33	9.28	3.85	27.85	9.31	3.67
		$D^{*+}$	11.34	9.43	3.55	0.02	–	–	11.37	9.43	3.54
		$D^{*\pm}$	19.87	9.40	3.41	19.35	9.28	3.85	39.22	9.34	3.63

Table B.2: Fragmentation model dependences in the production of  $D^{*\pm}$  mesons. Listed are the production probabilities  $p$  and the mean  $\langle E \rangle$  and variance  $\sigma^2$  of the energy spectra.

Fragmentation Model	Fragmentation Function Set		Charmed Partner								
			Meson			Baryon			Meson or Baryon		
			$p$ (%)	$\langle E \rangle$ ( GeV)	$\sigma$ ( GeV)	$p$ (%)	$\langle E \rangle$ ( GeV)	$\sigma$ ( GeV)	$p$ (%)	$\langle E \rangle$ ( GeV)	$\sigma$ ( GeV)
LUND string	HERMES, Peterson $\epsilon_c = 0.025$	$\bar{D}^{*0}$	22.34	9.90	3.56	23.11	9.77	4.21	45.45	9.84	3.90
		$D^{*0}$	15.04	9.22	3.34	0.01	–	–	15.05	9.22	3.34
		$(\gamma)D^{*0}$	37.38	9.63	3.49	23.12	9.77	4.21	60.50	9.68	3.78
LUND string	HERMES, Peterson $\epsilon_c = 0.050$	$\bar{D}^{*0}$	22.44	9.89	3.56	23.10	9.75	4.19	45.54	9.82	3.89
		$D^{*0}$	14.98	8.96	3.17	0.01	–	–	14.99	8.96	3.17
		$(\gamma)D^{*0}$	37.42	9.52	3.44	23.11	9.75	4.19	60.53	9.61	3.74
LUND string	HERMES, Peterson $\epsilon_c = 0.075$	$\bar{D}^{*0}$	22.39	9.90	3.56	23.08	9.73	4.18	45.47	9.81	3.89
		$D^{*0}$	15.00	8.80	3.08	0.01	–	–	15.01	8.80	3.08
		$(\gamma)D^{*0}$	37.39	9.45	3.42	23.09	9.73	4.18	60.48	9.56	3.73
LUND string	HERMES	$\bar{D}^{*0}$	22.42	9.89	3.56	23.15	9.68	4.15	45.57	9.78	3.87
		$D^{*0}$	14.93	8.15	2.77	0.01	–	–	14.93	8.15	2.77
		$(\gamma)D^{*0}$	37.35	9.20	3.38	23.15	9.68	4.15	60.50	9.38	3.70
LUND string	Default, Peterson $\epsilon_c = 0.050$	$\bar{D}^{*0}$	18.21	9.36	3.48	24.95	9.11	3.96	43.15	9.22	3.77
		$D^{*0}$	11.96	9.23	3.29	0.01	–	–	11.97	9.23	3.29
		$(\gamma)D^{*0}$	30.17	9.31	3.40	24.96	9.11	3.96	55.12	9.22	3.67
LUND string	Default	$\bar{D}^{*0}$	18.25	9.36	3.48	24.93	9.13	3.98	43.18	9.22	3.78
		$D^{*0}$	11.94	9.24	3.29	0.01	–	–	11.95	9.24	3.29
		$(\gamma)D^{*0}$	30.19	9.31	3.41	24.94	9.13	3.98	55.14	9.23	3.68
Independent	HERMES	$\bar{D}^{*0}$	21.83	9.87	3.55	23.64	9.67	4.11	45.47	9.77	3.85
		$D^{*0}$	14.58	8.96	3.33	0.02	–	–	14.60	8.96	3.32
		$(\gamma)D^{*0}$	36.41	9.51	3.49	23.66	9.67	4.11	60.07	9.57	3.75
Independent	Default	$\bar{D}^{*0}$	17.65	9.33	3.48	25.52	9.05	3.92	43.17	9.16	3.75
		$D^{*0}$	11.56	9.31	3.47	0.02	–	–	11.58	9.31	3.47
		$(\gamma)D^{*0}$	29.21	9.32	3.48	25.54	9.05	3.92	54.75	9.19	3.69

Table B.3: Fragmentation model dependences in the production of  $D^{*0}$  mesons. Listed are the production probabilities  $p$  and the mean  $\langle E \rangle$  and variance  $\sigma^2$  of the energy spectra.

Fragmentation Model	Fragmentation Function Set		Charmed Partner								
			Meson			Baryon			Meson or Baryon		
			$p$ (%)	$\langle E \rangle$ ( GeV)	$\sigma$ ( GeV)	$p$ (%)	$\langle E \rangle$ ( GeV)	$\sigma$ ( GeV)	$p$ (%)	$\langle E \rangle$ ( GeV)	$\sigma$ ( GeV)
LUND string	HERMES, Peterson $\epsilon_c = 0.025$	$D^{*-}$	4.50	12.97	2.28	7.31	13.90	3.00	11.81	13.55	2.78
		$D^{*+}$	5.95	12.66	2.16	0.00	–	–	5.95	12.66	2.16
		$D^{*\pm}$	10.46	12.79	2.21	7.31	13.90	3.00	17.76	13.25	2.62
LUND string	HERMES, Peterson $\epsilon_c = 0.050$	$D^{*-}$	4.54	12.96	2.27	7.21	13.89	3.02	11.75	13.53	2.79
		$D^{*+}$	5.35	12.48	2.05	0.00	–	–	5.35	12.48	2.05
		$D^{*\pm}$	9.90	12.70	2.17	7.21	13.88	3.02	17.11	13.20	2.63
LUND string	HERMES, Peterson $\epsilon_c = 0.075$	$D^{*-}$	4.50	12.98	2.28	7.18	13.86	3.00	11.68	13.52	2.78
		$D^{*+}$	4.99	12.37	1.99	0.00	–	–	5.00	12.37	1.99
		$D^{*\pm}$	9.49	12.66	2.15	7.18	13.86	3.00	16.68	13.18	2.62
LUND string	HERMES	$D^{*-}$	4.47	12.95	2.28	6.97	13.82	3.02	11.44	13.48	2.79
		$D^{*+}$	3.52	12.17	1.93	0.00	–	–	3.53	12.17	1.93
		$D^{*\pm}$	7.99	12.61	2.17	6.97	13.82	3.02	14.96	13.17	2.67
LUND string	Default, Peterson $\epsilon_c = 0.050$	$D^{*-}$	3.44	12.80	2.20	7.22	13.51	2.82	10.66	13.28	2.66
		$D^{*+}$	4.64	12.67	2.16	0.00	–	–	4.64	12.67	2.16
		$D^{*\pm}$	8.08	12.73	2.18	7.22	13.51	2.82	15.30	13.10	2.53
LUND string	Default	$D^{*-}$	3.49	12.82	2.21	7.19	13.52	2.82	10.68	13.29	2.66
		$D^{*+}$	4.56	12.68	2.21	0.00	–	–	4.56	12.68	2.21
		$D^{*\pm}$	8.04	12.74	2.21	7.20	13.52	2.82	15.24	13.11	2.55
Independent	HERMES	$D^{*-}$	4.22	12.93	2.27	7.17	13.80	2.98	11.39	13.48	2.77
		$D^{*+}$	5.03	12.79	2.31	0.01	–	–	5.04	12.79	2.31
		$D^{*\pm}$	9.26	12.85	2.29	7.17	13.80	2.98	16.43	13.27	2.66
Independent	Default	$D^{*-}$	3.22	12.77	2.19	7.04	13.48	2.81	10.26	13.25	2.65
		$D^{*+}$	4.45	13.04	2.46	0.01	–	–	4.46	13.03	2.46
		$D^{*\pm}$	7.67	12.92	2.36	7.05	13.48	2.81	14.72	13.19	2.60

Table B.4: Fragmentation model dependences in the production of  $D^{*\pm}$  mesons with energies above 10 GeV matching the acceptance of the HERMES spectrometer. Listed are the production probabilities  $p$  and the mean  $\langle E \rangle$  and variance  $\sigma^2$  of the energy spectra.

Fragmentation Model	Fragmentation Function Set		Charmed Partner								
			Meson			Baryon			Meson or Baryon		
			$p$ (%)	$\langle E \rangle$ ( GeV)	$\sigma$ ( GeV)	$p$ (%)	$\langle E \rangle$ ( GeV)	$\sigma$ ( GeV)	$p$ (%)	$\langle E \rangle$ ( GeV)	$\sigma$ ( GeV)
LUND string	HERMES, Peterson $\epsilon_c = 0.025$	$\bar{D}^{*0}$	9.66	13.25	2.54	9.36	13.99	3.11	19.02	13.62	2.86
		$D^{*0}$	5.85	12.63	2.14	0.00	–	–	5.86	12.63	2.14
		$(\prime)D^{*0}$	15.51	13.02	2.41	9.36	13.99	3.11	24.87	13.38	2.74
LUND string	HERMES, Peterson $\epsilon_c = 0.050$	$\bar{D}^{*0}$	9.68	13.24	2.53	9.31	13.96	3.11	18.99	13.59	2.85
		$D^{*0}$	5.26	12.46	2.02	0.00	–	–	5.26	12.46	2.02
		$(\prime)D^{*0}$	14.94	12.97	2.39	9.31	13.96	3.11	24.25	13.35	2.73
LUND string	HERMES, Peterson $\epsilon_c = 0.075$	$\bar{D}^{*0}$	9.65	13.25	2.54	9.24	13.95	3.11	18.89	13.60	2.85
		$D^{*0}$	4.92	12.36	1.98	0.00	–	–	4.92	12.36	1.98
		$(\prime)D^{*0}$	14.57	12.95	2.40	9.24	13.95	3.11	23.81	13.34	2.74
LUND string	HERMES	$\bar{D}^{*0}$	9.67	13.25	2.53	9.09	13.94	3.12	18.76	13.58	2.85
		$D^{*0}$	3.44	12.14	1.90	0.00	–	–	3.44	12.14	1.90
		$(\prime)D^{*0}$	13.11	12.96	2.43	9.09	13.94	3.12	22.20	13.36	2.77
LUND string	Default, Peterson $\epsilon_c = 0.050$	$\bar{D}^{*0}$	6.85	13.06	2.44	8.73	13.57	2.90	15.57	13.35	2.72
		$D^{*0}$	4.57	12.65	2.14	0.00	–	–	4.57	12.65	2.14
		$(\prime)D^{*0}$	11.41	12.90	2.33	8.73	13.57	2.90	20.14	13.19	2.62
LUND string	Default	$\bar{D}^{*0}$	6.84	13.07	2.44	8.75	13.61	2.92	15.59	13.37	2.74
		$D^{*0}$	4.50	12.68	2.22	0.00	–	–	4.50	12.68	2.22
		$(\prime)D^{*0}$	11.34	12.92	2.37	8.75	13.61	2.92	20.09	13.22	2.64
Independent	HERMES	$\bar{D}^{*0}$	9.34	13.24	2.53	9.35	13.86	3.07	18.69	13.55	2.83
		$D^{*0}$	4.91	12.76	2.29	0.01	–	–	4.91	12.76	2.29
		$(\prime)D^{*0}$	14.24	13.08	2.46	9.36	13.86	3.07	23.60	13.39	2.75
Independent	Default	$\bar{D}^{*0}$	6.53	13.07	2.45	8.73	13.54	2.88	15.26	13.34	2.72
		$D^{*0}$	4.36	12.96	2.41	0.01	–	–	4.37	12.95	2.41
		$(\prime)D^{*0}$	10.89	13.03	2.44	8.73	13.54	2.88	19.63	13.26	2.66

Table B.5: Fragmentation model dependences in the production of  $D^{*0}$  mesons with energies above 10 GeV matching the acceptance of the HERMES spectrometer. Listed are the production probabilities  $p$  and the mean  $\langle E \rangle$  and variance  $\sigma^2$  of the energy spectra.

## Appendix C

### Open Charm Cross-section: Model Dependences

#### C.1 $D^{*\pm}$ Cross-sections

Fragm. Set	$\sigma_{\text{exp}}^{\text{mix}} (\text{pb})$			$\sigma_{\text{exp}}^p (\text{pb})$			$\sigma_{\text{exp}}^d (\text{pb})$		
	$D^{*\pm}$	$D^{*-}$	$D^{*+}$	$D^{*\pm}$	$D^{*-}$	$D^{*+}$	$D^{*\pm}$	$D^{*-}$	$D^{*+}$
HERMES $\epsilon_c = 0.025$	423.4	282.9	148.2	382.1	242.8	147.7	465.4	323.6	148.7
HERMES $\epsilon_c = 0.050$	430.9	284.8	162.0	389.0	244.3	161.7	473.4	325.8	162.3
HERMES $\epsilon_c = 0.075$	433.8	285.1	171.2	391.6	244.8	170.7	476.7	326.0	171.8
HERMES	433.9	287.6	193.5	391.4	246.4	193.3	476.9	329.3	193.7
HERMES Independent	421.6	288.5	139.8	379.6	247.4	139.2	464.1	330.3	140.4
Default $\epsilon_c = 0.050$	447.2	306.1	147.1	408.2	269.7	146.7	486.9	343.1	147.5
Default	444.2	303.9	146.7	405.4	267.7	146.4	483.6	340.6	147.1
Default Independent	433.5	307.1	128.0	394.7	270.2	127.4	472.8	344.5	128.6

Fragm. Set	$\sigma^{\text{mix}} (\text{pb})$			$\sigma^p (\text{pb})$			$\sigma^d (\text{pb})$		
	$D^{*\pm}$	$D^{*-}$	$D^{*+}$	$D^{*\pm}$	$D^{*-}$	$D^{*+}$	$D^{*\pm}$	$D^{*-}$	$D^{*+}$
HERMES $\epsilon_c = 0.025$	1016.3	664.1	374.7	917.1	570.0	373.5	1117.0	759.7	376.0
HERMES $\epsilon_c = 0.050$	1068.5	671.9	455.2	964.6	576.6	454.4	1174.0	768.7	456.1
HERMES $\epsilon_c = 0.075$	1098.7	676.2	514.4	991.8	580.7	512.8	1207.2	773.2	516.0
HERMES	1199.8	691.4	825.6	1082.5	592.5	824.6	1318.9	791.7	826.5
HERMES Independent	1069.0	695.4	405.9	962.7	596.3	404.0	1177.0	796.0	407.7
Default $\epsilon_c = 0.050$	1192.0	824.1	380.0	1087.9	726.1	379.0	1297.6	923.7	381.0
Default	1188.3	817.7	384.8	1084.5	720.4	383.8	1293.6	916.5	385.7
Default Independent	1180.5	850.4	332.1	1074.9	748.4	330.5	1287.7	954.1	333.6

Table C.1: Fragmentation model dependences of the extracted cross-sections for the electro-production of  $D^{*\pm}$  mesons. While in the upper panel the cross-sections are given for the at HERMES experimentally accessible  $D^{*\pm}$  energy range, the total cross-sections extrapolated to the full energy range are contained in the lower panel.



Fragmentation Set	$\sigma^{ep \rightarrow c\bar{c}X}$		
	$D^{*\pm}$	$D^{*-}$	$D^{*+}$
HERMES $\epsilon_c = 0.025$	2176.8	2089.0	2515.9
HERMES $\epsilon_c = 0.050$	2285.5	2110.2	3053.6
HERMES $\epsilon_c = 0.075$	2352.2	2124.1	3458.7
HERMES	2570.5	2174.7	5546.5
HERMES Independent	2316.0	2189.8	2817.8
Default $\epsilon_c = 0.050$	2734.3	2598.9	3198.8
Default	2725.1	2576.3	3243.0
Default Independent	2740.6	2686.9	2907.3

Table C.2: *Fragmentation model dependences of the extracted cross-section for the production of open charm in lepton-proton scattering.*



# List of Figures

2.1	<i>Schematic diagram of deep-inelastic lepton-nucleon scattering.</i>	3
2.2	<i>Schematic picture of deep-inelastic lepton-nucleon scattering in the one-photon exchange approximation.</i>	5
2.3	<i>World data for the ratio of longitudinal and transverse photo-absorption cross-sections of free nucleons, <math>R(x, Q^2) = \sigma_L/\sigma_T</math>.</i>	9
2.4	<i>World data on the proton structure function <math>F_2^p</math> from fixed target experiments.</i>	9
2.5	<i>Definition of scattering angles in polarised DIS.</i>	11
2.6	<i>The virtual photon asymmetries <math>A_1</math> and <math>A_2</math>.</i>	12
2.7	<i>Deep-inelastic lepton-nucleon scattering in the parton model.</i>	14
2.8	<i>Elementary processes of QED and QCD.</i>	16
2.9	<i>The logarithmic slope <math>d \ln F_2 / d \ln Q^2</math> of the deuteron structure function.</i>	17
2.10	<i>Schematic diagrams for higher order QCD corrections and higher twist effects.</i>	19
2.11	<i>Schematic picture of semi-inclusive deep-inelastic lepton-nucleon scattering.</i>	19
2.12	<i>The <math>x</math>-dependence of the <math>F_2</math> structure function ratio for calcium and deuterium.</i>	23
2.13	<i>Ratios of cross-sections of inclusive deep-inelastic lepton scattering from nucleus <math>A</math> and <math>D</math> as a function of <math>x</math>.</i>	24
2.14	<i>The ratio <math>R^A/R^D</math> for nucleus <math>A</math> and <math>D</math> as a function of <math>Q^2</math>.</i>	24
2.15	<i>Time scales and interaction cross-section involved in the hadronisation process.</i>	26
2.16	<i>Nuclear suppression for copper in the gluon bremsstrahlungs model.</i>	27
3.1	<i>Cross-sections for the photoproduction of charm quark pairs as a function of the photon energy <math>E_\gamma</math>.</i>	30
3.2	<i>Feynman diagrams for the production of charm quarks through photon-gluon fusion including higher order corrections.</i>	31
3.3	<i>Total charm photoproduction cross-section as a function of the photon-nucleon centre of mass energy.</i>	32
3.4	<i>Total cross-section for the photoproduction of charm quark pairs as a function of the photon-nucleon centre of mass energy.</i>	34
3.5	<i>Gluon density in the proton extracted from charm electro- and photoproduction and comparison with indirect results from <math>F_2</math> scale breaking.</i>	37
3.6	<i>Peterson fragmentation function <math>D_c^H(z)</math> for different values of the phenomenological parameter <math>\epsilon_c</math>.</i>	37
3.7	<i>Charmed particle production probabilities per open charm event.</i>	40
3.8	<i>Production probabilities of primarily produced charmed particles per open charm event.</i>	41

3.9	<i>Comparison of the energy distributions for charmed particles and anti-particles on the quark and hadron level.</i>	43
3.10	<i>Comparison of the energy distributions for charmed hadrons and anti-hadrons depending on the multiplicity of primarily produced light hadrons in the final state.</i>	44
3.11	<i>Differences in the production probabilities of primarily produced charmed particles per open charm event for various fragmentation models and functions.</i>	45
4.1	<i>The electron storage ring of HERA at DESY.</i>	48
4.2	<i>Schematic side and top view of the HERMES spectrometer.</i>	49
4.3	<i>Schematic diagram of the HERMES target region.</i>	50
4.4	<i>Schematic diagram of the polarised hydrogen target used in 1996 and 1997.</i>	51
4.5	<i>Momentum and scattering angle resolutions in the HERMES spectrometer for the force-bridge method.</i>	54
4.6	<i>Integrated radiation length of the HERMES spectrometer.</i>	55
4.7	<i>Responses of the particle identification detectors for 1997 data.</i>	57
4.8	<i>PID parameters for all particle tracks from 1997 data.</i>	57
4.9	<i>Pion identification efficiency as a function of the pion momentum.</i>	58
4.10	<i>The Bhabha coincidence rate <math>R_L</math> for a typical fill during polarised data taking in 1997.</i>	60
4.11	<i>Offline data production scheme.</i>	64
5.1	<i>Permutated plane efficiencies for forward and backward partial tracks.</i>	69
5.2	<i>Permutated plane efficiencies of full tracks for electrons and hadrons.</i>	69
5.3	<i>DIS trigger efficiency as a function of the positron momentum.</i>	70
5.4	<i>Photoproduction trigger efficiency.</i>	70
6.1	<i>Generated energy distributions for the <math>D^{*+}</math> and <math>D^{*-}</math> mesons in the decays <math>D^{*\pm} \rightarrow (K^{\mp}\pi^{\pm})\pi_s^{\pm}</math>.</i>	79
6.2	<i>Reconstruction efficiency as a function of the <math>D^*</math> energy in the decays <math>D^{*\pm} \rightarrow (K^{\mp}\pi^{\pm})\pi_s^{\pm}</math>.</i>	79
6.3	<i>Reconstructed momentum distributions for the decay products in the decays <math>D^{*\pm} \rightarrow (K^{\mp}\pi^{\pm})\pi_s^{\pm}</math>.</i>	79
6.4	<i>Mass resolutions in the decays <math>D^{*\pm} \rightarrow (K^{\mp}\pi^{\pm})\pi_s^{\pm}</math>.</i>	80
6.5	<i>Mass difference spectra for the <math>D^{*\pm}</math> decay candidates.</i>	83
6.6	<i>Background subtracted mass difference spectrum for the <math>D^{*\pm}</math> decay candidates. A clean signal can be observed near the expected mass difference.</i>	83
6.7	<i>Mass difference spectra for the <math>D^{*+}</math> decay candidates.</i>	84
6.8	<i>Mass difference spectrum for the <math>D^{*-}</math> decay candidates.</i>	84
6.9	<i>Energy spectra for neutral pions and photons from <math>D^{*0}</math> decays.</i>	89

6.10	Yield of reconstructable $D^{*0}$ decays normalised to the number of reconstructable $D^{*\pm}$ decays. . . . .	89
6.11	Monte Carlo prediction for the reconstructed $\pi^0$ mass spectrum in the decays of $D^{*0}$ mesons. . . . .	90
6.12	Reconstructed mass spectrum for the $\pi^0$ candidates in the decays of $D^{*0}$ mesons. . . . .	90
6.13	Mass difference spectrum for the $D^{*0}$ decay candidates. . . . .	91
6.14	Differential detection efficiency in the decays $D^{*\pm} \rightarrow (K^\mp \pi^\pm) \pi_s^\pm$ . . . . .	94
6.15	Energy resolution for the $D^{*\pm}$ mesons in the decays $D^{*\pm} \rightarrow (K^\mp \pi^\pm) \pi_s^\pm$ . . . . .	94
7.1	Cross-sections for the photoproduction of charm quark pairs as a function of the photon energy $E_\gamma$ . . . . .	106
B.1	Differences in the production probabilities of primarily produced charmed particles per open charm event for various fragmentation models and functions. . . . .	110
B.2	Differences in the production probabilities of primarily produced charmed particles per open charm event for various fragmentation models and functions (cnt'd). . . . .	111
B.3	Differences in the production probabilities of primarily produced charmed particles per open charm event for various fragmentation models and functions (cnt'd). . . . .	112

# List of Tables

2.1	<i>Notation for transitions in forward virtual Compton amplitudes.</i>	7
3.1	<i>Charm production processes in lepton-nucleon scattering.</i>	31
3.2	<i>Particle properties for a selected list of charmed particles.</i>	37
3.3	<i>Mass differences between various combinations of <math>D</math> and <math>D^*</math> mesons.</i>	38
3.4	<i>Selected decay channels for the <math>D</math> and <math>D^*</math> mesons.</i>	38
3.5	<i>Fragmentation model dependences in the production of charmed hadrons.</i>	46
4.1	<i>Properties of the HERMES tracking chambers.</i>	53
5.1	<i>Summary of the data quality criteria for the 1997 data set.</i>	76
6.1	<i>Event selection criteria used in the analysis of <math>D^{*\pm} \rightarrow (K^\mp \pi^\pm) \pi_s^\pm</math> decays.</i>	81
6.2	<i>Signals for the <math>D^{*\pm}</math> and <math>D^{*-}</math> decays before and after background subtraction.</i>	86
6.3	<i>Signals for the <math>D^{*+}</math> and <math>D^{*-}</math> decays without background subtraction for the individual target types.</i>	86
6.4	<i>Signals for the <math>D^{*\pm}</math> decays before and after background subtraction after all data quality cuts have been applied.</i>	87
6.5	<i>Uncorrected and effective time integrated luminosities in <math>\text{pb}^{-1}</math> split into the different target types where <math>^1\vec{H}</math> denotes polarised hydrogen. All data quality cuts have been included revealing the big impact of the pre-scaling on the unpolarised hydrogen and deuterium samples.</i>	94
6.6	<i>Integrated efficiencies for the detection of <math>D^{*\pm}</math> decays at various intermediate steps of the analysis.</i>	97
6.7	<i>Integrated efficiencies <math>\langle\epsilon\rangle_{\text{tot}}</math> for the detection of <math>D^{*\pm}</math> decays.</i>	97
6.8	<i>Extracted cross-sections for the electroproduction of <math>D^{*\pm}</math> mesons on the experimentally used target mixture.</i>	99
6.9	<i>Averaged cross-sections for the electroproduction of <math>D^{*\pm}</math> mesons.</i>	99
6.10	<i>Total cross-section for the electroproduction of open charm.</i>	100
A.1	<i>Definition of kinematical variables in deep-inelastic scattering.</i>	108
B.1	<i>Fragmentation model dependences in the production of charmed hadrons.</i>	114
B.2	<i>Fragmentation model dependences in the production of <math>D^{*\pm}</math> mesons.</i>	115
B.3	<i>Fragmentation model dependences in the production of <math>D^{*0}</math> mesons.</i>	116
B.4	<i>Fragmentation model dependences in the production of <math>D^{*\pm}</math> mesons with energies above 10 GeV.</i>	117
B.5	<i>Fragmentation model dependences in the production of <math>D^{*0}</math> mesons with energies above 10 GeV.</i>	118
C.1	<i>Fragmentation model dependences of the extracted cross-sections for the electroproduction of <math>D^{*\pm}</math> mesons.</i>	120
C.2	<i>Fragmentation model dependences of the extracted cross-section for the production of open charm in lepton-proton scattering.</i>	121

# Bibliography

- [A<sup>+</sup>:74a] J. J. Aubert et al., *Phys. Rev. Lett.* **33**, 1404 (1974).
- [A<sup>+</sup>:74b] J. E. Augustin et al., *Phys. Rev. Lett.* **33**, 1406 (1974).
- [A<sup>+</sup>:86] K. Abe et al., *Lifetimes, cross sections, and production mechanisms of charmed particles produced by 20-GeV photons*, *Phys. Rev. D* **33**, 1–18 (1986).
- [A<sup>+</sup>:87] M. I. Adamovich et al., *Cross sections and some features of charm production at  $\gamma$  energies of 20 – 70 GeV*, *Phys. Lett. B* **187**, 437 (1987).
- [ADF<sup>+</sup>:95] K. Ackerstaff, M. Düeren, M. Ferstl, M.-A. Funk, P. Green, P. Oelwein, W. Wander and P. Welch, *A Tcl/Tk based database interface to ADAMO and DAD*, in *Proc. of CHEP 95*, Rio de Janeiro, September 1995.
- [AEL:95] M. Anselmino, A. Efremov and E. Leader, *The theory and phenomenology of polarized deep-inelastic scattering*, *Phys. Rep.* **261**, 1 (1995), *Erratum: Phys. Rep.* **281**, 399–400 (1997).
- [AGIS:81] B. Andersson, G. Gustafson, G. Ingelman and T. Sjöstrand, *On high energy leptonproduction*, *Z. Phys. C* **9**, 233 (1981).
- [AGIS:83] B. Andersson, G. Gustafson, G. Ingelman and T. Sjöstrand, *Parton Fragmentation and String Dynamics*, *Phys. Rep.* **97**, 31 (1983).
- [Alt:82] G. Altarelli, *Phys. Rep.* **81**, 1 (1982).
- [AP:77] G. Altarelli and G. Parisi, *Asymptotic freedom in parton language*, *Nucl. Phys. B* **126**, 298 (1977).
- [B<sup>+</sup>:69a] E. D. Bloom et al., *Phys. Rev. Lett.* **23**, 930 (1969).
- [B<sup>+</sup>:69b] M. Breidenbach et al., *Observed behavior of highly inelastic electron-proton scattering*, *Phys. Rev. Lett.* **23**, 935 (1969).
- [B<sup>+</sup>:93] R. Brun et al., *GEANT - Detector Description and Simulation Tool*, CERN Program Library Long Writeup W5013, CERN CN Division, Application Software and Databases Group, Geneva, Switzerland, 1993.

- [BC:83] A. Bialas and T. Chmaj, *Phys. Lett.* **B 133**, 241 (1983).
- [Bec:00] M. Beckmann, *Extraction of polarised quark distributions of the nucleon from deep-inelastic scattering at the HERMES experiment*, PhD thesis, Albert-Ludwigs-Universität Freiburg, Germany, May 2000.
- [Ben:98a] T. Benisch, *Polarisierte Bhabha-Streuung und Luminositätsmessung im HERMES Experiment*, PhD thesis, Friedrich-Alexander-Universität Erlangen-Nürnberg, Germany, March 1998.
- [Ben:98b] T. Benisch, Private Communication, 1998.
- [BFR:96] R. D. Ball, S. Forte and G. Ridolfi, *Next-to-leading order determination of the singlet axial charge and the polarized gluon content of the nucleon*, *Phys. Lett.* **B 378**, 255–266 (1996).
- [BG:64] B. J. Bjorken and S. L. Glashow, *Phys. Lett.* **11**, 255 (1964).
- [BG:87] A. Bialas and M. Gyulassy, *Nucl. Phys.* **B 291**, 793 (1987).
- [BHPS:80] S. J. Brodsky, P. Hoyer, C. Peterson and N. Sakai, *The intrinsic charm of the proton*, *Phys. Lett.* **B 93**, 451 (1980).
- [Bjo:69] J. D. Bjorken, *Phys. Rev.* **179**, 1547 (1969).
- [BP:69] J. D. Bjorken and E. A. Paschos, *Phys. Rev.* **185**, 1975 (1969).
- [BPS:81] S. J. Brodsky, C. Peterson and N. Sakai, *Intrinsic heavy-quark states*, *Phys. Rev.* **D 23**, 2745–2757 (1981).
- [BR:90] S. Barshay and D. Rein, *Z. Phys.* **C 46**, 215 (1990).
- [Bra:95] B. Braun, *Spinrelaxation von Wasserstoff und Deuterium in Speicherzellen*, PhD thesis, Ludwig-Maximilian-Universität München, Germany, June 1995.
- [Bro:98] S. Brons, *Analysis of  $D^{*+} \rightarrow D^0 \pi^+$  and  $D^{*-} \rightarrow \bar{D}^0 \pi^-$  in the 1996 and 1997 HERMES data*, HERMES internal note 98-057, 1998.
- [C<sup>+</sup>:75a] U. Camerini et al., *Photoproduction of the  $\Psi$  Particles*, *Phys. Rev. Lett.* **35**, 483–486 (1975).
- [C<sup>+</sup>:75b] E. G. Cazzoli et al., *Phys. Rev. Lett.* **34**, 1125 (1975).
- [C<sup>+</sup>:83] A. Chen et al., *Phys. Rev. Lett.* **51**, 634 (1983).
- [C<sup>+</sup>:98] C. Caso et al., *Review of Particle Physics*, *Eur. Phys. J.* **C 3**, 1 (1998).
- [CCFR:98] U. K. Yang et al. (CCFR Collaboration), *Measurements of the longitudinal structure function and  $|V_{cs}|$  in the CCFR experiment*, in *Proceedings of the 6th International Workshop on Deep Inelastic Scattering and QCD (DIS98)*, pages 131–136, Brussels, Belgium, April 4–8, 1998.



- [CG:69] C. G. Callan and D. J. Gross, *Phys. Rev. Lett.* **23**, 156 (1969).
- [COMPASS:96] G. Baum et al. (COMPASS Collaboration), *COMPASS: A proposal for a Common Muon and Proton apparatus for Structure and Spectroscopy*, 1996, CERN/SPSLC 96-14.
- [d'A:95a] G. d'Agostini, *A multidimensional unfolding method based on Bayes' theorem*, *Nucl. Instrum. Methods A* **362**, 487–498 (1995).
- [d'A:95b] G. d'Agostini, *Probability and measurement uncertainty in physics – a Bayesian primer* –, <http://arXiv.org/abs/hep-ph/9512295>.
- [DGMV:97] M. Düren, P. Geiger, N. Makins and E. Volk, *The HERMES Monte Carlo documentation*, 1997, <http://www-hermes.desy.de/~herprod>.
- [dS<sup>+</sup>:98] D. de Schepper et al., *The HERMES polarized <sup>3</sup>He internal gas target*, *Nucl. Instrum. Methods A* **419**, 16 (1998).
- [dSHJ<sup>+</sup>:00] D. de Schepper, J. O. Hansen, H. E. Jackson, T. G. O'Neill, D. Potterveld and J. L. Orrell, *The HERMES Čerenkov detector*, HERMES internal note 00-021, 2000.
- [Due:95] M. Dueren, *The HERMES experiment: From the design to the first results*, Habilitation thesis, Germany, 1995.
- [E139:94] J. Gomez et al. (E139 Collaboration), *Measurement of the A dependence of deep-inelastic electron scattering*, *Phys. Rev. D* **49**, 4348–4372 (1994).
- [E140:90] L. W. Whitlow, S. Rock, A. Bodek, S. Dasu and E. M. Riordan (E140 Collaboration), *A precise extraction of  $R = \sigma_L/\sigma_T$  from a global analysis of the SLAC deep inelastic  $e-p$  and  $e-d$  scattering cross sections*, *Phys. Lett. B* **250**, 193 (1990).
- [E140:94] S. Dasu et al. (E140 Collaboration), *Phys. Rev. D* **49**, 5641 (1994).
- [E143:98] K. Abe et al. (E143 Collaboration), *Measurements of the proton and deuteron spin structure functions  $g_1$  and  $g_2$* , *Phys. Rev. D* **58**, 112003:1–54 (1998).
- [E143:99] K. Abe et al. (E143 Collaboration), *Measurements of  $R = \sigma_L/\sigma_T$  for  $0.03 < x < 0.1$  and fit to world data*, *Phys. Lett. B* **452**, 194–200 (1999).
- [E154:97] K. Abe et al. (E154 Collaboration), *Phys. Lett. B* **405**, 180 (1997).
- [E665:95] M. R. Adams et al. (E665 Collaboration), *Shadowing in inelastic scattering of muons on carbon, calcium and lead at low  $x_{Bj}$* , *Phys. Rev. Lett.* **74**, 1525–1529 (1995).
- [EFP:82] R. K. Ellis, W. Furmanski and R. Petronzio, *Nucl. Phys. B* **207**, 1 (1982).

- [EMC:83a] J. J. Aubert et al. (EMC Collaboration), *Production of charmed particles in 250 GeV  $\mu^+$ -iron interactions*, Nucl. Phys. **B 213**, 31–64 (1983).
- [EMC:83b] J. J. Aubert et al. (EMC Collaboration), *Production of charmonium in 250 GeV  $\mu^+$ -iron interactions*, Nucl. Phys. **B 213**, 1–30 (1983).
- [EMC:83c] J. J. Aubert et al. (EMC Collaboration), *The Ratio of the Nucleon Structure Functions  $F_2^N$* , Phys. Lett. **B 123**, 275 (1983).
- [EMC:89] M. Arneodo et al. (EMC Collaboration), *Measurement of the  $u$  valence quark distribution function in the proton and  $u$  quark fragmentation functions*, Nucl. Phys. **B 321**, 541–560 (1989).
- [EMC:91] J. Ashman et al. (EMC Collaboration), *Forward produced hadrons in  $\mu p$  and  $\mu d$  scattering and investigation of the charge structure of the nucleon*, Z. Phys. **C 52**, 361–388 (1991).
- [EN:89] R. K. Ellis and P. Nason, *QCD radiative corrections to the photoproduction of heavy quarks*, Nucl. Phys. **B 312**, 551–570 (1989).
- [F<sup>+</sup>:77] G. J. Feldman et al., *Observation of the decay  $D^{*+} \rightarrow D^0 \pi^+$* , Phys. Rev. Lett. **38**, 1313–1315 (1977).
- [FC:98] G. J. Feldman and R. D. Cousins, *Unified approach to the classical statistical analysis of small signals*, Phys. Rev. **D 57**, 3873–3889 (1998).
- [Fey:69] R. P. Feynman, *Very high-energy collisions of hadrons*, Phys. Rev. Lett. **23**, 1415 (1969).
- [Fey:72] R. P. Feynman, *Photon-hadron interactions*, Benjamin, Reading, MA, 1972.
- [FF:78] R. D. Field and R. P. Feynman, *A parameterization of the properties of quark jets*, Nucl. Phys. **B 136**, 1–76 (1978).
- [FK:72] J. I. Friedmann and H. W. Kendall, Ann. Rev. Nucl. Part. Sci. , 203 (1972).
- [FMNR:95] S. Frixione, M. L. Mangano, P. Nason and G. Ridolfi, *Total cross sections for heavy flavour production at HERA*, Phys. Lett. **B 348**, 633–645 (1995).
- [FMP<sup>+</sup>:97] S. Frixione, M. L. Mangano, E. Predazzi, P. Nason and G. Ridolfi, *Heavy-quark production*, in *Heavy Flavours II, Advanced Series on Directions in High Energy Physics*, edited by A. J. Buras and M. Lindner, World Scientific Publishing Co., Singapore, 1997.
- [FNR:95] S. Frixione, P. Nason and G. Ridolfi, *Differential distribution for heavy flavour production at HERA*, Nucl. Phys. **B 454**, 3–24 (1995).
- [FS:81] L. L. Frankfurt and M. I. Strikman, *On high energy leptonproduction*, Nucl. Phys. **B 181**, 22 (1981).

- [Fun:98] M.-A. Funk, *A measurement of the polarised parton densities of the nucleon in deep-inelastic scattering at HERMES*, PhD thesis, Universität Hamburg, Germany, 1998.
- [G<sup>+</sup>:76] G. Goldhaber et al., Phys. Rev. Lett. **37**, 255 (1976).
- [G<sup>+</sup>:77] G. Goldhaber et al., Phys. Lett. **B 69**, 503 (1977).
- [Gei:98] P. Geiger, *Measurement of the fragmentation functions at HERMES*, PhD thesis, Ruprecht-Karls Universität Heidelberg, Germany, February 1998.
- [GIM:70] S. L. Glashow, J. Iliopoulos and L. Maiani, Phys. Rev. **D 2**, 1285 (1970).
- [GN:72a] V. N. Gribov and L. N. Lipatov.
- [GN:72b] V. N. Gribov and L. N. Lipatov.
- [Got:74] K. Gottfried, Phys. Rev. Lett. **32**, 957 (1974).
- [GP:96] T. Gousset and H. J. Pirner, Phys. Lett. **B 375**, 349 (1996).
- [GR:88] M. Glück and E. Reya, *Spin-dependent parton distributions in polarized deep inelastic lepton nucleon scattering*, Z. Phys. **C 39**, 569–573 (1988).
- [H1:96] S. Aid et al. (H1 Collaboration), *Photoproduction of  $D^{*\pm}$  mesons in electron-proton collisions at HERA*, Nucl. Phys. **B 472**, 32–51 (1996).
- [H1:99] C. Adloff et al. (H1 Collaboration), *Measurement of  $D^*$  meson cross sections at HERA and determination of the gluon density in the proton using NLO QCD*, Nucl. Phys. **B 545**, 21–44 (1999).
- [Han:63] L. N. Hand, Phys. Rev. **129**, 1834 (1963).
- [HERMES:90] K. Coulter et al. (HERMES Collaboration), Proposal, 1990, DESY-PRC-90-01.
- [HERMES:93] K. Coulter et al. (HERMES Collaboration), Technical Design Report, 1993, DESY-PRC-93-06.
- [HERMES:98] K. Ackerstaff et al. (HERMES Collaboration), *The HERMES spectrometer*, Nucl. Instrum. Methods **A 417**, 230–265 (1998).
- [HERMES:00a] A. Airapetian et al. (HERMES Collaboration), *Measurement of the spin asymmetry in the photoproduction of high- $p_T$  hadrons at HERMES*, Phys. Rev. Lett. **84**, 2584–2588 (2000).
- [HERMES:00b] K. Ackerstaff et al. (HERMES Collaboration), *Nuclear effects on  $R = \sigma_L/\sigma_R$  in deep-inelastic scattering*, Phys. Lett. **B 475**, 386 (2000).

- [Hey:74] A. J. Hey, *What do we learn from deep inelastic scattering with polarized targets?*, in *Proc. 9th Rencontre de Moriond: High energy leptonic interactions*, March 3-9, 1974.
- [HM:83] E. Hoffman and R. Moore, *Z. Phys. C* **20**, 71 (1983).
- [HS:98] B. W. Harris and J. Smith, *Phys. Rev. D* **57**, 2806 (1998).
- [IRS:96] G. Ingelman, J. Rathsman and G. A. Schuler, *AROMA 2.2 - A Monte Carlo generator for heavy flavour events in ep collisions*, DESY-96-058.
- [Ji:97a] X. Ji, *Phys. Rev. D* **55**, 7114 (1997).
- [Ji:97b] X. Ji, *Phys. Rev. Lett.* **78**, 610 (1997).
- [Kai:97] R. Kaiser, *Measurement of the spin structure of the neutron using polarised deep-inelastic scattering*, PhD thesis, Simon Fraser University, Vancouver, Canada, 1997.
- [KNP:96] B. Kopeliovich, J. Nemchik and E. Predazzi, *Hadronization in nuclear environment*, in *Proc. of the Workshop on Future Physics at HERA*, edited by G. Ingelman, A. De Roeck and R. Klanner, pages 1038–1042, DESY, Hamburg, Germany, 1996.
- [Kol:98a] M. Kolstein, *Exclusive  $\rho^0$ -meson electroproduction at HERMES*, PhD thesis, Vrije Universiteit te Amsterdam, The Netherlands, October 1998.
- [Kol:98b] H. Kolster, *The HERMES gaseous internal polarized proton target and its use in the HERA positron storage ring*, PhD thesis, Ludwig-Maximilians-Universität München, Germany, February 1998.
- [Kop:90] B. Kopeliovich, *Phys. Lett. B* **243**, 141 (1990).
- [Kum:97] S. Kumano, *Flavour asymmetry of antiquark distributions in the nucleon*, <http://arXiv.org/abs/hep-ph/9702367>.
- [LP:82] E. Leader and E. Predazzi, *An introduction to gauge theories and the “new physics”*, Cambridge University Press, 1982.
- [M<sup>+</sup>:93] I. McLaren et al., *EPIO - Expertimental Physics Input Output Package*, CERN Program Library Long Writeup I101, CERN CN Division, Application Software and Databases Group, Geneva, Switzerland, 1993.
- [Mei:00] F. Meißner, *Measurement of the  $J/\Psi$ -cross section and double-spin asymmetries in vector meson production in polarised lepton-nucleon scattering at HERMES*, PhD thesis, Humboldt-Universität Berlin, Germany, February 2000.

- [Men:98] F. Menden, *Measurement of the valence quark spin distributions of the nucleon using deep inelastic scattering at HERMES*, Master's thesis, Simon Fraser University, Vancouver, Canada, 1998.
- [MN:92] M. L. Mangano and P. Nason, *Heavy quark multiplicities in gluon jets*, Phys. Lett. **B 285**, 160–166 (1992).
- [MT:97] W. Melnitchouk and A. W. Thomas, Phys. Lett. **B 414**, 134 (1997).
- [N<sup>+</sup>:77] H. K. Nguyen et al., Phys. Rev. Lett. **39**, 262 (1977).
- [NA14/2:93] M. P. Alvarez et al. (NA14/2 Collaboration), *Study of charm photoproduction mechanisms*, Z. Phys. **C 60**, 53–62 (1993).
- [Nac:77] O. Nachtmann, in *Weak Interactions*, Eds. M. K. Gaillard and M. Nicolic, Institut National de Physique Nucleaire et de Physique de Particules, Paris, 1977.
- [Nac:86] O. Nachtmann, *Phänomene und Konzepte der Elementarteilchenphysik*, Vieweg, 1986.
- [NDE:88] P. Nason, S. Dawson and R. K. Ellis, *The total cross section for the production of heavy quarks in hadronic collisions*, Nucl. Phys. **B 303**, 607–633 (1988).
- [NMC:91] P. Amaudruz et al. (NMC Collaboration), *Gottfried sum from the ratio  $F_2^n/F_2^p$* , Phys. Rev. Lett. **66**, 2712–2715 (1991).
- [NMC:92] P. Amaudruz et al. (NMC Collaboration), *Measurements of  $R^d - R^p$  and  $R^{Ca} - R^C$  in deep inelastic muon scattering*, Phys. Lett. **B 294**, 120–126 (1992).
- [NMC:93] M. Arneodo et al. (NMC Collaboration), *Quark and gluon distributions and  $\alpha_s$  from nucleon structure functions at low  $x$* , Phys. Lett. **B 309**, 222–230 (1993).
- [NMC:95] P. Amaudruz et al. (NMC Collaboration), *A re-evaluation of the nuclear structure function ratios for  $D$ ,  $He$ ,  ${}^6Li$ ,  $C$  and  $Ca$* , Nucl. Phys. **B 441**, 3–11 (1995).
- [NMC:96] M. Arneodo et al. (NMC Collaboration), *The  $Q^2$  dependence of the structure function ratio  $F_2^{Sn}/F_2^C$  and the difference  $R^{Sn} - R^C$  in deep inelastic muon scattering*, Nucl. Phys. **B 481**, 23–39 (1996).
- [NMC:97] M. Arneodo et al. (NMC Collaboration), *Measurement of the proton and deuteron structure functions,  $F_2^p$  and  $F_2^d$ , and of the ratio  $\sigma_L/\sigma_T$* , Nucl. Phys. **B 483**, 3–43 (1997).
- [NNNT:96] F. S. Navarra, M. Nielsen, C. A. A. Nunes and M. Teixeira, *Intrinsic charm component of the nucleon*, Phys. Rev. **D 54**, 842–846 (1996).

- [Oel:95] P. Oelwein, *Messung der longitudinalen Elektronenpolarisation beim Speicherring HERA und Monte-Carlo-Studien zur Kalibration des HERA-Elektronen-Polarimeters*, diploma thesis, Max-Planck-Institut für Kernphysik Heidelberg, Germany, 1995.
- [OPAL:95] R. Akers et al. (OPAL Collaboration), *Measurement of the multiplicity of charm quark pairs from gluons in hadronic  $Z^0$  decays*, Phys. Lett. **B 353**, 595–605 (1995).
- [Ous:94] J. K. Ousterhout, *Tcl and Tk Toolkit*, Addison-Wesley Massachusetts, 1994.
- [P<sup>+</sup>:76] L. Peruzzi et al., Phys. Rev. Lett. **37**, 569 (1976).
- [Pan:68] W. K. H. Panofsky, in *Proc. of the 14th International Conference on High Energy Physics, Vienna*, CERN Scientific Information Service, Geneva, 1968.
- [PHE:92] August 1992, BNL-PROPOSAL-R5.
- [PNN<sup>+</sup>:98] S. Paiva, M. Nielsen, F. S. Navarra, F. O. Duares and L. L. Barz, Mod. Phys. Lett. **13**, 2715 (1998).
- [Pro:94] Programming Techniques Group, *ADAMO - An entity-relationship programming system, Version 3.3*, ECP Division, CERN, Geneva, 1994.
- [PSSZ:83] C. Peterson, D. Schlatter, I. Schmitt and P. M. Zerwas, *Scaling violations in inclusive  $e^+e^-$  annihilation spectra*, Phys. Rev. **D 27**, 105–111 (1983).
- [Rit:83] K. Rith, *Review of present structure function data*, in *Proc. Int. Conf. on High Energy Physics, Brighton*, Rutherford Laboratory, 1983.
- [Rob:90] R. G. Roberts, *The structure of the proton*, Cambridge University Press, Cambridge, 1990.
- [Ruh:99] M. Ruh, *Measurement of the polarised quark distributions of the nucleon at HERMES*, PhD thesis, Albert-Ludwigs-Universität Freiburg, Germany, October 1999.
- [Sey:94] M. H. Seymour, Z. Phys. **C 63**, 99 (1994).
- [Sey:95] M. H. Seymour, Nucl. Phys. **B 436**, 16 (1995).
- [Shi:00] T. Shin, *The nuclear dependence of structure function ratios from unpolarised deep inelastic scattering*, PhD thesis, Massachusetts Institute of Technology Boston, Massachusetts, USA, February 2000.
- [Sjö:94] T. Sjöstrand, *High energy physics event generation with PYTHIA 5.7 and JETSET 7.4*, Computer Phys. Comm. **82**, 74 (1994).
- [SMC:98] B. Adeva et al. (SMC Collaboration), Phys. Rev. **D 58**, 112002 (1998).

- [SSV:88] T. Sloan, G. Smadja and R. Voss, *The quark structure of the nucleon from the CERN muon experiments*, Phys. Rep. **162**, 45 (1988).
- [ST:64] A. A. Sokolov and I. M. Ternov, Sov. Phys. Dokladi **8**, 1203 (1964).
- [STAR:99] S. E. Vigdor et al. (STAR Collaboration), 1999, hep-ex/9905034.
- [SU:85] K. Saito and T. Uchiyama, Z. Phys. **A 322**, 299 (1985).
- [Tal:98] H. Tallini, *Measurement of the quark spin distributions of the nucleon at HERMES*, PhD thesis, University of Liverpool, Great-Britain, 1998.
- [Tip:99] B. E. Tipton, *Measurement of polarised parton distributions with spin-dependent deep-inelastic scattering*, PhD thesis, Massachusetts Institute of Technology, Boston, Massachusetts, USA, 1999.
- [VBH:92] R. Vogt, S. J. Brodsky and P. Hoyer, Nucl. Phys. **B 383**, 643 (1992).
- [vdB<sup>+</sup>:97] J. F. J. van den Brand et al., *Evidence for Nuclear Tensor Polarization of Deuterium Molecules in Storage Cells*, Phys. Rev. Lett. **78**, 1235–1238 (1997).
- [vH:00] J. J. van Hunen, *Deep-Inelastic Scattering off <sup>14</sup>N*, PhD thesis, University Utrecht, The Netherlands, March 2000.
- [Vol:97] E. Volk, *Towards total cross-sections: Tracking efficiencies*, talk presented at HERMES Collaboration Meeting, August 1997, DESY, Hamburg.
- [vW:34] C. F. von Weizsäcker, Z. Phys. **88**, 612 (1934).
- [WAD<sup>+</sup>:95] W. Wander, K. Ackerstaff, M. Düeren, M. Ferstl, M.-A. Funk, P. Green, P. Oelwein, D. Potterveld and P. Welch, *DAD - Distributed ADAMO Database System at HERMES*, in *Proc. of CHEP 95*, Rio de Janeiro, September 1995.
- [Wan:96] W. Wander, *Rekonstruktion hochenergetischer Streueignisse im HERMES Experiment*, PhD thesis, Friedrich-Alexander-Universität Erlangen-Nürnberg, Germany, April 1996.
- [Wat:82] A. D. Watson, *Spin-spin asymmetries in inclusive muon proton charm production*, Z. Phys. **C 12**, 123–125 (1982).
- [Wei:98] C. Weiskopf, *Untersuchung der Bhabha-Asymmetrien mit dem HERMES-Luminositätsmonitor*, diploma thesis, Friedrich-Alexander-Universität Erlangen-Nürnberg, Germany, 1998.
- [Wil:34] E. J. Williams, Phys. Rev. **45**, 729 (1934).







